Data-Driven Framework for QoE-Optimized and Congestion-Aware Deployment of Public EV Charging Infrastructure

Nassr Al-Dahabreh

A Thesis

in

The Department

of

Concordia Institute for Information Systems Engineering

Presented in Partial Fulfillment of the Requirements

For the Degree of

Doctor of Philosophy

in

Information and Systems Engineering at

Concordia University

Montréal, Québec, Canada

January 2026

CONCORDIA UNIVERSITY
SCHOOL OF GRADUATE STUDIES

It is hereby certified that the thesis prepared

By: **Mr. Nassr Al-Dahabreh**

Thesis title: **Data-Driven Framework for QoE-Optimized and Congestion-Aware Deployment of Public EV Charging Infrastructure.**

and submitted in partial fulfillment of the requirements for the degree of

Doctor of Philosophy (Information and Systems Engineering)

complies with the regulations of the University and meets the accepted standards with respect to originality and quality.

Signed by the final examining committee:

	Chair
Dr. Carol Fung	
	Thesis Supervisor
Dr. Chadi Assi	
	Thesis Co-Supervisor
Dr. Ribal Atallah	
	Arms-Length Examiner
Dr. Mohsen Ghafouri	
	Examiner
Dr. Nizar Bouguila	
	Examiner
Dr. Sandra Cespedes	
	External Examiner
Dr. Diala Naboulsi	

Approved by

Chair of Department or Graduate Program Director

01/16/2026

Dr. Mourad Debbabi, Dean
Gina Cody School of Engineering and Computer Science

Abstract

Data-Driven Framework for QoE-Optimized and Congestion-Aware Deployment of Public EV Charging Infrastructure.

Nassr Al-Dahabreh, Ph.D.

Concordia University, 2026

As electric-vehicle (EV) adoption accelerates, driven by policy commitments and financial incentives, the public charging network must scale to meet rising demand while preserving a satisfactory quality of experience (QoE). Infrastructure growth is uneven across regions, producing local capacity shortfalls that erode user confidence and deter public charging use. Addressing these challenges requires systematic visibility into session dynamics, robust demand forecasts, and principled deployment rules that reduce uncertainty in per-site waiting-time estimation. This thesis develops analytical, theoretical, and data-driven methods to: (i) characterize per-site session dynamics and waiting-time statistics; (ii) define reliable, key QoE metrics (waiting time, blocking probability, utilization, queue length); (iii) deliver a client-server decision-support platform for site-level visualization and diagnostics; (iv) propose demand-management incentives and queueing models to improve QoE; and (v) quantify and forecast the QoE impact of new deployments. Using large, real-world datasets, the study shows that charging times are frequently better modeled by Erlang-k distributions and that per-site request processes can be accurately approximated by single-server queueing systems under common scheduling policies. These empirical findings establish the probabilistic foundation required for reliable waiting-time estimation and capacity planning. The derived QoE metrics drive a tailored machine-learning forecasting pipeline trained on empirical data, and extensive simulation validates the forecasts and supports evidence-based expansion decisions. To limit overload and reduce congestion, the thesis introduces a Data-driven, Incentive-based Charging Truncation (DICT) policy that encourages drivers to stop charging near 80% state of charge. A closed-form fit for the resulting service-time distribution is derived and analyzed within an M/G/C/K queueing framework. DICT is benchmarked against resizing and proximity-based expansion strategies to identify conditions where incentive policies outperform or complement physical expansion. Finally, a counterfactual machine-learning framework estimates how Level-3 fast-charger deployments affect congestion and QoE at nearby sites. The framework controls for spatial proximity, charger capacity

and power ratings, and local amenities; it maps counterfactual demand trajectories into queueing inputs to produce site-level QoE forecasts that inform deployment choices. Together, these contributions integrate empirical discovery, queueing theory, forecasting, decision-support software, and incentive design to enable capacity-aware, QoE-preserving expansion of public EV charging infrastructure.

Acknowledgments

I gratefully acknowledge the many people whose expertise, encouragement, and support made this Ph.D. possible. My deepest gratitude goes to my supervisor, Professor Chadi Assi, for his exemplary mentorship and sustained intellectual leadership. His incisive feedback, high standards for clarity, and unwavering encouragement guided this research from conception to completion. Professor Assi's generosity with his time and his readiness to challenge and refine ideas have been central to my development as a scholar and have substantially strengthened the quality of this thesis.

I am profoundly thankful to my co-supervisor, Dr. Ribal Atallah, for his insightful technical guidance and practical support. Dr. Atallah's constructive critiques and domain expertise contributed significantly to the formulation and validation of the key models and methods presented here.

I also wish to express my appreciation to the members of my examination committee, Dr. Nizar Bouguila and Dr. Sandra Cespedes, for their thoughtful reviews, incisive questioning, and constructive recommendations. Their diverse perspectives and careful scrutiny helped broaden the scope of this work and improve its clarity and practical relevance. I am likewise grateful to Prof. Maurice Khabbaz, Dr. Mohammad Ali Sayed, and Dr. Mohamed Elhattab for their timely feedback and suggestions during the research stages. In addition, I would like to express my sincere appreciation to the External Examiner, Dr. Diala Naboulsi, and the Arms-Length Examiner, Dr. Mohsen Ghafouri, for kindly agreeing to join my examination committee and for their valuable time and insights.

Warm thanks to my colleagues at Concordia University. Their technical assistance, collaborative spirit, and stimulating discussions made complex problems approachable and turned long hours into productive teamwork. I value the many informal conversations and shared problem solving sessions that materially advanced this project. Above all, I am eternally grateful to my parents and to my extended family for their unconditional love, patience, and enduring belief in me. Their trust laid the foundation for every milestone achieved here. I dedicate this thesis to them with deep respect and heartfelt thanks.

Contents

List of Figures

List of Acronyms

Table 1: List of Acronyms

Short	Long form
AC	Alternating Current
AI	Artificial intelligence
AMI	Advanced Metering Infrastructure
ARIMA	Autoregressive Integrated Moving Average
BEVs	fully Battery-powered EVs
Bi-LSTM	Bidirectional Long Short-Term Memory
BMS	Battery Management System
ConvLSTM	Convolutional Long-Short-Term Memory Networks
CSDP	Charging Station Dimensioning and Placement
CSF	Closest Station First
CSs	Charging Stations
DC	Direct Current
DICT	Data-driven Incentive-based Charging Truncation
EREVs	Range Extender EVs
ETS	Exponential Smoothing
EV	Electric Vehicle
EVCP	per-EV charger power
EVCR	EV-to-Charger Ratio
EVCSs	EV Charging Stations
EVs	Electric Vehicles
EVSE	Electric Vehicle Supply Equipment
GCN	Graph Convolutional Networks
GNNs	Graph Neural Networks
HQ	Hydro-Quebec
hr	Hour
ICE	Internal Combustion Engine
IEA	International Energy Agency
IRS	Incentive-augmented Resizing
kW	kiloWatt
kWh	kiloWatt-hour
L2	Level 2
L3	Level 3

(continued on next page)

Short	Long form
LDV	Light-Duty Vehicle
LSTM	Long Short-Term Memory networks
ML	Machine Learning
MSE	Mean Squared Error
MWT	Minimum Waiting Time
NDS	New Site Deployment
P-EVCSs	Public EV Charging Stations
PCI	Public Charging Infrastructure
PHEVs	Plug-in Hybrid Electric Vehicles
PMU	Phasor Measurement Unit
QoE	Quality of Experience
QoS	Quality of Service
RSS	Random Station Selection
SARIMAX	Seasonal Autoregressive Integrated Moving Average Exogenous
SCADA	Supervisory Control and Data Acquisition
SoC	State of Charge
SRS	Site Resizing
SVM	Support Vector Machine

Chapter 1
Introduction

Overview

As the urgency to address climate change grows, governments, industry, and communities worldwide are accelerating the shift from fossil-fuel transport to electric mobility. The transition is already substantial: Global EV sales, including Battery Electric Vehicles (BEVs) and Plug-in Hybrid Electric Vehicles (PHEVs), increased from about 14.2 million units in 2023 to roughly 17 million units in 2024 [11], an increase of approximately 2.8 million vehicles ($\approx 19.7\%$). Actual EV sales in 2024 also exceeded that year's market estimate of 16.5 million EVs by about 0.5 million vehicles, as illustrated in Figure 1.1. BEVs accounted for approximately 10.63 million units of 2024 sales ($\approx 62.5\%$ of total EV sales), while PHEVs contributed roughly 6.38 million units ($\approx 37.5\%$) [12]. Early 2025 data indicate the momentum persists: EVs comprised roughly 22% of new-EV sales in the first five months of 2025, and the market is forecast to expand by about 25% for the full year, reaching ≈ 21.8 million new electric cars [13].

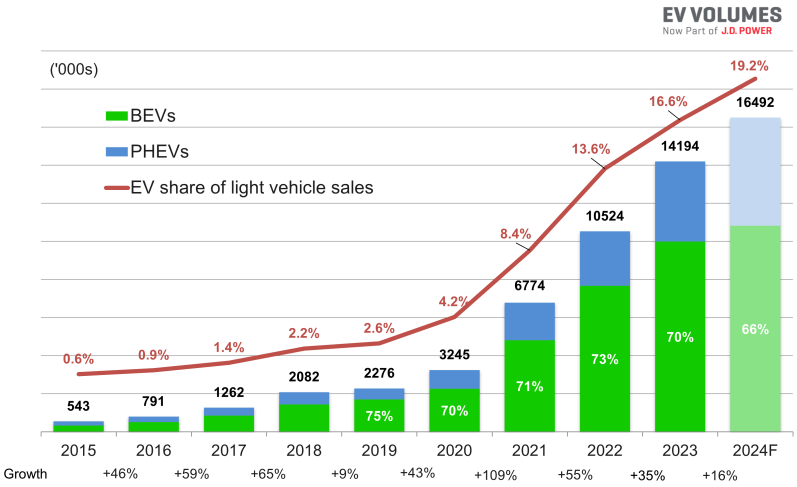

Figure 1.1: Global sales of new BEV and PHEV vehicles (2014–2024) [1].

While home charging remains the dominant charging method for many EV owners, the scale

and distribution of public EV charging infrastructure are now the decisive constraints for broader adoption, especially for drivers without private charging access. Public EV charging capacity grew very quickly in 2024. Figure 1.2 illustrates trends in the global stock of public charging points, broken down by speed and region, from 2018 to 2024.

In 2024, more than 1.3 million public charging points were brought online worldwide, an annual increase of over 30%. The number of chargers deployed in that single year was roughly equivalent to the entire global public charging stock in 2020. Expansion has been geographically concentrated: about two-thirds of the net growth since 2020 occurred in China, which today accounts for roughly 65% of global public charging points and approximately 60% of the world's electric light-duty vehicle (LDV) fleet. [2].

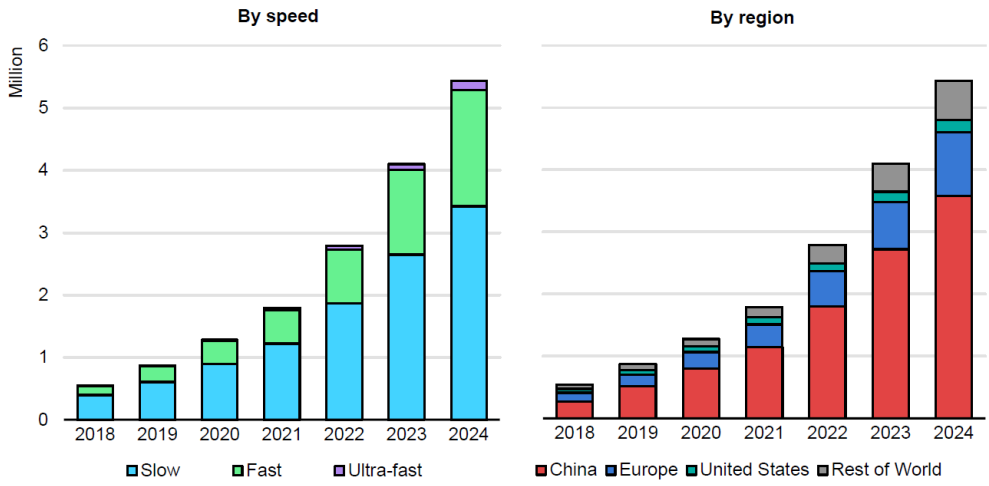

Notes: Chargers less than or equal to 22 kW are classified as slow, chargers greater than 22 kW and up to 150 kW as fast, and 150 kW and above as ultra-fast.
Sources: IEA analysis based on country submissions and data from EV Volumes and EAFO.

Figure 1.2: Global stock of public charging points by speed and region, 2018–2024. [2]

Europe likewise saw substantial growth: public charging points on the continent rose by more than 35% in 2024 compared with 2023, bringing the total to just over 1 million. Expansion across the European Union (EU) was uneven: 11 of the 27 Member States increased their public charging stock by more than 50% in 2024. At the national level, the Netherlands recorded the largest fleet of public points with more than $180,000, followed by Germany ($\approx$ 160,000) and France ($\approx$ 155,000). Austria added roughly 8,000 public chargers in 2024, most of which were supported through a subsidy program that ended at the start of 2025. These figures underscore both the rapid pace of deployment and the persistent geographic imbalances, highlighting

the need for targeted, regionally informed investment. Beyond simple counts, charging power, measured in kilowatts (kW), is crucial for evaluating whether public infrastructure can satisfy EV demand. Higher-power fast and ultra-fast stations deliver substantially more energy per site each day, increasing throughput and reducing dwell times. By 2024, the global stock of fast chargers (22–150 kW) reached about 2 million, while ultra-fast chargers (≥ 150 kW) expanded by more than 50% in 2024 and now constitute approximately 10% of the fast-charger fleet. Declining hardware costs have supported this shift: average prices for ultra-fast chargers fell by roughly $\approx 20\%$ between 2022 and 2024 [2].

China accounted for the bulk of global fast-charging growth in 2024: its fast-charger stock increased from about 1.2 million in 2023 to roughly 1.6 million in 2024, yielding an estimated public charging capacity in excess of greater than 3 kW per electric light-duty vehicle (LDV). The United States expanded absolute fast-charger counts from roughly $40{,}000$ in 2023 to more than $50{,}000$ in 2024, but in the United States (U.S.), the public charging capacity remains below ≈ 1.5 kW per LDV. The EU accelerated deployment as well: excluding ultra-fast units, the EU's fast-charger stock climbed nearly 50% year-on-year to $\approx 71{,}000$ in 2024 (implying an average public charging capacity near 2.6 kW per LDV). EU ultra-fast deployment was also strong (about $+60\%$, to more than $77{,}000$), and roughly 20% of EU ultra-fast points now provide ≥ 350 kW, reflecting operator preparations for future higher-power vehicles [2].

National statistics expose divergent short-term patterns that underline a trade-off between charger availability (EVs per public charger or per Electric Vehicle Supply Equipment (EVSE)) and charging throughput (kW per EV), as shown in Figure 1.3. From 2023 to 2024 several large markets registered increases in EVs per public charger, United States $26 \rightarrow 32.6$, Canada $21 \rightarrow 27.6$, China $8 \rightarrow 9.6$, the Netherlands $5 \rightarrow 5.5$, and Japan $18 \rightarrow 18.6$, indicating mounting pressure on access where charger roll-out lagged vehicle growth. At the same time, most of these countries upgraded the average public charging power available per vehicle, moving toward higher-capacity stations that raise throughput and shorten dwell times (for example, Germany $0.8 \rightarrow 2.5$ kW/EV, Sweden $0.9 \rightarrow 2.2$ kW/EV, the UK $0.6 \rightarrow 1.4$ kW/EV, the US $0.8 \rightarrow 1.3$ kW/EV, and the Netherlands $2.5 \rightarrow 3.2$ kW/EV). Despite a small year-on-year decline, China still records the highest public charging capacity per light-duty vehicle (LDV) in this sample (approximately ≈ 3.2 kW/EV) [2]. These concurrent trends show that higher-power stations increase throughput but do not automatically resolve spatial access gaps. A public charging site with many ultra-fast chargers can serve more vehicles per day, yet residents of dense urban

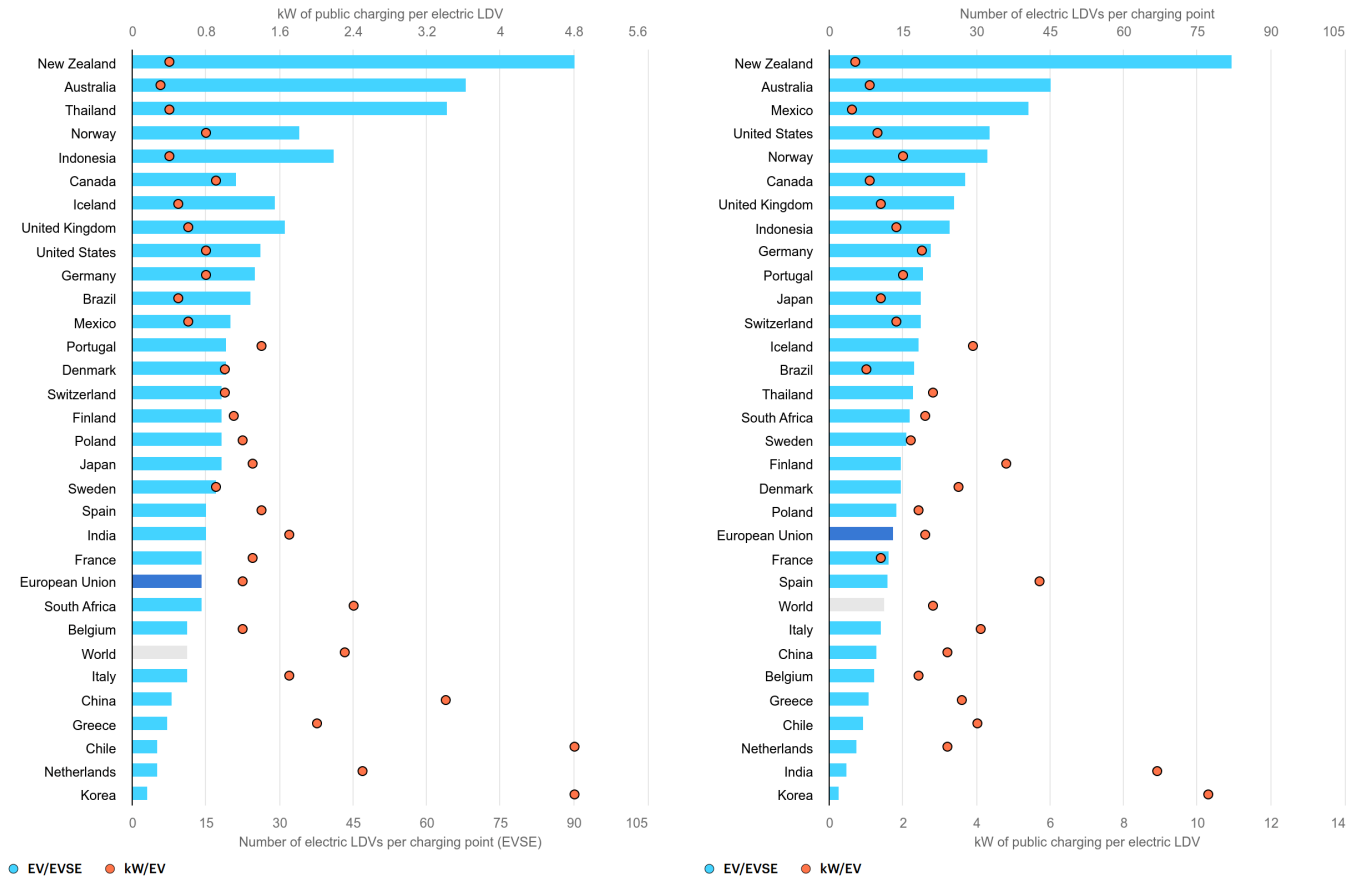

(a) 2023 (b) 2024

Figure 1.3: Number of electric light-duty vehicles per public charging point and kilowatt per electric light-duty vehicle (2023–2024). Sources: [3, 4].

neighborhoods without private parking can still face limited day-to-day access if charger counts in those neighborhoods are inadequate.

Policy benchmarks provide useful calibration points. The European Union's Alternative Fuels Infrastructure Regulation (AFIR) benchmark implies roughly 1.3 kW of public charging capacity per BEV, while the International Energy Agency's (IEA) Announced Pledges Scenario points toward an operational average nearer ≈ 1.6 kW per EV. A practical planning range of about 1.3–1.6 kW/EV, combined with urban density targets of 10–15 EVs per public charger in areas where home charging is limited, provides a pragmatic rule-of-thumb to reconcile access and throughput objectives.

In practice this implies a mixed site strategy:

- Deploy many lower-power or destination chargers across urban neighbourhoods to relieve access pressure and keep EVs per public charger low.
- Concentrate fast and ultra-fast chargers on corridors and hub locations (motorway interchanges, logistics nodes, major service areas) to raise local kW/EV, increase throughput, and shorten dwell times.

Guided by targets near 1.3–1.6 kW/EV and urban EV/charger goals of less than (10–15) EVs per charger where home charging is limited, this combined approach may help ensure both reliable access and efficient service as EV fleets continue to expand. Although national level indicators track broad trends, they are neither sufficient nor reliably indicative of user Quality of Experience (QoE) at individual public charging sites, which directly shape drivers' experiences. Assessing these indicators' success therefore requires site-level monitoring and user-centric metrics rather than relying solely on aggregated stock and capacity figures.

The QoE of EV users at public EV charging stations depends on availability, convenience and reliability. Poorly distributed or insufficiently managed infrastructure generates operational inefficiencies, excess strain on popular stations during peak hours, long waiting times, and underutilized assets elsewhere, all of which undermine user confidence and slow EV adoption. Real-time tracking and forecasting of EV demand patterns, waiting times, occupancy and station reliability are therefore essential for informed deployment decisions. Key performance metrics, such as the EV-to-charger ratio and kW-per-EV are useful but partial; richer, data-driven, key metrics, measures and predictive analytics enable planners to model future demand, identify optimal locations and prioritize investments to minimize congestion and improve QoE.

Accordingly, the combined evidence from vehicle sales, charger rollouts and power-capacity

trends (2020–2024, into early 2025) points to a clear conclusion: continued, targeted investments are required to achieve both equitable access and adequate throughput. Rapid expansion has begun to close the gap, but the uneven geographic distribution of chargers and divergent national trajectories mean that planning must be both local and strategic. A balanced programme, mixing high counts of lower-power urban chargers with strategically placed fast/ultra-fast hubs, and powered by real-time data and predictive analytics, will best support QoE, reduce range anxiety and enable the next stage of rapid EV adoption.

1.1 Problem Statement and Motivation

Accelerating the adoption of electric vehicles (EVs) requires accurate site-level waiting-time estimates, robust QoE metrics, and scalable capacity-planning policies for the Public Charging Infrastructure (PCI) of EVs. However, the expansion of PCI has not kept pace with the rapid growth of EV adoption, creating operational challenges and diminishing user satisfaction. A key issue is the scarcity of precise data on EV arrival times and charging behaviors, which leads to unreliable waiting-time estimates and undermines QoE. widespread private charging both stresses local distribution networks and leaves public chargers under-utilized, while range anxiety persists due to long, unpredictable queues and inconsistent service durations. Attempts to use surveillance cameras for arrival detection face feasibility, security, and synchronization challenges and cannot capture external drivers such as weather, road conditions, traffic policies, or sudden shifts in EV penetration caused by emergencies or grid disruptions. These limitations highlight the need for novel, data-driven methods to accurately characterize and model EV arrivals at the public EV charging stations. Likewise, much of the recent literature depends on simplifying assumptions (e.g., Poisson arrivals, exponential service times) that misrepresent real-world dynamics involving traffic flows, heterogeneous road networks, and dynamic operator policies.

Such simplifications generate inaccurate performance metrics, obscure site-level congestion, and hinder effective planning. Also, existing global QoE metrics, such as EV-per-Charger Ratio (EVCR) and per-EV Charger Power (EVCP) neglect critical factors such as waiting times, blocking probabilities, and utilization patterns, limiting their diagnostic value. Furthermore, the absence of reliable long-term (multi-year) forecasting models prevents operators from anticipating rising EV demand, and little work has evaluated planning strategies across diverse EV communities. Addressing these research gaps is essential for sustainable PCI deployment and

maintaining user confidence in public charging systems.

In response to these challenges, this thesis presents a data-driven investigation and forecasting framework that: accurately models the public EV charging service, defines and implements novel QoE metrics tailored to public EV charging, implement and trains machine-learning models on empirical records to forecast long-term EV charging demand, and translates those forecasts into quantitative recommendations for capacity-expansion decisions that preserve acceptable QoE. The thesis also introduces an interactive Django/python tool to compute and visualize site-level QoE metrics, including utilization, waiting time, occupancy, and blocking, with configurable spatial and temporal filters. The tool features a location-aware mapping interface to reveal bottlenecks and high EV-demand clusters and support data-driven planning.

To reduce persistent overloads during the public EV charging service, this thesis proposes a Data-driven Incentive-based Charging Truncation (DICT) policy. The empirical service-time distributions observed under DICT are fitted to closed-form theoretical models and embedded within an M/G/1/K analytical queue to quantify blocking, waiting, and utilization impacts. Extensive simulation runs and empirical validation verify model fidelity, and DICT is benchmarked against alternative strategies such as resizing and proximity-based deployments, generating practical, evidence-based guidance for planners and operators.

Finally, a causal deployment-evaluation framework is introduced, leveraging large-scale machine learning method to estimate counterfactual EV demand trajectories for proposed and actual Level-3 EV charging sites deployments. These demand projections are translated into M/G/C/K queue inputs to quantify both congestion displacement and congestion relief at nearby incumbent EV charging stations, enabling accurate assessment of deployment impacts on network-wide QoE.

Accordingly, this section outlines the motivation and the precise problem statements addressed by the thesis.

1.1.1 Leveraging Real-World Data Sets For QoE Enhancement In Public Electric Vehicles Charging Networks

This thesis targets enhancing the quality of charging experience in Electric Vehicle (EV) Public Charging Infrastructure (PCI) networks. The estimation uncertainty of waiting times at charging stations (CSs) hinders the proliferation of such networks and, hence, decelerates EV adoption. Currently, most EV owners prefer to use private chargers; thus, overloading the energy distribu-

tion network leaving PCIs under-utilized. Consequently, it becomes important for PCI operators to provide customers with accurate waiting time estimates at various CSs; therefore, allowing them to make more informed CS selections. The per-CS EV waiting times reveal possible CS overloads, which, when frequently repetitive, indicate the need for PCI up-scaling to satisfy increasing demands; hence, ensuring elevated customer QoE. we leverage recent real-world data to unveil the statistical properties of EV charging times that, unlike existing studies, are found to be best captured by an Erlang-k distribution. Also, the per-CS charging request arrival processes are characterized under various scheduling policies. It is established hereafter that CSs can be accurately modelled as single-server queuing systems. Finally, extensive simulations are conducted to verify the accuracy of the proposed models and provide further insights into the waiting time performance achieved by each of the adopted scheduling policies.

1.1.2 A Data-Driven Framework for Improving Public EV Charging Infrastructure: Modeling and Forecasting

This thesis presents an investigation and assessment framework, which, supported by realistic data, aims at provisioning operators with in-depth insights into the consumer-perceived Quality-of-Experience (QoE) at public Electric Vehicle (EV) charging infrastructures. Motivated by the unprecedented EV market growth, it is suspected that the existing charging infrastructure will soon be no longer capable of sustaining the rapidly growing charging demands; let alone that the currently adopted ad hoc infrastructure expansion strategies seem to be far from contributing any quality service sustainability solutions that tangibly reduce (ultimately mitigate) the severity of this problem. Without suitable QoE metrics, operators, today, face remarkable difficulty in assessing the performance of EV Charging Stations (EVCSs) in this regard. We aim at filling this gap through the formulation of novel and original critical QoE performance metrics that provide operators with visibility into the per-EVCS operational dynamics and allow for the optimization of these stations' respective utilization. Such metrics shall then be used as inputs to a Machine Learning model finely tailored and trained using recent real-world data sets for the purpose of forecasting future long-term EVCS loads. This will, in turn, allow for making informed optimal EV charging infrastructure expansions that will be capable of reliably coping with the rising EV charging demands and maintaining acceptable QoE levels. The model's accuracy has been tested and extensive simulations are conducted to evaluate the achieved performance in terms of the above-listed metrics and show the suitability of the recommended infrastructure expansions.

1.1.3 A Novel Data-driven Incentive-based Charging Service Truncation Scheme to Improve the QoS Performance of Public EV Charging Stations

This thesis addresses the inadequate Electric Vehicle (EV) public charging infrastructure expansion strategies currently adopted by operators with a particular focus on EV-user-perceived Quality of Service (QoS). Our real-world case studies of Public EV Charging Stations (P-EVCSs) reveal the continuous deterioration of QoS despite increasing P-EVCS deployments. This is mainly due to excessive charging overload; a tangible proof of the ill-designed expansion scheme. Herein, a Data-driven Incentive-based Charging Truncation (DICT) scheme is proposed to alleviate the per-P-EVCS load by encouraging EV users to limit charging their batteries once they reach an 80% State of Charge (SoC). A mathematical framework is established to characterize the statistical properties (particularly probability distributions) of the per-EV service time under DICT. Precisely, extensive simulations of the DICT EV charging policy were conducted to collect a 10^6 sample EV service time dataset. Thorough numerical analyses fit these samples' probability distribution with a theoretical distribution whose closed-form expression is derived. An analytical M/G/1/K queueing model is then established to capture P-EVCS dynamics and characterize its performance in terms of QoS metrics. Extensive simulations are carried out to validate the proposed queueing model and assert its accuracy compared to real-world data, yielding an average error of [2.85%–12.57%] for blocking probability, [2.08%–5.85%] for the average waiting queue length, and [2.48%–6.45%] for the average waiting time. Finally, DICT is benchmarked against alternative strategies, including site resizing and in-proximity new site deployments to offer strategic insights and recommendations to improve public EV charging infrastructure and sustaining QoS.

1.1.4 A Data-Driven Framework for Improving Public EV Charging Infrastructure Deployment: Quantifying EV Demand Shifting Via Machine Learning

We present a cause-and-effect evaluation framework to quantify how new Level-3 public EV charging stations (P-EVCSs) affect congestion and user Quality of Experience (QoE) at nearby incumbent sites. Moving beyond correlational analyses, the framework uses a with/without comparative design with empirical controls for spatial proximity, charger capacity (port counts

and power ratings), and surrounding amenity access. It estimates counterfactual "what-if" EV demand trajectories through large-scale machine learning models, maps those projections to proper input parameters for M/G/C/K queueing models, which, in turn, are used to estimate key performance metrics such as the average waiting time, utilization and queue length. Validation using empirical charging records shows that counterfactual scenarios consistently predict higher session volumes, utilization, and queueing than actual scenarios, which are further amplified by seasonality. The analysis indicates that the examined recent deployment site functions as an effective absorptive node for surrounding sites, with effectiveness varying according to those sites' capacities and locations. Nevertheless, the deployment exhibits a low average waiting time (≈ 0.174 minutes), modest utilization ($\approx 2.2\%$), and negligible average blocking ($\approx 0.035\%$ EVs), and so physically relieved nearby sites during peak periods. Site-level findings show marked congestion displacement: removal of a recently deployed high-power Level-3 (L3) site (i.e, Site A2) results in an approximately 92.6% increase in waiting time at the nearby mid-sized Site A3; The study finds that prioritizing the deployment of high-power L3 sites within approximately ≈ 3 km of target areas is associated with a substantial congestion-relief effect. Accordingly, this thesis provides operators/service providers and planners with a data-driven approach to evaluate and optimize fast charging P-EVCS deployment strategies in evolving urban environments.

1.2 Thesis Main Contributions

The key contributions of this thesis are summarized as follows:

- **Accurate waiting time modeling for public EV charging stations:**

  A thorough numerical analysis of most recent, real-world EV charging records extracted from public EV charging stations (EVCSs) network is conducted to characterize per-station service time statistics and arrival processes. A mathematical framework is developed that models any EVCS as a realistic stochastic single-server queuing system, dynamically captures system behavior under different EV-to-CS allocation schemes, and derives closed-form waiting time distributions and the per-CS average waiting time. A custom and high fidelity simulation environment is developed for certifying the analytical model and generates extensive numerical results for critical QoE metrics (utilization and average waiting time), supporting practical insights into infrastructure dimensionality and

preliminary resolution strategies for rapid EV penetration.

- **QoE metrics and long-term load forecasting for PCI operators:**

  A comprehensive data-driven framework fills the identified gap in per-site QoE evaluation and long-term demand forecasting for Public Charging Infrastructure (PCI). A suite of novel per-EVCS QoE metrics are formulated and implemented to provide operators with event-driven, station-level visibility into utilization and operational dynamics, enabling informed charger deployment and network sizing. Historical charging records and relevant exogenous features are incorporated into a machine learning forecasting model to generate accurate, site-level EV demand projections up to one year ahead. Empirical validation and simulation experiments demonstrate the framework's applicability for QoE-aware, data-driven infrastructure expansion planning.

- **Interactive Client–Server Decision-Support Tool for Analysis at the City and Site Levels:**

  A Django/python web-framework decision support tool is designed and implemented to visualize, analyze, and interpret city/site specific EVCS performance. The tool computes and fetches empirical and model-based QoE metrics (utilization, waiting time, charger occupancy, blocking probability), supports customizable temporal and spatial queries (daily activity, 4-hour windows, weekday/weekend differentiation), and provides an interactive, location aware mapping interface to identify bottlenecks and high demand clusters for targeted planning, resource allocation, and maintenance scheduling. The core back-end and front-end components are implemented mainly in python, HyperText Markup Language, version 5 (HTML5), and cascading style sheets (CSS), and several performance metrics are computed from a subset of analyzed public EV charging sites.

- **Develop a data-driven Incentive-based Charging Truncation (DICT) scheme to sustain QoE:**

  The DICT scheme incentivizes the truncation of public EV charging at approximately 80% state of charge (SoC) to reduce per-charger occupancy and increase effective service capacity during the public charging service. A set of 10^6 simulated per-EV service time durations is used to identify a highly accurate approximation of the service time distribution under the DICT scheme and to derive a closed-form expression that improves the

scheme's analytical tractability. An analytical M/G/1/K queueing model is developed to capture P-EVCS dynamics under DICT and quantifies the impacts on key performance metrics. DICT is benchmarked against multiple alternative and hybrid schemes, such as Site Resizing Scheme (SRS), New Site Deployment Scheme (NDS), and Incentive- augmented Resizing Scheme (IRS) using a thorough simulation framework. The performance of EVCSs is evaluated mainly across utilization, average waiting time, blocking probability, number of blocked EVs, number of served EVs, and number of waited EVs.

- **Causal evaluation of Level-3 deployments and site-level congestion effects:**

  A causal inference framework is developed to isolate the true effect of new Level-3 fast charging sites deployment on EV charging demand and QoE at the public EV charging infrastructure, moving beyond correlational analyses. The framework controls for critical confounders (spatial proximity, dynamic charging outlet capacities in terms of ports and power ratings, and local amenity access) and generates counterfactual EV demand trajectories via large-scale, customized machine learning model. The counterfactual projections are mapped to M/G/C/K queueing inputs to estimate waiting time, utilization, and waiting queue length at each public EV charging site. Also, temporal tracking of public EV demand evolution at new deployments enables detection of sustained QoE impacts and emerging congestion hotspots, thereby supporting prescriptive site selection and deployment decisions.

1.3 Thesis Structure and Organization

The remainder of this thesis is structured as follows. Chapter 2 presents the background and reviews the relevant literature. Chapter 3 presents a numerical analysis of recent, real-world EV charging records and develops a stochastic single-server queueing framework to derive per-station waiting time distributions and average waiting time. Chapter 4 formulates a suite of per-site QoE key performance metrics and describes a machine learning forecasting pipeline that estimates one year, site-level EV demands projections to support QoE-aware expansion planning. Chapter 5 describes the design and implementation of an interactive Django/python client–server decision support tool for site-level visualization and analysis of QoE. Chapter 6 introduces the Data-driven Incentive-based Charging Truncation (DICT) scheme, derives its M/G/1/K analytical formulation, and presents extensive simulation benchmarks. Chapter 7 develops a causal

inference framework to evaluate Level-3 deployments and their congestion effects on neighboring sites, mapping counterfactual EV demands to queueing impacts. Chapter 8 concludes the thesis and outlines directions for future research and practical deployment.

Chapter 2
Background and Literature Review

This chapter begins with key concepts and technologies for EVs and public EV charging, followed by a detailed literature review that demonstrates the thesis's significance and original contributions as discussed in Chapter 1.2.

2.1 Background

2.1.1 A concise history of EVs

Battery Electric Vehicles (BEVs) have undergone repeated cycles of rapid advancement and adoption followed by periods of decline, only to regain attention when technological, economic, or regulatory conditions shift. Although frequently portrayed as a recent innovation, the technical foundations of EVs reach back to the nineteenth century.

EVs possess several fundamental advantages that explain the current resurgence of interest: they eliminate tailpipe emissions, demand less routine mechanical maintenance than internal combustion vehicles, and can operate on a variety of low carbon energy sources. Continuous improvements in energy storage and power electronics have steadily increased driving range and performance while lowering lifecycle costs. Together, these factors make EVs a leading option for reducing transport emissions and improving urban air quality when deployed at scale.

The evolution of EVs can be usefully segmented into six broad periods:

- **1830–1880: Early innovations.** The first experiments combining electric motors and batteries with wheeled platforms occurred in the early nineteenth century. Inventors across Europe and North America built small demonstration vehicles and electric-driven carts. Early battery technology limited range and operational practicality, but these demonstrations established the basic feasibility of electrically powered road vehicles.

- **1880–1914: First commercial wave.** Advances in rechargeable battery chemistry and motor design in the late nineteenth century enabled the first commercially useful electric

vehicles. Manufacturers produced passenger cars, city taxis, and light delivery vehicles suited to urban use, where short distances and access to electricity were advantageous. In some cities, electric vehicles briefly held a substantial share of the local market because they were quiet, easy to operate, and well matched to short urban trips.

  - **Trouvé Tricycle (1881).** Gustave Trouvé's three-wheeler demonstrated compact electric propulsion with a battery-mounted motor and an unusual asymmetric wheel layout, making it an early example of an urban EV.

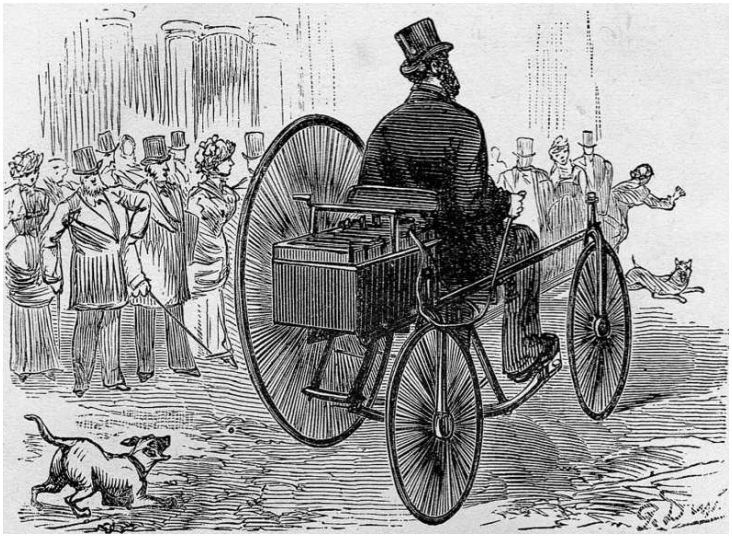

Figure 2.1: Trouvé Tricycle (1881). [5]

- **1914–1970: Market retreat.** A convergence of technological, economic, and infrastructural developments shifted the balance toward gasoline-powered cars. Mass production techniques, falling fuel costs, improvements in internal combustion engines, and innovations such as the electric starter expanded the practicality and affordability of gasoline vehicles. As a result, electric vehicles lost commercial momentum and largely disappeared from mainstream markets through the mid-twentieth century.

- **1970–2003: Reappraisal and prototypes.** Rising fuel prices, oil shocks, and growing environmental awareness prompted renewed research into electric and hybrid drivetrains beginning in the 1970s. Industry and government programs produced prototypes and limited trials; regulators began to consider stricter emissions standards. Although many vehicles developed in this period had limited range and modest performance by modern

standards, these projects sustained technical expertise and public awareness of alternative propulsion technologies.

  - **General Motors (GM) EV1 (late 1990s).** GM's lease-only EV1 demonstrated modern EV capabilities (roughly an 80 mile range and brisk acceleration) but the program was later discontinued; it remains a notable case in modern EV history.

Figure 2.2: General Motors EV1 (late 1990s). [6]

- **2003–2020: Commercial resurgence.** The early twenty-first century brought dramatic improvements in lithium-based batteries, power electronics, and vehicle integration. New entrants and legacy manufacturers began producing commercially viable passenger EVs that combined practical range, strong performance, and modern conveniences. Declining battery costs and policy support made electrified vehicles progressively more competitive, accelerating consumer adoption.

- **Commercial vehicle electrification.** Electric powertrains have long been used in niche commercial applications, vehicles with frequent stop–start duty cycles (for example, milk floats and urban delivery trucks) are especially well suited to electric operation because of high idling losses for Internal Combustion Engine (ICE) vehicles. Recent improvements in battery energy density and charging systems, together with regulatory pressure to reduce fleet emissions, have triggered larger scale deployment of battery electric trucks and buses across a growing set of use cases.

Several recurring factors explain why electric vehicles have alternated between prominence and obscurity:

- **Energy storage technology:** battery weight, energy density, cost, and charging time strongly influence vehicle range and economics.
- **Fuel and infrastructure economics:** the relative price and availability of liquid fuels, and the presence (or absence) of charging infrastructure, affect consumer choices.
- **Manufacturing and cost reductions:** scale economies and production methods determine affordability.
- **Regulation and policy:** emissions standards, purchase incentives, and fleet mandates can accelerate or redirect industry investment.
- **Use-case fit:** operational patterns (urban vs. long-distance travel, stop–start vs. continuous highway driving) influence where electrification is most competitive.

Accordingly, today's EV deployment is driven by a combination of technological progress, industrial investment, and policy support. Major manufacturers (e.g., General Motors, Mercedes-Benz, Volkswagen) have committed to significantly expanding their electric lineups, regulators in many jurisdictions are tightening vehicle-emissions standards, and fleet purchasers are increasingly adopting zero-emission trucks and buses where economically and operationally feasible. Continued reductions in battery costs, improvements in charging infrastructure, and supportive policy frameworks will be decisive in determining the speed and scale of the transition.

Respectively, the history of electric vehicles shows that technical feasibility alone is not sufficient: economic conditions, infrastructure, policy, and the match between vehicle capabilities and user needs all matter. The present period differs from earlier cycles because of stronger alignment among technology, policy, and public concern about climate and air quality. Whether EVs continue to expand will depend on how these drivers evolve and whether electrification remains the most practical solution for decarbonizing mobility across passenger and commercial segments.

Source: Rizon Truck, "A History of Electric Vehicles: The Ups, Downs, & Ups." `https://www.rizontruck.com/blogarticle/a-history-of-electric-vehicles-timeline-the-ups-downs-ups/`.

2.1.2 Evolution of EVs charging

EVs adoption has driven parallel advances in charging technology and infrastructure. As EVs moved from niche experiments to mainstream models, charging systems evolved from primitive rectifier installations to a diverse ecosystem of home, public, and high-power rapid chargers.

Early developments. Electrically powered automobiles required external power conversion early on. In the first decades of the twentieth century, industrial rectifiers such as the Mercury Arc Rectifier were installed in homes, garages, and public parking facilities to supply Direct Current (DC) power suitable for charging vehicle batteries. These early chargers were practical for small, local fleets but limited by the prevailing battery and electrical-distribution technologies of the era.

- **General Electric (GE) Mercury Arc Rectifier (c. 1912).** One of the first electric car chargers, this device converted Alternating Current (AC) to DC for vehicle batteries and was installed in both private and public charging contexts.

Figure 2.3: GE Mercury Arc Rectifier, circa 1912. An early electric car charger. [7].

Late twentieth-century milestones. Commercial and demonstration programs during the 1990s marked the first modern integration of dedicated charging equipment with consumer electric vehicles. In 1996 General Motors introduced the EV1, a lease-only passenger car whose provision included a home charging installation capable of replenishing the vehicle's battery over several hours. The early 2000s saw the emergence of publicly accessible charging points; the installation of one of the first public chargers in California (circa 2002) represented a turning point in making charging available beyond private garages.

- **General Motors EV1 (1996).** In 1996 GM introduced the lease-only EV1 with home charger; the program was ended in 1999.

Acceleration in the 2000s and 2010s. The introduction of mainstream and high-performance EVs accelerated charger development. Tesla's 2008 Roadster broadened expectations for performance and daily usability, and later mass-market models such as the 2010 Nissan Leaf made overnight home charging a practical solution for many drivers. Tesla's Model S (introduced in

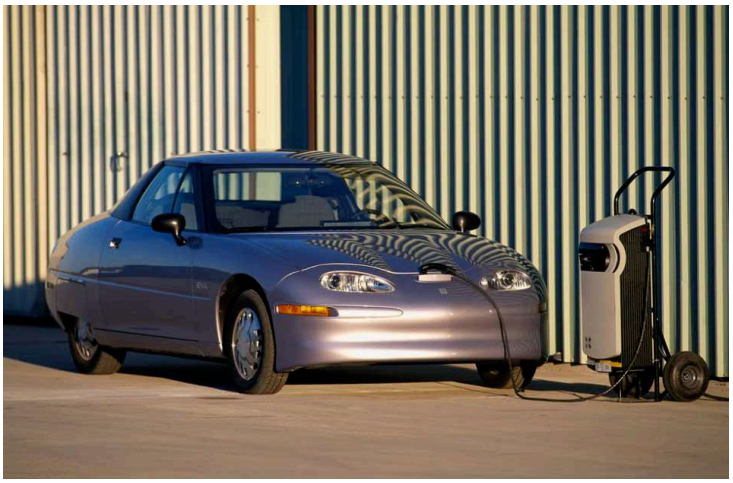

Figure 2.4: Figure 8. EV1 home charging station (c. 1996). [8].

the early 2010s) further advanced charging expectations by demonstrating fast-charge capability in networked fast-charging stations, enabling partial recharges on timescales suitable for longer trips.

Trends and outlook. EV charging technology continues to improve in energy transfer rate, interoperability, and user convenience. Networked fast charging stations, improved onsite power management, and the rollout of standardized connectors have broadened access. Emerging technologies (for example, wireless charging for stationary or dynamic use) and continued reductions in charging time are likely to complement further battery technology advances. As EV ownership expands, charging infrastructure, both public and private will remain a central enabler of electrified transport.

2.1.3 Smart Charging: Rapid Refill, Safety, and Longevity

The 20–80% charging practice for electric-vehicle (EV) lithium-ion batteries is widely recommended as a practical compromise between rapid energy replenishment and preserving cell longevity. By charging primarily within the mid-State of Charge (SoC) band (roughly 20% to 80%), vehicles can accept high charging power for the bulk of the session and avoid the pronounced current taper that occurs as SoC approaches full capacity. Limiting the upper bound to about 80% reduces heat generation and the electrochemical stresses, such as elevated cell voltages and the increased risk of lithium-plating, that accelerate capacity fade. Likewise, avoiding repeated deep discharge below $\approx$ 20% helps prevent undue mechanical and chemical strain on electrode materials. Operating within this band therefore delivers most range quickly, maintains an operational buffer for unexpected trips, and simplifies condition monitoring because batteries exposed to fewer extreme SoC cycles exhibit more predictable ageing behavior [14].

Source: Electric Car Charger, "A Short History of Electric Car Chargers." https://electriccarcharger.au/short-history-of-electric-car-chargers/.

2.1.4 Public EV Charging Ecosystem

The public EV charging ecosystem comprises several key elements, which include the following:

- **Charging Stations and Charging Types**

  The public charging stations are the physical locations where EVs can recharge their batteries. These stations are equipped with charging points or outlets that provide electrical energy to EVs. Public charging stations can be categorized based on the speed and technology used to deliver energy as follows:

  - **Level 1 Charging**: This is the slowest charging option, providing 120 volts (V) alternating current (AC) through a standard household outlet. It is rarely used in public charging infrastructure due to its long charging times. It requires between 8–12 hours to fully charge.
  - **Level 2 Charging**: A common type of public charging, this method delivers 240V AC power and is widely available at the public EV stations, homes, and workplaces. It takes around (4–8) hours to reach up to 80% SoC, as an average charging duration.
  - **DC Fast Charging (Level 3)**: Also known as ”fast charging,” this technology delivers DC to the battery, providing rapid charging (Up to 80% SoC in approximately (20–60) minutes, as an average charging duration). It is essential for long-distance travel, making it a crucial part of highway charging networks.
  - **Ultra-Fast/High-Power Chargers**: Newer ultra-fast chargers (350 kW and above) are being deployed to further reduce charging times for vehicles that are compatible with such high-power charging (Up to 80% SoC in approximately (10–20) minutes, as an average charging duration).

  The efficiency of EVCSs is influenced by the type of chargers available, the number of spots, and the operational flow of EVs using the service. The availability and configuration of these stations directly affect the speed at which EVs can be charged and how many EVs can be serviced in a given time.

- **Public EV Charging Network Service Providers/Operators**

  The public charging networks are managed by private vendors, utilities, or government bodies that operate public charging stations. Common network providers such as:

  - Tesla Supercharger Network (for Tesla vehicles).

- ChargePoint.
- Hydro-Quebec (in Canada).

These providers often provide mobile applications (apps) that help EV drivers find charging stations, check availability, and pay for charging.

- **Charging Standards**

Different standards for EV charging exist based on the connector types used, including:

- **CHAdeMO**: Common in Japanese vehicles like Nissan and Mitsubishi.
- **CCS (Combined Charging System)**: Standard in European and North American vehicles.
- **Tesla Connector**: Proprietary connector used by Tesla but compatible with adapters for other vehicles.

- **Power Grid and Renewable Energy**

The power grid and renewable energy sources are used to generate, distribute, and balance electricity demand efficiently and sustainably. P-EVCSs are integrated with the power grid, sourcing the necessary electricity from it.

- **Electric Vehicles (EVs)**

EV types are categorized according to how the vehicle is powered and how its battery is recharged. This thesis does not include non-battery technologies (e.g. hydrogen fuel-cell vehicles or other zero-emission powertrains), which are beyond the scope of this thesis. Accordingly, the most common types of EVs include:

1. **Battery Electric Vehicles (BEVs)**:
   - **Power Source**: BEVs run exclusively on electricity stored in large battery packs.
   - **Charging**: These vehicles need to be plugged into external sources such as home chargers, public charging stations, or fast chargers to recharge their batteries.
   - **Emissions**: BEVs produce zero tailpipe emissions, making them environmentally friendly.
2. **Plug-in Hybrid Electric Vehicles (PHEVs)**:

- **Power Source**: PHEVs have both a battery electric drivetrain and an Internal Combustion Engine (ICE). They can run on battery power alone or use the ICE when the battery is depleted or for extended range.
- **Charging**: The battery can be charged by plugging into an external power source, like BEVs, but PHEVs can switch to gasoline if necessary.
- **Emissions**: PHEVs have lower emissions compared to traditional gasoline vehicles, especially when driving in electric mode, but they do emit tailpipe emissions when the ICE is in use.
- **Subtype: Extended-Range Electric Vehicles (EREVs)**: A plug-in design in which the electric motor normally provides propulsion; if the battery becomes depleted, the ICE starts to generate electrical power to maintain drive, instead of directly powering the drivetrain.

3. **Hybrid Electric Vehicles (HEVs)**:
   - **Power Source**: HEVs combine a traditional internal combustion engine with an electric motor. Unlike PHEVs, they cannot be charged by plugging in; instead, the battery is charged through regenerative braking and the ICE.
   - **Emissions**: HEVs reduce emissions compared to conventional vehicles but still rely on gasoline, so they produce tailpipe emissions.

- **Waiting Spots/Queue (Pre-Charging Stage)**

  These are designated areas where EVs wait before reaching the charging outlets. This is essentially the queue before the service (charging) begins.

- **Charging Spots (Service Stage)**

  Charging spots are locations within the charging site where EVs receive service (i.e., they are actively charging). These represent the locations where EVs are plugged in to charge their batteries.

2.1.5 Public EV Charging Ecosystem: A Queuing Model Perspective

As shown in Figure (2.5) below, the public EV charging ecosystem can be understood as a complex system where EVs are serviced (charged) through a network of charging infrastructure. This ecosystem involves multiple components, each influencing the system's performance and

the user experience for EV drivers. Key components and dynamics include waiting spots, charging spots, charging sites, the number of charging outlets per site/station, service/charging time, waiting time before start charging, total system time, and charging service pricing.

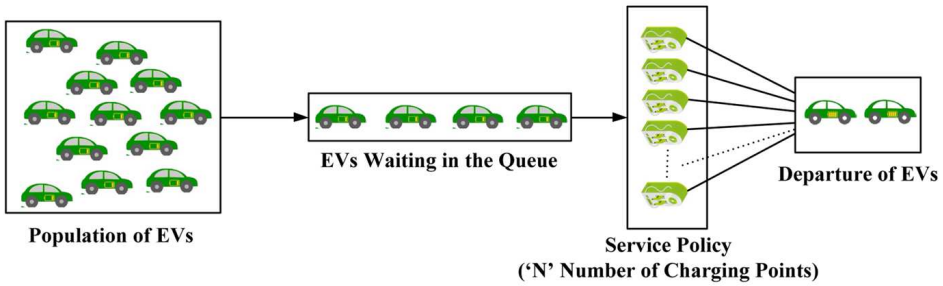

Figure 2.5: A Queuing Model for EVs Public Charging Infrastructure [9].

2.1.6 Public EV Charging Stations Dataset records

This thesis uses an extensive dataset of EV charging sessions collected from public EV charging stations in Quebec. The dataset is provided by our industrial partner. These sessions capture both slow and fast charging events across a range of charging power levels. Each recorded session includes key attributes such as the delivered/charged energy, start and end timestamps, the specific charging outlet and site identifiers, and associated geographic information. Although the dataset is rich in detail, certain information essential to our analysis is absent, most notably, the actual vehicle arrival times and any waiting durations experienced before charging. The lack of these variables poses a significant challenge in accurately characterizing the quality of experience (QoE) during public EV charging events. Addressing this limitation and developing methods to infer or estimate these missing parameters forms an important component of the analysis presented in subsequent chapters of this thesis.

Furthermore, following a comprehensive review of the available sessions, certain sessions in the dataset are deemed invalid. To ensure robust analysis and reliable model development, the dataset underwent extensive cleaning and filtering. Sessions with intervals longer than two hours, shorter than three minutes, indicating no energy consumption, or without recorded payments were systematically excluded. After this process, all valid sessions are organized chronologically by occurrence date for each station/site, with each site is assigned a unique identifier to group EV charging outlets with the same address code.

2.2 Literature Review

This chapter provides a comprehensive literature review that motivates the study and underscores the novel contributions of the thesis.

2.2.1 Related Work: Modeling Public EV Charging Dynamics and QoE Measurement

The literature encloses numerous studies that aimed at characterizing the EV charging process and most importantly crucial QoE metrics similar to those targeted in this work. Nonetheless, due to the trendy business-imposed confidentiality of realistic EV charging-related data (*e.g.*, [15]), such studies were developed using traditional and trendy approaches founded on top of inadequately created EV load profiles based on ICE data surveys. Consequently, such studies are obviously misleading especially since EVs have largely different characteristics than ICE vehicles. [16], has, in a first step, broken the custom through the revelation of $63{,}937$ real-world EV charging session data records collected between 2016 and 2019 for two regions in Scotland. Along the same lines, [17] published similar data for six major cities in Europe and the United States. This paved the way for new realistic studies to emerge, of which, those cited in the survey of [17] and, in particular, that of [18] where synthetic data generators were developed for the purpose of creating EV charging load profiles that were indistinguishable from realistic profiles and that, later on, were used by multiple researchers to evaluate the contribution of Renewable Energy Resources (*e.g.*, [19, 20]) as well as identifying peak load times (*e.g.*, [21]) and, hence, recommend guidelines for grid investment (*e.g.*, [22, 23]).

The realistic EV charging data made available to the above-surveyed studies is restrictive to specific cities/regions and, currently, can be confidently classified as being relatively outdated. Today, various regions of the world are witnessing rising multi-level partnerships between governmental authorities, third party CS operators and researchers from both academia and industry allowing these latter to grab access to recently collected EV charging-related data for the purpose of providing new accurate insights into the dynamics of EV charging processes and their impact on the grid. For instance, the authors of [24] assessed the ability of Charging Network Operators (CNOs) to optimize the utilization of charging network infrastructure through dynamic pricing schemes having the objective of driving EVs away from congested CSs and hence, reducing the EV waiting times. However, [24] failed at adequately characterizing EV mobility as none of the essential vehicular traffic parameters (*e.g.* vehicular density, speeds and flow rates) were taken into consideration regardless of their notable impact on the EVs' SoCs and, hence, waiting times.

The work of [25] paralleled the work [24] as it also aimed at developing schemes that allowed CSs to dynamically modify their service fees in a real-time manner in view of their experienced loads. Although such an approach was capable of achieving load balancing among CSs, it was built on top of highly restrictive assumptions that are impractical in nature; hence, confining this work to remain theoretical in service of benchmarking purposes only. The work of [26] addressed the problem of optimal CS placement while, in addition to pricing constraints, they jointly considered route optimization to achieve an optimal trade-off between travel times and charging costs.

The secure and economic charging infrastructure operation is a challenge that, lately, has been capturing significant attention. Truly, apt coordination between system operators and EV aggregators is of utmost importance to ensure satisfaction of security requirements while jointly minimizing EV charging costs without any EV users' energy demand violations. The work of [27] proposed a decentralized cooperative hierarchical multi-agent system whose operation is governed by an EV charging scheduling scheme that aimed at effectively achieving the aforementioned objectives without any a priori information regarding EV arrivals to the different CSs. Although seminal findings were presented therein, these were quite restricted to cost and energy consumption-related parameters' optimization. Moreover, the authors only considered use cases where EVs were being charged in parking spaces. Consequently, session times were equated to vehicle parking durations that appeared to be drawn from Weibull distributions as dictated by relatively old data collected from previous existing work (*e.g.*, [28–30]); this being contradictory to recently acquired data that confirming the inaccuracy of these distributions especially for in-transit EVs.

Now, opposite to [27], the authors of [31] considered the the United Kingdom's (UK) rising first solar EV charging forecourt and demonstrated how the expected EV load allowed for determining the system's ability to serve as a bulk power supply. With this in mind, the authors boldly underlined the importance of early EV arrivals forecast for site operational optimality. This is not to mention that learning the energy demand patterns provides insightful guidelines for site expansion and/or new site deployment at strategic locations. Yet, when operating with a limited number of chargers, the optimal scheduling of EV charging and power allocation is a problem with a wide selection of constraints (*e.g.*, battery constraints, charging time, range anxiety, delays, limited grid energy supply, etc) that have been modeled by numerous researchers (*e.g.* [32–34]) and subdivided into distinct or, sometimes, intersecting subsets. The resolutions of this problem's variants had led to the optimization of different objectives (*e.g.*, cost minimization, end SoC maximization, etc).

At this level, it is important to attract the reader's attention to the fact that the EV arrival process and, hence, the a priori prediction of energy demand are, solely, not enough to study the performance of CSs. Recently, public CS network operators have expressed an upsurged need for

insightful metric evaluations such as the experienced per-CS load, average EV service and waiting times as well as the waiting line size. Modeling individual CSs (or an aggregation thereof into mega stations) as queuing systems has proven its efficiency in evaluating such metrics. Yet, the major flaws in a wide variety of existing such models reside in: *i*) capturing these systems' operational/functional dynamics, *ii*) identifying their statistical properties, and, *iii*) modeling the various processes governing these queuing systems using accurate distributions. For instance, the work of [35] inaccurately modeled a CS as an $M/M/1$ queueing system. This is especially true since, as highlighted in the above-surveyed publications and will be further stressed hereafter according to realistic data, the EV service time (*i.e.* charging time) is not exponentially distributed. Further to that, depending on the employed CS-to-EV allocation schemes governing the distribution of EVs to the various deployed CSs in an area, the EV arrivals to a CS may not necessarily follow an Poisson process as feebly assumed in [36].

Clearly, regardless of the notable progress and proliferation of EVs and their market penetration over the last few years, the collection of EV-charging-related data from at least the past six years constitutes a tangible proof that the transportation electrification sector still has not reached a state of maturity. Indeed, the continuous EV manufacturing improvements, variety of systems embedded in these battery-powered vehicles as well as the contemporary technological advancements battery production and integration have been steadily experiencing are, by themselves, leading to significant variations in the statistical properties of energy demands, EV service and, hence, CS development and operability. All of this dictates that this field is traversing a transient period that requires continuous updates of existing analytical technical models that serve as fundamental inputs to crucial large-scale strategic planning and industrial development for governments and third party operators. The purposes of such updates is the sustainability of accuracy throughout this transition and the provisioning of useful insights into the realistic consumer QoE as well as the indication of charging infrastructure expansion necessities. Obviously, the existing literature exhibits an obvious gap in this direction; let alone the development feasibility of models with a far vision of generalization that may, with slight variations, easily account for statistical changes in demand arrivals and service processes exhibited by various CS-to-EV assignment schemes; hence, promoting future system behaviour predictability and tractability. This work aims at presenting a first step towards the closure of this gap through the presentation of a real-world data-driven analytically tractable CS queuing model that quantifies fundamental per-CS performance metrics formulated using general symbolic expressions for distribution functions representing EV arrival and charging processes. All the details pertaining to this model are presented next.

2.2.2 Related Work: Data-Driven Modeling, Forecasting, and QoE Analysis of Public EV Charging Infrastructure

EV charging demand forecasting has been a subject that has recently received significant attention; this being attested by the increasing number of published studies presenting different approaches and shedding the light on the goodness of the resulting forecasts [37]. Unfortunately, however, inputs to these existing forecasting models consist of simulated data generated by restrictive simulation frameworks that cannot really account for comprehensive real-world dynamics (*e.g.*, housing stock, area/location characteristics, EV characteristics, actual travel distances, population growth rates, among so many others) affecting EV charging processes [38, 39]. In addition, a few publications do rely on some realistic data sets that, alas, happen to be quite limited in terms of the number of recorded samples corresponding to a very limited number of attributes characterizing such processes [40, 41]. A prime selection of these studies is surveyed hereafter. Howbeit, it is important to keep in mind that the distinguishing features that differentiate this present work from these existing publications are: *i*) the exploitation of a large database of realistic records provisioning in-depth insights into actual EV charging processes taking place all over the entire Quebec province [41, 42], *ii*) beyond EV charging demand, this work presents a whole new set of QoE performance metrics and an accurate model to forecast future values of these metrics with such predicted results serving as guidelines for optimal EV charging infrastructure expansion and EV-to-charger assignment and scheduling [43].

In [44], the authors surveyed existing EV charging infrastructure planning methodologies that targeted the resolution of specific challenges addressed from either a transportation system perspective or that of a distribution network or, also, a combination of both. Most of these studies were theoretical in nature or based on custom-built simulation frameworks focusing on a limited subset of EV charging aspects while overlooking a large number of important factors due to the lack of visibility into them. For instance, the vast majority of these studies commonly limited their scope to the charging infrastructure itself with a focus on installation cost optimization while neglecting end-user QoE.

The work of [45] presented a multi-stage EVCS deployment planning framework in an attempt to achieve an acceptable trade-off between investment costs and peak distribution grid demands. Precisely, the authors attempted to balance between EV drivers' convenience and investors' revenues without compromising capacity constraints imposed by operators over a certain pre-determined time horizon. It appears that the key driver to this framework's business succcess is the actual phase-like expected growth of the EV traffic volume, which dictates the per-stage needed additional investments targeting EV infrastructure resizing and revenues thereof originating from EV consumers' satisfaction; all this being subject to power system constraints. However, unfortunately, the proposed mathematical model in [45] was, contrary to the authors'

claims, quite restrictive as, first, it was based on a relatively old and non-realistic EV traffic model proposed in [46] and its restrictive assumptions leading to fictitious and non-accurate simulated distributions of the number of EVs on the road. Second, that model adopted traffic parameter values that do not conform to EV traffic in particular but rather to the vehicular mobility of all kinds of vehicles on the roads as described by the authors' traffic data source in [47]; let alone, the fact that the collected data dates since 2016 (quite outdated) and that it does not incorporate any observations pertaining to the utilization and performance of deployed charging infrastructure back then. Last but not least, the model was too simplistic, stochastic in nature and aimed at separately optimizing individual non-related metrics; hence, failing to reach an even acceptable sub-optimal trade-off among these metrics that should have been jointly optimized.

The work of [48] presented one among the very few data-driven methodologies targeting the optimization of EVCS deployment within a given geographical area. Therein, the authors leveraged the PageRank algorithm (refer to [49]), Graph Theory, geographical aspects and trip data to estimate the spacial distribution of EV charging demands. More precisely, a considered study area was subdivided into cells and each cell received a PageRank score that described that cell's appeal to EV drivers. Next, a Regression Model (RM) was adopted for the purpose of mapping the PageRank scores to actual charging demands using data from existing EVCS. This RM's results were fed as input to a Capacitated Maximal Coverage Location Model (CMCLM) for the purpose of optimizing EVCS deployments with the objective of maximizing coverage. Unarguably, this presented methodology in [48] is ingenuous reflecting the authors' remarkable technical skills in combining trajectory data (provided by Inrix[1] partially extracted using probing sensors (*e.g.*, cell phones and automated vehicle location sensors) blending that using Google Place Application Programming Interface (API) with Point of Interest (PoI) data that reflected urban context and infers executed trip purposes and finally integrating socioeconomic data and land-use information (provided by Wasatch Front Regional Council[2]) used as features of people's parking behaviors that could impact the EV charging demand.

However, one concern, at this point, is the fact that the majority of the used data (*e.g.*, transportation-related data) is outdated (since it dates from 2016 and 2018); let alone that such data was not solely restricted to EVs but rather an entire fleet of vehicles of different types, among which are EVs. Consequently, such data may not accurately reflect current and future trends in EV adoption and EV charging demands. This is especially true given the rapid evolution of EV adoption and charging behavior patterns. Second, it is not clear how trip purposes have been linked to EV charging demand impact. It is understandable that trajectories do indicate traffic flows in and out of specific regions, of which those experiencing high traffic flows are more likely to also exhibit high EV charging demands and, hence, may constitute good lo-

[1]https://inrix.com/

[2]https://wfrc.org/

cations for new charging stations. Accordingly, regardless of its purpose, an executed trip will contribute to traffic flow variations of its outbound origin and its inbound destination. In this sense, regional clusters with high connectivity and traffic flows may, to a certain extent be considered as appropriate locations for further EVCS deployments. Third, the authors presented a complex chain of interconnected machine learning models to capture the argued multifaceted nature of EV charging demand and optimal placements of new charging stations based on a variety of factors. While, to this end, the complexity of this model appears to be a point of strength, it can also set to be a limitation of this study when it comes to interpretability, transparency, credibility and utility of generated results; let alone their accuracy. The lack of knowledge and visibility into of the existing charging stations' dynamics and, hence, the per station achieved QoE performance, in a way or another, truncates future demand expectations and, hence, alters the optimality of the charging infrastructure resizing. This drawback could not, however, be worked around by the authors of [48] given not just the difficulty but, often, the rather impossibility of accessing public EV charging stations utilization information without due authorization from such stations' operators/owners. This is an issue that this present work does not suffer from given our pre-authorized access to such information.

The work of [50] presents a data-driven management framework for EV charging stations with the objective of allowing operators/consumers to plan for peak charging times and, hence, avoid congestion. Although the authors criticize some existing short-term EV demands forecasts, their work does not serve the purpose of filling such a gap. This is especially true since their deep and supervised machine learning framework only allows for only up to one-week forecasts, which, is truly far from being long-term. Also, the utilized models therein only predict the overall energy consumptions per station. Although, the authors do consider some nice features (e.g., weather conditions, distinction between regular weekdays, weekends, and holidays, etc), such are not enough to give operators/consumers an indication of a station's load, the waiting-in-line delay to receive service, the chargers' utilization and the possibility of blocking (i.e., inability to provide service to an arriving EV to the station). All such gaps are accounted for in this present work whereby the presented model herein is capable of providing one full year of forecasts (extendable to two years ahead) not just in terms of energy consumption but also in terms of all of the above-listed crucial metrics as a function of the expected EV penetration rate.

In [51], a Charging Station Dimensioning and Placement (CSDP) framework was presented with the objective of provisioning minimum-cost fast charging infrastructure targeting the accommodation of growing EV charging demands in a metropolitan area powered by a single power grid. Through CSDP, the authors jointly accounted for EVCS placement and capacity as well as the EV charging workload distribution among available EVCS to minimize EV waiting times and reduce range anxiety. They also factored in the power distribution network's voltage sensitivity, the possible need for voltage regulators (for maintaining voltage stability) and

transformers with proper rating (for supporting peak demand). The above CSDP problem was formulated into an Integer Linear Program (ILP) characterized by its remarkable complexity that the authors worked around through the development of two heuristics. The efforts invested in developing CSDP were, indeed, seminal; especially that very little information was present at that time about EV integration, charging demands, available EVCS and their underlying functional and operational dynamics. It was, truly, an epoch of assumptions and visions that researchers attempted to concretize through the development of theoretical models and approximations that they strived to bring as close as possible to reality. Today, available real-world data continues to rule out these assumptions (*e.g.*, truncated Normal distribution associated to energy demands in [52], the Normally distributed EV batter State-of-Charge (SoC) in [53], the exponential EV charging time in [51, 54], among others). Now, although the authors of [51] presented enough evidence of the feasibility of modelling an EVCS as a multi-server queueing system, their CSDP Workload Assignment (CSDP-WA) and sizing ILP formulations were founded on top of a highly restrictive approximation of that EVCS model using multiple single-server queues that was later shown to reflect overly pessimistic EV waiting time performance. Consequently, forecasting future demands and EVCS performances based on such allocated workload and sizing policies can surely not serve for proper charging infrastructure expansion planning.

The work of [55] presented a big-data driven EV charging demand forecasting model accounting for vehicular traffic volume data for both vehicles and busses as well as weather conditions in addition to other variables typically considered in other existing models (*e.g.*, initial battery SoC, battery type, charging power classifications, etc). Compared to older studies (*e.g.*, [56–59]) the authors of [55] also fed their model with the per-vehicle starting time of the charging process and initial battery SoC, which they assumed to be accurately drawn from Gaussian distributions with distinct parameters. Despite the interesting technically insightful features of the work of [55], it suffered from major drawbacks, first, pertaining to the non-realistic and inaccurate distributions the authors used to model the majority of their above-listed model's variables. Second, the work restricted the charging processes to take place in residential and workplaces for regular consumer EVs and in parking stations for busses. Third and most importantly, the historical traffic volume data used to train their model pertained to all types of vehicles on highways, national routes and local roads rather than just EV data. Regardless of the fact that such data dated since 2014 (*i.e.*, non-representative of today's current traffic states), the authors clearly mentioned the fact that EV traffic volume at that time was much less than that pertaining to other conventional vehicles. Yet, because of their ill-paused assumption that such vehicular traffic patterns may conform to future EV-exhibited patterns due to the expected significant EV penetration growth, their reported forecasting results seriously lack accurracy. This is especially true since the EV penetration growth patterns are way different than those of conventional vehicles (as attested by currently available data); let alone, the fact that today's EV

traffic patterns continue to be affected by those pertaining to typical ICE vehicles. As a matter of fact, realistically today, roads are being populated by both EV and non-EV vehicles concurrently and the presence of various publically accessible charging stations incurs significant changes in the charging demand trends. Of course such newly impactful factors did not exist back at the time when the work of [55] was published; hence, could not be considered back then.

In [60], the authors proposed a hybrid Long Short-Term Memory (LSTM) neural network with the objective of merging heterogeneous features pertaining to EV charging processes and, hence, accurately predict the discrete EV charging occupancy over a well defined time horizon. The reported results therein gauged the merit of the proposed algorithm and evidence its superiority over select existing benchmarks (*e.g.*, hyper-parameter search [61], logistic regression [62], Support Vector Machines (SVM) [63], random forest [64] and Adaboost [65]). The work of [60], indeed, aims at quantifying one fundamental metric, namely, the per-charger occupancy, proposed hereafter in this present work. As much as it is quite insightful on a technical aspect, it suffers from several drawbacks, among which, the most important is the adopted restrictive public data that describes EV charging sessions in terms of a limited number of variables allowing the designed complex forecast model to only generate relatively accurate results for only very short-term predictions ranging from 10 minutes to only almost 4 hours. Beyond that, the model's complexity exponentially overshoots in terms of the number of features to be considered as well as run-time only to exhibit incremental improvement over existing benchmarks. Of course, such a model would not be suitable nor insightful aiming at planning infrastructure expansion for months (let alone a minimum of a year) ahead. The forecast models presented in [66] and those surveyed by [67] suffer from exactly the same issue despite their elevated accuracy of the predicted station utilization and EV charging demands for a period of time that does not bypass three days. Those models and deep-learning-based algorithms, obviously, cannot be of any utility when it comes to long-term EV infrastructure expansion planning and provide only marginal insights into the per-EVCS QoS performance.

2.2.3 Related Work: Public EV Charging Station Performance, Queueing, and Incentive-Based EV Demand Shaping

Over the past decade, EV charging demand forecasting and infrastructure planning have matured substantially. Nonetheless, many models remain limited in representing real-world operations or in supporting strategic, long-term investment decisions. Early work often relied on idealized traffic scenarios, static user assumptions and simplified grid constraints, which frequently neglected user charging behavior, socioeconomic drivers, station-level utilization and perceived QoE. Representative contributions illustrate both progress and recurring limitations. Planning and siting studies have combined mobility analytics, optimization and coverage models

to propose candidate locations and phased deployment strategies. For example, Yi *et al.* fuse PageRank, trajectory data and regression to generate demand inputs for a capacitated maximal-coverage model; however, their pipeline relies on mixed-fleet mobility inputs (2016–2018) and lacks station-utilization records, which reduces demand specificity and validation ability [48,49]. Unterluggauer *et al.* survey cost- and grid-focused planning methods that typically omit QoE considerations [44]. Other spatial and bilevel planning approaches improve robustness to routing and uncertainty [68, 69], yet remain sensitive to the quality of demand inputs.

Queueing, dimensioning and ILP-based methods pioneered the joint consideration of deployment and capacity under distribution constraints. Kabir *et al.* and related works formulated placement capacity problems and proposed heuristics for tractability [51]. While seminal, some tractable queue approximations (notably single-server substitutions) can bias waiting-time estimates and mislead sizing decisions when EVCS operate as multi-server systems. Extensions that co-optimize siting, conductor upgrades and scheduling under distribution constraints help but depend on accurate demand and service models [69, 70]. Big-data and data-driven forecasting pipelines enrich models with traffic, weather and per-vehicle features (e.g., start time, SoC). Arias *et al.* and others demonstrate the value of per-vehicle inputs but sometimes rely on restrictive distributional assumptions or mixed-vehicle traffic datasets that reduce realism for modern EV patterns [55–59]. Deep and hybrid machine-learning models (e.g., Ma *et al.*'s hybrid LSTM, Spatiotemporal Prediction Network (STPNet), and Adaptive Graph-Based Network (AGBN)) capture spatiotemporal dependencies and improve short-horizon uncertainty estimates [60, 71, 72]. These approaches attain high accuracy at minutes, days horizons but typically depend on small public datasets, scale poorly without station specific tuning, and show only modest gains when naively extended to multi-month or multi-year horizons [66,67,73]. Holistic and real-time control work integrates behavioral economics, shared mobility and renewable integration. Prospect-theory pricing, shared depot access, storage scheduling and Reinforcement Learning (RL) controllers have all been shown to reduce peaks or improve QoE in simulation or controlled studies [74–77].

System level studies also warn that ignoring short-term operational limits can overstate vehicle-to-grid potential and create operational risks [78]. Field and scenario studies (e.g., Su *et al.*) illustrate how integrated deployment and operational choices can materially improve utilization, reduce wait times and reduce costs, underscoring the value of real utilization data for planning [79]. A smaller but growing literature explicitly evaluates station Quality of Service (QoS) and user-centric metrics. Many studies nonetheless focus primarily on throughput or energy delivered [80–82] or on utilization and cost minimization [57, 83], leaving fewer direct treatments of waiting time, blocking probability or station occupancy [84, 85]. Some Operations Research (OR)-based approaches have tried to model time-varying arrivals and service processes, but cascaded simplifications and inappropriate approximations often yield overly optimistic charac-

terizations of peak performance [86]. To address this, queueing studies such as Antoun *et al.* estimate generalized service time distributions from data to derive closed-form waiting time, queue-length and blocking expressions [54]. ElHattab *et al.* show that Erlang-k fits observed charging service times well and use transform techniques to obtain tractable waiting-time results and natural extensions for modeling reneging [87]. Contemporary work on *censored demand* documents how supply insufficiency suppresses observed demand, complicating demand quantification and resource-allocation decisions [88, 89].

Building on this queueing and censored-demand literature, we propose a data-driven, incentive-based *Charging Service Truncation* scheme (DICT). Unlike censored demand (unobserved demand suppressed by scarcity), DICT actively incentivizes drivers currently charging at a public EVCS to truncate their session once a predefined SoC threshold is reached (e.g., 80% SoC). By encouraging voluntary early termination, DICT increases outlet turnover and the admissibility of queued arrivals, thereby reducing mean waiting time $\overline{W}$ and blocking probability P_B when drivers accept incentives. Crucially, DICT generates observable truncation events and measurable reductions in per-EV service times, enabling empirical quantification of QoS improvements and informing operator decisions on resizing, scheduling and incentive design. In sum, prior work advances forecasting, siting and real-time control but leaves four main gaps: (1) scarcity of large, up-to-date, station-level empirical datasets for validated station modeling; (2) incomplete integration of exogenous, capacity and QoE features into forecasts; (3) insufficient per-site tuning and scalability of predictive models; and (4) the challenge of generating robust long-horizon forecasts and reliable uncertainty bounds. The present study addresses these gaps by leveraging a province-wide, pre-authorized EVCS dataset, integrating station-level capacity and exogenous features, evaluating multi-horizon forecasts (including one-year horizons), and linking predicted QoS metrics to practical resizing and deployment decisions using the DICT incentive mechanism as a concrete, empirically testable intervention.

2.2.4 Related Work: Data-Driven, QoE-Aware Planning for Public EV Charging

Over the past decade, EV charging demand forecasting and infrastructure planning have matured into rich fields of study. Yet despite numerous contributions, many models remain unable to reflect the intricacies of real-world operations or to support strategic, long-term investment decisions. Early academic work typically relied on idealized traffic scenarios, static user behaviors, and simplified grid constraints. As a result, they overlooked critical elements, such as EV users charging behavior, socioeconomic influences, station-level utilization and occupancy, and above all, the user's perceived QoE. Unterluggauer *et al.* studied several cost-focused planning models that largely ignored QoE. Vashisth *et al.* proposed a multi-stage deployment scheme,

only to examine its realism undercut by outdated traffic inputs and synthetic EV flows [44–47]. Yi *et al.* took an innovative step through merging PageRank, graph analytics, regression, and maximal coverage. However, their reliance on non-EV traffic data (2016–2018) and absence of utilization measures limited both accuracy and interpretability [48, 49]. Orzechowski *et al.* demonstrated the power of deep learning to generate one-week energy forecasts. Yet, their framework still omitted key operational metrics, such as waiting queue delays, charger occupancy, and blocking probabilities [50]. Similarly, the queue theoretic and big data approaches of Kabir *et al.* and Arias *et al.* introduced valuable traffic and stochastic insights but rested on restrictive assumptions, such as Gaussian state of charge profiles and mixed-fleet traffic patterns, yielding overly conservative or off target long-term projections [51–59]. Short-horizon predictors, such as Ma, *et al.*'s hybrid LSTM and the 3-day deep-learning benchmarks explored by Amini and Manujith, achieved impressive accuracy over minutes to hours, but they held little sway in annual/multi-year infrastructure design [60–65].

Su, *et al.*, used POLARIS across six Austin counties to colocate 115 DC fast-charging plugs at 23 public stations within an 81 sq mi geofence for 200 shared automated EVs. This setup delivered 330 mi/day per vehicle, 92 daily trips, 2.7 recharges (2.4 h/session), cut waiting times from 10.7 to 3.1 min (8 min only at two freeway sites), and reduced infrastructure costs by 12%, [79].

In response, more holistic frameworks have emerged. Bao *et al.* applied prospect theory to time-of-use pricing, capturing how drivers perceive fees and battery state-of-charge; by optimizing price schedules with particle-swarm techniques, they successfully flattened demand peaks and cut station energy costs [74]. Meng *et al.* demonstrated that opening bus-depot chargers to public EVs, when paired with M/M/C/K queues and smart energy storage scheduling reduced grid stress, optimized charger counts, and saved 5.7% in operating costs, [75]. Rafi *et al.* presented a multi period planning framework for heavy-duty EV charging infrastructure, using depot-level historical data and a hybrid optimizer. They compared grid-only and solar-plus-storage configurations under a 2-layer model accounting for PV variability, vehicle flow, and charger reliability. Their phased roll-out strategy cuts initial annual costs by up to 78% compared to full upfront deployment, and so, values gradual scaling under uncertainty [90].

On the planning front, Woo *et al.* combined kernel-density demand estimation with a minimax genetic game algorithm to disperse load and prevent station overcrowding in Jeju Island [68]. Brahmachary and Ahmed forecasted distribution network loads via Random Forests, then co-optimized EV charger siting, conductor upgrades, load scheduling, and harmonic filtering in a Mixed-Integer Linear Program (MILP) that balanced losses against an average happiness index, [70]. Gan *et al.* advanced a bi-level model that fused Origin–Destination analysis, dynamic path-finding, and Latin Hypercube sampling. The upper tier minimized planning and user costs. The lower tier tackled operational and carbon costs under renewable uncertainties, [69].

Bitencourt *et al.* integrated a socio-economic Bass diffusion model, augmented with macroeconomic regressions into Open Source energy MOdelling SYStem (OSeMOSYS) expansion planning and unit commitment operations. their case study showed that ignoring short-term operational limits overstated vehicle-to-grid injection potential and raised load-shedding risk, pointing to the need for coordinated expansion and operation optimization [78]. The frontier of real-time management has likewise evolved. Cui *et al.* merged Long Short-Term Memory (LSTM)–Graph Neural Network (GNN) traffic forecasts with Origin-Destination (OD) demand modeling, then trained a Deep Deterministic Policy Gradient agent to adjust prices dynamically for boosting station profits, easing road congestion, and elevating driver satisfaction in iterative simulations [76]. Li *et al.* reached similar conclusions using Soft Actor-Critic reinforcement learning to jointly optimize pricing and station placement in a Chinese industrial park [77].

Finally, Guerrero-Silva *et al.* presented a principal component analysis (PCA)-driven systematic review of EV charging infrastructure, identifying four main themes of smart-grid integration, strategic station siting, renewable energy coupling, and policy impacts. They proposed a taxonomy that spanned classical optimization to deep reinforcement learning. They argued that hybrid Artificial Intelligence (AI)–optimization frameworks are vital for building scalable, resilient, and adaptive charging networks [91].

Chapter 3
Leveraging Real-World Data Sets For QoE Enhancement In Public Electric Vehicles Charging Networks

3.1 Problem Statement and Motivation

EV adoption rates are quite different from one country to another. Regardless though, the migration towards a universal zero-emission clean energy transportation is exhibiting a slow yet steady progress. As a matter of fact, EVs have recorded a notable market penetration so far.

Nonetheless, additional data is required to enable the aggressive exploitation of their potential and capture the plethora of opportunities they instantiate. Moreover, range anxiety and scanty charging stations (CSs) are among the primary persisting challenges impeding the rising slope of EV adoption [32, 92]. To alleviate such concerns, governmental authorities continue to join efforts with private partners and operators with the objective of rapidly expanding their charging infrastructure (*e.g.*, [93, 94]) through the deployment of additional CSs; hence, offering on-the-go EV charging services allowing EV owners to charge and frequently recharge their EVs.

Above and beyond, the newly rising public CSs need to be equipped with revolutionary technology (*e.g.* fast chargers) allowing rapid charging of EVs; hence, improving consumers' Quality-of-Experience (QoE) and motivating them to further exploit the public charging network [32, 92]. Indeed, long waiting times and outlet uncertainty are among the fundamental problematic factors promoting consumer hesitation in resorting to public CSs, [95]; these, mainly being contributed by the lack of a practical check-in systems capable of overseeing the entire public CS network and, hence, accurately predicting the availability of charging outlets, their utilization as well as waiting times that may be possibly endured by newly incoming EVs.

To work around such issues and improve EV owners' QoE, the trending operators' practice has been to approximate per-CS waiting times subject to some goal-oriented but restrictive assumptions (*e.g.*, fixed rate of charge and EV battery capacities), [51, 54, 96, 97]. For instance, in [96], the authors proposed to optimize the EV charging time within a framework that as-

sumed the ability of EVs to communicate their energy demands to individual public CSs prior to their arrival to these CSs. In such a context, they claimed that, having a priori and global knowledge of the charging requests, the operator would be able to optimally allocate the best available CS on a per-EV basis using their proposed Best Available EV Public Supply Station (BA-EVPSS) scheme. However BA-EVPSS is founded on top of the modeling of each CS as an $M/M/s$ queuing system that, unfortunately, turns out to suffer from serious drawbacks. First, it does not account for vehicular mobility. Here, it is important to mention that any EV initiating a charging request will need to navigate towards its allocated "*best*" CS. This travel time, although a function of various critical vehicular traffic parameters, was ignored in [96].

Second, the arrivals of EVs to a CS were assumed in [96] to follow a Poisson process. While such an assumption is highly embraced in the literasture (since it promotes analytical tractability), recent studies (including the one presented hereafter in this chapter) clearly show that the per-CS EV arrivals not necessarily follow a Poisson process but are rather dependent on many factors including but not limited to vehicular traffic parameters, topology of road networks, policies adopted by the grid to allocate EVs to available CSs. Most importantly, the EV charging time is absolutely not exponentially distributed as confirmed by realistic real-world collected data samples as was shown earlier by [54]. However, along these lines, new updated data sets also reveal that the charging time model presented in [54] also fails to accurately represent recently collected EV charging time data and, hence, will surely fail at predicting future EV charging times. Consequently, all of the derived crucial QoE parameters in [54] appear to be, unfortunately, misleading; hence, quite inappropriate for use by operators today for assessing QoE performance and plan future expansions accordingly. Indeed, the work of [51, 97] also suffer from similar shortcomings.

This chapter revisits the problem of QoE enhancement in public EV charging networks. In particular, the objective is to represent public CSs using accurate analytical models developed as part of a mathematical framework which mitigates the above-elaborated shortcomings by leveraging realistic data collected from real-world CS deployments and EV charging use cases. For this purpose, a public EV charging scenario that is similar to the one presented in [54] is adopted, illustrated in Figure 3.1.

The Figure shows a snapshot of a metropolitan area with a number of deployed CSs along the sides of that area's road network (*e.g.*, *A*, *B* and *C*). EVs navigating along these roads and their drivers may issue charging requests at random times. In this context, this chapter addresses the important development of EV-to-CS assignment strategies that account for EV mobility parameters and, thus, the EVs' range anxiety as well as these EVs available State-of-Charge (SoC) and battery capacities. To this end, such schemes shall enable the modelling and performance analysis of per-CS QoE in terms of crucial metrics such as the per-CS average waiting time and outlet utilization. Indeed, on one hand, providing drivers with early insights into their envi-

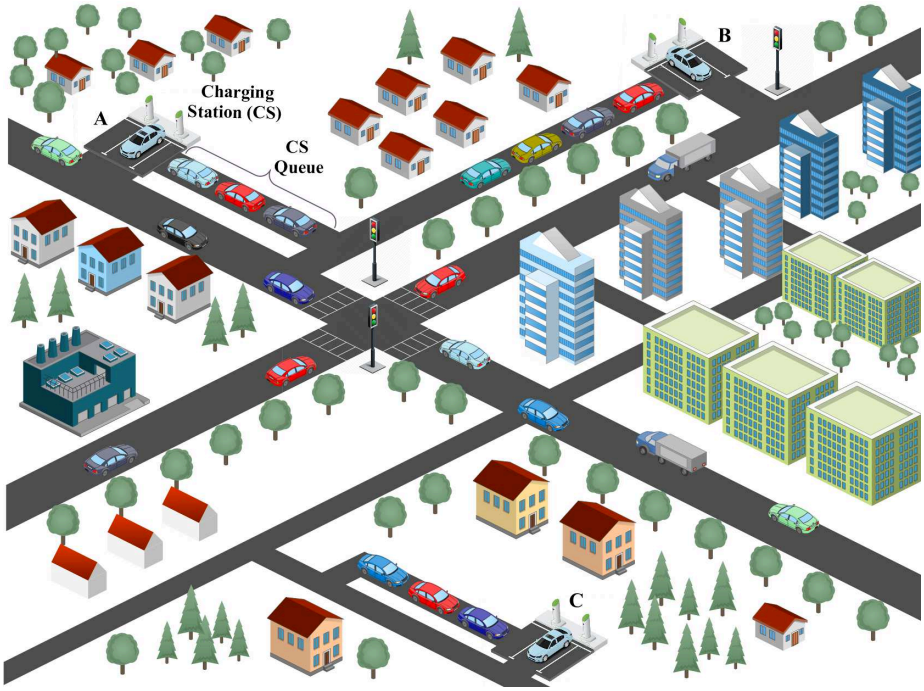

Figure 3.1: Electric vehicle charging scenario.

sioned waiting time interval will enable them to make suitable decisions on whether to accept charging at their allocated CS. On the other hand, allowing operators to identify the overall load experienced by a CS throughout different intervals of the day will allow them to better plan the expansion of their charging infrastructure as well as the placement of new CSs intended to be deployed.

3.2 Modeling of an EV Public CS

At the core of the analytical framework established hereafter in this work lies a stochastic queuing model (*e.g.*, as shown in Figure 3.2) that aims at capturing the dynamics of any arbitrary target public CS (*e.g.* CS *A* in Figure 3.1) and study its performance in terms of multiple metrics, of which the most important and point of focus of this present work is the per-CS average EV waiting time (*i.e.*, the time interval bounded by the instant of arrival of an EV to a certain tagged CS and the instant at which that EV starts charging its batteries). For this purpose, the fundamental stochastic processes governing the behavior of such a queuing system, namely, the EV arrival process and EV charging (*i.e.* service) process, need to be characterized first starting with the EV arrival process.

3.3 EV Arrival Process

Independent discrete events that occur at random instants such that the average event inter-occurrence time is known, are typically modeled using Poisson processes that, in turn, foster

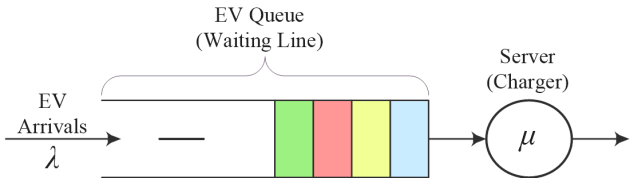

Figure 3.2: Queuing system representation of a public CS.

analytical simplicity and tractability. This trend has, so far, been widely adopted when it comes to characterizing EV arrivals to CSs (*e.g.* [35, 54, 98] and references therein); this, arguably, not being generally adequate especially whenever charging requests issued by different EVs are not totally independent. As a matter of fact, with the help of state-of-the-art wireless communication and networking technologies, public CS operators today, via custom-built smart mobile applications, are striving to connect EV drivers to public CS networks and, consequently, displaying on their mobile or EV navigation systems' screens a bird's eye overview of the available public CSs within a particular area of interest; this having the objective of allowing these drivers to make more informed CS selections given their current locations, SoCs, CS charging costs and possible waiting times they may experience upon arrival to the selected CS until the charging process starts. This approach, if intelligently exploited may, on one hand, improve the QoE of EV consumers and, on the other hand, allow operators to have early per-CS energy demand estimates.

Armed with such a priori insights into the expected load the different CSs may experience throughout the day, operators may then design and implement wise incentive-driven CS-to-EV allocation and scheduling schemes for the purpose of optimizing various operational objectives (*e.g.*, power balance, energy availability, profitability, etc) while jointly accounting for consumer QoE-related objectives (*e.g.*, waiting time minimization, maximization of number of served EVs, maximization of final EV SoC, etc). Obviously, under such incentive-driven schemes, the drivers' CS selection are no longer independent but rather biased and controlled. As such, throughout the performance analysis of CS operating under the rules dictated by these schemes, the assumption that EV arrivals to individual CSs follow independent Poisson processes with different parameters will lead to misleadingly overoptimistic results. At this point, it is worthwhile mentioning that the development of scheduling schemes by itself is outside the scope of this present work. However, it is inevitable, for all purposes of gauging the merit of the presented CS queuing system modeling and analysis, to consider a subset of different CS-to-EV allocation and scheduling policies and, therefore, characterize the per-CS EV arrival processes and their integral effect on the performance of CSs operating under each of these policies. Precisely, hereafter, the below four scheduling policies are adopted:

• **Random Station Selection** (RSS): Within a certain tagged area of interest (similar to the one depicted in Figure 3.1), a certain number of N CSs is deployed. Under the RSS policy, any of these CSs is equally likely to be assigned to an EV issuing a charging request regardless of the requesting EV's destination and the relative distance separating this EV from the allocated CS. Accordingly, any of the deployed CSs within the considered area will be selected with a probability $p_s^{\text{RSS}} = N^{-1}$.

• **Closest Station First** (CSF): Again, with N CSs (indexed $1, \cdots, i, \cdots, N$) deployed within an area of interest, any EV, say v, issuing a charging request shall, under CSF, be guided to the closest station to that EV based on the geographical locations of the requesting EV and the N CSs. Accordingly, knowing that the CS locations are fixed and that v is randomly located within the considered area, it is easy to show that any CS, say without loss of generality (w.l.o.g.) CS j, shall be selected with a probability $p_s^{\text{CSF}} = \Pr\left[d_{v,j} = \min_{1 \leq i \leq N}\{d_{v,i}\}\right]$ where $d_{v,i}$ denotes the random distance separating EV v from CS i. Note that CSF completely disregards the load experienced by the selected CS.

• **Minimum Waiting Time** (MWT): Under this scheme, EV drivers are provided with information about the per-CS load and average waiting time. Based on that, the driver of each EV shall, upon placing the recharge request, select the least loaded CS (*i.e.*, exhibiting the least average waiting time).

The EV scheduling schemes having been presented as above, it is now time to characterize the per-CS EV arrival process. For this purpose, given that the available data sets do not incorporate any records pertaining to EV arrival times to the CSs, simulations shall be conducted using the custom-built simulator presented hereafter in Section 3.7 over a square area similar to the one shown in Figure 3.1. The area size is A and within this area a number of N CSs are deployed arbitrarily at known and fixed locations captured by two dimensional coordinates $\left(x_c^{(i)}, y_c^{(i)}\right)$ where $(1 \leq i \leq N)$.

EV arrivals to this entire area are assumed to follow a Poisson process with a parameter λ. Such an assumption is justified by the fact that the arrival of an arbitrary EV at a certain point in time neither does relate to any earlier EV arrivals nor does it provide any information regarding the arrivals of any EVs at subsequent times as well as the entry points of these EVs to the considered area. In this sense, EV arrivals to the considered area are completely independent. Now, the adopted simulator has been augmented with programmed modules each implementing the rules dictated by one of the above-presented scheduling schemes. In addition, the simulator also

accounts for realistic vehicular mobility through the incorporation of a vehicular traffic generator programmed to generate vehicle mobility traces following the guidelines of [99] and using macroscopic parameter values provided therein. Extensive simulations have been conducted for various simulator input parameter values, for each set of which, results for over 10^9 EV arrivals have been recorded and averaged out over multiple runs of the simulator to ensure that at least 95% confidence interval is achieved. Due to space limitations and, for all purposes of certifying the EV arrival process characterization correctness, only a subset of these results is reported hereafter. These pertain to the following simulation input parameter values: *i*) $A = 9$ km^2, *ii*) $N = 5$ and *iii*) $\lambda = 6$ EVs/hr.

Now, in view of the above-detailed RSS scheme, an arriving EV will, with a probability of p_s^{RSS} be assigned to any of the deployed CSs within the considered area. Knowing that the overall arrival process to the entire area is a Poisson process with a parameter λ, then the per-CS EV arrivals follow a thinned Poisson process with a parameter $\lambda_c^{\text{RSS}} = \lambda p_s^{\text{RSS}}$. Similarly, under CSF, a CS is selected by an EV if and only if it is the closest to that EV among all other CSs. This occurs with a probability p_s^{CSF}. Consequently, the per-CS EV arrivals also follow a thinned Poisson process with a parameter $\lambda_c^{\text{CSF}} = \lambda p_s^{\text{CSF1}}$. At this point, given that the EV arrivals under both RSS and CSF follow Poisson processes, then the EV inter-arrival times to these CSs follow exponential distributions with respective means $\left[\lambda_c^{\text{RSS}}\right]^{-1}$ and $\left[\lambda_c^{\text{CSF}}\right]^{-1}$. Figures 3.3(a) and Fig.3.3(b) concurrently plot the theoretical and simulated cumulative distribution functions (c.d.f.) pertaining to the per-CS EV inter-arrival times achieved under RSS and CSF respectively. These figures constitute tangible proofs of the accuracy and correctness of the per-CS EV arrival process characterizations under these two schemes.

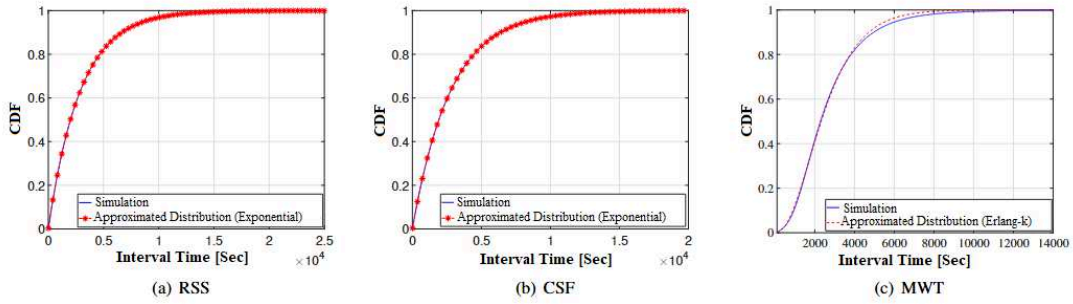

Figure 3.3: Theoretical V.S. simulated c.d.f. of EV inter-arrival times under the RSS, CSF and MWT Schemes.

Next, under the MWT scheme, EV arrivals to a certain tagged CS are tightly correlated to that CS's load (informally the achieved average waiting time), which, in turn, is dependent on the intensity of other EV arrivals. Clearly, this viciously circular implicit inter-dependence of EV arrivals drives the per-CS EV arrival process away from being a Poisson process and

[1] p_s^{CSF}'s derivation is straightforward but is omitted due to space limitation.

remarkably augments the complexity of its characterization. To work around this complexity, extensive simulations are conducted to observe and record a large number of data samples (*i.e.*, 10^9) pertaining to the EV inter-arrival times experienced by the considered CSs. Then, a plot of per-CS EV inter-arrival time c.d.f.s reveals that all of these c.d.f.s exhibit similar variation trends. As a sample, only one per-scheme-per-CS c.d.f. is reported herein (*i.e.*, the blue curves in Figure 3.3(c)). At this stage, the next step is to derive accurate theoretical approximations for these c.d.f.s. For this purpose, let $\mathcal{I}$ be an r.v. representing the EV inter-arrival time experienced by the tagged CS. The Square Coefficient of Variation (SCoV) $c_{\mathcal{I}}^2 = \sigma_{\mathcal{I}}^2 \cdot \left(\mu_{\mathcal{I}}^2\right)^{-1}$ captures the degree of variability of $\mathcal{I}$, where $\sigma_{\mathcal{I}}^2$ and $\mu_{\mathcal{I}}$ are respectively the variance and mean of $\mathcal{I}$ computed numerically over the set of collected sample values. Simple numerical analysis shows that, under MWT, $c_{\mathcal{I}}^2 \leq 0.5$. Hence, following the recommendations of [100], under MWT, $\mathcal{I}$'s c.d.f. may be respectively approximated by that of an Erlang-k distribution expressed as:

$$F_{\mathcal{I}}^{E_k}(\tau) = 1 - \sum_{i=0}^{k-1} \frac{1}{i!} e^{-\mu_{\mathcal{I}}^{-1}\tau} \left[\mu_{\mathcal{I}}^{-1}\tau\right]^i \quad , \tau \geq 0 \tag{3.1}$$

where, $\mu_{\mathcal{I}}^{-1}$ is the approximated rate parameter while $k = \left(c_{\mathcal{I}}^2\right)^{-1}$ is the shape parameter.

Observe in Figure 3.3 that the concurrently plotted simulated and theoretical c.d.f. approximation curves clearly almost overlap; this being a sign of a remarkable accuracy. To further certify this accuracy, the well known Kolmogorov-Smirnov Test (KST) is used to compare $F_{\mathcal{I}}^*$ being the empirical inter-arrival time distribution function, and its earlier derived theoretical counterpart, $F_{\mathcal{I}}^{E_k}$ expressed in Equation (3.1). KST consists of measuring the largest vertical distance, D, between $F_{\mathcal{I}}^e$ and $F_{\mathcal{I}}^{E_k}$. Here, two test hypotheses are established; these being:
• Null Hypothesis (H_0): the collected data can be accurately fitted using $F_{\mathcal{I}}^{E_k}$ with a minimum of 95% confidence.
• Alternate Hypothesis (H_A): the collected data cannot be fitted using $F_{\mathcal{I}}^{E_k}$; that is $H_A = \overline{H_0}$.
In addition, to ensure 95% confidence level, then the Alpha level is $\alpha = 1 - 0.95 = 0.05$ (*i.e.*, the probability of rejecting H_0 when this latter is true). Now, for a number of sample data values of $n > 50$, the KST table value corresponding to $\alpha = 0.05$ is $\kappa = 1.36\left[\sqrt{n}\right]^{-1}$. As such, computing:

$$D = \sup_{\forall t \in T} \left|F_{\mathcal{I}}^{E_k} - F_{\mathcal{I}}^*\right| \tag{3.2}$$

where T is the set of all available $n = 290$ EV inter-arrival time data samples, it is found that $D = 0.0298 < \kappa = 0.043$; this constituting a tangible proof of the accuracy of $F_{\mathcal{I}}^{E_k}$.

3.4 EV Service Process

In the context of the scenario considered in this work and illustrated in Figure 3.1, the service provided to a certain EV consists of charging that EV. Hence, the service process is exactly equivalent to the charging process, the statistical characteristics of which shall be determined hereafter. For this purpose, at the heart of this subsection lies hardcore numerical analysis conducted on an extensive EV charging database shared by Quebec's major electricity provider, Hydro-Quebec.

This database encloses around four million records collected throughout January 2018 through February 2022 from various regions almost uniformly covering the vast majority of EVs navigating along the road network merely spanning the entire Quebec province and utilizing its CSs to refuel with energy. Records comprise massive information regarding the charging process (*e.g.*, charging outlets, power rates, models of charging EV, EV start and finish SoCs, inter-session time gaps etc), of which, the start and finish times of EV charging sessions are of particular interest as these shall be used here to extract the per-EV service durations and, then, model the EV service time using an accurate distribution.

Although a similar approach was adopted in [54], the EV service time distribution was derived therein on top of a restrictive charging model adopted from [101], which, by itself, was formulated on top of inaccurate assumptions. Here, again, KST is used here below to mathematically demonstrate the inaccuracy (which can be observed from Figure 3.4(a)) between $F_{\mathcal{S}}^{*}$ being the empirical service time distribution function resulting from the collected realistic data, and its earlier derived theoretical counterpart, $F_{\mathcal{S}}^{e}$, in [54] for one particularly chosen CS[2]. For a set T of $n = 297$ available data EV service time data points, it is found that $D = 0.198 >> \kappa = 0.0426$; this constituting a tangible proof of the inaccuracy of the EV service time distribution derived in [54].

Now, in an attempt to derive a more accurate distribution for the EV service time, the guidelines of [100] followed in Section 3.3 to approximate the per-CS EV inter-arrival time distribution are, again, followed at this stage. Recall, from Equation (3.2) that T denotes the set of collected EV service time samples pertaining to one particular CS. Again, results reported for this chosen CS also apply for all other CSs but have been omitted to avoid redundancy and due to space limitation. The mean μ_T and variance σ_T^2 and hence the SCoV $c_T^2 = \sigma_T^2 \cdot (\mu_T^2)^{-1}$ can be easily numerically computed. Here, it so happens that $c_T^2 < 0.5$. This suggests that the data

[2]The notable difference between $F_{\mathcal{S}}^{*}$ and $F_{\mathcal{S}}^{e}$ is observable for all CSs. Only the results pertaining to one CS are reported herein due to space limitations.

points in T can be best fitted using an Erlang-k distribution with a shape parameter $k = (c_T^2)^{-1}$ and rate parameter $\mu_{\mathcal{S}} = \mu_T^{-1}$ where, in the sequel, $\mathcal{S}$ shall represent the per-EV service time. As such, the c.d.f. of $\mathcal{S}$ is given by:

$$F_{\mathcal{S}}^{t}(\tau) = 1 - \sum_{i=0}^{k-1} \frac{1}{i!} e^{-\mu_{\mathcal{S}}\tau} \left[\mu_{\mathcal{S}}\tau\right]^{i} \quad , \tau \geq 0 \tag{3.3}$$

At this point, in addition to Figure 3.4(b) that shows an almost perfect overlap between $F_{\mathcal{S}}^{*}$ and $F_{\mathcal{S}}^{t}$, the evaluation of a KST test yield a value of $D = 0.03 < \kappa = 0.0659$, which proves the accuracy of this newly chosen distribution.

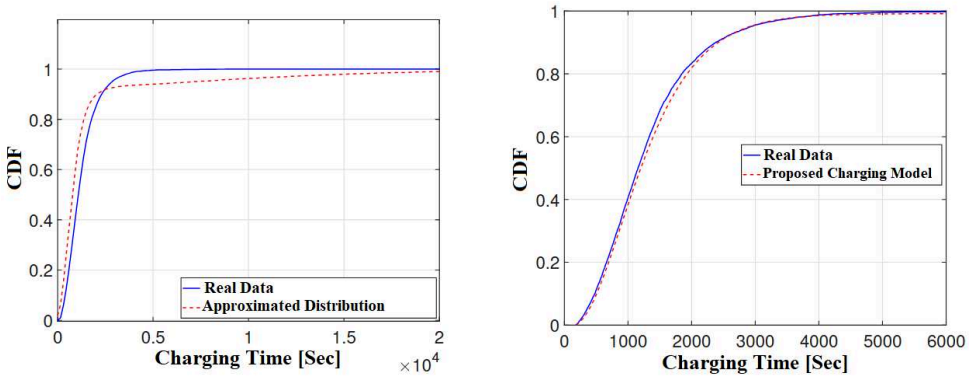

(a) $F_{\mathcal{S}}^{*}$ V.S. $F_{\mathcal{S}}^{e}$ ([8]). (b) $F_{\mathcal{S}}^{*}$ V.S. $F_{\mathcal{S}}^{t}$

Figure 3.4: EV service time distribution approximation

3.5 EV Public CS Model

In view of the above-presented EV arrival and service processes, an EV public CS can be modeled as a single-server queueing system such as the one illustrated in Figure 3.2. The system is assumed to be subject to general EV arrivals so as to capture all possible EV arrival patterns under any scheduling scheme. In addition, as revealed in Section 3.4, the per-EV service time is realistically captured by an Erlang-k distribution, which, in turn, is a phase-type distribution. Consequently, this queueing system has dynamics that are quite different from Markovian queueing systems that are typically governed by arrival processes with independent and identically distributed (i.i.d.) exponential inter-arrival times and/or i.i.d. exponential service times. Consequently, a public CS is, hereafter, represented using one of the most complex queueing models; this being the $G/G/1$ queue, the dynamics' evolution of which, is captured by Lindley's equation. The next section presents an elaborated analytical adaptation of the waiting time experienced by arriving EVs to a public CS.

Table 3.1: List of Mathematical Symbols.

Symbol	Meaning
V_i	The i^{th} EV arriving to station *C*.
t_i	Arrival time instant of EV i. to station *C*.
τ_i	Random inter-arrival time between EVs $i-1$ and i.
$\mathcal{I}(t)$	EV inter-arrival time's cumulative distribution function.
$f_{\mathcal{I}}(t)$	EV inter-arrival time's probability density function.
$\overline{\mathcal{I}}$	Average EV inter-arrival time.
λ	EV arrival rate.
s_i	Random service time of EV i at station *C*.
$\mathcal{S}(t)$	EV service time's cumulative distribution function.
$f_{\mathcal{S}}(t)$	EV service time's probability density function.
$\overline{\mathcal{S}}$	Average EV service time.
μ	EV service rate.
ω_i	Waiting time of EV i in the queue of station *C*.
$\mathcal{W}(t)$	Stationary EV waiting time cumulative distribution function.
$\overline{\mathcal{W}}(t)$	Complementary EV waiting time distribution.
$f_{\mathcal{W}}(t)$	EV waiting time probability density function.
$\mathcal{U}(t)$	Unfinished work.

3.6 Waiting Time Analysis

Consider a system composed of a station *C* with EVs arriving to *C* for the purpose of charging their batteries. The inter-arrival times of EVs to the station are unknown but assumed to be i.i.d. random variables (r.v.s) drawn from a distribution that has a cumulative distribution function (c.d.f.) $\mathcal{I}(t)$. The service time received by an EV at *C* can be defined, at large, as the difference between the real-world finish and starting times of that EV's charging session (refer to Section 3.4). The per-EV service times are also assumed to be i.i.d. r.v.s. drawn from a distribution that has a c.d.f. $\mathcal{S}(t)$. As a first step, *C* is assumed to have a single charging outlet and an open waiting space allowing arriving EVs to line up waiting for their respective turns to receive service. As such, *C* can be modeled as a single-server queueing system where service is provided to the EVs following a First-Come-First-Served (FCFS) policy. Our interest lies in the mathematical characterization of the EV waiting time, i.e., the time an EV shall wait in line from the time instant it arrives until the time instant it starts charging. The mathematical symbols utilized throughout the analysis presented hereafter together with their significance are summarized in Table 3.1.

In the context of the above-mentioned EV charging system scenario, the unfinished work, denoted by $\mathcal{U}(t)$, as seen by an arriving EV to *C* can no longer be claimed to be Markovian. However, a close observation of the system dynamics reveals that there exists an essential Markov process that is embedded within $\mathcal{U}(t)$ and mainly defined at the distinct EV arrival times. More specifically, such arrival times constitute regeneration points, at each of which, the past system's history being apposite to the system's future operational comportment is totally encapsulated within $\mathcal{U}(t)$'s current value. In other words, under an FCFS service policy, $\mathcal{U}(t)$'s value just before the arrival of an arbitrary EV, say V_i, is equivalent to that EV's waiting time ω_i. This is actually the Markovian process that lies at the heart of the analysis presented hereafter. Typical queue-related timing diagrams are used as illustrative representations of different historical cases of the system under consideration, namely:

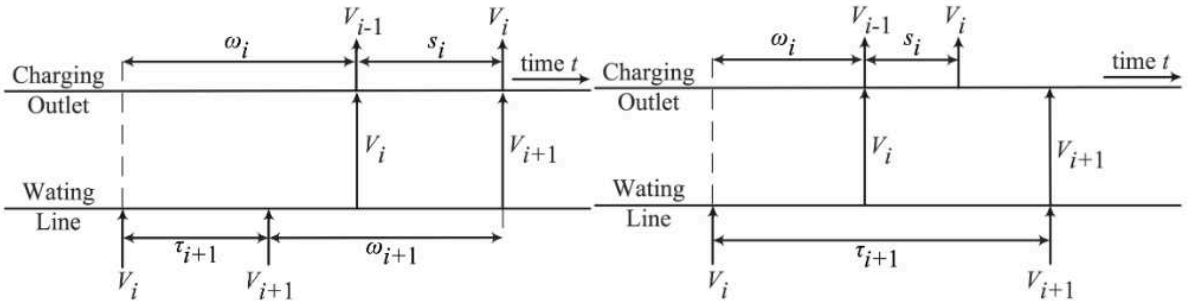

Figure 3.5: Illustrative timing diagrams

- **Case 1:** (Figure 3.5(a)) EV V_{i+1} arrives to *C* before V_i completes service and frees the charging outlet.
- **Case 2:** (Figure 3.5(b)) EV V_{i+1} arrives to *C* and finds the charging outlet to be idle (*i.e.* free)[3].

Observing Figure 3.5(a), it is obvious that:

$$t_{i+1} + \omega_{i+1} = t_i + \omega_i + s_i \;\Rightarrow\; \tau_{i+1} + \omega_{i+1} = \omega_i + s_i$$

where $\tau_{i+1} = t_{i+1} - t_i$. The above equation allows establishing a condition that confirms the fact that V_{i+1} will arrive to *C* only to find this latter's charging outlet to be busy. It is:

$$\omega_{i+1} = \omega_i + s_i - \tau_{i+1} \quad \text{iff} \quad \omega_i + s_i + \tau_{i+1} \geq 0 \tag{3.4}$$

Keep in mind here that, if ever, an EV arrives to a busy charging outlet, it will have to wait in line and, hence, its waiting time must be positive. The $\omega_i + s_i - \tau_{i+1} \geq 0$ in Condition (3.4)

[3]Using queueing systems jargon, in this case, the considered queueing system is said to be empty.

is there to ensure this fact. Alternatively, as shown in Figure 3.5(b), V_{i+1} that arrives after V_i departs will not have to wait. In this case, one can establish that:

$$\omega_{i+1} = 0 \quad \text{iff} \quad \omega_i + s_i + \tau_{i+1} \leq 0 \tag{3.5}$$

At this point, parallel to the work of [102], define an original but pivotal r.v. $u_i \triangleq s_i - \tau_{i+1}$, which, for all purposes of system stability is required to have a negative expectation (*i.e.*, $\mathbb{E}[u_i] < 0$). Using u_i, Equations (3.4) and (3.5) can be combined into a rudimentary yet essential expression as follows:

$$\omega_{i+1} = \begin{cases} \omega_i + u_i & , \quad \omega_i + u_i \geq 0 \\ 0 & , \quad \omega_i + u_i < 0 \end{cases} \tag{3.6}$$

To clarify, ω_i in (3.6) refers to the unfinished work that V_i found when it arrived to station *C* at time t_i and s_i is V_i's service time. If, after adding these two quantities and subtracting from this addition the interval τ_{i+1} (*i.e.*, the amount of time until the arrival of V_{i+1}), the overall result is positive, it then directly translates into the amount of unfinished work that V_{i+1} will find upon its arrival to the system at time t_{i+1}. In other words, this is exactly equivalent to the amount of time V_{i+1} will have to wait in line until it receives service; that is ω_{i+1}. Otherwise, if the above result was negative, it then points out that there exists a certain amount of time that has elapsed since t_i (*i.e.* the arrival of V_i) and this elapsed time is greater than the persisting amount of unfinished work in the system following V_i's arrival. This directly means that, upon the arrival of V_{i+1}, the *C*'s charging outlet was free. In the sequel, for all purposes of notation simplicity, (3.6) will be re-written as:

$$\omega_{i+1} = (\omega_i + u_i)^+ \tag{3.7}$$

where $(v)^+ \triangleq \max[0, v]$. Having defined the waiting times of EVs (*i.e.*, the r.v.s. ω_i with $i \in \mathbb{Z}^+$), attention now goes to identifying the nature of the stochastic process inferred by the sequence $\{\omega_0, \omega_1, \cdots, \omega_i, \omega_{i+1}, \cdots\}$. As a matter of fact, recalling the assumption that $\{\tau_0, \tau_1, \cdots, \tau_i, \tau_{i+1}, \cdots\}$ and $\{s_0, s_1, \cdots, s_i, s_{i+1}, \cdots\}$ constitute sequences of intra-sequence and inter-sequence mutually i.i.d. r.v.s., then it becomes quite observable that the sequence $\{\omega_0, \omega_1, \cdots, \omega_i, \omega_{i+1}, \cdots\}$ infers a Markovian process with stationary transition probabilities. This can, actually, be confirmed by Equation (3.6) where it is clear that the value of ω_{i+1} depends on the earlier sequence of r.v.s. $\{\omega_k | k \in [0; i]\}$. However, this dependency is entirely summarized by the value of the r.v. ω_i to which is added another r.v. u_i; this latter r.v. being completely independent from $\{\omega_k | k \leq i\}$.

Keeping in mind that, over the system's observation period, w.l.o.g. the initial EV to arrive to *C* is V_0 and its waiting time is w_0 (seen as an initial condition), then Equation (3.7) can be solved recursively as follows:

$$
\begin{aligned}
\omega_1 = (\omega_0 + u_0)^+ &= \max[0, \omega_0 + u_0] \\
\omega_2 = (\omega_1 + u_1)^+ &= \max[0, \omega_1 + u_1] \\
&= \max\left[0, \max[0, \omega_0 + u_0] + u_1\right] \\
&= \max\left[0, u_1, \omega_0 + u_0 + u_1\right] \\
&\vdots \\
\omega_i = (\omega_{i-1} + u_{i-1})^+ &= \max[0, \omega_{i-1} + u_{i-1}] \\
&= \max[0, u_{i-1}, u_{i-1} + u_{i-2}, \cdots \\
&\qquad u_{i-1} + \cdots + u_1, \\
&\qquad u_{i-1} + \cdots + u_0 + \omega_0] \qquad (3.8)
\end{aligned}
$$

Eventually, given the i.i.d. nature of $\left\{u_k \middle| k \leq i\right\}$, it is possible to relabel these r.v.s. and then define, for instance, $\mathcal{U}_0 = 0$ and $\mathcal{U}_i = \sum_{k=0}^{i-1} u_k$. As such, ω_i in (3.8) can be rewritten as:

$$
\begin{aligned}
\omega_i &= \max[0, u_0, u_0 + u_1, u_0 + u_1 + u_2, \cdots, \\
&\qquad u_0 + \cdots + u_{i-2}, u_0 + \cdots + u_{i-1} + \omega_0] \\
&= \max\left[\mathcal{U}_0, \mathcal{U}_1, \cdots, \mathcal{U}_{i-1}, \mathcal{U}_i + \omega_0\right] \qquad (3.9)
\end{aligned}
$$

In view of this very last arrangement of ω_i in (3.9), if $\omega_0 = 0$, then ω_i increases as function of i. As such:

$$
\widehat{\omega} = \lim_{i \to \infty} \omega_i = \sup_{i \geq 0}[\mathcal{U}_i] \qquad (3.10)
$$

Note here that $\widehat{\omega}$ may be infinite. However, in the context of the considered EV charging system scenario analysis, having an infinite $\widehat{\omega}$ has no physical meaning as it cannot possibly represent a certain EV waiting time. In contrast, here, interest lies in characterizing the probability distribution of EV waiting time, which is only feasible if and only if, $\widehat{\omega}$ is certainly finite. This is especially true since, only then, the sought Markov chain becomes ergodic and, therefore, ω_i's probability distribution will converge to the distribution of the EV waiting time $\widehat{\omega}$, $\mathcal{W}(t)$, which is most favorably derived under system stability conditions; that is whenever $\mathbb{E}[u_i] < 0$, [102]. Indeed, expanding $\mathbb{E}[u_i]$ reveals the following:

$$
\mathbb{E}[u_i] = \mathbb{E}[s_i - \tau_{i+1}] = \mathbb{E}[s_i] - \mathbb{E}[\tau_{i+1}] \qquad (3.11)
$$

Typically, denoting by $\overline{\mathcal{S}}$ the average EV service time, $\mu = \overline{\mathcal{S}}^{-1}$ the service rate, $\overline{\mathcal{I}}$ the average EV inter-arrival time, $\lambda = \overline{\mathcal{I}}^{-1}$ the arrival rate, then the charging station's load is, as usual, expressed as $\rho = \lambda\mu^{-1}$. Thus, it is easily shown that:

$$\mathbb{E}[u_i] = \overline{\mathcal{S}} - \overline{\mathcal{I}} = \frac{\rho - 1}{\lambda} \tag{3.12}$$

Here, clearly, for a system to be stable, it is necessary that $\rho < 1$; hence, knowing that $\lambda > 0$, this implies that $\mathbb{E}[u_i] < 0$. Under such conditions, $\mathcal{W}(t)$ does not depend on ω_0. Hence:

$$\mathcal{W}(t) = \lim_{i \to \infty} \text{Pr}[\omega_i \leq t] = \text{Pr}[\widehat{\omega} \leq t] \tag{3.13}$$

The remaining of this analytical framework is dedicated for deriving an expression for $\mathcal{W}(t)$. To start with, define the c.d.f. of u_i as $F_{U,i}(u) = \text{Pr}[u_i = s_i + \tau_{i+1} \leq u]$, which can be expressed as a function of $\mathcal{I}(t)$ and $\mathcal{S}(t)$ as:

$$F_{U,i}(u) = \int_{t=0}^{\infty} \text{Pr}\left[s_i \leq u + t \middle| \tau_{i+1} = t\right] \text{d}\mathcal{I}(t) \tag{3.14}$$

However, s_i is independent of τ_{i+1}. Consequently, $\text{Pr}\left[s_i \leq u + t \middle| \tau_{i+1} = t\right] = \text{Pr}[s_i \leq u + t] = \mathcal{S}(u+t)$. This, obviously, will lead expressing the right-hand-side (r-h-s) of Equation (3.14) independently of i. Consequently, the subscript i can be dropped all-in-all from $F_{U,i}(u)$ to have:

$$F_U(u) = \int_{t=0}^{\infty} \mathcal{S}(u + t) \text{d}\mathcal{I}(t) \tag{3.15}$$

At this point, define EV V_i's c.d.f. as $\mathcal{W}_i(t) = \text{Pr}[\omega_i \leq t]$. Hence, for $t \leq 0$, using (3.6), the waiting time distribution for EV V_{i+1} can be expressed as:

$$\begin{aligned} \mathcal{W}_{i+1}(t) &= \text{Pr}[\omega_i + u_i \leq t] \\ &= \int_0^{\infty} \text{Pr}\left[u_i \leq t - \tau \middle| \omega_i = \tau\right] \text{d}\mathcal{W}_i(\tau) \end{aligned} \tag{3.16}$$

However, u_i and ω_i being independent of each other, then $\text{Pr}\left[u_i \leq t - \tau \middle| \omega_i = \tau\right] = \text{Pr}[u_i \leq t - \tau] = F_{U,i}(t - \tau)$. Combining this result with Equation (3.13) leads to having:

$$\mathcal{W}(t) = \int_0^{\infty} F_U(t - \tau) \text{d}\mathcal{W}(\tau) \quad , \forall t \geq 0 \tag{3.17}$$

In addition, it is obvious that, for $t < 0$, then $\mathcal{W}(t) = 0$. Combining this fact with Equation (3.17) leads to having *Lindley's Integral Equation* (refer to [102]), which is an integral equation of the Wiener-Hopf type (refer to [103, 104]) and is:

$$\mathcal{W}(t) = \begin{cases} \displaystyle\int_0^{\infty} F_U(t - \tau) \text{d}\mathcal{W}(\tau) & , \quad t \geq 0 \\ 0 & , \quad t < 0 \end{cases} \tag{3.18}$$

In [105], two other different forms of Equation (3.18) are given, one of which is of most interest herein as it may be solved using spectral methods, [106]. This latter form obtained by a simple change of variable where $u = t - \tau$, is expressed as:

$$\mathcal{W}(t) = \begin{cases} \int_{-\infty}^{t} \mathcal{W}(t-u)\mathrm{d}F_U(t) & , \quad t \geq 0 \\ 0 & , \quad t < 0 \end{cases} \tag{3.19}$$

As indicated in [104–107], the right-hand-side of Equation (3.19) resembles a convolution but is not truly one except for the positive half of the time axis t. This is why the resolution of this integral equation exhibits notable complexity. Nevertheless, luckily, [105] pioneered the notion of the complementary waiting time to complete the sought convolution over the negative half of the t axis. Precisely:

$$\overline{\mathcal{W}}(t) \triangleq \begin{cases} 0 & , \quad t \geq 0 \\ \int_{-\infty}^{t} \mathcal{W}(t-u)\mathrm{d}F_U(u) & , \quad t < 0 \end{cases} \tag{3.20}$$

Next, noting that $\mathrm{d}F_U(u) = f_U(u)\mathrm{d}u$ where $f_U(u)$ is the probability density function (p.d.f.) of u_i, it follows that:

$$\mathcal{W}(t) + \overline{\mathcal{W}}(t) = \int_{-\infty}^{t} \mathcal{W}(t-u) f_U(u)\mathrm{d}u \quad , \forall t \in \mathbb{R} \tag{3.21}$$

Before proceeding any further, it is very important attract the reader's attention on the fact that the presented transform-based solution is founded on top of a key assumption that regards the p.d.f. of the EV inter-arrival time; that is $f_{\mathcal{I}}(t)$. Specifically, it is insistingly required that $f_{\mathcal{I}}(t)$ decays no slower than some negative exponential function, say $e^{-\Delta t}$ ($\Delta > 0$), for very large inter-arrival time intervals. This requirement stems from the ultimate need to force $\overline{\mathcal{W}}(t)$ to decay to zero as rapidly as possible whenever $t \to \infty$. A close contemplation of the expression of $F_U(u)$ in Equation (3.15) leads the way towards a solid justification supporting the realization of this ultimate objective. In particular therein, observe that whenever $u \to -\infty$, the only way to maintain a positive argument for the EV service time distribution (*i.e.*, $u + t$) is to have large values of t; this latter being, by itself, the argument of the EV inter-arrival time distribution. This truly reveals that the variations of $F_U(u)$ are mainly steered by those of the EV inter-arrival times. Therefore, now, it becomes straightforward to show that $F_U(u) \xrightarrow[u \to -\infty]{} 0$ asymptotically to $e^{\Delta u}$. Carrying this rationale to Equation (3.20), one can easily show that $\overline{\mathcal{W}}(t) \xrightarrow[t \to -\infty]{} 0$ also asymptotically to $e^{\Delta t}$.

At this point, define the below useful transforms:

$$\overline{\Gamma}(s) \triangleq \int_{-\infty}^{\infty} \overline{\mathcal{W}}(t) e^{-st}\mathrm{d}t \qquad , \Re(s) < \Delta \tag{3.22}$$

$$\Gamma(s) \triangleq \int_{-\infty}^{\infty} \mathcal{W}(t) e^{-st}\mathrm{d}t \qquad , \Re(s) > 0 \tag{3.23}$$

$$F^*_{\mathcal{W}}(s) \triangleq s\Gamma(s) = \int_{0}^{\infty} f_{\mathcal{W}}(t) e^{-st}\mathrm{d}t \quad , \Re(s) > 0 \tag{3.24}$$

$$F_{\mathcal{I}}^{*}(s) \triangleq \int_{0}^{\infty} f_{\mathcal{I}}(t)e^{-st}\mathrm{d}t \qquad ,\Re(s) > 0 \tag{3.25}$$

$$F_{\mathcal{S}}^{*}(s) \triangleq \int_{0}^{\infty} f_{\mathcal{S}}(t)e^{-st}\mathrm{d}t \qquad ,\Re(s) > 0 \tag{3.26}$$

In view of the above, definitions and the above-emphasized decaying requirements for $f_{\mathcal{I}}(t)$, note that the analyticity of $F_{\mathcal{I}}^{*}(-s)$ is bound to the region $\Re(s) < \Delta$. Further to the above it is shown in [105] that the transform of $f_U(u)$ is given by:

$$F_{U}^{*}(s) = F_{\mathcal{I}}^{*}(-s) \cdot F_{\mathcal{S}}^{*}(s) \tag{3.27}$$

Also, using the Laplace Transform Theorems (refer to [108]) coupled with Equation (3.27), the transform of the fundamental equation in (3.21) is given by:

$$\begin{aligned} \Gamma(s) + \overline{\Gamma}(s) = \Gamma(s) \cdot F_{U}^{*}(s) &= \Gamma(s) \cdot F_{\mathcal{I}}^{*}(-s) \cdot F_{\mathcal{S}}^{*}(s) \\ \Rightarrow \overline{\Gamma}(s) &= \Gamma(s)\left[F_{\mathcal{I}}^{*}(-s) \cdot F_{\mathcal{S}}^{*}(s) - 1\right] \end{aligned} \tag{3.28}$$

Now, it is time to find a suitable factored form for the term $\mathcal{F}(s) = F_{\mathcal{I}}^{*}(-s) \cdot F_{\mathcal{S}}^{*}(s) - 1$ that would simplify and push the remaining of the presented analysis hereafter one step closer towards tractability in an attempt to reach out an expression for the EV waiting time distribution or, at least, for its transform. The seminal work of Erlang and Cox (refer to [105, 109]) approximates complex distributions using mixtures of series/parallel exponential phases/stages with transforms expressed as rations of polynomials in s. As such, if coining similar individual approximations for $F_{\mathcal{I}}^{*}(-s)$ and $F_{\mathcal{S}}^{*}(s)$ is feasible, then $\mathcal{F}(s)$ will also be feasibly expressed as:

$$\mathcal{F}(s) = \frac{\mathcal{N}(s)}{\mathcal{D}(s)} \tag{3.29}$$

This is yet another restrictive aspect of the presented solution herein in the sense that its validity is only limited to cases where $F_{\mathcal{I}}^{*}(-s)$ and $F_{\mathcal{S}}^{*}(s)$ have rational transforms resulting in $\mathcal{F}(s)$ being rational itself. In addition, it is desirable that $\mathcal{N}(s)$ and $\mathcal{D}(s)$ satisfy the following:

- Further to being analytic and having no zeroes in the right half-plane, $\Re(s) > 0$, $\mathcal{N}(s)$ must satisfy the condition:

$$\lim_{|s|\to\infty} s^{-1}\mathcal{N}(s) = 1 \tag{3.30}$$

- $\mathcal{D}(s)$ should be analytic in the left half-plane, $\Re(s) < \Delta$, with no zeroes therein and must satisfy the condition:

$$\lim_{|s|\to\infty} s^{-1}\mathcal{D}(s) = -1 \tag{3.31}$$

The limiting opposite polarity emphasized by conditions (3.30) and (3.31) necrotizes both $F_{\mathcal{I}}^{*}(-s)$ and $F_{\mathcal{S}}^{*}(s)$ down to zero as $s \to \infty$ along the imaginary axis. This is especially required

to ensure that the moments corresponding to both distributions $\mathcal{I}(t)$ and $\mathcal{S}(t)$ are finite and these distributions have absolutely no discontinuities; hence, leading to $\mathcal{F}(s) = -1$. To this end, truly, the most tedious task throughout this whole spectral factorization solution methodology is the determination of $\mathcal{N}(s)$ and $\mathcal{D}(s)$ having the above-demanded characteristics. Yet, if the existence of such rational transforms is taken for granted, then Equation (3.28) can be re-written as:

$$\Gamma(s) \cdot \mathcal{N}(s) = \overline{\Gamma}(s) \cdot \mathcal{D}(s) \tag{3.32}$$

with both the r-h-s and l-h-s of this last equation being analytical in the joint region $0 < \Re(s) < \Delta$. As a matter of fact, the analyticity of $\mathcal{N}(s)$ over the region $R : \Re(s) > 0$ was earlier established. In addition $\Gamma(s)$ is analytical over the same region since $\Gamma(s) = \mathcal{L}[\mathcal{W}(t)]$ with, obviously $\mathcal{W}(t)|_{t<0} = 0$. Hence, $\Gamma(s) \cdot \mathcal{N}(s)$ must be analytic over R. Similarly, $\overline{\Gamma}(s)$ and $\mathcal{D}(s)$ are analytical over the region $R' : \Re(s) < \Delta$. Thus, $\overline{\Gamma}(s) \cdot \mathcal{D}(s)$ will be analytical over R' as well. By virtue of the equality in (3.32), the analyticity of the r-h-s and l-h-s products must extend to the regions $\Re(s) < 0$ and $\Re(s) > \Delta$ respectively with zero singularities throughout the whole finite s-plane. In other words, $\Gamma(s) \cdot \mathcal{N}(s)$ and $\overline{\Gamma}(s) \cdot \mathcal{D}(s)$ being equal and both analytic and bounded $\forall s < \infty$, then, by *Liouville's Theorem* (refer to [110]) $\Gamma(s) \cdot \mathcal{N}(s) = \overline{\Gamma}(s) \cdot \mathcal{D}(s) = \psi$ where ψ is a constant that has been proven in [105] to be:

$$\psi = \mathcal{W}(0) = \mathbf{Pr}[\widehat{\omega} = 0] \tag{3.33}$$

From Equation (3.33), one can conclude that ψ is equivalent to the probability that a certain EV arrives to an idle station and, hence, does not have to wait (*i.e.*, its waiting time is equal to zero). Note that this probability is not always equivalent to the fraction of time during which the station is found idle (*i.e.*, $1 - \rho$)[4]. From all of the above, it directly follows that:

$$\Gamma(s) = \psi \cdot \mathcal{N}^{-1}(s) \tag{3.34}$$

Once ψ and $\mathcal{N}(s)$ are determined, then so will be $\Gamma(s)$. Next, use the Inverse Laplace Transform to compute:

$$\mathcal{W}(t) = \mathcal{L}^{-1}[\Gamma(s)] \tag{3.35}$$

Finally, the mean waiting time can be computed as:

$$\overline{W} = E[W] = \int_0^\infty t\mathcal{W}(t)\mathrm{d}t = -\frac{\mathrm{d}\Gamma(s)}{\mathrm{d}s}\Big|_{s=0} \tag{3.36}$$

[4] ψ would be equal to $1 - \rho$ only for an $M/G/1$ system.

3.7 Numerical Analysis and Simulations

A MATLAB-based custom-built simulator was developed to examine the validity and accuracy of the waiting time analysis presented in Section 3.6 Under each of the proposed EV scheduling schemes in Section 3.3 (*i.e.*, RSS, CSF and MWT), the model's characterizing metrics and EV waiting times were computed for a total of 10^7 EVs and averaged over multiple simulator runs to ensure the realization of a 95% confidence interval. The following input parameter values were assumed: 1), area size of 9 km^2, 2) Number of CSs, $N_{CS} = 5$, 3) EV arrivals to the entire area follow a Poisson process with parameter $\mu_{\mathcal{I}}^{-1} \in [1; 8]$ EVs/hr, 4) per-EV speeds are drawn from a truncated Normal distribution over the range $[V_{\text{min}}; V_{\text{max}}] = [10; 50]$ m/s.

3.7.1 Model Verification and Performance Analysis

To verify the accuracy of the earlier-presented waiting time analysis, CS dynamics were simulated and captured under the RSS and CSF scheduling schemes. In particular, under each of these schemes, the average waiting time experienced by EVs arriving to each and every one of the simulated CSs were recorded and plotted against the per-CS Offered load in (EVs/sec). Given the fact that all CSs have exhibited similar result trends only the average waiting time experienced by one of these CSs (under RSS) are reported herein in Figures 3.6(a). Regarding CSF, it is also true that all CSs exhibited results with exactly similar trends. However, one of these CSs, in fact the one that, on average, happened to be the closest to the majority of the arriving EVs, exhibited much higher waiting time values than the remaining other stations. The results corresponding to this particular station are reported herein in Figure 3.6(d). The reported average waiting time is plotted in both of Figures 3.6(a) and 3.6(d) are in units of seconds. It is quite clear that these two figures constitute a tangible proof of the validity and accuracy of the presented analysis in Section 3.6. This is especially true since in each of these figures, curves corresponding to simulation results almost overlap with their theoretical counterparts with minor differences only ranging between 2.53% and 4.18%.

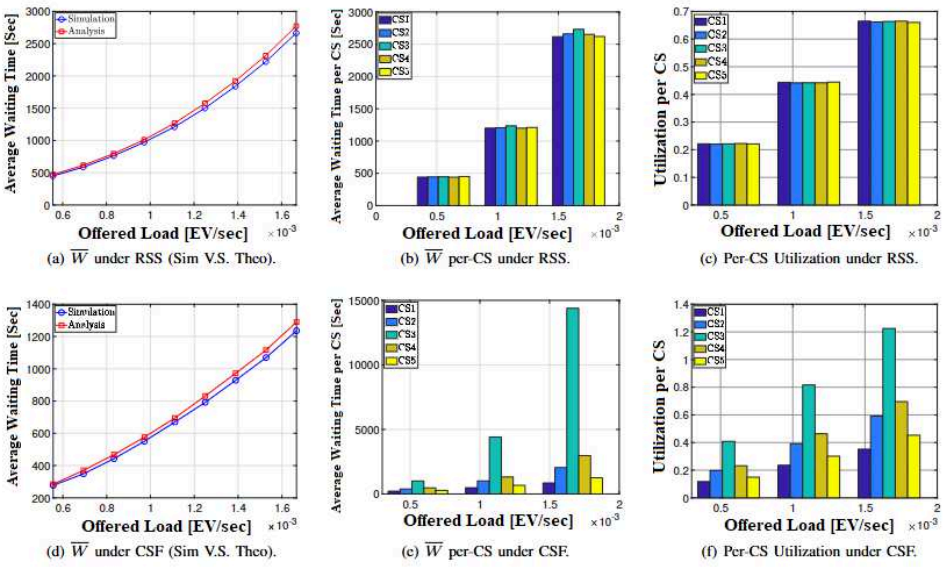

Figure 3.6: Achieved average waiting times and per-CS utilization under RSS versus CSF

The theoretical analysis' correctness being established, it is now important to elaborate on the waiting time trends under both of the RSS and CSF schemes. Indeed, as shown in the figures, the achieved average waiting time increases as a function of the per-CS Offered load; this being a direct result of the increase of the experienced load to the entire CS deployment area whereby more EVs arrive to the overall area and, hence, the likelihood that more EVs arrive to each CS will also increase. Under RSS, for a fixed value of per-CS EV arrival rate, all CSs exhibit merely identical and uniform results as shown in Figure 3.6(b). This is especially true since, under RSS, an arriving EV is equally likely to choose any of the available CSs within the simulated area; hence the experienced EV load is equally balanced over all available CSs within that area. This is further confirmed by Figure 3.6(c).

In contrast, under CSF, any arriving EV shall select the station that is closest to it. Hence, depending on the location of the arriving EV and the locations of the various CSs within the overall considered area, only one of these CSs shall be determined to be the closest to that EV. The reported results herein in Figures 3.6(e) and 3.6(f) show that the third CS appears to be, on average, the closest to most arriving EVs. This is especially true since this CS happens to be exhibiting the highest waiting time (Figure 3.6(e)). By Little's Theorem this CS is, therefore, experiencing the largest average number of EVs waiting in line to receive service and will, thus, experience the highest utilization (Figure 3.6(f)). Here, it is important to mention that, under CSF, each EV will select and drive towards the closest CS independently of other EVs and regardless of the experienced waiting time. Hence, it is natural to observe that some CSs exhibit higher utilization than others. In particular, CSF might cause some CSs to become overloaded (*i.e.* unstable) and, thus, exhibit a utilization (*i.e.*, the load computed as the ratio of the arrival

rate to the service rate) that is higher than one (*e.g.*, CS3 in Figure 3.6(f)).

3.7.2 Further Performance Evaluations and Discussions

This subsection is dedicated to additional waiting time performance evaluation under the last scheme, namely MWT. Recall from Section 3.3 that under MWT, the selection of a particular CS among all available CSs within the considered area is contingent to the waiting time EVs will be experiencing at that CS until they receive service and depart. Specifically, to assist EVs in making informed CS selections and, hence, reduce their waiting times at selected stations, MWT provides requesting EVs with an estimate of the expected waiting time (computed at the instant the charging requests are being issued) they shall experience upon arrival at each and every available CS within the considered area. This incurs a strong dependency between EV arrivals and the individual CS states, each of these latter being summarized by the expected per-CS waiting times. In turn, the state-controlled per-CS EV arrival processes inevitably violate one of the fundamental assumptions underlying the analytical framework presented in Section 3.6. State-dependent waiting time analysis is currently outside the scope of this present work and is actually left for future work. However, it is of added value to provide further insights into the experienced per-CS dynamics under such biased EV arrival processes (already done in Section 3.3) and, accordingly, the achieved average waiting times and utilization under MWT.

The achieved average waiting time by MWT will increase as a function of the Offered load as shown in Figure 3.7 (a) illustrating this expected trend for one of the CSs (all other CSs exhibit similar variations in $\overline{W}$ as can be asserted by Figure 3.7 (b)). Contrary to any expectation, however, the figures indicate that, under MWT, EVs shall experience almost no waiting time (*i.e.*, in the order of a couple of seconds) under low Offered loads. Indeed, this is because MWT controls/biases the arrivals of EVs to CSs in the sense that, under MWT, an EV always chooses, first, to drive towards the CS exhibiting the lowest average waiting time. Starting off with a fresh empty system, all stations are equally likely to be selected. However, a smarter decision would be to select the closest among such CSs, say, for the sake of the example CS1.

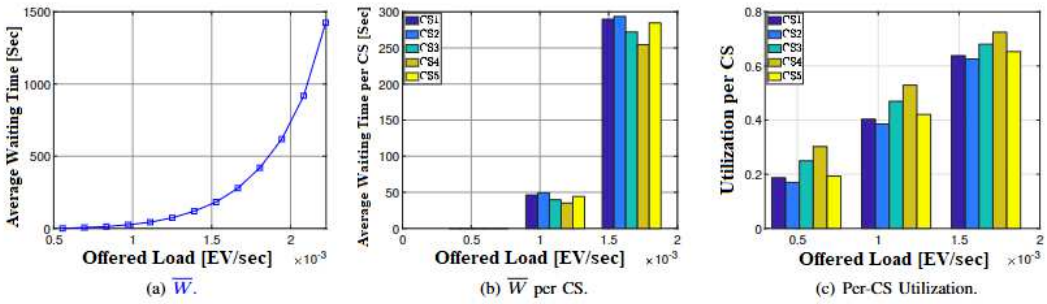

(a) $\overline{W}$. (b) $\overline{W}$ per CS. (c) Per-CS Utilization.

Figure 3.7: Results pertaining to the MWT EV scheduling policy.

This is actually how ties are broken under MWT. If the subsequent vehicle arrives to the area after its predecessor has completed service, then, again, this newly arriving vehicle will find all CSs empty (*i.e.*, zero waiting time) and, hence, shall select the one closest to it. Alternatively, whenever the newly arriving EV finds CS1 busy servicing its predecessor, it shall then select the next closest CS exhibiting the lowest waiting time among the remaining CSs (other than CS1) and so forth.

Under low Offered loads, it is more likely that arriving EVs either find stations empty or just about to finish serving their predecessors (*i.e.*, would become empty as the arriving EV drives towards the CS). This is confirmed by the relatively low per-CS utilization illustrated in Figure 3.7 (c); meaning that CSs are being utilized to serve EVs but are highly likely to be found empty upon arrivals of new EVs. Obviously, as the experienced load increases, these CSs shall become more likely to be found busy upon arrivals of new EVs and here, MWT will interfere and bias the selection process by always prioritizing the CS that jointly is the closest to the arriving EV and guaranteeing the lowest waiting time.

The above being said, what remains is to compare the waiting time performance of MWT to RSS and CSF as illustrated in Figure 3.8. For values of experienced loads that guarantee stable CSs, MWT's embedded intelligence allows it to beat RSS and CSF as it distributes the Offered load over all CSs in a smart way to maximize the per-EV benefit; this being the selection of the closest CS warranting the lowest waiting time. Worthy of mentioning here is the fact that, this way, MWT would be implicitly accounting for the per-EV requested charging times and instantaneously tries to direct EVs towards underutilized CSs as these always will exhibit the lowest waiting times. However, this behavior is expected to increase the average waiting time at these CSs. This is when MWT will interfere again and redirect newly arriving EVs to other CSs and so forth. In contrast, RSS aims at equally distributing EVs over all CSs regardless of the per-CS achieved average waiting time and the proximity of these CSs to the arriving EVs. Indeed, balancing the per-CS Offered load has the objective of reducing the per-CS queue length and, therefore, the per-CS average waiting time. However, elevated service times for some EVs

shall counter this effect; hence, placing RSS right in between MWT and CSF where this latter is witnessed to often overload one particular CS (*i.e.*, the closest to the majority of arriving EVs) causing remarkable rises in queueing delays.

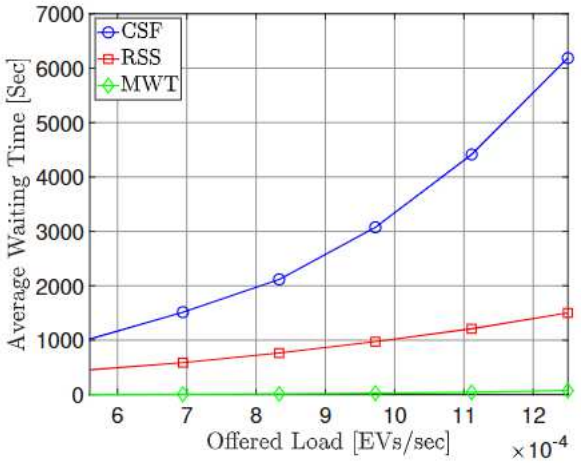

Figure 3.8: Comparison of RSS, CSF and MWT in terms of $\overline{W}$.

3.8 Conclusion

Year after year, real-world recorded data is revealing drastic changes in the statistical characteristics of EV charging processes taking place at public EV CSs. The literature encloses notable work proposing stochastic analysis that fail to adequately model such stations, capture their dynamics, and accurately evaluate their waiting time performance. This work aims at filling this gap and, first, thoroughly analyzes real-world data to extract statistical characteristics pertaining the EV charging times. Then, after close observations of EV arrivals, it is identified herein that, contrary to the majority of existing work assumptions, per-CS EV arrivals do not always follow Poisson processes. Indeed, depending on the EV-to-CS scheduling policies, EV inter-arrival times may be characterized by different phase-type distributions, one of which identified herein is the Erlang distribution. Armed with these findings, an extensive analytical framework is established in this work throughout which, as a first step, CSs are accurately modeled as $G/G/1$ queues. Thorough simulations and numerical analysis confirm the accuracy of the proposed model and its pertaining theoretical average waiting time derivation under one class of EV-to-CS scheduling policies. Another class of such scheduling policies is one that attempts to provide EVs with a priori knowledge of per-CS expected waiting times; hence, allowing these EVs to make informed CS selections in such a way to reduce their experienced delays. One of such scheduling schemes, namely, the MWT, has been investigated to provide some preliminary insights into the strong influence of CS states on the CS selection process; this later strongly biasing the per-CS EV arrivals. Extensive simulations are conducted to capture the achieved CS dynam-

ics and performance under MWT. However, the state-dependent queueing analysis pertaining to this scheme are left for future work.

Chapter 4
A Data-Driven Framework for Improving Public EV Charging Infrastructure: Modeling and Forecasting

4.1 Current QoE Metrics, Problem Statement and Motivation

Ever since 2010, the worldwide achieved average of EV-to-Charger Ratio (EVCR) has been fluctuating at slightly under 10 EVs/charger [111], though, despite its globally recognized eloquence, several countries have alarmingly scored two-to-three-fold this value. Keep in mind here that the main objective, now, is to show the inadequacy of the employed EV charging infrastructure expansion strategies in the majority of countries around the globe as well as the inappropriateness of the metrics that have been globally adopted to measure and indicate whether or not such expansions are being capable of coping with the rapid growth in EV market penetration rates. For this purpose, real-world data is required to ensure the correctness and credibility of the provisioned insights. Hence, following a legal agreement and officially approved research collaboration with Hydro-Quebec (HQ) [1], this work taps into HQ's complete database encompassing realistic daily records (overall 6 million) of a wide range of EV charging-related measurements pertaining to comprehensive aspects of EV charging stations' dynamics (*e.g.*, start time and duration of each charging session, per-session average drawn power and total drawn energy, initial installation date pertaining to each EVCS, per-EVCS nominal charging rate and geographical location)[2] for the various sites within Quebec (*i.e.*, around $7,454$ stations distributed over $3,878$ different locations) and spanning the past five years from 2018 to 2022. With access to such a panoptic database of EV charging records, it becomes easy to evaluate and graphically visualize

[1] HQ owns/operates, through a subsidiary, around 80% of the public EV charging infrastructure in Quebec, Canada.

[2] It is worthwhile noting here that HQ's database contains no information about the per-EV arrival time and waiting time until it starts receiving service. Such are vital QoE metrics that shall be intelligently derived herein using the available records. Such metrics will allow for individual per-EVCS performance evaluation as explained hereafter.

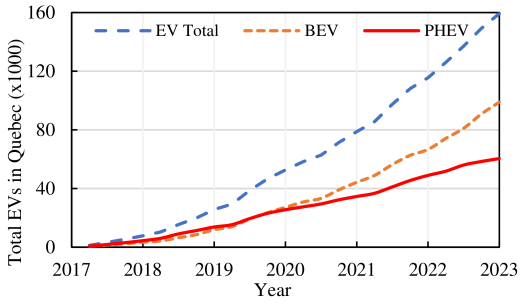

Figure 4.1: EV market penetration in Quebec.

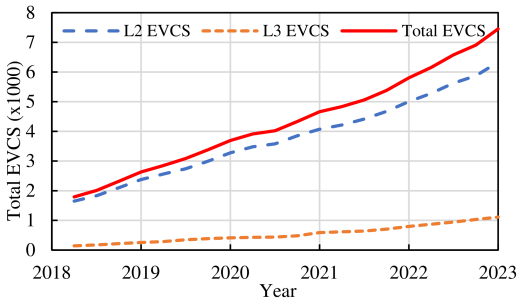

Figure 4.2: Number of deployed chargers in Quebec

(as shown hereafter in Figures 4.1 through) the evolution of Quebec's EV charging infrastructure using the same metrics adopted by the International Energy Agency (IEA). Curves illustrated in these figures shall serve as tangible proofs of the inappropriate QoE evaluations and, hence, the ill-suited EV charging infrastructure expansions they inspire.

Figure 4.1 shows a steadily increasing total number of EVs over the entire road network of Quebec starting from year 2017 until this present time. This induces expectations of further expansion of the EV charging infrastructure at least at a rate that can ensure such an infrastructure copes with the increasing EV market penetration rate; hence, maintaining proper consumer-perceived QoE levels. In addition, Figure 4.1 also shows that starting from year 2019, the number of fully Battery-powered EVs (BEVs) started to overshadow that of Plug-in Hybrid EVs (PHEVs). This is a major change that promotes an increased need for more frequent per-EV charging activities as well as the need for additional energy supply to cope with this increased energy demand. This is not to mention that BEV owners would surely highly appreciate faster charging processes with less waiting; this being an expectation originating from an innate desire of QoE equity with Internal Combustion Engine (ICE) vehicles' drivers. As such, intuitively, one's thoughts get immediately directed to an increase in the deployment of advanced Level 3 (L3) fast chargers concurrently to the expansion of existing EVCSs through the addition of more of the typical Level 2 (L2) chargers. To this end, Figure 4.2 presents the EV charging infrastructure expansions observed over the past five years in Quebec; those being mainly characterized

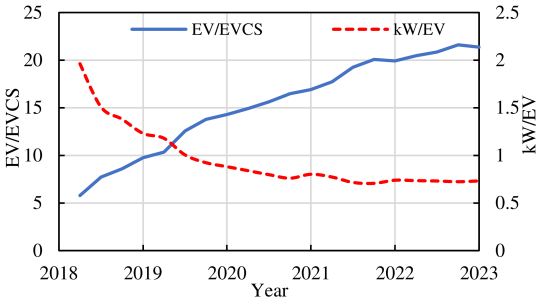

Figure 4.3: Quebec's achieved EVCP v.s. EVCR.

by the total numbers of L2 and L3 chargers that have been deployed and became operational and accessible by EV drivers. Here, observe that the number of L2 chargers increased by almost 300% from 2018 to 2022 whereas the number of L3 fast chargers shows a relatively shy ten-fold increase. Regardless though, one cannot deny that major efforts and investments have been and continue being made to improve the availability and accessibility to a QoE-acceptable EV charging infrastructure. Unfortunately however, such efforts, are mislead to go in the wrong direction. This is especially true since they are unable to throttle down and control Quebec's continuously increasing EVCR with rising slopes as shown in Figure 4.3. AS a matter of fact, Quebec's EVCR today scored 21 EVs/charger. Factoring in the chargers deployed by other operators would slightly bring down the province's EVCR to 17; this being way above the world's global average. In parallel, look at the achieved Per-EV Charger Power (EVCP) in Quebec; this being computed, following IEA's guidelines, as the ratio of the total average per-EV charging power for all available public chargers to the total number of EVs on the road. Here, note that the globally achieved EVCP amounts to 2.4 kW/EV. Figure 4.3 shows how Quebec's EVCP has been drastically decreasing over time for it to stabilize at around 0.73 kW/EV towards the end of 2022. At this point, also, when factoring in the contributions of the chargers pertaining to other operators in Quebec, the province's EVCP would only rise to 0.91 kW/EV.

The above constitutes a tangible proof that the above-adopted metrics and EV charging network expansion strategies are ill-developed and that there is urgent need to establish and implement new plans for expanding this infrastructure in such a way for it to, first, fill in the gap and cope with the remarkable rise in EV adoption and, second, steadily parallel this (expected) long-term rise and meet the increasing EV charging demands both in terms of frequency and QoE-driven performance. Obviously, in light of the ealier-presented discussion, EVCR and EVCP cannot serve the general purpose of assessing the suitability of the existing infrastructure and its state-of-the-art expansion schemes as they hide from operators the factors underlying: *i*) the non-homogeneous variations of EV adoption trends corresponding to different areas within the same country or province (as revealed by thorough analysis of realistic data), *ii*) the contrasted location-restrictive EVCS deployment feasibility, as well as, *iii*) the disparity in charging demand levels experienced in different locations. For instance, the number of EVCSs deployed

in a certain touristic area might appear to be satisfactory. Keep in mind though that in such an area, often, a large proportion of the EVs requesting to charge at that area's local EVCSs may happen to be incoming from other areas. IEA's adopted metrics, namely EVCR and EVCP, do not account for these EVs when evaluated for their areas of origin. It is, therefore, of notable importance to develop adequate real-world-data-driven and location-aware EVCS QoE performance metrics that can provision insights into the suitability of existing location-dependent EV charging networks and appropriate such networks' expansion schemes.

This chapter proposes a new set of critical EVCS QoE performance metrics, namely: *i*) the per-EVCS achieved maximum and average waiting times, *ii*) the per-charger occupancy and *iii*) the per-EVCS blocking probability. The design and quantification of all of these metrics is based on HQ's comprehensive database of realistic EV charging-related records. Truly, the proposed metrics herein prevail where their existing counterparts fail at provisioning operators with visibility and insights into event dynamics of EVCSs; thus, guiding them in formulating and implementing adequate well-informed EV network sizing and charger deployment plans coupled with optimal scheduling algorithms that aiming at improving the end-consumer-perceived EV charging QoE in any particular location. To gauge their merit, a charging load forecast model adopting these new metrics is presented hereafter to predict the future charging demand per EV charging site.

4.2 Novel Contributions

This chapter aims at filling the identified literature gap consisting of the non-existence of proper QoE evaluation metrics, and the lack of accurate long-term EV charging demand forecast tools. Its contributions are briefed as follows:

1) To the extent of the authors' awareness, this current work is the first to present a comprehensive data-driven framework targeting the per-EVCS QoE assessment. A number of metrics are formulated for the purpose of aiding the EVCS infrastructure operator gain a deeper understanding of their charging infrastructure utilization. These metrics shall provision EVCS infrastructure operators with in-depth visibility into the event-driven system dynamics pertaining to any particular EVCS deployed at any arbitrary location; hence, promoting operators' understanding of their charging infrastructure utilization allowing them to optimize additional chargers' deployment, and charging network sizing.

2) Comprehensive EV-charging-related historical data is exploited and fed into a newly developed Machine Learning (ML) based algorithm for long-term EV charging demand forecast. Measurement values pertaining to the number of requests in addition to external factors impacting the charging demand are fed as inputs to this algorithm allowing it to accurately predict up to one year of future per-EVCS EV charging demand.

4.3 Data Pre-processing and Preparation

As already mentioned in Section 4.1, the work presented in this chapter is driven by a comprehensive database of 6 million realistic charging session records pertaining to $7,454$ EVCSs deployed in $3,878$ locations. This data has been collected from the various EVCSs over the past 5 years starting from January 2018 until December 2022. Each charging session record encompasses the session's starting time, ending time, outlet identifier (ID), station ID, station postal code, and the amount of energy drawn from each outlet, among numerous other parameters that are of less interest to the work presented in this chapter. Nonetheless, a major drawback of this data set is that it lacks any information about EV arrival times to the different EVCSs as well as the amount of time spent at the station waiting to start charging. Consequently, in the absence of such crucial information, the per-EVCS QoE performance evaluation becomes quite challenging. This is carefully addressed in the remaining sections hereafter. At this point though, it is quite important to mention that after closely observing the available records, some of them can be identified as invalid. For instance, all records pertaining to sessions that: *i*) lasted less than 3 minutes or more than 2 hours, *ii*) have no recorded payments associated with them, and, *iii*) show that no energy has been drawn from the corresponding outlet, are assumed to be invalid records, and, hence, have been removed. Following this cleaning phase, the remaining records have been, first, arranged in ascending order of their corresponding postal codes, and then, for each station, records are ordered according to the starting times of each session. To this end, a careful examination of the postal codes and site IDs pertaining to each station reveals the operator's attempt to cluster regions based on the postal code. Consequently, all stations having the same postal code are considered as belonging to the same site and, hence, associated with the same site ID.

4.4 EVCS QoE Performance Metrics

This section presents two sets of novel metrics for assessing the Quality of Service (QoS) provided by public Electric Vehicle Charging Stations (EVCSs) in Quebec, Canada. The first set of metrics includes the number of charging requests, per-site utilization, per-site occupancy, idleness, and blocking probabilities, which are based on a comprehensive database of realistic measurements taken at different times and pertaining to various EV charging process variables. These metrics are subsequently used as inputs to a forecast model developed for predicting future EV charging loads. They are as follows:

• **Number of Charging Requests**, N_R, represents the number of unique charging requests experienced by an EVCS during a given time period. The provided data reveals that some EVs stop but then resume charging within a few seconds. In what follows, such short charging in-

terruptions are neglected (*i.e.*, the continuation of charging is not considered as a new request placed by the same EV but rather the same request identified using the account credentials of the user who initiated the charging session). Also, all charging sessions with only a few seconds durations are discarded.

• **Charging Site Utilization**, U, determines if a site is being underutilized or over-utilized. Through the observation of the variations of a site's daily instantaneous utilization, an operator can determine the exact EV charging demand at that site at any particular point in time. Also, U's long-term variations reveal the direct impact of EV consumers' socio-economical habits on EV charging requirements. Consequently, U provides operators with insights into the load experienced per site, which cannot be provided by N_R alone as this latter contains no information about the different charging sessions' durations. By discretizing time into mini slots of duration 1 minute each:

$$U \;=\; \frac{1}{T}\sum_{i=1}^{T}\frac{k_i}{n} \qquad 0 \leq U \leq 1, \tag{4.1}$$

where T is the total number of time slots within an observation period, $i \in \mathbb{N}$ used for indexing each time slot within T, k_i is the number of occupied EVCSs during time slot i and n is the number of per-site EVCSs.

• **Site Occupancy**, Ω, represents the probability that at least one of a given site's EVCSs is occupied (*i.e.*, the probability of that charging site being utilized):

$$\Omega \;=\; \frac{1}{T}\sum_{i=1}^{T}\mathcal{Z}_i, \tag{4.2}$$

where

$$\mathcal{Z}_i := \begin{cases} 0, & \text{if } k_i = 0, \\ 1, & \text{if } k_i \geq 1. \end{cases}$$

Hence $0 \leq \Omega \leq 1$.

• **Site Idleness Probability**, P_I, represents the fraction of the total observation duration T during which all EVCSs pertaining to a given site are idle. This metric quantifies the possibility of an EV arriving at a given site and finding all EVCSs available. As the complement of Ω:

$$P_I = \Pr\left[k_i = 0\right] = 1 - \Omega \tag{4.3}$$

• **Site Blocking Probability**, P_B, represents the proportion of T during which all of a given site's EVCSs are found to be completely busy (*i.e.*, the probability of an EV arriving at a given site and finding all EVCSs occupied and, hence, suffering from immediate denial of service):

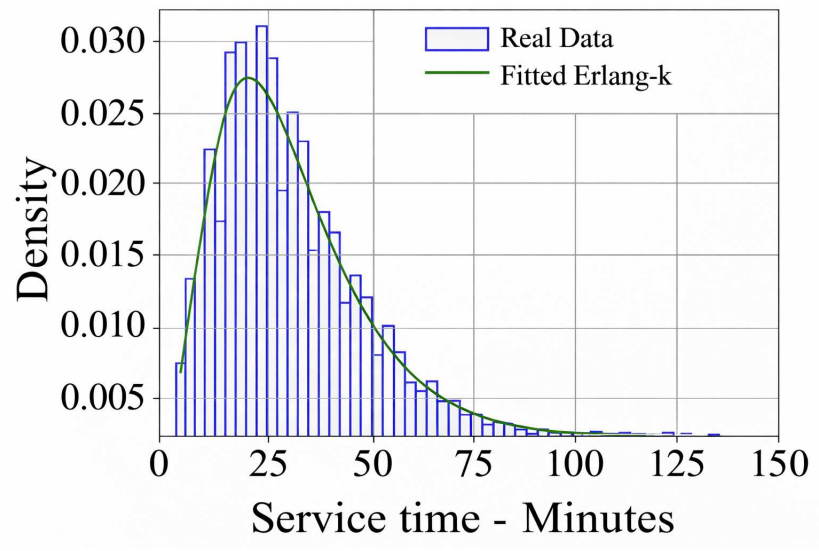

Figure 4.4: Sample service time data distribution.

$$P_B = \frac{1}{T}\sum_{i=1}^{T} X_i, \qquad X_i = \begin{cases} 1, & k_i = n, \\ 0, & k_i < n. \end{cases} \tag{4.4}$$

Beyond a certain QoE threshold, P_B indicates the failure of the existing charging infrastructure to sustain the growing EV charging demands experienced by the given site.

Next, the second set of metrics includes the longest per-site busy period and average EV waiting time, which are evaluated and reported by a custom-built simulator. These metrics aim to quantify the quality of perceived service by EV consumers at different public EVCSs and can be used by EV charging infrastructure operators worldwide to assess the performance of any charging site and plan EV charging network expansions as needed. They are:

• **Number of Delayed EVs**, N_D, represents the number of EVs that have experienced a certain delay at a given site waiting to receive service (*i.e.*, start charging). Any EV that starts charging within at most t minutes (e.g., $t \leq 5$minutes) from the end of a preceding charging session at a blocked site is considered to be a delayed EV. The value of t is not fixed and is empirically estimated and recorded by the operator on a per-site basis given the fact that it is affected by numerous uncontrollable factors that are external to the charging process (*e.g.*, parking lots' availability close to rest areas and shopping malls and their proximity to EVCSs, in-proximity services, etc). In the future, several solutions may be adopted to increase the accuracy of t's values (*e.g.*, the installation of cameras to provide video footage showing the advancement of a waiting EV into service position and, hence, the start of a new session).

• **Average Waiting Time**, $\overline{W}$, is the average queueing delay experienced by EVs waiting at a given site to start charging. $\overline{W}$ is generated using a custom-built python-based discrete-event simulator that models each site as an *M*/*G*/k queue.

4.5 QoE Evaluation Methodology

The adopted per-site QoE-oriented performance analysis methodology is presented. First, although the above-presented metrics may provide per-EVCS performance insights for the chosen site, it is observed that performance trends notably vary for different observation period categories (*e.g.*, regular weekdays, weekends, holidays, etc). As such, to capture such variations, QoE performance evaluations shall be conducted on daily basis spanning any required duration (*i.e.*, week, month, year). Precisely, the examined days throughout the analysis period shall be grouped based on their different categories. Then, for each one of these days, each of the above-listed metrics shall be evaluated. This will indicate the frequency whereby each of these metrics' respective values signaled a red flag for each one of these days' categories; this being of utmost importance to operators when developing EV charging infrastructure expansion plans. For instance, in touristic areas, the achieved QoE might be misleadingly perceived as good whenever values of the U, Ω, P_B, N_D, and $\overline{W}$, do not bypass a given threshold when evaluated for one whole month or year in one shot. The operator, here, may be deluded to trust a site's operational normality whereas, truly, these metrics' daily values may reveal an overall site under-utilization during normal work days and an over-utilization (*i.e.* low QoE) during weekends and holidays.

4.5.1 Simulation Framework

A custom-built discrete-event python-based simulator is developed herein for the purpose of modelling any EVCS pertaining to any charging site as an *M*/*G*/k queueing system. This simulator's input parameters' values are set according to simulated EVCS's information extracted from the given dataset. Precisely, EV arrivals are assumed to follow a Poisson process with a parameter $\lambda_E = N_E \cdot T^{-1}$ EVs/s with N_E being the number of observed EVs arriving to the simulated EVCS within the observation period T. N_E is dictated by HQ's recorded data. The per-EV service time is drawn from an empirically evaluated Erlang-k distribution that fits HQ's service time records for the simulated sites. Due to space limitation, only one such distribution example is illustrated herein in Figure 4.4 where the Root Mean Square Error (RMSE) between the realistic distribution and its theoretically fitted counterpart is of the order of 10^{-8} indicating a highly accurate fit. Finally, the simulated EVCS's number of outlets is k and is also provided by the operator. The fundamental objective of this developed simulator is to generate N_D and $\overline{W}$. Furthermore, future EV arrival forecasts are going to be generated hereafter. Such arrival forecasts may then serve as inputs to the above-mentioned simulator, which, then, shall return forecasts for future N_D and $\overline{W}$ values pertaining to a simulated EVCS.

4.5.2 Filling the Gap in the Dataset Created by COVID-19

In an attempt to combat the proliferation of COVID-19, governments around the Globe and, particularly in Quebec, imposed numerous and lengthy curfews, lockdowns and border closures. In addition, remote work and schooling policies were implemented all over the province. All these have remarkably affected the province-wide transportation sector. Precisely, during 18 months (from January 2020 to June 2021) the number of vehicles on the road decreased by almost 60% including the number of EVs. The decrease in this latter reflected itself in an abnormal decrease in EV charging demands as illustrated in Figure 4.5(a); hence, the reason behind referring to this time period hereafter as the "*gap period*". For all purposes of proper QoE performance forecasting, proper charging demand trend corrections (data augmentation) need to be applied to this gap period in order for it to appear as a smooth quasi-normal continuation to its predecessor and successor periods; that is, as if the pandemic never occurred. This is achieved as follows:

1) Among the 5 years data records pertaining to a given site, disregard all those corresponding to the gap period.

2) Compute an M days weighted moving average whereby, the number of requests for each target day of the gap period becomes equal to the average number of requests observed during the $\frac{M-1}{2}$ past and future days. As such, the target day is that M^{th} day that appears at the center of the M days period. This mathematically translates to:

$$\overline{N_{R,d}} = \frac{1}{M-1} \sum_{j=d-\frac{M-1}{2}}^{d+\frac{M-1}{2}} N_{R,j} \tag{4.5}$$

where d is the index of the targeted gap day and $N_{R,j}$ is the actual number of requests.

3) Compute the relative daily charging request difference $\Delta N_R = \left(N_{R,d} - \overline{N_{R,d}}\right) \overline{N_{R,d}}^{-1}$. Use all relative differences over the entire 42 months before and after the gap to generate ΔN_R's empirical probability distribution, $\mathcal{D}$.

4) Finally, to each computed $\overline{N_{R,d}}$ over the 18-month gap period, add a random ΔN_R value drawn from $\mathcal{D}$.

Figure 4.5(a) ($M = 30$) concurrently plots $N_{R,d}$ and $\overline{N_{R,d}}$ pertaining to one selected site over the entire 5-year period. The trend anomaly is clear during the gap period compared to its normal counterparts appearing before and after the gap. Most importantly, Figure 4.5(a) tangibly proves $\overline{N_{R,d}}$'s potency in capturing the seasonal/annual trends of $N_{R,d}$ while smoothing out its randomness. Figure 4.5(b) shows the reconstructed number of charging requests values corresponding to the gap period following the above-elaborated procedure. These results assert the suitability of the utilized approach since the reconstructed trend appears clearly as a smooth quasi-normal bridge connecting its predecessor to its successor curves.

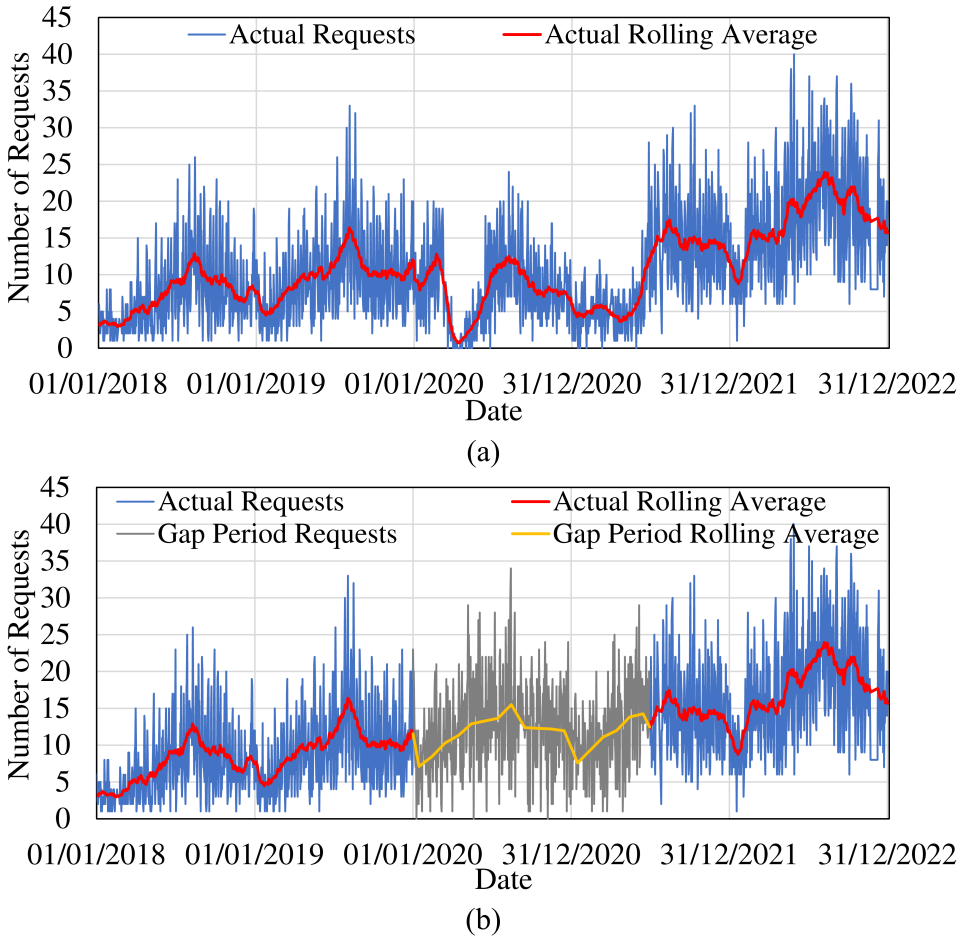

Figure 4.5: Five year charging requests (a) including the COVID-19 data and (b) requests after filling the gap caused by COVID-19

Table 4.1: Time stamp features

Feature Name	**Range of Values**
Weekday (Monday→Sunday)	$[0; 6]$
Day of the month	$[1; 31]$
Day of the year	$[1; 365]$
Month of the year	$[1; 12]$
Week of the year	$[1; 53]$
Week of the month	$[1; 4]$
Quarter of the year	$[1; 4]$
Recorded year	$[2018; 2022]$
Working Day	[0: Weekend/Holiday; 1: Business day]

4.5.3 Long-Term Forecast Model

As anticipated, the EV charging demand is expected to grow at an increasing pace in the coming years. This stresses the importance of creating a long-term forecast model that can accurately predict the EV charging load in terms of served request counts over an entire year while taking the load's seasonality into consideration.

• **Data Pre-Processing and Feature Engineering:** The first pre-processing step consists of chronologically arranging the charging records to create a continuously evolving time series and then extract from them the required features, the fundamental one of which are the timestamps listed in Table 4.1. Here, timestamp differentiation and proper interpretation are important especially because of the differential characteristics of regular weekdays' charging requests and their weekends/holidays counterparts. Table 4.2 lists additionally extracted categorical features constituting external factors that impact the charging demand. All of these features are then encoded using the mean encoding method described in [112] and [113] to reveal a logical correlation between them and their corresponding label (*i.e.*, $N_{R,d}$). Consequently, during the training phase, the model determines the relationship between the predicted value and the mean features' encoding instead of the actual $N_{R,d}$.

• **Forecast Model:** A Seasonal Auto-Regressive Integrated Moving Average with eXogenous factors (SARIMAX) statistical learning model (*e.g.*, [114]) is presented hereafter. This model takes as input a time series rendering it capable of accurately predicting future $N_{R,d}$ values while concurrently capturing its real-world historical data inputs' seasonality and patterns. In the sequel, it is proven that SARIMAX is capable of: *i*) accurately capturing and representing this seasonality for 1-year forecasts, and, *ii*) integrating multiple external variables and deduce their impact on the charging demand's behavior.

Table 4.2: Charging service features

Feature Name	**Range of Values**
Charging requests weighted rolling average	Float
Province-wide number of available public EVCSs	Integer
Province-wide number of registered EVs	Integer
Region-specific number of available public EVCSs	Integer
Region-specific number of registered EVs	Integer

Table 4.3: Charging Site Description and Number of EVCSs per Site

Site #	**Location**	**Number of EVCSs/Site**
1	City 1 Downtown	2
2	City 1 Residential Area	2
3	City 2 Residential Area	2
4	City 2 Mall Parking Lot	2
5	City 3 Downtown	1
6	Suburb 1	1
7	Suburb 2	2
8	Rural Area 1	1
9	Rural Area 2	2
10	Touristic Area 1	2
11	Touristic Area 2	1
12	Highway 1	2
13	Highway 2	2
14	Highway 3	4

As a matter of fact, the accessible data sets related to the addressed problem in this chapter enclose data sample points that constitute a time series. This is especially true since these samples represent the magnitude of changes in the EV charging load as a function of time. The objective here is to forecast future metric values (and their variations as a function of time as well) according to what can be learned from the past history embedded in the above-said time series. As such, given that such data exhibits seasonality patterns and given the availability of a strong exogenous factor in the time series, SARIMAX would be the best forecasting model fit in this case.

SARIMAX is defined by three main parameters, `p`, `d`, and `q`, respectively denoting the number of auto-regressive terms, the order of differentiation, and the order of moving averages. The determination of seasonal variations is required to establish a Seasonal Auto-Regressive

Function (SARF) in addition to a Non-seasonal Auto-Regressive Function (NARF) [115]. Additionally, the set of exogenous variables is fed into the model in an array-like parameter `exog`. Proper tuning SARIMAX's parameters allows for the generation of accurate forecasts based on the detected patterns and the exogenous features. The recorded daily per-site number of charging sessions and their corresponding exogenous variables are aggregated weekly to overcome $N_{R,d}$'s randomness. This kind of aggregation is acceptable and rather preferred for objectives similar to those adopted in this chapter (*i.e.*, forecasting a charging site's QoE future evolution).

Initially, the Box-Jenkins approach is used to estimate the most appropriate range for the `d` parameter. Then the Partial Auto-correlation function was used to determine an appropriate range for `p` and the Auto-correlation function was used to determine `q`. Augmented-Dickey-Fuller tests are executed to verify the existence of non-stationary conditions. A close examination of these tests' results reveals that the best model is one to which correspond fractional parameters' values. In fact, the Fractional Autoregressive Integrated Moving Average (ARIMA) is used when the data patterns exhibit long-range dependencies that cannot be captured using integer parameters. The interpretation of the fractional parameters becomes different than the interpretation of the integer parameters. Fractional differencing with $\mathtt{d} < 1$, is used to smoothen out very long-term data dependencies while simultaneously preserving the short-term dependencies. A value of $0.5 < \mathtt{d} < 1$ would indicate the presence of a strong historical dependence in the data. Additionally, using a fractional `d` eliminates the issue of over-differencing which might add white noise when large values greater than 1 are used. Additionally, it is favorable to choose low values of the `p` and `q` when using fractional values of `d` to learn the long-term dependencies of the data while simultaneously preserving the short-term fluctuations and dependencies. As a result, low values of the fractional auto-regressive term `p` are used to capture the short-term dependencies of the data. Finally, low values for the moving average order `q` are used to capture the short-term fluctuations and noise in the data. As a result, grid search is performed here to tune the parameters of the SARIMAX model adopted herein with low range of `p` and `q` and a fractional `d`. Additionally, the choice of exogenous variable is extremely important to improve the model's accuracy significantly. This is the number of EVs in the region (scaled by the average charging demand of a typical EV) was selected as an exogenous variable.

The model is trained and optimized against the data extending from 2018 to 2021 based on the above-described approach. Then, it is tested against non-training data (*i.e.*, pertaining to year 2022), to validate its ability to forecast an entire year accurately. Several accuracy metrics are used to evaluate the model's accuracy such as the root mean squared error (RMSE), mean squared error (MSE), mean absolute error (MAE), and mean absolute percentage error (MAPE).

The SARIMAX model proposed herein forecasts the weekly average number of requests with 99% confidence. This allows, at this point, to utilize this model to forecast the charging requests for the selected sites throughout the entire next year 2023. Note that the model requires

Table 4.4: Charging Site Occupancy in 2021 and 2022

	# Days 10%$\leq \Omega \leq$30%		# Days $\Omega \geq$ 30%	
Site Location	**2021**	**2022**	**2021**	**2022**
City 1 Downtown	239	131	107	232
City 1 Residential Area	182	192	8	13
City 2 Residential Area	247	233	14	20
City 2 Mall Parking Lot	178	245	20	67
City 3 Downtown	139	206	6	12
Suburb 1	127	190	3	10
Suburb 2	160	229	84	34
Rural Area 1	170	198	52	113
Rural Area 2	145	159	70	161
Touristic Area 1	154	85	110	263
Touristic Area 2	187	230	21	41
Highway 1	91	147	5	6
Highway 2	31	107	0	1
Highway 3	220	111	88	252

re-training using the data of each individual site for accurate forecasts to be generated. Additionally, a second year forecast is generated to guide the operator with some longer-term forecasts. However, it is important to highlight that the farther future forecasts are generated with a reduced results' confidence. Yet, every new year of data that is added to the data set enables longer and more accurate the forecasts.

Now, indeed, there are so many different prediction and forecasting models. It is quite interesting to compare the performance of the adopted SARIMAX model with fractional parameters to other models such as LSTM, exponential smoothing (ETS), ARIMA, and SARIMA. This is done in Section 4.6 below.

4.6 Analysis and Forecast Results

This section presents an evaluation of the performance of 14 selected charging sites in terms of the presented metrics in Section 4.4. Moreover, 4 of these sites are selected to showcase the prediction accuracy of the developed SARIMAX. The reported results also illustrate the average waiting time evolution between 2021 and 2022 as well as the predicted waiting time for 2023 highlighting the impact of the increasing EV charging demand on the user-perceived QoE.

Table 4.5: Charging Site Utilization in 2021 and 2022

	# Days $10\% \leq U \leq 30\%$		# Days $U \geq 30\%$	
Site Location	**2021**	**2022**	**2021**	**2022**
City 1 Downtown	267	303	12	38
City 1 Residential Area	69	70	0	0
City 2 Residential Area	108	116	0	0
City 2 Mall Parking Lot	91	186	0	0
City 3 Downtown	139	206	6	12
Suburb 1	127	190	3	10
Suburb 2	149	127	17	0
Rural Area 1	170	198	52	113
Rural Area 2	135	187	17	63
Touristic Area 1	165	210	27	123
Touristic Area 2	187	230	21	41
Highway 1	29	47	0	1
Highway 2	1	21	0	1
Highway 3	63	220	0	0

4.6.1 Occupancy, Utilization and Idle Probability

The number of EVCSs varies from one to another of the 14 sites selected from diverse province-wide locations to capture EV charging load variability. For privacy reasons, these sites' actual locations are replaced with generic names as listed in Table 4.3. Note that a site with 1 EVCS, yields $\Omega = U$.

Table 4.4 presents a summary of the number of days where the per-site occupancy belonged to the normal range of 10% to 30% as well as the number of days where that occupancy exceeded 30%. Table 4.5 on the other hand presents the number of days where the per-site utilization belonged to similar intervals. Ω and U are presented for both 2021 and 2022 to demonstrate the evolution of PCI utilization. Observe that 13 out of the 14 sites, witnessed an increase in Ω and U. Particularly, Touristic Area (TA) 2 and Suburban Area (SA) 1 exhibited an $\Omega > 30\%$ for more than double the days. Another insight that can be extracted from Table 4.4 and 4.5 is that the charging sites next to the Highways 1 and 2 are being lightly underutilized with a $U > 30\%$ on zero and one day respectively in 2021 and 2022. This could indicate the user's tendency to charge at their origin or destination points rather than spending time charging en route. Also, the charging site on Highway 3 suffers an $\Omega > 30\%$. However, its $U < 30\%$ throughout all of 2021 and 2022. A third observation can be made regarding the charging site in City 2's Mall Parking Lot. Even though the number of days where $10\% \leq U \leq 30\%$ doubled, it has never

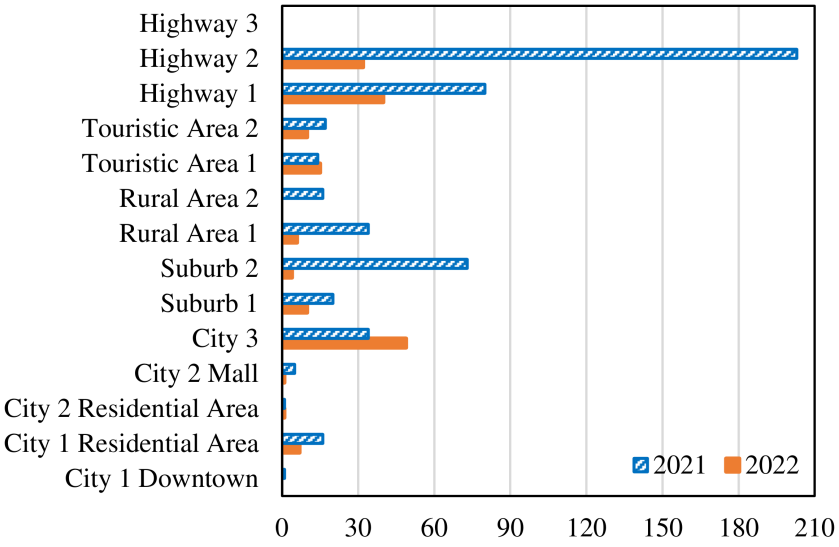

Figure 4.6: Number of Days with $P_I = 100\%$.

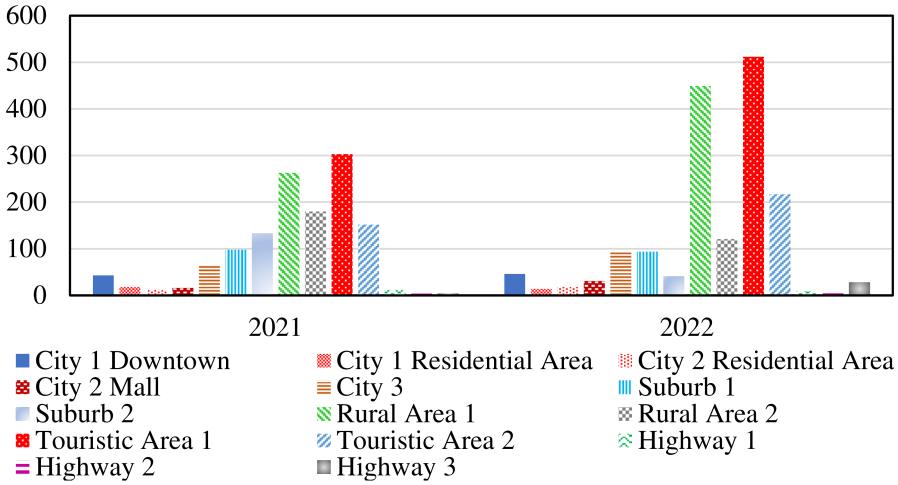

Figure 4.7: Evolution of N_D on the 14 sites between 2021 and 2022.

been over-utilized as the number of days where its $U > 30\%$ remains zero. However, this serves as an indicator that another EVCS should be added to that site.

On the other hand, P_I indicates whether or not a charging site is being underutilized. Table 4.6 presents the number of days where the 14 charging sites experienced a $P_I > 90\%$. This means that on those days the charging site was vacant and remained idle for 90% of the time; thus, indicating a very low utilization on that day. Table 4.6 that charging sites at Highways 1 and 2 are severely underutilized. As such, no new EVCSs need to be added at these locations in the near future. However, one important observation is that all sites experienced a drop in P_I including Suburb 2. This means that, even though the overall utilization of these sites decreased from 2021 to 2022, it became less likely to find them idle. The shaded bars in Table 4.6 represent the percentage of the year during which $P_I > 90\%$.

Finally, Figure 4.6 presents the number of days during which the charging sites were not used

Table 4.6: Number of Days the Charging Sites experienced $P_I > 90\%$.

	2021	2022
City 1 Downtown	19	2
City 1 Residential Area	175	160
City 2 Residential Area	104	112
City 2 Mall	167	53
City 3	220	147
Suburb 1	235	165
Suburb 2	121	102
Rural Area 1	143	54
Rural Area 2	150	45
Touristic Area 1	101	17
Touristic Area 2	157	94
Highway 1	269	212
Highway 2	334	258
Highway 3	57	2

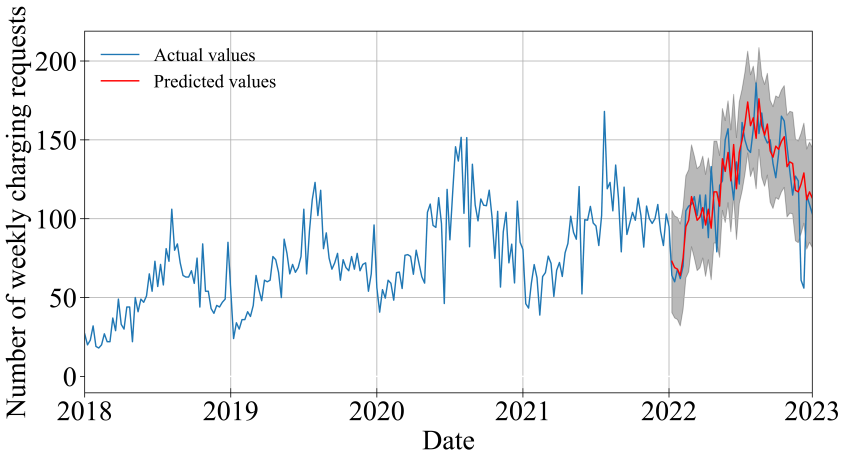

Figure 4.8: SARIMAX testing accuracy for charging site at Touristic Area 1.

at all (i.e. $P_I = 100\%$). This figure can give us three very important observations. The first is that even though certain sites have a high possibility of being idle, the number of days during which no charging occurred on these sites is relatively low. The second observation is on the site at Highway 2 that had a $P_I > 90\%$ for 258 days of the year but only had 32 days during which it was not used. This means that although such charging sites will experience low utilization, they are indeed needed almost every day by EV drivers. The third observation was seen at the charging site in City 3. Although this city experienced higher utilization and occupancy in 2022, the number of days during which it experienced an N_R of zero slightly increased. This type of anomaly represents a trend of more centralized EV charging. It can possibly mean that although user demand on this site increased, this demand was concentrated on certain days. This clearly demonstrates the importance of examining these metrics per day instead of aggregating entire months or entire years together.

Table 4.7: Blocking probability evolution from 2021 to 2022.

P_B	0%		0%-10%		10%-20%		>20%	
Year	**2021**	**2022**	**2021**	**2022**	**2021**	**2022**	**2021**	**2022**
City 1 Downtown	66	43	268	246	29	69	2	7
City 1 Residential Area	227	229	138	134	0	2	0	0
City 2 Residential Area	175	185	189	176	1	4	0	0
City 2 Mall	209	108	153	242	3	14	0	1
City 3	34	17	186	130	103	145	42	73
Suburb 1	20	10	215	155	104	149	26	51
Suburb 2	173	191	152	164	34	10	6	0
Rural Area 1	34	6	109	48	106	105	116	206
Rural Area 2	181	83	143	185	37	59	4	38
Touristic Area 1	179	45	136	161	43	104	7	55
Touristic Area 2	17	10	140	84	123	153	85	118
Highway 1	295	256	69	108	1	1	0	0
Highway 2	334	297	31	68	0	0	0	0
Highway 3	347	295	18	70	0	0	0	0

4.6.2 Blocking Probability

Another important metric studied at these 14 sites is the blocking probability, P_B. Due to the sensitivity of this metric, it is presented in Table 4.7 in steps of 10%. $P_B = 0$ means that a site was not blocked on a given day. A close inspection of Table 4.7 evides that the charging site next to Highway 1 was never blocked for 295 and 256 days in 2021 and 2022 respectively; hence, confirming that EV drivers were less likely to use this specific site. Also, the number of days during which $P_B = 0$ for most of the 14 sites decreased between 2021 and 2022. This goes in line with the results reported in Table 4.4 and Table 4.5 indicating an increase in these sites' U and Ω respectively in 2022. Unexpected, however, is P_B pertaining to Rural Area 1's site. While in 2021 this site had a $P_B \geq 20\%$ for 116 days, this number almost doubled to reach 206 days in 2022. That is, an arriving EV at this site had a 20% chance of not finding an available EVCS on 206 out of 365 days that year. This is a clear indication that an additional EVCS needs to be added within that site's region. While the charging site in City 1 Downtown also had a low chance of having $P_B = 0$, its performance was still acceptable in 2022 as most of the days experienced $0\% \leq P_B \leq 10\%$. These results are also reflected by N_D as discussed below.

4.6.3 Delayed EVs

Recall that N_D represents the number of EVs that had to wait at a blocked charging site; hence, the direct relationship between the P_B and N_D. This is revealed in Figure 4.7, which illustrates the evolution of N_D between 2021 and 2022 at the 14 sites. The figure indicates that the site in

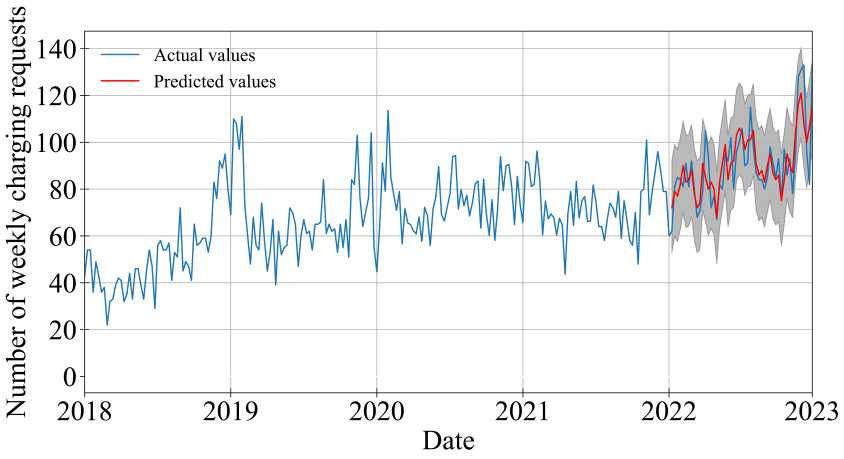

Figure 4.9: SARIMAX testing accuracy for charging site at City 1 Downtown.

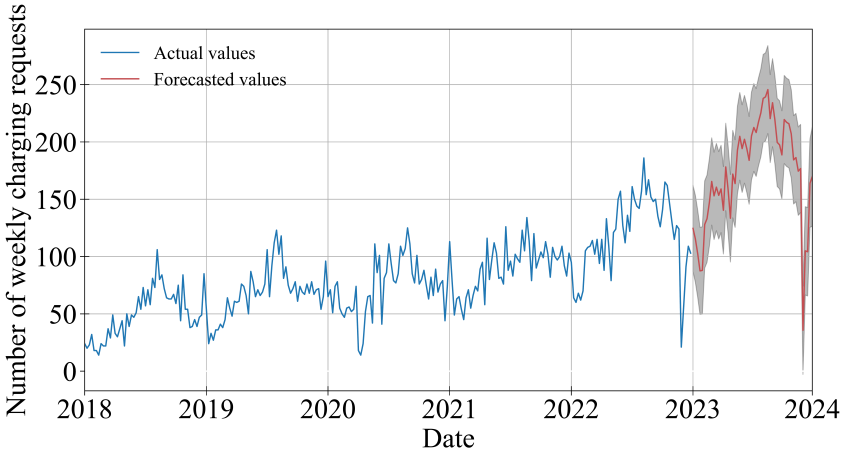

Figure 4.10: SARIMAX Touristic Area 1's weekly forecasts during 2023.

Touristic Area 1 experienced an increase in N_D by 67% meaning that the service will quickly deteriorate at this site in the coming year if the PCI in that area is not properly expanded. The results pertaining to Highway 1's charging site are consistent with their counterparts for U, Ω and P_B reported in their above-indicated respective tables. In confirmation of this site's low U and P_B, only 9 and 12 EVs had to wait to receive service there for during the entire years 2021 and 2022 respectively. Another important observation is the decrease in N_D in the Suburban Area 2 from 134 EVs in 2021 to 41 EVs in 2022. This result is consistent with the drop in this site's P_B.

4.6.4 SARIMAX Model Testing and Forecast

The SARIMAX model presented earlier in Section 4.5.3 is now used to predict future values of N_R for 4 of the 14 sites examined in this manuscript, namely, Touristic Area 1, City 1 Downtown, Rural Area 1, and City 2 Mall. The model is trained using the 2018 through 2021 data pertaining to each of these charging sites individually and then tested against the 2022 data. The

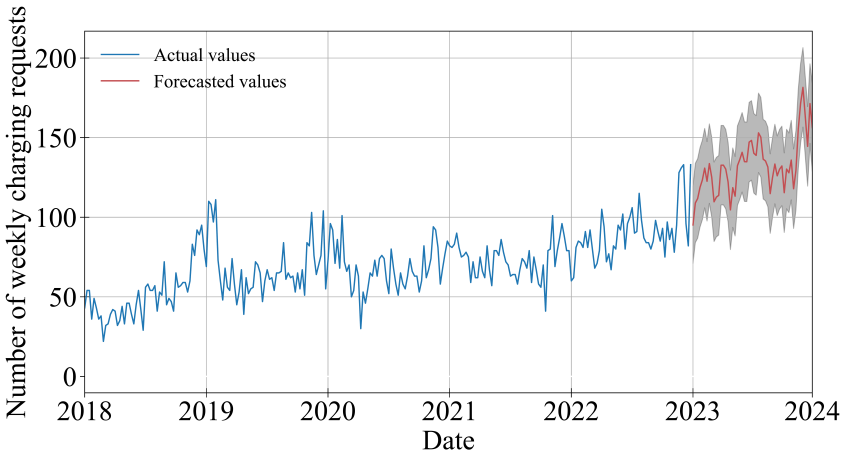

Figure 4.11: SARIMAX City 1 Downtown's weekly forecasts during 2023.

Table 4.8: Tabulated Quarterly Forecast Results.

Quarter	Touristic Area 1	City 1 DownTown	Rural Area 1	City 2 Mall
2023 Q1	1539	1452	526	1098
2023 Q2	2263	1709	811	895
2023 Q3	2841	1772	1278	1008
2023 Q4	2339	1898	801	1178
2024 Q1	2382	2260	795	1655
2024 Q2	3267	2444	1206	1202
2024 Q3	3927	2462	1740	1422
2024 Q4	2979	2500	1010	1526

grid search algorithm is then utilized to evaluate the best parameters that would achieve the most accurate results when validated against the 2022 data. The p, q, and d parameters of these models are presented in Table 4.9 for the reader's convenience. Figures 4.8 and 4.9 constitute tangible proofs of the model's forecast accuracy for the sites at Touristic Area 1 and City 1 Downtown. The SARIMAX model was able to accurately forecast the charging demand while very closely following the behavior of the actual time series. The shaded region in the figure also indicates that future demands are predicted with 99% confidence. The fine-tuned models are now used to forecast the demand for the entire year of 2023 for these 4 sites. textcolorblueAdditionally, these models were also used to generate a forecast for the weekly number of requests for a second year, 2024. Due to space limitation, only the forecast results of textcolorbluethe year 2023 of 2 sites are presented in Figure 4.10 and Figure 4.11. However, the total quarterly number of requests for the 4 sites for the entire 2-year period is presented in Table 4.8. Additionally, the accuracy evaluation metrics pertaining to the adopted model herein are presented in Table 4.10. For the sake of completeness, the accuracy of this model is compared to those of 5 other counterparts

Table 4.9: Tabulated Model Parameters.

Site Location	p	d	q	P	D	Q	Model MAPE
Touristic Area 1	0	0.6	1	0	1	1	12.12%
City 1 Downtown 1	1	0.8	1	0	1	1	8.15%
City 2 Mall 1	1	0.8	0	1	1	0	14.28%
Rural Area 1	0	0.4	1	0	1	1	10.83%

Table 4.10: Performance metrics for different models.

Site	Model	MSE	RMSE	MAPE	MAE
Touristic Area 1	ETS Without Seasonality	754.32	27.46	21.04%	21.53
	ETS With Seasonality	530.74	23.04	17.65%	18.67
	LSTM	690.50	26.28	19.11%	19.10
	ARIMA	486.29	22.05	17.28%	17.71
	SARIMA	621.69	24.93	18.78%	19.40
	SARIMAX	423.76	20.59	12.12%	15.06
City 1 Downtown	ETS Without Seasonality	688.89	26.24	22.82%	21.77
	ETS With Seasonality	276.84	16.79	12.55%	11.78
	LSTM	375.68	19.38	17.56%	15.39
	ARIMA	187.39	13.69	11.55%	10.84
	SARIMA	189.44	13.76	11.33%	10.60
	SARIMAX	90.04	9.49	8.15%	7.57

proven in the literature to outperform the presently suggested SARIMAX model with fractional parameters. Precisely, the results of the SARIMAX model presented above are compared with two ETS models, with and without seasonality, an LSTM model, an ARIMA model without seasonality, and finally with an SARIMA model without an exogenous variable. Table 4.10 clearly demonstrates the superiority of the presented SARIMAX model with fractional parameters in terms of forecast accuracy. Here, it is very interesting to observe the relatively poor performance of the LSTM model despite notable efforts to optimize its performance as well as the inclusion of the exogenous parameter as a feature for the LSTM's Neural Network (NN). This is a consequence of the relatively young age of the charging infrastructure, which would severely limit the success of training a Deep Learning algorithm due to the limited number of training samples in a 4-year period (201 weekly values per site). Also, traditionally, such forecasts rely on extensive historical information spanning tens of years (such as stock market forecasts).

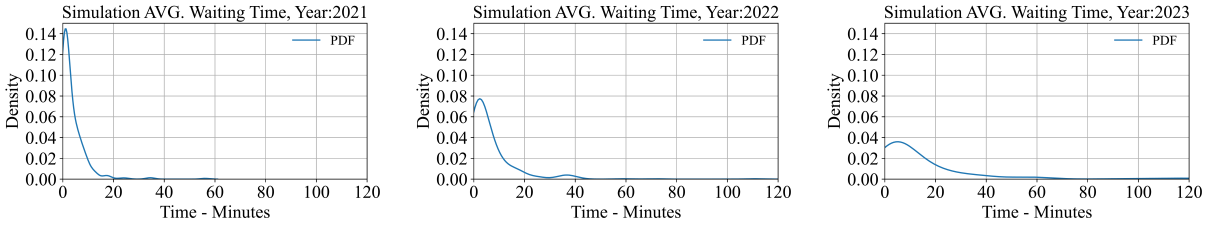

(a) 2021 (b) 2022 (c) 2023

Figure 4.12: Evolution of $\overline{W}$'s distribution during 2021 (left), 2022 (center), and 2023 (right) for the site at Touristic Area 1.

4.6.5 Waiting Time Evolution

After forecasting the number of charging requests for 2023 the $M/G/k$ simulator presented in Section 4.5.1 is used to study the evolution of the waiting time on the 4 selected sites throughout the years 2021 (including the filled Gap), 2022, and 2023 (forecasts). The daily number of requests is first extracted from the weekly forecast values. Then, these values are used to determine the EV arrival rates to the charging site. Subsequently, extensive simulations are performed with $25,000$ EV arrivals per simulation round generated using the determined arrival rates for all of the 365 days corresponding to each year. This guarantees the achievement of at least 95% confidence interval and reduces the impact of any outliers.

The results of the three years' simulations for Touristic Area 1 are presented in Figure 4.12. This figure demonstrates how the probability of low waiting times is decreasing while the probability of experiencing high waiting times is increasing year after year. This is demonstrated by the bulkier tale of the distribution and the more frequent $\overline{W}$ values above 60 minutes. To put things into perspective, the probability of experiencing a waiting time of zero is 20.4% and 9.3% in 2021 and 2022 respectively. This value drops to 3.8% in 2023. Additionally, the average waiting time in 2021 was 3.49 minutes and rises to 6.73 minutes and 14.68 minutes in 2022 and 2023 respectively. Additionally, 99% of the anticipated waiting times are within 30 minutes, 40 minutes, and 110 minutes in 2021, 2022, and 2023 respectively. The statistics related to the $\overline{W}$ results of the 4 analyzed sites are presented in Table 4.11.

4.6.6 Case Study: Charging Site at Touristic Area 2

Finally, a case study related to Touristic Area 2 is considered. By the end of 2021, this site contained a total of 9 Level 2 EVCSs and 2 Level 3 EVCSs. The site under study contains 1 of these Level 3 EVCSs. This region experienced a rapid deployment of Level 2 EVCS rising to reach a total of 33 Level 2 EVCSs by the end of 2022. However, no new Level 3 EVCSs were added in 2023 to this region. Based on the earlier conducted analysis, the utilization of the specific site of interest kept increasing in 2023 despite the addition of 24 new Level 2 EVCSs

Table 4.11: Waiting Time Statistics for 2021, 2022, and 2023

2021	Average	Probability $\overline{W} = 0$	99% Interval
City 1 Downtown	2.22 min	26%	6 min
City 2 Mall	1 min	50%	2 min
Rural Area 1	19.95 min	0%	36 min
Touristic Area 1	3.49 min	20.4%	30 min
2022	Average	Probability $\overline{W} = 0$	99% Interval
City 1 Downtown	3.68 min	10.5%	10 min
City 2 Mall	1.3 min	44%	3 min
Rural Area 1	24.98 min	0%	43 min
Touristic Area 1	6.73 min	9.3%	40 min
2023	Average	Probability $\overline{W} = 0$	99% Interval
City 1 Downtown	11.32 min	4.9%	24 min
City 2 Mall	2.9 min	22.6%	7 min
Rural Area 1	35.36 min	0%	85 min
Touristic Area 1	14.68 min	3.8%	110 min

within a very short distance. This site's P_B and $\overline{W}$ also increased. This confirms the fact that, even though the Level 2 PCI was greatly expanded in this region, it failed to catch up with the increasing EV charging demands; hence, the extreme importance of utilizing the herein presented methodology to determine the sites worthy of new Level 3 EVCS deployments for the purpose of maintaining adequate QoE performance and supporting the growing number of EVs and their charging demands.

4.7 Conclusion

This is the first data-driven study that develops a comprehensive set of metrics to evaluate the EV PCI performance of future smart cities. Also, the herein-developed forecast model accurately predicts the evolution of charging requests at a given site. The performance pertaining to 14 representative sites was analyzed through a close examination of the evolution of the occupancy, utilization, blocking probability, and the number of waiting EVs. A custom-built simulator is then used to estimate the average waiting time experienced by EVs during 2021 and 2022 as well as the predicted waiting time given the 2023 predicted charging demand. This study demonstrates the necessity of expanding the EV PCI in order to satisfy the ever-increasing charging demand and maintain acceptable consumer-perceived QoE levels.

Chapter 5
Interactive Decision-Support Tool for QoE Analysis at Public EV Charging Stations

5.1 Problem Statement and Motivation

5.1.1 Problem statement

Rapid and uneven growth in public EV charging demand is producing transient and persistent congestion at the public EV infrastructure. Operators and service providers must make deployment, incentive, and effective decisions under three linked informational gaps: (1) limited visibility into fine-grained daily time-window EV users behavior and seasonal dynamics; (2) absence of capacity-normalized spatial aggregation that weights congestion by the deployed fast charging sites; and (3) inadequate tools to explore how EV charging site performance correlates with local context (parking, social hubs, competitor EV charging stations). Without an interactive, analyst-driven interface that integrates empirical session records, queueing model derived waiting-time estimates, and configurable spatial aggregations, planners risk under/over-provisioning EV charging infrastructure, mis-targeting incentives, and degrading the EV user experience.

5.1.2 Motivation

1. Poorly targeted deployments or delayed reactions to service congestion lead to blocked EV users, long waiting times, and negative perceptions of public EV charging, threatening EV adoption momentum.

2. The deployment of Level-3 or fast charging stations is costly and limited; operators need capacity-aware spatial metrics (rather than raw counts) to prioritize investments where they will most effectively relieve EV demand.

3. Monthly and quarterly views can mask critical time-window patterns, including differences between business days and weekends, that drive the EV charging site utilization

and waiting-time spikes; operators therefore need interactive, time-windowed analysis to schedule maintenance, staffing, short-term interventions, or deployment.

4. Overlaying points of interest (POIs) and competitor EV charging stations reveals where demand is driven by trip purpose or competition, enabling more precise siting, partnership, and incentive design.

5. Capacity-weighted hexagon aggregates, per-site QoE metrics, and simulation-based waiting-time estimates provide defensible inputs to cost–benefit and counterfactual analyses (for example, to identify where a new level-3 site or a pricing rule will most reduce blocking).

5.2 Expected Contributions

- Enable faster and more accurate identification of hotspot locations and peak time windows for expansion or EV demand management interventions in the public EV charging infrastructure.
- Capacity-aware prioritization that maximizes reduction in EV user blocking per dollar invested.
- Service dashboards that bridge monitoring (monthly/quarterly reporting) and tactical action (day/week scheduling, incentive deployment).
- Strengthened coordination between planners and grid operators through shared analytical findings that support the need for detailed feasibility and grid-impact studies.

5.3 Research aims

- Build an interactive mapping tool that generates city-centred, basemap-selectable maps and overlays our industrial partner public EV charging sites markers, POIs, and competitor charging stations.
- Compute and expose a comprehensive set of QoE metrics at site and city levels (e.g., utilization, blocking probability, waiting-time, state-of-charge statistics, number of sessions, etc.).
- Implement a capacity-normalized hexagon choropleth metric to summarize effective L3 EV demand spatially and support fair, comparable hotspot ranking.

- Provide multi-scale temporal controls (four 4-hour windows, a 16-hour window, monthly, and quarterly views), and toggles for business days versus weekends, so operators can switch between granular tactical and aggregated strategic perspectives.
- Deliver exportable, publication-quality outputs (plots, Excel) to support further analysis, forecasting, and procurement rationales.

5.4 Tool overview and usage

This tool provides a robust, end-to-end framework for site-level performance benchmarking of public EV charging stations (Level-2 and Level-3). It computes and displays key QoE metrics, such as, the number of EV charging requests, waiting time, utilization, blocking probability, and site occupancy. The selected metrics can be queried and aggregated monthly or quarterly while considering a daily time window within the selected year. The average waiting time is estimated by a discrete event simulator and validated both empirically, using the dataset supplied by our industrial partner, and theoretically, using queuing models. All other QoE metrics are computed directly from the empirical dataset. By analyzing these key metrics, the tool delivers granular, site-specific insights, identifies bottlenecks, and supports optimized resource allocation across the examined Quebec cities. For the purpose of this thesis, the figures and outputs are restricted to Laval city in Quebec. Running the tool is straightforward: after installing the required dependencies, open the LocalHost Uniform Resource Locator (URL) in a web browser then select valid input values via the frontend controls (or select the automatic option) to start the analysis, as shown in Figure 5.1(a).

5.5 Interactive Map Generation

As shown in Figure 5.1(b), the operator should first select an administrative region out of 17 regions in Quebec province. After a region is selected, the *Selected City* field is populated automatically with all available cities in that region so the operator can pick the target city. Next, the operator selects the reporting period, either Quarterly or Monthly. If Quarterly is chosen, the operator selects a quarter (Q1–Q4); if Monthly is chosen, the operator selects a month. Based on feedback from our industrial partner, the analysis focuses on the public EV charging activity during the period [06:00–21:59]. This interval is further divided into four independent four-hour time windows to capture distinct charging behaviors and congestion patterns: [06:00–09:59], [10:00–13:59], [14:00–17:59], and [18:00–21:59]. Accordingly, the QoE metrics are computed for the selected reporting period and time window; thus, the metrics for a given window reflect the public EV charging sites performance during that interval.

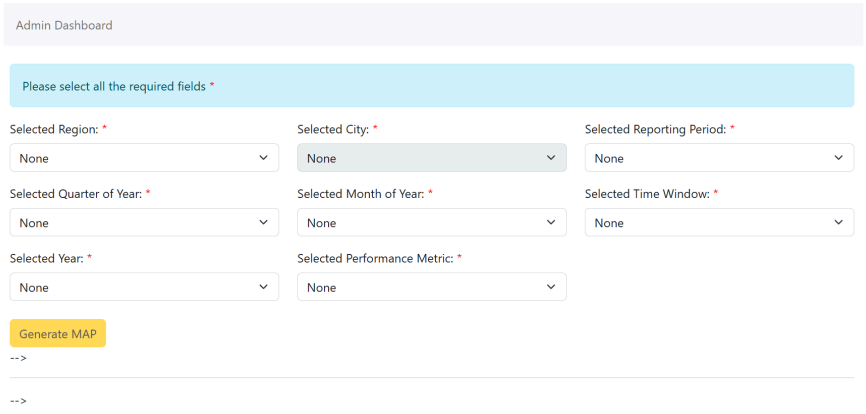

(a)

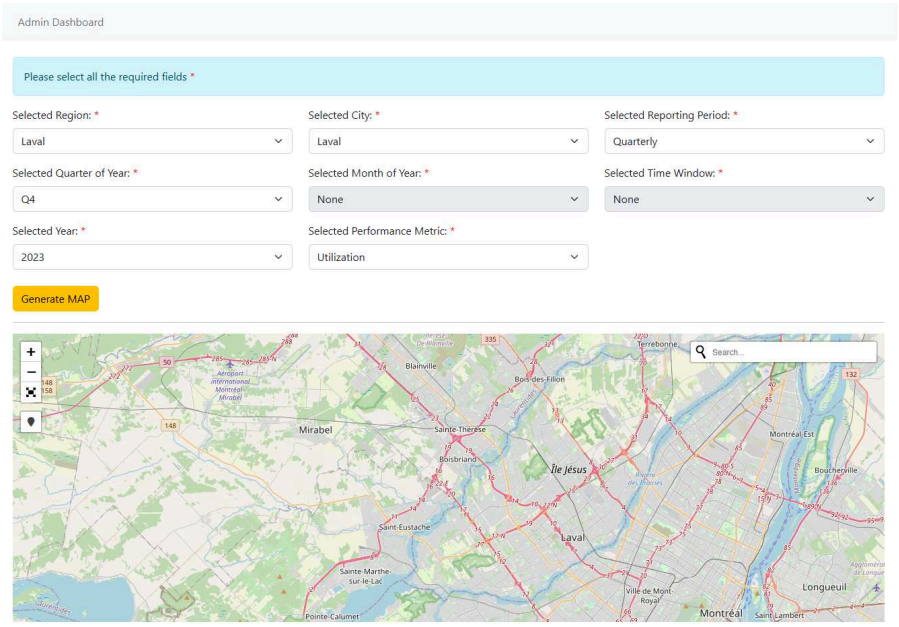

(b)

Figure 5.1: Main front-end views of the developed tool: (a) initial interface showing input controls; (b) generated map view for a selected city and parameters.

Selecting the quarterly reporting period configures the analysis to evaluate the overall charging site performance across the full daily service window [06:00–21:59], providing a broader perspective on network efficiency, reliability, and seasonal trends. This view is particularly useful for identifying persistent operational bottlenecks or long-term improvements in service delivery. In contrast, selecting the monthly reporting period enables more granular inspection of the individual four-hour time windows, allowing operators to analyze short-term variations, peak-hour EV demand patterns per site, and localized congestion effects with higher temporal precision.

Next, the operator should select the analysis year and choose a primary QoE performance metric, either utilization (the fraction of time a charging site is busy) or blocking probability

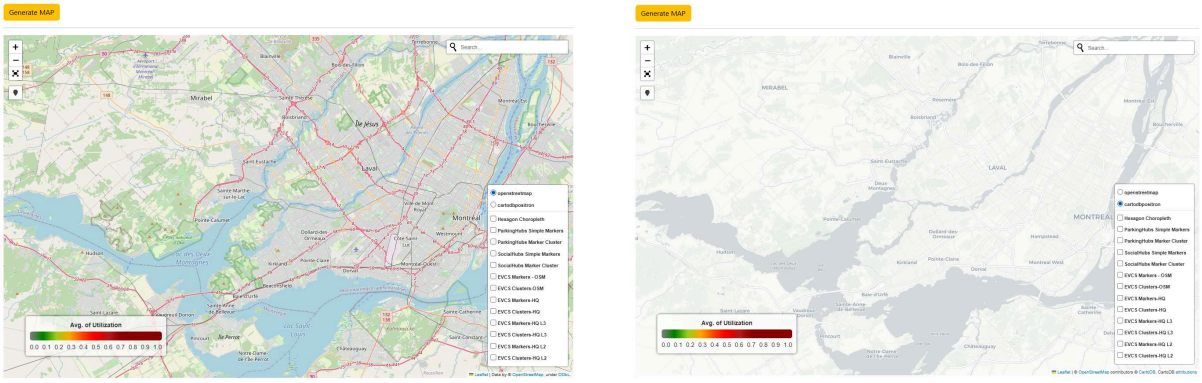

(a) (b)

Figure 5.2: Generated map view formats supported by the tool: (a) OpenStreetMap view; (b) CartoDB Positron view.

(the probability that an arriving EV cannot be served immediately). The utilization and blocking probability are efficient primary QoE metrics because they capture complementary sides of station performance: utilization measures overall capacity use, while blocking probability measures EV users experience and service availability by indicating the chance an arriving EV cannot be served immediately.

The selected primary metric is computed at the site level for all Level-2 and Level-3 public EV charging sites belonging to our industrial partner in the chosen city. Finally, pressing the *Generate Map* button commands the tool to render an OpenStreetMap-based map for the selected options; The generated map view is automatically aligned with the geographic coordinates (latitude and longitude) representing the center of the selected city.

As an example, Figure 5.1(b) shows the operator's selections: Region: Laval, City: Laval, Reporting period: Quarterly, Quarter: Q4, Year: 2023, and Primary performance metric: Utilization. After the operator clicks *Generate Map*, the tool renders a map of the selected city centered on Laval. The map's default basemap is OpenStreetMap (detail-rich); an alternative basemap, CartoDB Positron (cartodbpositron), suppresses minor details (small roads, tiny POIs) to place greater emphasis on overlaid analysis layers. The operator may switch between these map modes at any time using the control panel located in the map's lower-right corner, as shown in Figures 5.2(a)-(b).

5.6 Interactive Site Performance and Hexagon-Based Spatial Aggregation

The tool provides a detailed visualization of our industrial partner's public EV charging stations by leveraging the records from their exclusive dataset. The operator can inspect site-level performance by selecting the partner's EVCS/site markers from the control panel in the lower-right

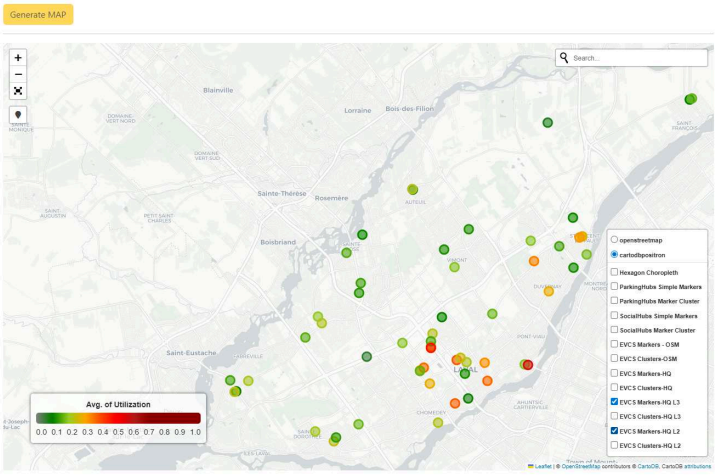

(a)

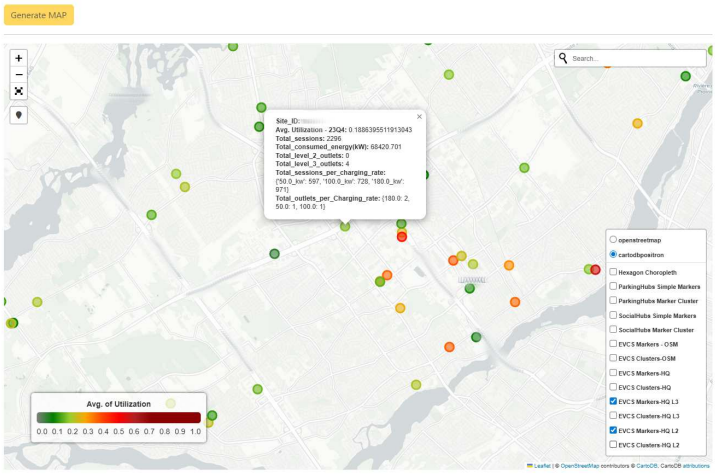

(b)

Figure 5.3: Map generation and site-level performance (Laval, Q4 2023); (a): Spatial distribution of our industrial partner Level-2 and Level-3 public EV charging sites.; (b): Example of site-level QoE performance metrics.

corner of the generated map. When this option is activated, the tool automatically displays the public EV charging sites according to the selected charging levels (L2 and/or L3) specified in the control panel, as illustrated in Figure 5.3(a) (showing both levels selected simultaneously).

As shown in Figures 5.3(a)-5.3(b), each charging site is plotted at its actual geographic coordinates as a colored circle, where the color encodes the selected QoE metric value (for example, average utilization per Level-2 and Level-3 site during Q4 2023). A dynamic color bar (bottom-left of the map) indicates the metric scale and automatically updated according to the selected QoE indicator (utilization or blocking probability).

Clicking a site marker on the generated map reveals its underlying empirical performance metrics. These site-level visualizations provide operators with immediate, data-driven insights into performance and congestion at each site for the selected reporting period (monthly or quarterly). Upon clicking a site marker, a popup window presents detailed statistics for the chosen analysis period (e.g., Q4 2023), as shown in Figure 5.3(b). The displayed metrics include the site

identifier (Site ID, omitted from the plot to protect site privacy), average utilization or blocking probability, total recorded charging sessions (overall and disaggregated by available charging rates), total energy charged by EVs (kWh), and the number of outlets per charging level at the analyzed site. These visualizations help infrastructure planners directly identifying areas and stations that require capacity adjustments or new deployments to alleviate congestion at over-utilized sites.

The tool also provides a hexagonal choropleth view for spatial aggregation and comparison. When the operator enables the *Hexagon Choropleth* from the control panel, as shown in Figure 5.4(a), the tool generates a hexagonal grid centered on the selected city (default coverage: $20\,\text{km}$ from the city center; default hexagon area: $5\,\text{km}^2$). Both values are configurable.

For each hexagon area (cell), the tool computes a single Weight score W_h: the capacity-weighted average of the selected primary metric (either site Utilization or site Blocking Probability) across our industrial partner managed Level-3 sites in the cell. Each station's primary metric is weighted by its effective L3 capacity (the total rated power available from L3 outlets). Thus, W_h measures EV demand intensity normalized by L3 capacity, supporting capacity-aware hotspot detection and the prioritization of infrastructure investments and deployments, as shown in Figure 5.4(b). The hexagon weight lies in the interval $0 \leq W_h \leq 1$. Because W_h is a capacity-weighted average of utilization or blocking probability metrics that are themselves bounded in $[0, 1]$, values closer to 1 indicate higher charging activity per cell and a greater likelihood of congestion within the hexagon during the analyzed period. Conversely, $W_h = 0$ denotes either no measured activity or zero effective L3 capacity in the cell, while $W_h = 1$ implies that the selected primary metric is at its maximum across the hexagon's capacity.

Mathematically, for a hexagon h with sites set S_h, let m_i denote the average primary metric for site i over the selected period (monthly or quarterly) and let C_i denote site i's L3 capacity (e.g., sum of outlet-rated powers in kW). The hexagon weight W_h is computed as the capacity-weighted average:

$$W_h \;=\; \begin{cases} \dfrac{\sum_{i \in S_h} m_i\, C_i}{\sum_{i \in S_h} C_i}, & \text{if } \sum_{i \in S_h} C_i > 0, \\ 0, & \text{if } S_h = \varnothing \text{ or } \sum_{i \in S_h} C_i = 0. \end{cases}$$

In addition, the tool can overlay surrounding amenities or points of interest (POIs) on the generated map, enabling the operator to visualize the local service context and assess site suitability for expansion. Relevant amenities for this research include parking areas/facilities, social hubs (restaurants, cafés, shopping malls), and EV charging stations operated by other providers. Displaying these layers helps the operator validate candidate locations, compare actual charging activity with expected footfall, and prioritize new deployments in areas with high traffic volumes and anticipated EV penetration.

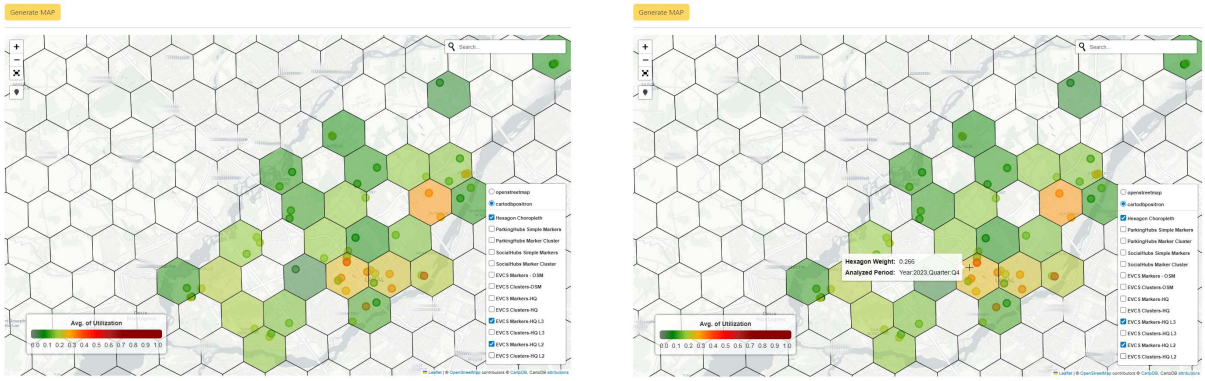

(a) (b)

Figure 5.4: Hexagon-layer map visualization (Laval, Q4 2023); (a): Hexagon layer applied to our industrial partner Level-2 and Level-3 public EV charging sites map.; (b): Example of computed hexagon weights.

Figures 5.5 (a-b) show the distribution of available parking spots in Laval city during the selected analysis period (e.g., Q4 2023). As shown in Figure 5.5(a), clicking on a parking marker displays its corresponding OpenStreetMap metadata, which provides detailed information about each parking site. The OpenStreetMap view presents the precise locations of these parking areas and their surrounding environments, as shown in Figure 5.5(b), enabling service providers to identify optimal locations for new deployments or network expansions. Equivalent visualizations are available for social hubs and competing EV public charging vendors (e.g., FLO), allowing the operator to assess vendor dominance and the competitive landscape as shown in Figures 5.5(c,d), respectively.

Also, as shown in Figure 5.6, the tool allows users to select options from the *right-side control panel* to display combined (mixed) views of multiple layers, such as our industrial partner charging stations, parking areas, social hubs, and competing vendors. This integrated visualization provides a broader neighborhood perspective, helping to identify optimal candidate locations that enhance accessibility and attract more EV users. The customized mixed view allows the operator to display and evaluate the spatial distribution of our industrial partner public EV charging stations relative to surrounding amenities and other service providers. This visualization is essential for identifying deployment overlaps, assessing spatial service balance, evaluating our industrial partner infrastructure performance in the context of competing charging sites operated by other vendors, and analyzing accessibility to support informed planning decisions.

In addition, the map *right-side control panel* allows the operator to toggle Level-2 and Level-3 our partner's sites and amenities independently or jointly, and to activate supplementary visualization layers such as cluster views, as shown in Figures 5.7(a)–(d). These clusters aggregate counts by station or amenity type and by district. This clustered view enables operators to quickly identify spatial patterns, for example, areas with dense parking facilities, social hubs,

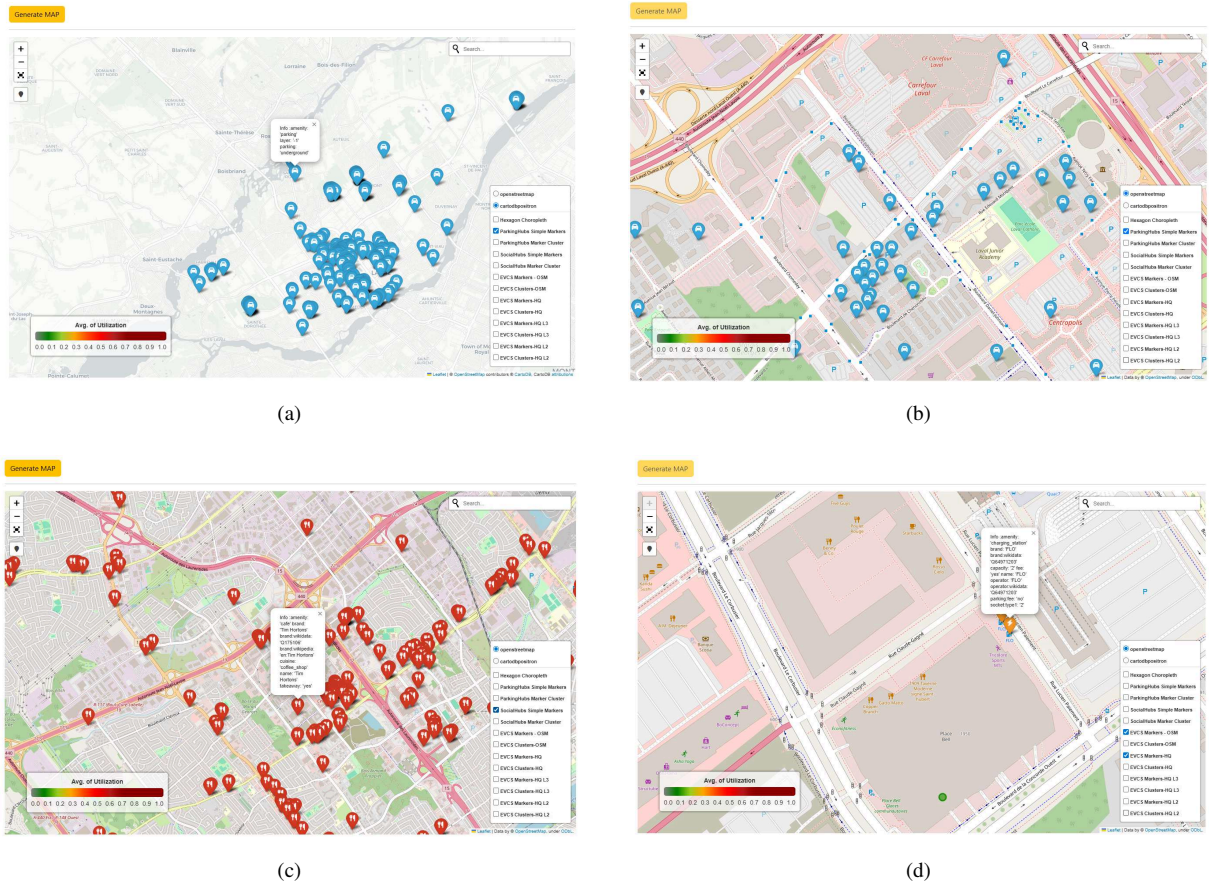

(a) (b)

(c) (d)

Figure 5.5: POIs-overlay and competing service providers views with clickable OSM metadata shown (Laval, Q4 2023); (a): CartoDB Positron overview with parking facilities; (b): OpenStreetMap zoom for a selected parking zone; (c): zoomed-in social-hubs (restaurants, cafés, malls); (d): comparative view of our industrial partner and other public EV charging sites providers.

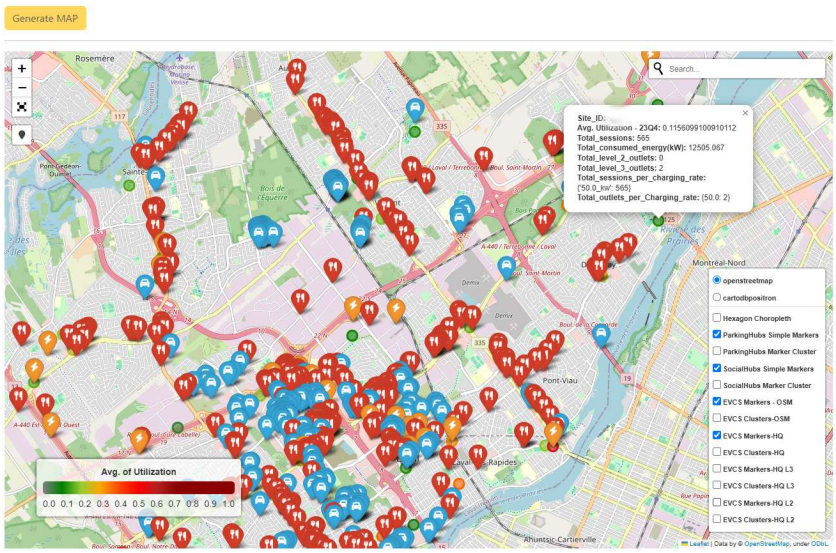

Figure 5.6: Combined marker overlay illustrating parking facilities, social hubs, our industrial partner's public EV charging stations, and those of other service providers within a selected Laval zone (Q4 2023). The right-side control panel enables mixed views of multiple layers to assess spatial relationships and candidate deployment areas.

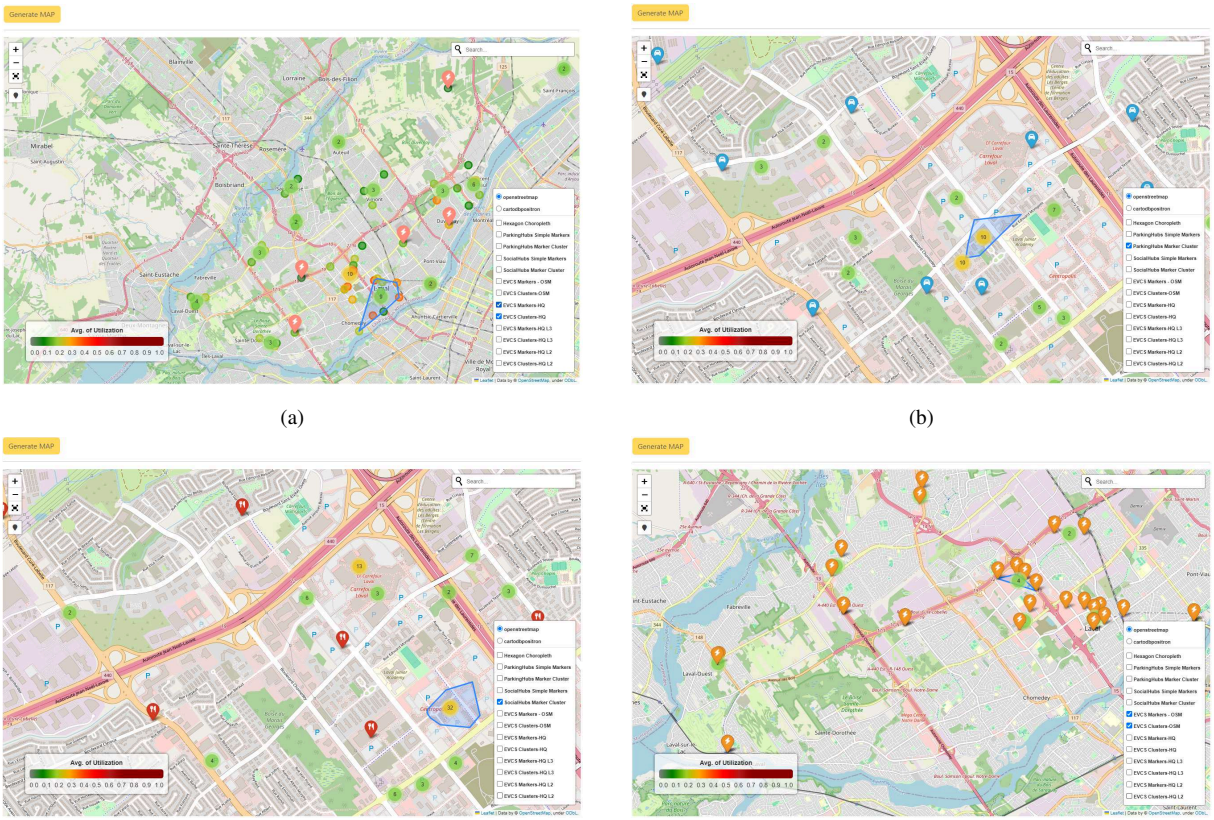

(a) (b)

(c) (d)

Figure 5.7: Clustered EV stations view and POIs (Laval, Q4 2023); (a): Clustered view of our industrial partner (L2/L3) public EV charging stations.; (b): Clustered view of parking facilities.; (c): Clustered view of social hubs.; (d): Clustered view of other public EV charging stations service providers.

or competing charging providers, and to highlight active hotspots of public EV charging and service gaps within the existing network. Visualizing these clusters is therefore essential for assessing potential EV demand, understanding user mobility flows, and identifying underserved or oversaturated regions; consequently, operators can make more informed and balanced decisions when prioritizing new EV charging deployments and coordinating infrastructure planning across the city.

It is worth noting that this tool is primarily intended to transform empirical records of the examined public EV charging infrastructure from raw data into human-friendly, reliable visualizations that support the core analyses performed by our industrial partner and infrastructure planners. The tool is not designed to carry out actual resizing, expansion, or deployment on behalf of service providers or planners, since those decisions require detailed information about the power-grid status, site-specific capabilities, and the organizations' own maintenance and deployment standards and policies, which are not available at this stage of the thesis.

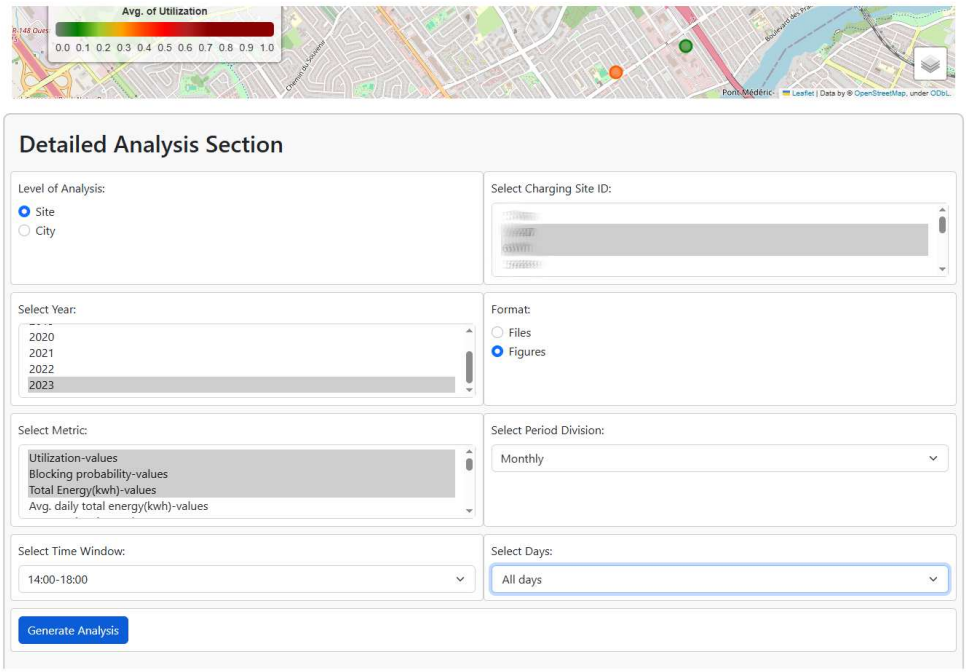

Figure 5.8: Illustration of the detailed-analysis interface, generated following the primary analysis map, showing per-site and per-city analysis options, available QoE performance metrics, and additional parameters.

5.7 Public EV Charging Performance at Site and City Levels (QoE)

5.7.1 Site Level Analysis

After generating the initial map analysis for a selected city (e.g., Laval), as discussed in section 5.5, the operator can request a detailed analysis at either the site or city level through the detailed-analysis form interface, as shown in Figure 5.8. This form is automatically displayed once the tool has successfully generated the primary analysis discussed in Section 5.5.

When the **Site** option is selected, as shown in Figure 5.8, the operator can choose one or more site identifiers (IDs) from the *Select Charging Site ID* list box. The actual Site ID values shown in the generated form snapshot are masked to preserve the privacy and confidentiality of the examined sites.

The tool automatically fills the *Select Charging Site ID* list box with the active Level-3 (fast-charging) site IDs that were operational during the selected reporting period (e.g., Q4 2023); sites that were offline or under maintenance during that period are excluded. Per our industrial partner requirements, the detailed-site analysis focuses on Level-3 sites, so Level-2 sites are not available in this stage. The detailed analysis form also requires the operator to specify:

- **Select Year:** one or multiple years (multi-select allowed).

- **Select Metric:** one or more QoE metrics to report per site.
- **Select Time Window:** the daily time window(s) for analysis (e.g., 06:00–09:59, 10:00–13:59, etc.).
- **Select Period Division:** Monthly or Quarterly aggregation.
- **Select Daily Category:** Business days, Weekends, or All days.
- **Format:** output format for results (Excel sheet and/or plot).

The QoE metrics available for detailed analysis of public EV charging sites are defined as follows:

- **Avg. utilization:** Mean fraction of time the site (or its charging outlets) is busy during the selected period.
- **Total number of sessions:** The count of charging sessions that both started and ended within the selected period at the selected site.
- **Total energy (kWh):** The total energy delivered by all charging sessions that both started and ended within the selected period at the selected site.
- **Avg. blocking probability:** Average probability that an arriving EV cannot begin charging immediately during the selected period at the selected site.
- **Avg. waiting time:** The mean delay (in minutes) prior to service initiation for EVs at the selected site during the chosen period. Waiting time values are estimated using a discrete-event simulator based on an M/G/C/K queueing model and averaged over the analysis period.
- **Estimated maximum Avg. waiting time:** The maximum average waiting time (in minutes) generated by the discrete-event simulator implementing M/G/C/K queueing model, during the specified period for the selected site.
- **Estimated minimum Avg. waiting time:** The minimum average waiting time (in minutes) generated by the discrete-event simulator implementing M/G/C/K queueing model, during the specified period for the selected site.
- **Avg. service time:** Mean duration of a recorded charging session (in minutes), averaged over all sessions in the selected period for the selected site.

- **Avg. energy per session (kWh/session):** The total energy (kWh) delivered divided by the number of sessions that both started and ended during the selected period at the selected site. This metric indicates the typical energy consumption per EV at the site and reveals EVs charging behavior patterns.

- **Peak load factor:** A ratio value that quantifies how continuously site capacity is used. It is defined as the *average power* charged by EVs over the reporting period divided by the *peak power* observed and provided by the site during the same period. Reported as a percentage. A higher value indicates the site operates closer to its peak for a larger fraction of time (higher utilization); a lower value indicates demand is concentrated in short peaks (low utilization).

$$\text{Peak load factor} = \frac{\text{Average power over period (kW)}}{\text{Peak power during period (kW)}} = \frac{\frac{\text{Total energy during period (kWh)}}{\text{Period duration (h)}}}{\text{Peak power (kW)}}$$

- **Number of active days:** The count of days within the selected period that had at least one recorded charging session at the selected site. This metric reflects the frequency of use, accessibility, and reliability of the public EV charging service.

- **Avg. daily total energy:** The average amount of energy (kWh) charged by EVs per active day during the selected period at the specified site. It is computed by dividing the total energy charged into EVs by the number of active days within the period. This metric reflects the typical daily EV energy demand at the site and can indicate usage intensity and overall site activity.

- **Avg. daily total number of sessions:** The average number of charging sessions per active day during the selected period at the selected site, computed by dividing the total number of sessions by the number of active days. This metric reflects the averaged daily usage frequency, site accessibility, throughput, and overall demand patterns.

- **Occupancy of N outlet(s):** The fraction of time that N fast-charging outlets are occupied during the selected period at the selected site. This metric indicates how efficiently the charging outlets are utilized and highlights periods of peak demand or potential congestion.

- **Avg. charging rate (kW):** The average charging power per session during the selected period at the selected site, computed as the total energy delivered (kWh) divided by the total service time (hours) for all recorded sessions. This metric indicates the typical power delivered to vehicles and provides insight into charging efficiency and the performance of the site's infrastructure.

- **Num. of days with $> 70\%$ utilization:** The number of active days during the selected period at the selected site where the site's recorded average utilization is higher than 70%. This metric highlights periods of sustained high demand, signaling potential capacity constraints. The 70% threshold is recommended by our industrial partner and is commonly used in operations research to indicate that a resource is approaching full capacity while still allowing for manageable operational flexibility.

- **Num. of days with $> 30\%$ blocking probability:** The number of active days during the selected period where the site's blocking probability is higher than 30%. This metric identifies days with significant service denial, reflecting congestion and potential user dissatisfaction. The 30% threshold is recommended by our industrial partner and is used to flag days where the probability of EVs being denied service is operationally critical, warranting attention for planning or expansion.

- **Ending SoC $> 80\%$:** The percentage of recorded sessions during the selected period at the selected site where sessions ended with a battery state of charge (SoC) greater than 80%. This metric indicates the frequency of near-top-up charging behavior, which can reduce effective charging power and extend session durations, impacting site throughput and operational efficiency.

- **Ending SoC $> 90\%$:** The percentage of recorded sessions during the selected period at the selected site where sessions ended with a battery state of charge (SoC) greater than 90%. This metric highlights the prevalence of sessions reaching near-full charge, often associated with prolonged dwell times, increased queueing, and potential congestion at the site.

- **Starting SoC $< 50\%$:** The percentage of recorded sessions during the selected period at the selected site in which the battery's state of charge (SoC) was below 50% at the start of the session. This metric provides insight into moderately low starting charge patterns, helping assess typical user charging behavior and identify opportunities for improving station utilization or planning supplementary capacity.

- **Starting SoC $< 30\%$:** The percentage of recorded sessions during the selected period at the selected site in which the battery's state of charge (SoC) was below 30% at the start of the session. This metric may reflects potential accessibility limitations of nearby public EV charging infrastructure, gaps in user pre-charging behavior, or insufficient user awareness of battery management. Frequent low-SoC sessions may indicate that EV users are often forced to charge at critically low battery levels; it can also result from high vehicle utilization and long-distance travel patterns that naturally deplete batteries before charging opportunities arise.

- **Avg. SoC delta (ΔSoC):** Average increase in battery State of Charge per session at the selected site during the selected period, calculated as the difference between ending SoC and starting SoC (ending SoC − starting SoC), averaged across all sessions. This metric reflects the typical energy delivered per charging session and provides insight into EV user charging patterns. In the context of fast chargers, ΔSoC values are often constrained by practical limits, most EV users typically charge up to 80% to optimize charging time and battery health. Therefore, unusually low ΔSoC values may indicate short top-up sessions or partial charging behavior, while values approaching the upper bound indiate full utilization of the charger's capacity.

When the operator finishes filling in the required options in the form shown in Figure 5.8 and clicks the *Generate Analysis* button, the tool exports the requested results as Excel files and/or ready to view plots. This allows the operator to immediately inspect, save, or import the results into external tools for further analysis. This workflow enables infrastructure planners to compare site-level performance over time, prioritize capacity expansions or new deployments, and consider surrounding amenities and competing providers when making decisions.

5.7.1.1 A Case Study: QoE Assessment of Congestion and Seasonal Dynamics at a Real Public EV Charging Site

For clarity, this section presents a representative set of QoE performance metrics generated by the tool for two anonymized public EV charging sites. Both sites are Level-3 (fast-charging) stations, each equipped with a 50 kW outlet. To protect confidentiality, the sites are referred to as *Site xxxx* and *Site yyyy*, respectively, rather than by their actual identifiers. Both examined sites are operated by our industrial partner and located in City xxyy, Québec. Specifically, *Site xxxx* is situated in a mall area, while *Site yyyy* is located near a major university, with approximately 6 km (or about 10 minutes drive by car) separating them. Both sites typically experience high traffic due to their surrounding contexts. To streamline the discussion and avoid redundancy, this section focuses primarily on the QoE metrics of *Site xxxx*, emphasizing the correlations among these metrics and analyzing EV users' behavior and performance during public charging sessions.

The analysis in this section pursues two main objectives: (1) to demonstrate the tool's ability to generate a clear, reliable assessment or view of the performance of our industrial partner managed public EV charging sites; and (2) to characterize EV user experience at an individual site by tracing a few QoE metrics introduced earlier in this chapter. By examining the resulting session-level and derived QoE measures, this section provides a logical, stepwise account of charging service at the examined Site. Finally, we identify and quantify meaningful correlations among these QoE metrics so the findings provide a robust, evidence-based assessment of the site's service performance and guide interpretation and further analysis.

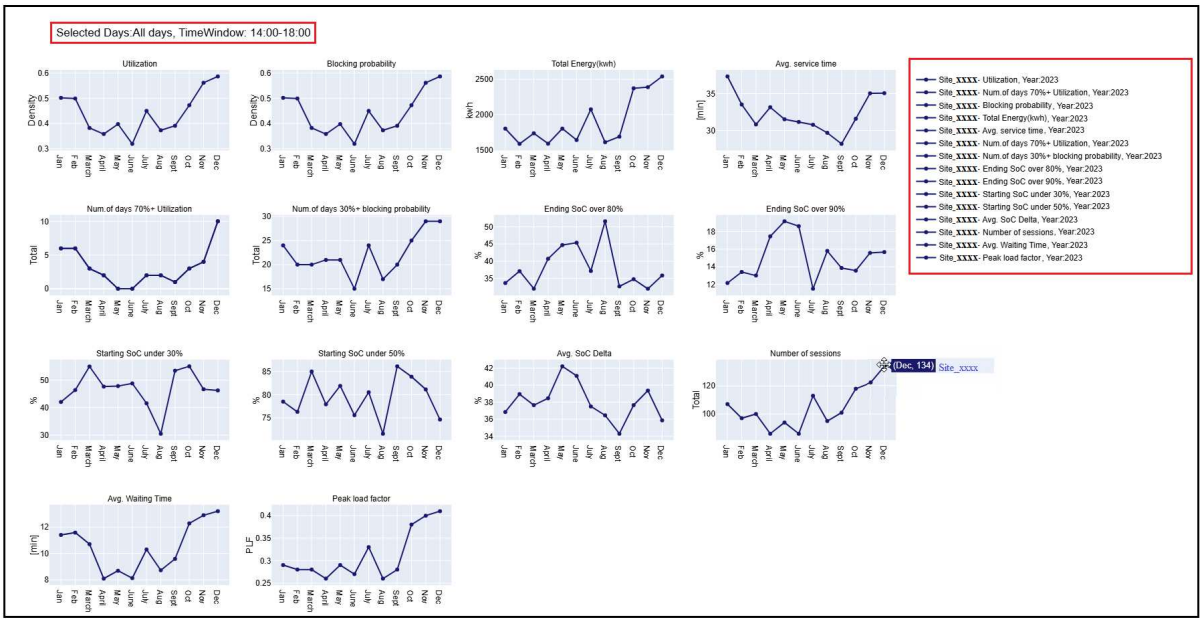

Figure 5.9: Detailed visualization of QoE metrics for *Site xxxx* in 2023. Metrics are computed using monthly aggregation across all days and the daily time window 14:00–18:00, representing the site's busiest period. Each plot shows the corresponding metric on the y-axis and monthly intervals on the x-axis.

Figure 5.9 displays the key QoE performance metrics queried via the tool interface described in section 5.6 and illustrated in Figure 5.8. All plots in Figure 5.9 were generated by the tool for Site xxxx during *2023*, using *monthly* aggregation across *all days* (weekdays and weekends) and the daily *time window 14:00–18:00*. This time window was selected because it corresponds to the site's busiest period and is therefore the most relevant interval for assessing the resulting QoE.

Each generated plot in Figure 5.9 is titled with the corresponding QoE metric name; the y-axis shows the metric values (with units) and the x-axis represents the monthly time intervals for the examined year.

The right-side control panel (highlighted by the red square in Figure 5.9) allows the operator to activate or deactivate individual metric trends on the plots. Within the control panel, each trend is identified by the Site_ID, the QoE metric name, and the analyzed year. The utility of this control panel becomes especially clear when multiple sites and multiple years are selected for comparison.

As an example, Figure 5.10 presents detailed QoE performance results generated by the tool for *Site xxxx* and *Site yyyy* over the 2022–2023 period. For each site, the tool reports the monthly aggregated averages of utilization and total energy charged by EVs; both sites operate a public fast-charging outlet with a total capacity of 50 kW per site. Because both sites have identical installed capacity and are located in close proximity, they form an ideal pair for comparative analysis. This comparison highlights the influence of local EV demand patterns, land use, and

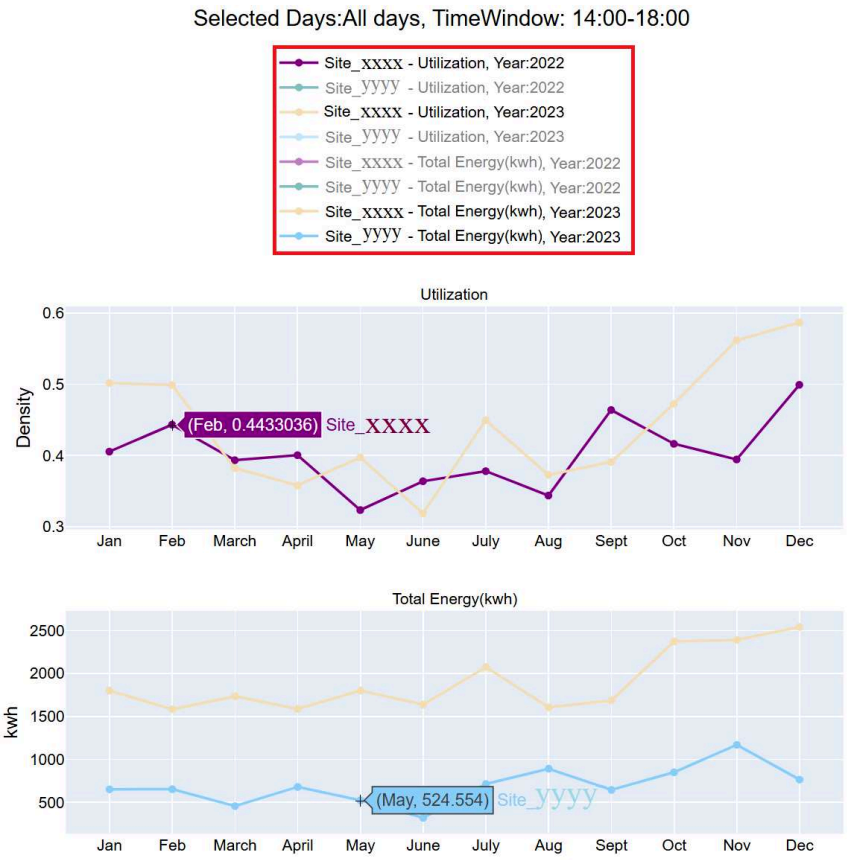

Figure 5.10: Monthly Avg. of utilization and total energy charged by EVs for *Site xxxx* and *Site yyyy* during 2022–2023. Both sites operate public fast-charging stations with 50 kW total capacity each and are located approximately 3 km apart. This figure illustrates site-level comparative analysis, enabling operators to examine month-to-month utilization, aggregate energy, and seasonal or spatial variations in performance.

operator practices at each site, and also facilitates the investigation of possible spatial spillover effects. Figure 5.10 further illustrates the tool's flexibility, where operators can focus the analysis on a specific subset of metrics or sites even when the original query spans multiple years, sites, and QoE performance dimensions.

When the tool generates the site-level detailed analysis using the parameters that can be selected in the detailed analysis form shown in Figure 5.8 and discussed in Section 5.6, each generated metric plot initially displays the full set of trend lines for every site and year selected in the detailed-analysis form. Operators can refine the view by toggling individual series on or off via the right-hand control panel (outlined in red in Figure 5.10). For example, the utilization plot in Figure 5.10 shows the monthly utilization for Site xxxx during 2022–2023; the utilization series for Site yyyy is grayed out because it was deactivated in the control panel located at the top of the figure. This filtered view makes it easy to compare month-to-month utilization for the same site across the selected years. Similarly, the total energy plot presents the aggregate energy charged at Sites xxxx and yyyy during 2023, enabling direct comparison of charging volumes and supporting data-driven decisions about site expansion or nearby infrastructure investment.

As shown in Figure 5.10, the interactive view enables the operator to trace each metric's behavior per site by activating the desired series in the right-hand control panel. By toggling series on or off, an operator can compare related trends simultaneously, for example, month-by-month utilization and total charged energy for a single site across the same year, or the same metric for multiple years to reveal seasonal shifts. The tool also applies consistent color-coding: all metrics that belong to the same site and year use the same color to simplify visual mapping and trend tracing. For instance, in Figure 5.10, the utilization and total energy plots for Site xxxx in 2023 are both displayed in yellow, making that site's performance easy to follow across different plots. Additional metric series can be enabled as needed to deepen the analysis using the control panel highlighted in red in Figure 5.10.

Moving forward to the core analysis in this section, a systematic and empirical assessment of *Site xxxx*'s performance is conducted using a staged analysis flow derived from the main resulting metric plots shown in Figure 5.9. This analysis begins with a primary QoE performance metric: utilization. The utilization metric is calculated from the site's charging records as the ratio of total occupied charging time to the total available service window for the analyzed period. It serves as an effective first-order indicator because it (a) directly reflects congestion pressure at the charging site, (b) is straightforward to compute and interpret, and (c) is relatively insensitive to individual extreme sessions compared with some other metrics. Other QoE metrics are computed empirically from the same records, with the notable exception of the waiting time, which is estimated via a discrete-event simulation implementing an M/G/C/K queueing model. Accordingly, the utilization metric is selected as the initial focal point for Site xxxx analysis, providing an accessible entry point before deeper inspection of other derived metrics.

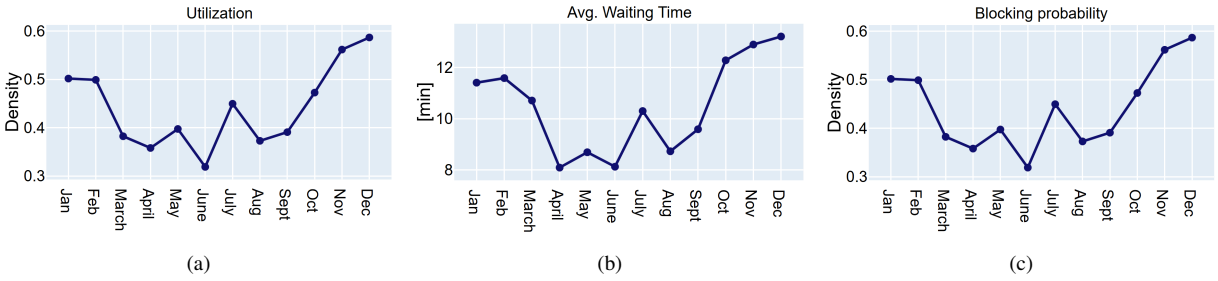

Figure 5.11: Detailed site-level performance analysis for *Site xxxx* in 2023. The metrics show: (a): average of utilization.; (b): average of waiting time.; (c): average of blocking probability.

As shown in the utilization plot in Figure 5.11(a), the recorded average of utilization at Site xxxx increases notably during the cold season (October–December) compared to the warmer months (April–August). This pattern is expected. Low ambient temperatures increase EV energy demand for cabin heating and battery thermal management, reduce battery efficiency and effective range, and often prompt drivers to precondition or recharge more frequently. Those effects lengthen the individual charging sessions and raise energy delivered per session, which

together drive higher outlet occupancy and hence higher utilization. In addition, EV charging sites located near high-traffic amenities (such as shopping malls) typically see larger and more frequent visits, especially in colder months when people consolidate trips, further increasing utilization at the examined mall site.

The estimated average waiting time at Site xxxx, as shown in Figure 5.11(b), provides as a direct, user-centered indicator of service experience and operational stress. Longer waits generally correspond to lower perceived service quality. From a queueing perspective, the average waiting time reflects the balance between arrival rate and effective service capacity and is highly sensitive to variability in arrivals and service durations; consequently, modest increases in utilization near capacity can generate disproportionate increases in waiting time. The waiting time estimates reported here were generated by a discrete-event simulation implementing an M/G/C/K queueing model. Thus, the estimated average waiting time is indicative of changes in average queue length and in the rate at which the queue clears under the site's observed conditions. Together, the utilization and waiting-time traces give a coherent, grounded view of the site's congestion dynamics and user experience over the year.

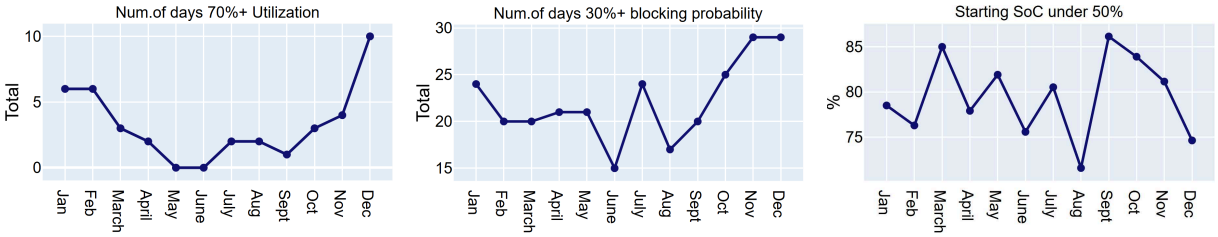

Figure 5.12: Detailed site-level performance analysis for *Site_ID_xxxx* in 2023. The metrics represent the number of days during the analyzed period when: (a): Avg. of utilization exceeded 70%.; (b): Avg. of blocking probability exceeded 30%. And (c): the ratio of EV charging sessions started with a battery state of charge below 50%.

Also, as shown in Figure 5.11(b), the average waiting time trend closely mirrors other QoE metrics, primarily utilization and blocking probability, shown in Figures 5.11(a) and (c). This co-movement arises because those metrics share common underlying drivers, such as the intensity of EV charging requests, the service time distribution, seasonal demand shifts, and peak-hour effects. Also, at Site xxxx, a single 50 kW outlet means time-averaged blocking and utilization effectively coincide, when the outlet is occupied, the site is both utilized and blocked. In addition, an upward shift in mean utilization naturally increases the number of days exceeding thresholds (e.g., utilization $> 70\%$ or blocking probability $> 30\%$), explaining the rise in exceedance counts shown in Figures 5.12(a)-(b).

In addition, Figure 5.12(c) reports the proportion of sessions that start with battery SoC below 50%. The plot reveals a distinctive winter charging pattern (October–December): although the share of sessions that begin below 50% declines in the cold months, the share of sessions terminating above 80% SoC also falls, as shown in Figure 5.13(a). Moreover, the computed

average difference between the starting and ending state of charge (SoC) rises gradually from September through November, reaching a December maximum that does not exceed 36% as shown in Figure 5.13(b), indicating reduced variability in session termination levels. Collectively, these performance signals indicate a shift toward more frequent short "top-up" charging sessions, predominantly observed in December: More EV drivers arrive with moderate SoC, add a modest amount of energy, and depart before the slow final phase of charging.

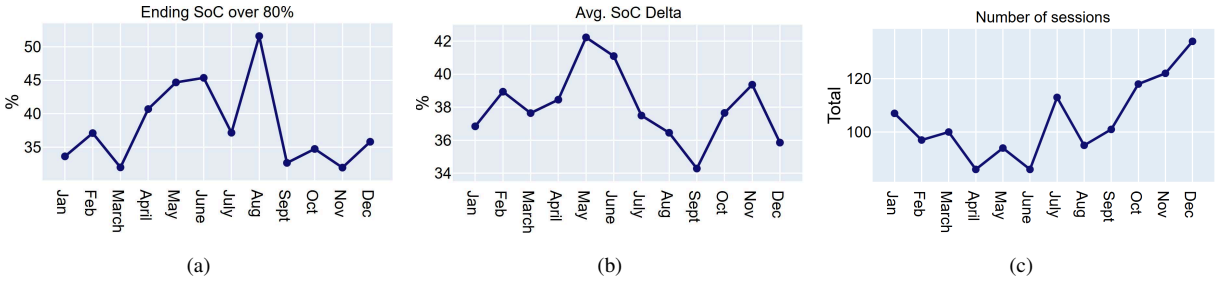

(a) (b) (c)

Figure 5.13: Detailed site-level performance analysis for *Site_ID_xxxx* in 2023. Metrics include: (a) the percentage of sessions ending above 80% state of charge (SoC).; (b) the average difference between starting and ending (SoC) across recorded sessions.; and (c) the total number of recorded charging sessions.

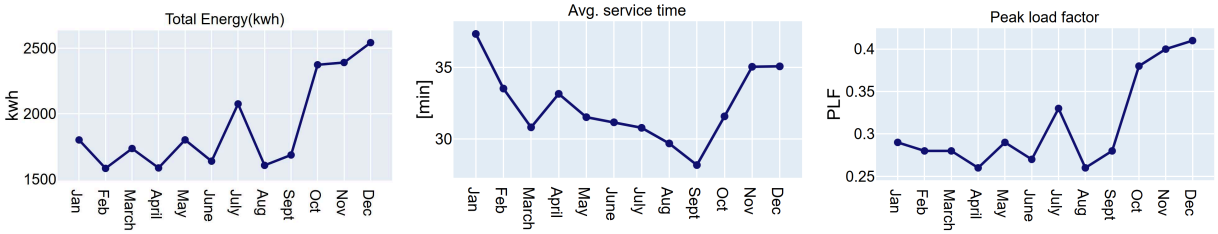

(a) (b) (c)

Figure 5.14: Detailed site-level performance analysis for *Site_ID_xxxx* in 2023. Metrics include: (a): total energy charged by EVs.; (b): average service time per session.; and (c): average peak load factor.

Two factors likely drive this behavior. First, physical/technical constraints. Cold ambient temperatures reduce battery acceptance and effective range, and most DC-fast protocols reduce power as SoC climbs, making the final 10–20% of charge much slower; the fast-charging rate typically tapers dramatically beyond $\approx$ 80% SoC. In cold conditions, staying outdoors while charging is uncomfortable and the time cost of the tapered final phase rises, so EV drivers tend to abandon charging before reaching $>$ 80% SoC at the examined site *xxxx*. This both lowers the fraction of sessions ending above 80% and reduces the per-session SoC delta. Second, behavioral factors. Winter trip patterns (holiday shopping) and consolidated errands, which generate intra-week demand spikes, together with comfort considerations, these factors increase the incidence of short stops at the mall charger, with the number of sessions peaking in December 2023, as shown in Figure 5.13(c). Consequently, an apparent paradox emerges in December 2023: the site records more charging sessions but smaller average increases in the SoCs of EVs. This paradox is reconciled by total energy delivered: despite reduced per-session SoC gains, the substantially

higher session count produces a net increase in energy dispensed at Site *xxxx* in December, as shown in Figure 5.14(a).

Proceeding, figure 5.14(b) shows that the average service time peaks during the coldest months (January–February), reaching approximately 37.3 minutes. As shown in Figure 5.11(b), the estimated average waiting time also peaks at about 11.6 minutes. The number of recorded sessions declines during extreme cold, dropping to 97 in February, as shown in Figure 5.13(c). Utilization and blocking probability metrics capture the impact of these longer sessions when they occur, as shown in Figures 5.11(a) and (c), respectively.

By contrast, as shown in Figure 5.13(c), *Site xxxx* shows an increase in session count from October to December (approximately 114–134 sessions). Over the same period, the estimated average waiting time rises moderately from 12.3 to 13.2 minutes, while the average service time remains near 35 minutes, as shown in Figures 5.11(b) and 5.14(b), respectively. Similarly, as shown in Figure 5.11(a), the recorded utilization increases to roughly 0.47–0.59 between October and December, compared with values below 0.50 in January–February. Accordingly, the peak load factor (PLF) also rises steadily from 0.38 to 0.41 between October and the end of December, versus values below 0.29 during January–February, as shown in Figure 5.14(c).

As a result, the observed Peak Load Factor (PLF) provides meaningful insight into site *xxxx*'s efficiency and performance. PLF is the ratio of average power drawn by EVs to the peak power available at the charging site over the reporting period; a higher PLF (approaching 1) indicates more sustained loading during peak times and therefore more efficient use of installed capacity. However, an elevated PLF also implies reduced operational headroom and greater temporal stress on the system, which can increase the likelihood of congestion and longer queues. Thus, the October–December increase in PLF indicates that the site operated more efficiently but under greater load pressure, consistent with the observed rise in session count and estimated average waiting time.

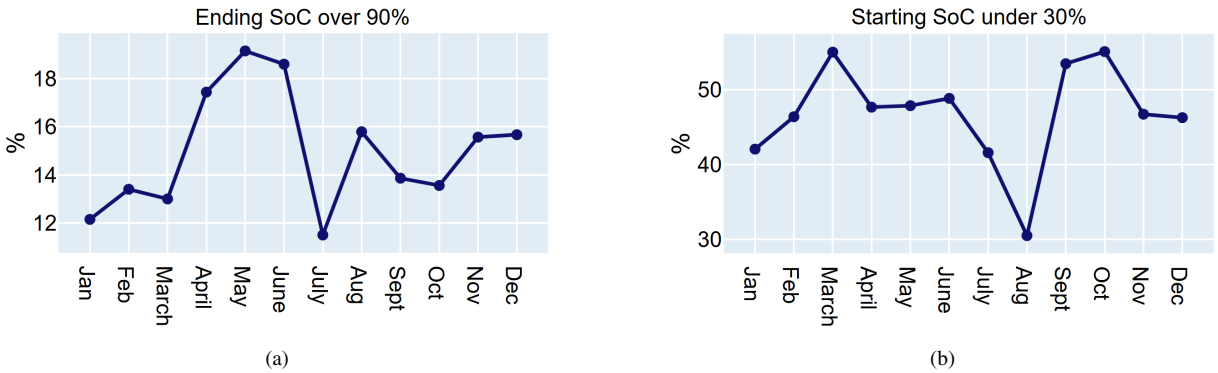

Figure 5.15: Detailed site-level performance analysis for *Site_ID_xxxx* in 2023. Metrics include: (a) the percentage of sessions ending with a state of charge (SoC) above 90%.; and (b) the percentage of sessions starting with a state of charge (SoC) below 30%.

Proceeding, between April and the end of June, Site *xxxx* recorded a marked increase in the

proportion of sessions that terminate above 90% SoC, as shown in Figure 5.15(a). This pattern is best explained by longer average dwell times at the mall; reduced site-level congestion (the number of recorded sessions decreases notably during April–June, as shown in Figure 5.13(c), and improved charging throughput associated with warmer ambient and battery temperatures. Longer charging visits with fewer queued users allow vehicles to remain connected through the charging taper. At the same time, elevated cell temperatures increase the effective charging power and delay the onset of tapering. Together, these factors enable typical sessions to reach higher terminal SoC values, thereby increasing the recorded average SoC delta over the same period (April–June), as shown in Figure 5.13(b). Service related factors (e.g., temporary promotions or improved charger reliability) and a seasonal shift toward destination shopping rather than short-stay top-ups may further amplify this effect. Also, the share of sessions that begin below 30% SoC increases markedly between August and October, as shown in Figure 5.15(b). This rise is consistent with end-of-summer travel and the resumption of term-time commuting, which increase the incidence of drivers arriving after long antecedent trips or following a full day's use with depleted batteries.

In conclusion, extending the same QoE analysis across a broader set of public charging locations both enriches and establishes a robust empirical benchmark of public EV user preferences. Also, from a sufficiently large multi-site dataset we can derive empirical probability distributions that describe how drivers select public EV stations as a function of season and location. Those empirically derived distributions provide realistic inputs for academic research and planning models, and avoid the misleading use of ad-hoc or random choice distributions. At the same time, the site-level analysis presented here characterizes EV user behavior at Site *xxxx* and therefore may not generalize to locations with different fast-charging capacities, local conditions, land-use types, or site characteristics. Per-site examination, however, provides a reliable, time-resolved view of local performance and implicitly captures congestion trends driven by the increasing penetration of EVs within the examined city or across the province of Quebec. Extending the QoE analysis across many sites yields a more complete picture of how QoE evolves over time and how changes correlate between sites; those cross-site correlations can directly inform service providers and infrastructure planners when evaluating network expansion and deployment scenarios. Finally, a clear understanding of spatial and seasonal variation in public EV charging behavior helps service providers and operators monitor and sustain EV user satisfaction during the public EV charging service.

5.7.2 City Level Analysis

When the **City** option is selected in the detailed analysis (Figure 5.16), the tool reports metrics that summarize EV users' charging preferences and the rollout progress of our industrial partner's publicly managed charging infrastructure across the entire city. Metrics are organized

by charging level (L2 vs L3) and reported as the number of charging sessions and the number of deployed outlets for each level. For this section, these metrics are presented on a monthly cadence across the full evaluation period rather than as quarterly aggregates, which provides higher temporal resolution and greater operational usefulness.

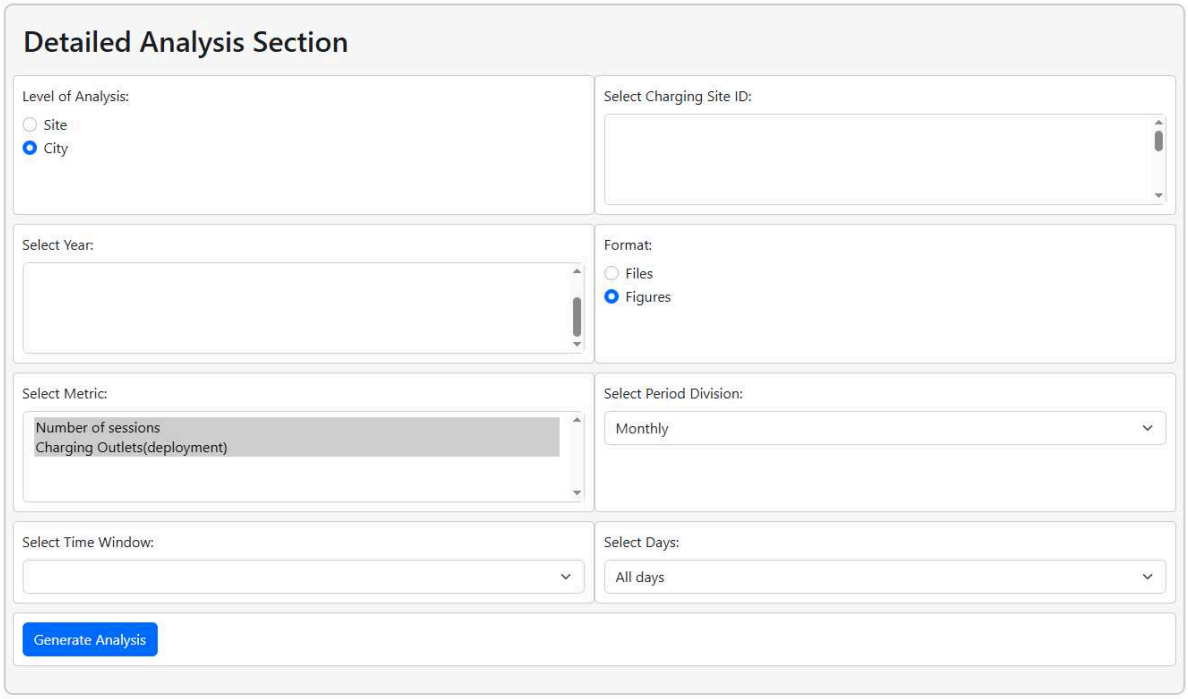

Figure 5.16: City-level analysis form for generating performance metrics of the selected city.

The selected period division is set to a monthly cadence. A monthly view reveals short-term demand shifts by uncovering usage-pattern changes that quarterly aggregates can mask, and it enables faster anomaly detection, for example, sudden increases in sessions, equipment faults, or atypical behavior following deployments or incentives, so operators can respond sooner. This finer granularity also supports targeted operations: maintenance, staffing, and local outreach can be scheduled to match observed month-to-month EV demand. Monthly inputs improve forecasting responsiveness by supplying more up-to-date data for models, facilitating rolling adjustments to deployment plans. Finally, monthly series better highlight seasonality and event sensitivity, exposing seasonal cycles, holiday or event effects, and weather-related fluctuations more clearly than quarterly data. Quarterly aggregation remains useful for high-level, strategic reporting and long-term trend assessment, but the monthly cadence provides provides more specific insights needed for timely, evidence-based decisions at the city level.

Proceeding to the description of the selected options in the *Detailed Analysis* form shown in Figure 5.16, the *Select Days* filter is set to **All days** to capture overall behavioral patterns across both business days and weekends, rather than isolating specific day categories.

The requested metrics are provided in a time-series format so that trends in L2 and L3 ses-

sions can be examined in parallel with our industrial partner infrastructure rollout, two independent panels, as shown in Figure 5.17. The deployment of public EV infrastructure is represented as the count of available outlets by charging level rather than by individual site, providing a complementary view organized by users' charging preferences, as reflected in the number of Level-2 and Level-3 sessions.

The results are shown chronologically from the earliest record in the dataset through the most recent available charging event for the examined city (e.g., Laval), enabling a continuous view of the public EV infrastructure evolution over the selected reporting cadence (monthly). In addition, the chronological presentation of the monthly sessions and deployments also permits a clear assessment of the network's accessibility and operational efficiency.

This city-level presentation yields multiple operational and planning advantages: it reveals how user preference shifts between L2 and L3 as infrastructure expands; highlights peak demand periods and seasonal patterns; identifies capacity shortfalls or over-provisioning and rising congestion risk at the outlet level; supports equitable and targeted deployment by exposing spatial or temporal imbalances; and improves forecasting, maintenance scheduling, and operational planning. Altogether, the city-level time-series view supports evidence-based decisions for future deployments, incentive design, and performance monitoring of the public EV charging network. As shown in Figure 5.17, from 2018 through 2023, the examined city experienced strong and accelerating growth in public EV charging demand, with the most pronounced surge occurring in late 2023. Although the number of deployed charging outlets increased steadily in discrete steps over the same period, the deployment did not keep pace with the rapid rise in sessions during 2023. As a result, it is highly expected that the utilization per outlet increased substantially, generating heightened congestion risk. Notably, Level-3 sessions grew proportionally faster than Level-2 sessions, while Level-3 outlets continue to represent a much smaller share of the public charging network. Several factors likely explain these patterns. Rising EV adoption on the roads of the examined city and more frequent public charging per EV are primary demand drivers, and an observable behavioral shift toward faster charging, reflected by the faster growth in L3 sessions, suggests drivers increasingly favor quick-charge options. Also, as shown in Figure 5.17, the stepwise, planned nature of outlet deployments created a lag between supply and demand, which became most evident during the late-2023 spike. In addition, recurring monthly peaks point to seasonal or event-driven variation in EV demand that amplifies these imbalances at predictable intervals.

Taken together, these trends imply near-term capacity stress and elevated operational risk at high-utilization sites. The combination of rapidly rising sessions, underrepresented level-3 capacity, and seasonal peaks argues for targeted Level-3 expansion at hotspot locations, more proactive EV demand management measures (e.g., time limits, dynamic pricing, reservations, and deployment of advanced high-rate chargers), and closer monitoring of site-level performance

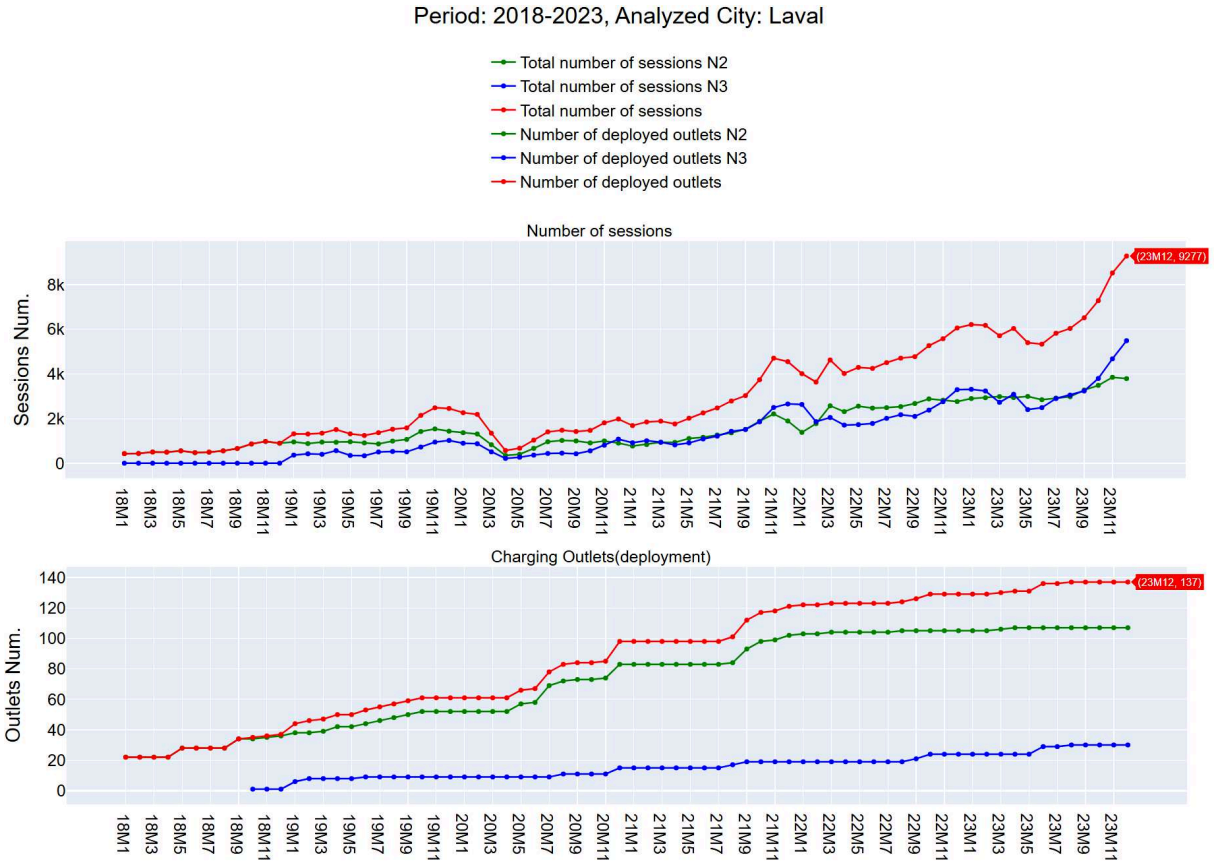

Figure 5.17: Monthly charging metrics for Laval (2023). Top panel: number of charging sessions by level (Level-2, Level-3) and total sessions. Bottom panel: number of deployed charging outlets by level (Level-2, Level-3) and total outlets. The x-axis denotes months in format `YYM#` (e.g., 18M1–23M12), representing sequential months from 2018 to 2023.

to reduce queuing and preserve quality of experience of EV users.

5.8 Conclusion

This chapter presents an interactive, operator-focused mapping and analysis tool that converts empirical charging-session records into easy-to-interpret spatio-temporal intelligence for assessing EV users QoE and Infrastructure planning of the public EV charging in Quebec. The tool supports configurable temporal granularity (monthly, quarterly, daily time windows), per-site QoE metrics (utilization, blocking probability, waiting-time, state-of-charge statistics, PLF, etc.), amenity and service competitor overlays, and a hexagonal choropleth map view for identifying hot spots of public EV charging. Together, these features close three gaps identified for our industrial partner and similar operators: (1) fine-grained visibility into when and where congestion occurs; (2) capacity-aware spatial comparisons that fairly prioritize L3 investments considering L2 charging; and (3) contextualized siting intelligence that links charging performance to local land use and competitive conditions.

The tool generates evidence that supports both tactical and strategic decision-making. Tactically, it enables earlier detection of peak-month/quarter and seasonal congestion patterns, better scheduling of maintenance and on-site interventions, and targeted EV demand-management measures, for example, time limits, dynamic pricing, reservation policies, or deployment of advanced high-rate chargers that can be designed and implemented by operators to target specific time windows and congestion hotspots. Strategically, capacity-weighted hexagon aggregation and per-site QoE summaries support cost-effective prioritization of L3 expansions, defensible resource allocation, and stronger justification for coordinated grid-level feasibility studies. The case study discussed in this chapter demonstrates the value of combining empirical charging session records to deliver user-centered performance assessment at both the site and city scale. At the same time, the tool has practical limits that frame its immediate applicability. It synthesizes only the available session records and OpenStreetMap (OSM)-sourced context layers; it does not and cannot substitute for site-specific grid constraints, real-time network state, or operator policies that govern actual deployments. Privacy and data quality considerations (site anonymization, offline/maintenance filtering, SoC measurement variability) require continued attention.

Finally, waiting-time estimates depend on the fidelity of the fitted service-time models and on the assumptions embedded in the discrete-event simulation. This dependence arises because current public EV reservation systems typically do not record actual vehicle arrival times at charging sites; without recorded arrivals, the pre-charge waiting time cannot be measured empirically and must be inferred from modeled service times and simulated queue dynamics. As a result, waiting-time outputs should be interpreted cautiously and validated against direct arrival data if and when those data become available.

Chapter 6
A Novel Data-driven Incentive-based Charging Service Truncation Scheme to Improve the QoS Performance of Public EV Charging Stations

6.1 Data-Driven Problem Overview, Motivation and Statement

Driven by realistic data collected from major Québec operators and provided through our industrial partner, this study presents a comprehensive chronological analysis of the Public-EV Charging Station (P-EVCS) deployments across six major Québec cities. For illustrative purposes, Figure 6.1(c) shows how P-EVCS deployments evolved in one of these cities, using annual map snapshots captured at the end of each fourth quarter from 2019 to 2023[1]. The maps highlight the number and locations of deployed P-EVCSs, revealing significant regional variations in deployment strategies and outcomes as shown in Figure 6.1. For instance, City A experienced the most significant expansion, growing from approximately 435[2] sites in 2019 to about 783 in 2023. In contrast, City B showed more modest growth, increasing from 9 sites in 2019 to 28 sites in 2023. Other cities displayed diverse growth patterns, reflecting unique urban deployment strategies and the evolving EV users' charging demands. These variations underscore the importance of tailoring deployment approaches to meet region-specific demands effectively. By focusing on key sites (highlighted as red squares on the maps), we tracked performance over time, with a particular emphasis on average waiting time ($\overline{W}$), a critical QoS metric. Figure 6.1(b) captures the yearly variations in $\overline{W}$ at these selected sites alongside deployment data Figure 6.1(c) and EV penetration rates Figure 6.1(d). This comparison highlights the relationship

[1]Data snapshots begin in 2019 as a stable benchmark year, preceding COVID-19 disruptions to economic activities, transportation, and EV adoption, Data from 2020 is excluded for clarity due to pandemic-related fluctuations.

[2]For clarity and fit of the figures, the number of sites being too large has been represented using a logarithmic scale.

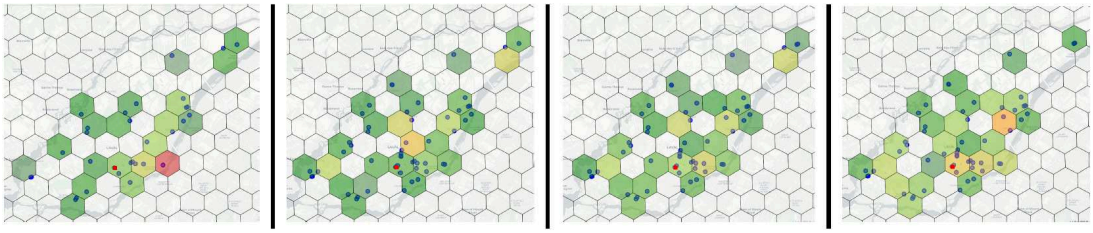

(a) Chronological evolution of P-EVCS deployments (Map View).

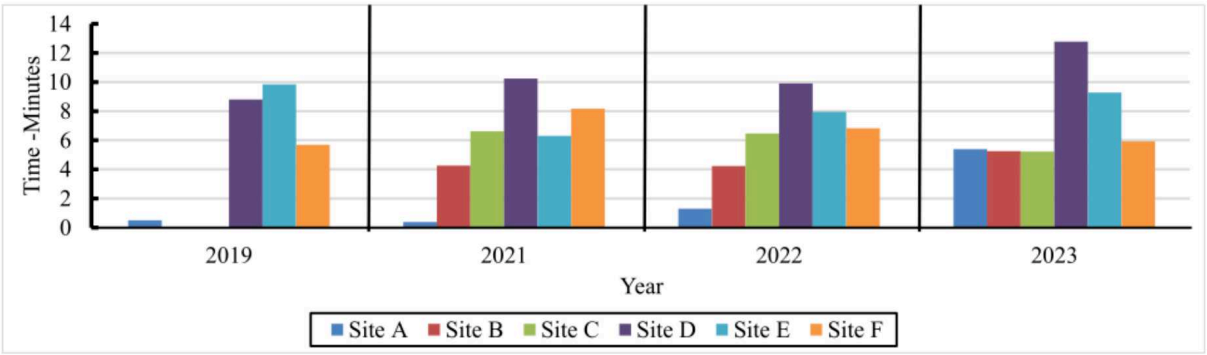

(b) Chronological evolution of P-EVCS Avg. Waiting Time.

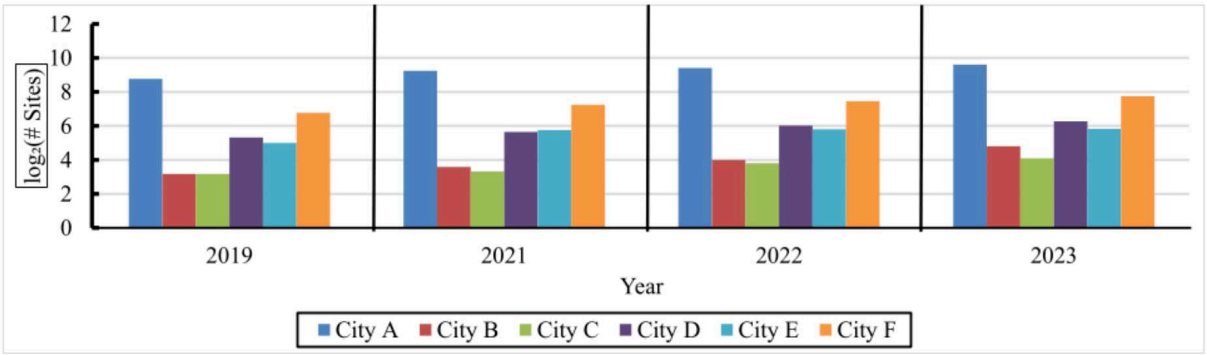

(c) Chronological evolution of P-EVCS deployments.

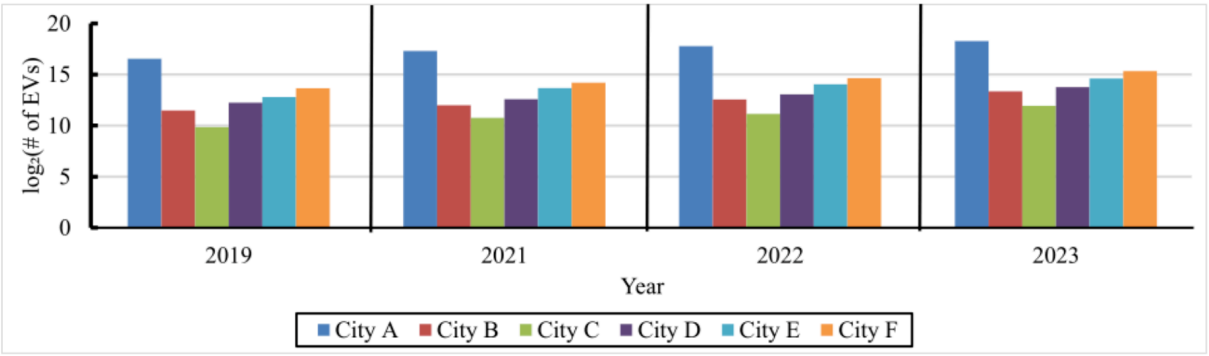

(d) Chronological evolution of EV penetration.

Figure 6.1: Chronological evolution visualized through: (a) a map view, and trends in (b) average waiting time, (c) P-EVCS deployments, and (d) EV penetration analysis.

between infrastructure growth and user experience. Notably, five of the six sites are located in high-traffic areas, such as shopping malls and restaurants, attracting a diverse array of EV users

and providing insights into charging behavior under high-demand conditions. The selected sites generally offered consistent charging capabilities, enabling controlled comparisons across locations. However, one site initially equipped with two 50 kW fast-charging outlets provided unique insights into the potential benefits of doubling outlet capacity. This configuration demonstrated improved QoS by reducing service overload and waiting times, particularly during peak periods. In contrast, a site located in a touristic area revealed distinct charging behavior, with longer charging durations reflecting the needs of users in less time-sensitive contexts. This variety in the selected sites, highlights the importance of tailoring station designs and service levels to match user profiles and site characteristics. Despite a significant infrastructure growth, the data reveals a concerning trend: average waiting times ($\overline{W}$) at most sites increased over the analyzed period. For instance, at Site A, $\overline{W}$ increased notably from 0.51 minutes in 2019 to 5.40 minutes in 2023, even as the city significantly expanded its P-EVCS network. This pattern is echoed in other cities. At Site D, $\overline{W}$ climbed from 8.81 minutes in 2019 to 12.78 minutes in 2023, despite an increase in the number of charging stations from 40 to 77 during this period. These increases are attributed to mainly: a) rise in EV arrivals, as depicted in Figure 6.1(d), and, b), a concurrent reduction in service rate, both of which lead to an accumulation of EVs in the waiting queue, ultimately resulting in the observed increase in W.

Conversely, some sites showed notable improvements. For example, the touristic Site C location experienced a seasonal variation in waiting times, with higher $\overline{W}$ during spring and summer and decreased service overload during winter. Similarly, Site F witnessed a 37% reduction in $\overline{W}$ between 2021 and 2023, following a threefold increase in nearby fast-charging stations. Overall, the study underscores the inadequacy of current expansion strategies that prioritize increasing the number of sites without catering for the distribution of the rising EV demands across per-city P-EVCS as well as the need to account for adaptive scaling. The results highlight the need for more sophisticated approaches to infrastructure planning, including QoS-aware strategies and incentive-driven service management. One promising solution involves incentivizing EV users to voluntarily truncate their charging sessions, reducing charger occupancy times without compromising their ability to reach destinations. This approach not only optimizes P-EVCS performance but also ensures sustained QoS under increasing demand.

6.2 Novel Contributions

This chapter's novel contributions are summarized as:

1) The development of a Data-driven Incentive-based Charging Truncation DICT scheme encouraging EV users to limit their charging at the site to 80% of their batteries' SoCs. This scheme aims at limiting the per-EV charger's occupancy and, hence, allowing for more EVs to use the charger within a given observation period. Consequently, this scheme contributes to

reducing the average EV waiting time at the site, $\overline{W}$, and the EV blocking probability, P_B, as waiting spaces become more likely available to fit more arriving EVs.

2) Establish an analytical M/G/1/K queueing model to capture the dynamics of a target P-EVCS and evaluate its performance in terms of the above-mentioned QoS metrics. In this regard, a large number of 10^6 per-EV service time samples experienced under DICT are collected for the purpose of characterizing their probability distribution. Owing to the complexity and general aspect of this distribution, a highly accurate approximation is identified, for which a closed-form expression is derived to promote the queueing model's tractability.

3) The development of multiple benchmarking schemes, namely: *i*) Site Resizing Scheme SRS aiming at augmenting the site with more chargers, *ii*) New site Deployment Scheme NDS aiming at strategically deploying more sites in the vicinity of the target site with the objective of offloading part of the arriving EVs to the target site, and, *iii*) Incentive-augmented Resizing Scheme (IRS), the chargers at the target site are increased and EV users are incentivized to stop charging at 80% of their batteries' SoCs.

4) The development of a thorough data-driven simulation framework for the purpose of evaluating the performance of the above-mentioned four schemes in terms of: *a*) utilization, *b*) average waiting time, *c*) blocking probability, *d*) number of blocked EVs, *e*) number of served EVs, *f*) number of waited EVs, as well as comparing these performances and drawing recommendations to the operator, lessons learned and conclusions.

6.3 DICT Scheme: A Detailed Description

Before delving into DICT's underlying details, it is important to remind the reader that, according to one of the operators of public EV charging (refer to [10]), the charging power of an EV plugged into a Direct Current (DC) fast-charge station is measured in kilowatts (kW) and the three main factors affecting an EV's charging time are: *i*) the type of charging station, *ii*) the vehicle's battery and Battery Management System (BMS) characteristics, and, *iii*) the battery's temperature, which is indirectly affected by the outside temperature. For example, a plugged EV that charges at 40 kW at a 100-kW P-EVCS, accumulates 20 kWh within an interval of 30 minutes; hence, increasing its travel range by an additional 100 km. However, an EV charging at a mere 20 kW at that same P-EVCS requires double the time to accumulate the same amount of 20 kWh of energy. Yet, it is important to keep in mind that it is the EV itself that determines the charging power limited by the maximum power the P-EVCS can supply. In other words, the EV communicates with the P-EVCS through its BMS and informs the P-EVCS how much power it can receive based on the battery's SoC and temperature.

Now, as of November 2020, Circuit Électrique par Hydro-Québec (CEHQ) has been accumulating real-time data (*i.e.*, thousands of records) pertaining to the charging process of EVs

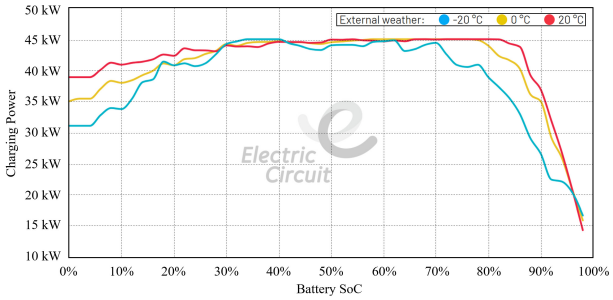

Figure 6.2: Sample EV Charging Profile as obtained from [10].

taking place within a certain range of outdoor temperatures. Figure 6.2 shows the charging profile of an arbitrary EV charging at a 50 kW P-EVCS. All other EV charging profiles as shown in [10] exhibit similar behavioral trends. Noteworthy from this figure is the fact that once the EV's battery's SoC attains 80%, the charging power requested by the EV rolls off quite rapidly. At this point, denote by t_s the time instant at which an arbitrary EV, say EV n, starts charging. That EV's battery's initial SoC is denoted by SoC_i. Let t_e be the time instant whenever the charging EV's battery attains its originally requested ending SoC, denoted by SoC_e. In all cases where $SoC_e \leq 80\%$, the EV's charging service time is $T_C = t_e - t_s$. Now, consider the case where $SoC_e > 80\%$ and denote by t_{80} the time instant when that EV's battery attains an SoC of 80%. Here, it is important to distinguish between the time interval, $T_{s,80} = t_{80} - t_s$, taken by the EV's battery's SoC to rise from SoC_i to 80% and its counterpart interval, $T_{80,e} = t_e - t_{80}$, taken by that battery's SoC to rise from 80% to SoC_e. In this latter case, the charging EV's service time would be more conveniently expressed as $T_C = T_{s,80} + T_{80,e}$, which, in reality, boils down to $t_e - t_s$ but preserves the distinction between the two intervals $T_{s,80}$ and $T_{80,e}$. The importance of such a distinction arises from a close observation of CEHQ's collected data, which reveals that, for EVs requesting an $SoC_e > 80\%$, often $T_{80,e}$ constitutes a notably large fraction of $T_{s,80}$, if, at all, it is not even much larger than $T_{s,80}$ (especially whenever $95\% \leq SoC_e \leq 100\%$). Such an observation is crucial as it allows for the operator to come up with attractive offers to highly demanding EV users; hence, incentivizing them to truncate their charging process whenever their EVs' batteries' reach an SoC of 80% saving a large proportion of charging time (*i.e.*, $T_{80,e}$) that could be efficiently allocated to serve the next in-line EV waiting in the queue of a relatively overloaded P-EVCS. This way EVs are cleared out faster in an attempt to reduce the queue size; therefore reducing the P-EVCS's load and improving its QoS performance in terms of blocking and experienced average EV waiting time. Truly, the more attractive the offers, the more of these highly demanding EV users are going to adhere to the provisioned incentives and so the larger would the P-EVCS performance improvement become. This is the fundamental idea behind the herein proposed DICT scheme. The DICTated EV charging service time distribution is characterized next.

6.4 Modelling and Analysis

6.4.1 EV Charging Service Time Characterization

Consider the target site (indicated as a red dot in Figure 6.1(a) monitored throughout an arbitrary one of the observation years. A total number of N per-EV charging service time samples collected by the operator all over this particular year are grouped into a set $\mathcal{T} = \{T_1, T_2, T_3, \cdots, T_n, \cdots T_N\}$. As proven in [87], these original service time values constitute a sequence of independent and identically distributed (i.i.d.) random variables (r.v.s) having an Erlang-k probability density function (p.d.f.) $f_T(t)$ and a cumulative distribution function (c.d.f.) $F_T(\tau)$ such that:

$$f_T(t) = \frac{\mu^k t^{k-1} e^{-\mu t}}{(k-1)!} \quad ; \quad t \geq 0 \tag{6.1}$$

$$F_T(\tau) = 1 - \sum_{n=0}^{k-1} \frac{1}{n!} e^{-\mu\tau} (\mu\tau)^n \quad ; \quad \tau \geq 0 \tag{6.2}$$

where μ and k are the rate and shape parameters respectively. Accordingly, T has a mean $\overline{T} = E[T] = k\mu^{-1}$, variance $\sigma_T = k\mu^{-2}$ and a second moment $m_T^{(2)} = E[T^2] = k(k+1)\mu^{-2}$.

It is further observed that a subset of size N_γ of the values in $\mathcal{T}$ are matched with EVs originally requesting an ending SoC such that $SoC_e > 80\%$[3]. Such samples shall be grouped in a subset $\mathcal{T}_\gamma$. All other service time values correspond to EVs requesting to charge until their batteries attain an $SoC_e \leq 80\%$. These $N_\lambda = N - N_\gamma$ samples are grouped in subset $\mathcal{T}_\lambda$.

Now, under the influence of incentives provisioned by the operator, a proportion, p_α, of the users having service times originally in $\mathcal{T}_\gamma$ are going to voluntarily adhere to DICT's policy and truncate their respective EV charging processes once their EVs' batteries reach an SoC of 80%. All such truncated service time values shall be grouped in a subset $\mathcal{T}_\alpha$. These time periods are truly random given the randomness and independence of the respective initial SoCs pertaining to each of the arriving EVs to the P-EVCS. Service time values in $\mathcal{T}_\alpha$ are computed using Equations (2), (3) and (4) of [54] under the assumption of a constant maximum charging rate provisioned by the P-EVCS for any arbitrary $SoC_i < 80\%$ all the way up to the truncating SoC threshold of 80%. Such an assumption is inspired by the power model illustrated in Figure (6.2) coupled with a brief explanation in [10] and fully justified in Section IV of [54]. Last but not least, with a probability of $1 - p_\alpha$, all remaining users reject the offered incentives and require the satisfaction of their original charging demands.

Next, without loss of generality (w.l.o.g.), Let T_λ, T_γ and T_α be random EV service time values belonging to the individual subsets $\mathcal{T}_\lambda$, $\mathcal{T}_\gamma$ and $\mathcal{T}_\alpha$. The sample values in each of these subsets are characterized by probability distributions having the respective p.d.f.s $f_\lambda(t)$, $f_\gamma(t)$ and $f_\alpha(t)$ with $t \geq 0$ and respective c.d.f.s. $F_\lambda(\tau)$, $F_\gamma(\tau)$ and $F_\alpha(\tau)$ with $\tau \geq 0$.

[3]The 80% threshold is conventionally recommended by battery manufacturers to enhance battery longevity, [116].

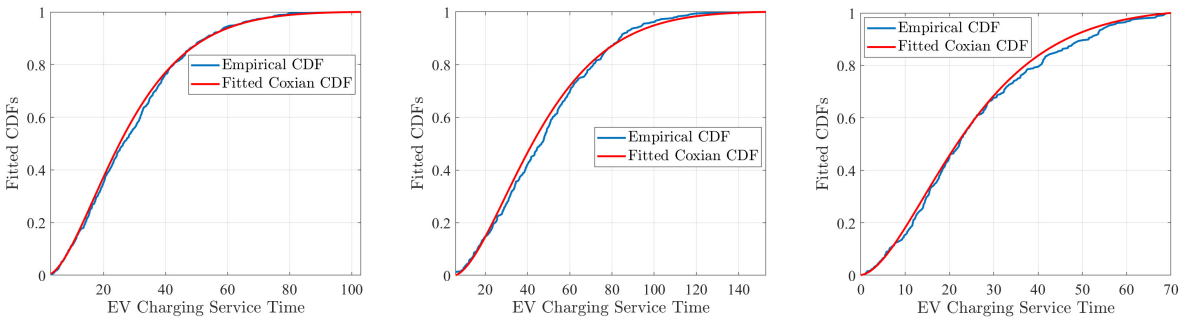

(a) $F_\lambda(\tau)$ v.s. $\widetilde{F_\lambda}(\tau)$ (b) $F_\gamma(\tau)$ v.s. $\widetilde{F_\gamma}(\tau)$ (c) $F_\alpha(\tau)$ v.s. $\widetilde{F_\alpha}(\tau)$

Figure 6.3: Empirical v.s. Theoretical fit of EV service time c.d.f.s.

Given the anticipated highly variable end-user demands for EV charging as well as the envisioned technological advancements pertaining to the design of fast chargers and EV batteries with increased efficiency, a fine-grained characterization of the EV service time components is of interest. Extensive simulations (using the simulator presented in Section 6.5 hereafter) followed by thorough numerical analyses reveal that the squared coefficients of variations c_λ^2, c_γ^2 and c_α^2 respectively pertaining to 10^6 sample points in each of the sets $\mathcal{T}_\lambda$, $\mathcal{T}_\gamma$ and $\mathcal{T}_\alpha$ are within the range $[0.5; 1)$ suggesting that their probability distributions are best approximated by Coxian-2 distributions (refer to [117] for approximation details) having respective theoretically fitted c.d.f.s denoted by $\widetilde{F_\lambda}(\tau)$, $\widetilde{F_\gamma}(\tau)$ and $\widetilde{F_\alpha}(\tau)$ with empirical counterparts denoted by $F_\lambda(\tau)$, $F_\gamma(\tau)$ and $F_\alpha(\tau)$. Figures 6.3(a)−6.3(c) concurrently plot the empirical c.d.f.s together with their theoretically fitted counterparts. These figures together with the R^2 coefficients respectively computed for each c.d.f. pair, all being in the range $[0.99; 1)$, tangibly prove these approximations' accuracy and validity.

Now, denote by T_D a randomly generated EV service time value under DICT. With probability $p_\lambda = N_\lambda \cdot N^{-1}$, $T_D \in \mathcal{T}_\lambda$. Else, with probability $1 - p_\lambda = p_\gamma$, $T_D \in \mathcal{T}_\gamma$. But, with probability p_α, $T_D \in \mathcal{T}_\alpha \subset \mathcal{T}_\gamma$. Therefore:

$$T_D = p_\lambda T_\lambda + p_\gamma \left[p_\alpha T_\alpha + (1 - p_\alpha) T_\gamma\right] \tag{6.3}$$

Let $f_D(t)$ denote the p.d.f. of T_D. It is expressed as:

$$f_D(t) = p_\lambda f_\lambda(t) \circledast p_\gamma \left[p_\alpha f_\alpha(t) \circledast (1 - p_\alpha) f_\gamma(t)\right] \quad , t \geq 0 \tag{6.4}$$

where $\circledast$ denotes the convolution operator. At this point, it is worthwhile mentioning that the mathematical closed-form derivation for $f_D(t)$, although feasible, it involves a tedious process that shall only yield a marginally useful expression whose numerical evaluation requires complex and time-exhaustive algorithms. Instead, a relatively straightforward approach adopted herein involves numerically computing the c.d.f. of the empirically generated data, denoted as $F_D(\tau)$, and then fit this latter using a highly accurate theoretical approximation, $\widetilde{F_D}(\tau)$, which shall

promote the tractable derivation and numerical computation of important statistical EV service time characteristics as well as P-EVCS performance metrics.

Again, using the simulator presented in Section 6.5 below, extensive simulations are conducted to generate EV service times under DICT according to Equation (6.3) using an battery SoC threshold of 80%. Multiple runs of the simulator are made to cover all examined sites and, for each site, all values of the incentive probability $p_\alpha \in (0; 1]$ (with a step size of 0.1) are considered. A number of 10^6 EV service time samples are collected and grouped into per-run sets. The same fitting process adopted above is repeated again at this stage for each of the per-run sets. The results of this process are all uniform across all the per-run sets. This is why, due to space limitation, only a single such result is exposed herein; the results pertaining to one of the examined sites, namely Site D, with $p_\alpha \in [0.25; 0.5; 0.75; 1]$.

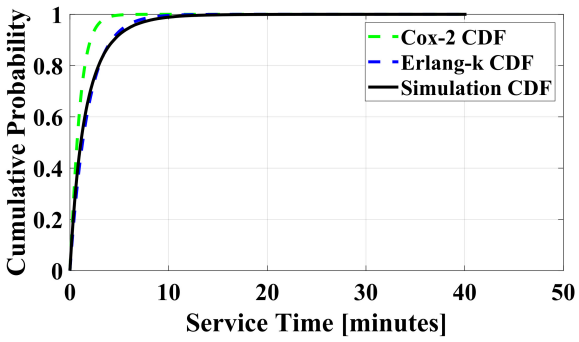

Figure 6.4: Site D; Incentive: 25%; CDFs: DICT (Convolution), Cox-2, Erlang-k, Simulation.

Once again, as illustrated in Figure 6.4, $\widetilde{F_D}(\tau)$ happens to coincide with an Erlang-k distribution that best characterizes the DICT-generated EV service time samples. This is especially true since, for all of the considered scenarios, the achieved Mean Square Error (MSE) between the empirical c.d.f. and its theoretically fitted Erlang-k counterpart fluctuates between the order of 10^{-4} to 10^{-5} compared to a constant order of 10^{-3} achieved by the Coxian-2 distribution. Indeed, the Erlang-k distribution exhibits a 22.5 to 36 times superior accuracy compared to its Coxian-2 counterpart.

6.4.2 Analytical Derivation of EV Service-Time Distribution under DICT

This section presents the detailed derivation of the service time distribution under the DICT scheme. The final expression is obtained by solving the convolution operators defined in Eq. (6.4), through the application of the Cox-2 distribution. These distributions were empirically characterized and discussed in depth in Section 6.4.1.

To simplify the analysis and clearly differentiate between the internal parameters of each Cox-2 distribution (based on the two-stage service time approach) and the variables specific to

the DICT scheme, the original Eq. (6.4) is revised as given in Eq. (6.5) below:

$$f_D(t) = p_\theta f_\theta(t) \circledast p_\zeta \left[p_\alpha f_\beta(t) \circledast (1 - p_\alpha) f_\delta(t) \right] \quad , t \geq 0 \tag{6.5}$$

• Streamlining The Convolutional Operations:

Step 1: Define the applied Distributions

Let $f_\theta(t)$, $f_\beta(t)$, and $f_\delta(t)$ in Eq. (6.5) denote the probability density functions (p.d.f.s) of $f_\lambda(t)$, $f_\alpha(t)$, and $f_\gamma(t)$ in Eq. (6.4), respectively. These distributions are modeled by Cox-2 as follows:

$$f_\theta(t) = p_{\theta_1} \mu_{\theta_1} e^{-\mu_{\theta_1} t} + (1 - p_{\theta_1}) \mu_{\theta_2} e^{-\mu_{\theta_2} t} \tag{6.6}$$

$$f_\beta(t) = p_{\beta_1} \mu_{\beta_1} e^{-\mu_{\beta_1} t} + (1 - p_{\beta_1}) \mu_{\beta_2} e^{-\mu_{\beta_2} t} \tag{6.7}$$

$$f_\delta(t) = p_{\delta_1} \mu_{\delta_1} e^{-\mu_{\delta_1} t} + (1 - p_{\delta_1}) \mu_{\delta_2} e^{-\mu_{\delta_2} t} \tag{6.8}$$

Step 2: Solving The Inner Convolution

Given the convolution $(f \circledast g)(t) = \int_0^t f(u) g(t - u)\, du$, the inner convolution in Eq. (6.5) is defined as follows:

$$h(t) = p_\alpha f_\beta(t) \circledast (1 - p_\alpha) f_\delta(t) \tag{6.9}$$

,

Expanding $f_\beta(t)$ and $f_\delta(t)$:

$$f_\beta(t) = p_{\beta 1} \mu_{\beta 1} e^{-\mu_{\beta 1} t} + (1 - p_{\beta 1}) \mu_{\beta 2} e^{-\mu_{\beta 2} t} \tag{6.10}$$

$$f_\delta(t) = p_{\delta 1} \mu_{\delta 1} e^{-\mu_{\delta 1} t} + (1 - p_{\delta 1}) \mu_{\delta 2} e^{-\mu_{\delta 2} t} \tag{6.11}$$

Then, by applying the convolution for each pair of terms:

$$\begin{aligned} h(t) = p_\alpha (1 - p_\alpha) \Bigg[\int_0^t \Bigg(& p_{\beta 1} \mu_{\beta 1} e^{-\mu_{\beta 1} u} \\ & + (1 - p_{\beta 1}) \mu_{\beta 2} e^{-\mu_{\beta 2} u} \Bigg) \Bigg(p_{\delta 1} \mu_{\delta 1} e^{-\mu_{\delta 1} (t-u)} \\ & + (1 - p_{\delta 1}) \mu_{\delta 2} e^{-\mu_{\delta 2} (t-u)} \Bigg) du \Bigg] \end{aligned} \tag{6.12}$$

• **Solving Equation (6.12)**:

- In Eq. (6.12), the terms inside the integral are expanded, giving four separate integrals as follows:

$$\begin{aligned} h(t) = p_\alpha(1-p_\alpha)\Big[& p_{\beta1}\mu_{\beta1}p_{\delta1}\mu_{\delta1}\int_0^t e^{-\mu_{\beta1}u}e^{-\mu_{\delta1}(t-u)}du \\ & + p_{\beta1}\mu_{\beta1}(1-p_{\delta1})\mu_{\delta2}\int_0^t e^{-\mu_{\beta1}u}e^{-\mu_{\delta2}(t-u)}du \\ & + (1-p_{\beta1})\mu_{\beta2}p_{\delta1}\mu_{\delta1}\int_0^t e^{-\mu_{\beta2}u}e^{-\mu_{\delta1}(t-u)}du \\ & + (1-p_{\beta1})\mu_{\beta2}(1-p_{\delta1})\mu_{\delta2}\int_0^t e^{-\mu_{\beta2}u}e^{-\mu_{\delta2}(t-u)}du\Big] \end{aligned} \tag{6.13}$$

- The following integral formula is applied to solve each of the four integrals defiend in Eq. (6.13):

$$\begin{aligned} \int_0^t e^{-\mu_1 u}e^{-\mu_2(t-u)}du &= e^{-\mu_2 t}\int_0^t e^{-(\mu_1-\mu_2)u}du \\ &= \frac{e^{-\mu_2 t}-e^{-\mu_1 t}}{\mu_1-\mu_2} \end{aligned} \tag{6.14}$$

Accordingly;

  - First Integral Result:

$$\int_0^t e^{-\mu_{\beta1}u}e^{-\mu_{\delta1}(t-u)}du = \frac{e^{-\mu_{\delta1}t}-e^{-\mu_{\beta1}t}}{\mu_{\beta1}-\mu_{\delta1}} \tag{6.15}$$

  - Second Integral Result:

$$\int_0^t e^{-\mu_{\beta1}u}e^{-\mu_{\delta2}(t-u)}du = \frac{e^{-\mu_{\delta2}t}-e^{-\mu_{\beta1}t}}{\mu_{\beta1}-\mu_{\delta2}} \tag{6.16}$$

  - Third Integral Result:

$$\int_0^t e^{-\mu_{\beta2}u}e^{-\mu_{\delta1}(t-u)}du = \frac{e^{-\mu_{\delta1}t}-e^{-\mu_{\beta2}t}}{\mu_{\beta2}-\mu_{\delta1}} \tag{6.17}$$

  - Fourth Integral Result:

$$\int_0^t e^{-\mu_{\beta2}u}e^{-\mu_{\delta2}(t-u)}du = \frac{e^{-\mu_{\delta2}t}-e^{-\mu_{\beta2}t}}{\mu_{\beta2}-\mu_{\delta2}} \tag{6.18}$$

- Solving equations $[6.15-6.18]$ are substituted into equation (6.13), resulting in:

$$
\begin{aligned}
h(t) = p_\alpha(1-p_\alpha)\Bigg[& p_{\beta1}\mu_{\beta1}p_{\delta1}\mu_{\delta1}\frac{e^{-\mu_{\delta1}t}-e^{-\mu_{\beta1}t}}{\mu_{\beta1}-\mu_{\delta1}} \\
& + p_{\beta1}\mu_{\beta1}(1-p_{\delta1})\mu_{\delta2}\frac{e^{-\mu_{\delta2}t}-e^{-\mu_{\beta1}t}}{\mu_{\beta1}-\mu_{\delta2}} \\
& + (1-p_{\beta1})\mu_{\beta2}p_{\delta1}\mu_{\delta1}\frac{e^{-\mu_{\delta1}t}-e^{-\mu_{\beta2}t}}{\mu_{\beta2}-\mu_{\delta1}} \\
& + (1-p_{\beta1})\mu_{\beta2}(1-p_{\delta1})\mu_{\delta2}\frac{e^{-\mu_{\delta2}t}-e^{-\mu_{\beta2}t}}{\mu_{\beta2}-\mu_{\delta2}}\Bigg]
\end{aligned} \tag{6.19}
$$

Step 3: Solving The Outer Convolution

Given that:

$$
\begin{aligned}
f_D(t) = p_\theta p_\zeta \Bigg[\int_0^t & \left(p_{\theta1}\mu_{\theta1}e^{-\mu_{\theta1}u} + (1-p_{\theta1})\mu_{\theta2}e^{-\mu_{\theta2}u}\right) \\
& \cdot h(t-u)\,du\Bigg]
\end{aligned} \tag{6.20}
$$

The integral in equation (6.20) is solved in two stages as follows:

1. The first integral is defined as:

$$
I_1 = p_{\theta1}\mu_{\theta1}\int_0^t e^{-\mu_{\theta1}u}h(t-u)\,du \tag{6.21}
$$

2. The second integral is:

$$
I_2 = (1-p_{\theta1})\mu_{\theta2}\int_0^t e^{-\mu_{\theta2}u}h(t-u)\,du \tag{6.22}
$$

Step 3.1: Detailed Calculation for I_1 term:

The integral I_1 can be expressed as follows:

$$
I_1 = p_{\theta1}\mu_{\theta1}\,p_\alpha(1-p_\alpha)\left[I_{1,1}+I_{1,2}+I_{1,3}+I_{1,4}\right] \tag{6.23}
$$

Where;

$$
\begin{aligned}
I_{1,1} &= p_{\theta 1}\mu_{\theta 1}p_{\beta 1}\mu_{\beta 1}p_{\delta 1}\mu_{\delta 1}\int_0^t e^{-\mu_{\theta 1}u}\frac{e^{-\mu_{\delta 1}(t-u)}-e^{-\mu_{\beta 1}(t-u)}}{\mu_{\beta 1}-\mu_{\delta 1}}\,du \\
I_{1,2} &= p_{\theta 1}\mu_{\theta 1}p_{\beta 1}\mu_{\beta 1}(1-p_{\delta 1})\mu_{\delta 2}\int_0^t e^{-\mu_{\theta 1}u}\frac{e^{-\mu_{\delta 2}(t-u)}-e^{-\mu_{\beta 1}(t-u)}}{\mu_{\beta 1}-\mu_{\delta 2}}\,du \\
I_{1,3} &= p_{\theta 1}\mu_{\theta 1}(1-p_{\beta 1})\mu_{\beta 2}p_{\delta 1}\mu_{\delta 1}\int_0^t e^{-\mu_{\theta 1}u}\frac{e^{-\mu_{\delta 1}(t-u)}-e^{-\mu_{\beta 2}(t-u)}}{\mu_{\beta 2}-\mu_{\delta 1}}\,du \\
I_{1,4} &= p_{\theta 1}\mu_{\theta 1}(1-p_{\beta 1})\mu_{\beta 2}(1-p_{\delta 1})\mu_{\delta 2}\int_0^t e^{-\mu_{\theta 1}u}\frac{e^{-\mu_{\delta 2}(t-u)}-e^{-\mu_{\beta 2}(t-u)}}{\mu_{\beta 2}-\mu_{\delta 2}}\,du
\end{aligned}
\tag{6.24}
$$

Solving $I_{1,1}$:

$$
I_{1,1} = p_{\theta 1}\mu_{\theta 1}p_{\beta 1}\mu_{\beta 1}p_{\delta 1}\mu_{\delta 1}\int_0^t e^{-\mu_{\theta 1}u}\frac{e^{-\mu_{\delta 1}(t-u)}-e^{-\mu_{\beta 1}(t-u)}}{\mu_{\beta 1}-\mu_{\delta 1}}\,du \tag{6.25}
$$

$$
\begin{aligned}
I_{1,1} = \frac{p_{\theta 1}\mu_{\theta 1}p_{\beta 1}\mu_{\beta 1}p_{\delta 1}\mu_{\delta 1}}{\mu_{\beta 1}-\mu_{\delta 1}}\Bigg[&e^{-\mu_{\delta 1}t}\cdot\frac{1-e^{-(\mu_{\theta 1}-\mu_{\delta 1})t}}{\mu_{\theta 1}-\mu_{\delta 1}} \\
&-e^{-\mu_{\beta 1}t}\cdot\frac{1-e^{-(\mu_{\theta 1}-\mu_{\beta 1})t}}{\mu_{\theta 1}-\mu_{\beta 1}}\Bigg]
\end{aligned}
\tag{6.26}
$$

Solving $I_{1,2}$:

$$
I_{1,2} = p_{\theta 1}\mu_{\theta 1}p_{\beta 1}\mu_{\beta 1}(1-p_{\delta 1})\mu_{\delta 2}\int_0^t e^{-\mu_{\theta 1}u}\frac{e^{-\mu_{\delta 2}(t-u)}-e^{-\mu_{\beta 1}(t-u)}}{\mu_{\beta 1}-\mu_{\delta 2}}\,du \tag{6.27}
$$

$$
\begin{aligned}
I_{1,2} = \frac{p_{\theta 1}\mu_{\theta 1}p_{\beta 1}\mu_{\beta 1}(1-p_{\delta 1})\mu_{\delta 2}}{\mu_{\beta 1}-\mu_{\delta 2}}\Bigg[&e^{-\mu_{\delta 2}t}\cdot\frac{1-e^{-(\mu_{\theta 1}-\mu_{\delta 2})t}}{\mu_{\theta 1}-\mu_{\delta 2}} \\
&-e^{-\mu_{\beta 1}t}\cdot\frac{1-e^{-(\mu_{\theta 1}-\mu_{\beta 1})t}}{\mu_{\theta 1}-\mu_{\beta 1}}\Bigg]
\end{aligned}
\tag{6.28}
$$

Solving $I_{1,3}$:

$$
I_{1,3} = p_{\theta 1}\mu_{\theta 1}(1-p_{\beta 1})\mu_{\beta 2}p_{\delta 1}\mu_{\delta 1}\int_0^t e^{-\mu_{\theta 1}u}\frac{e^{-\mu_{\delta 1}(t-u)}-e^{-\mu_{\beta 2}(t-u)}}{\mu_{\beta 2}-\mu_{\delta 1}}\,du \tag{6.29}
$$

$$
\begin{aligned}
I_{1,3} = \frac{p_{\theta 1}\mu_{\theta 1}(1-p_{\beta 1})\mu_{\beta 2}p_{\delta 1}\mu_{\delta 1}}{\mu_{\beta 2}-\mu_{\delta 1}}\Bigg[&e^{-\mu_{\delta 1}t}\cdot\frac{1-e^{-(\mu_{\theta 1}-\mu_{\delta 1})t}}{\mu_{\theta 1}-\mu_{\delta 1}} \\
&-e^{-\mu_{\beta 2}t}\cdot\frac{1-e^{-(\mu_{\theta 1}-\mu_{\beta 2})t}}{\mu_{\theta 1}-\mu_{\beta 2}}\Bigg]
\end{aligned}
\tag{6.30}
$$

Solving $I_{1,4}$:

$$I_{1,4} = p_{\theta 1}\mu_{\theta 1}(1-p_{\beta 1})\mu_{\beta 2}(1-p_{\delta 1})\mu_{\delta 2}\int_0^t e^{-\mu_{\theta 1}u}\frac{e^{-\mu_{\delta 2}(t-u)} - e^{-\mu_{\beta 2}(t-u)}}{\mu_{\beta 2}-\mu_{\delta 2}}\,du \tag{6.31}$$

$$\begin{aligned} I_{1,4} = \frac{p_{\theta 1}\mu_{\theta 1}(1-p_{\beta 1})\mu_{\beta 2}(1-p_{\delta 1})\mu_{\delta 2}}{\mu_{\beta 2}-\mu_{\delta 2}}\Bigg[e^{-\mu_{\delta 2}t}\cdot\frac{1-e^{-(\mu_{\theta 1}-\mu_{\delta 2})t}}{\mu_{\theta 1}-\mu_{\delta 2}} \\ -e^{-\mu_{\beta 2}t}\cdot\frac{1-e^{-(\mu_{\theta 1}-\mu_{\beta 2})t}}{\mu_{\theta 1}-\mu_{\beta 2}}\Bigg] \end{aligned} \tag{6.32}$$

Step 3.2: Detailed Calculation for I_2 term:

The integral I_2 can be expressed as:

$$I_2 = (1-p_{\theta 1})\mu_{\theta 2}\,p_\alpha(1-p_\alpha)\left[I_{2,1}+I_{2,2}+I_{2,3}+I_{2,4}\right] \tag{6.33}$$

Where;

$$\begin{aligned} I_{2,1} &= (1-p_{\theta 1})\mu_{\theta 2}p_{\beta 1}\mu_{\beta 1}p_{\delta 1}\mu_{\delta 1}\int_0^t e^{-\mu_{\theta 2}u}\frac{e^{-\mu_{\delta 1}(t-u)} - e^{-\mu_{\beta 1}(t-u)}}{\mu_{\beta 1}-\mu_{\delta 1}}\,du \\ I_{2,2} &= (1-p_{\theta 1})\mu_{\theta 2}p_{\beta 1}\mu_{\beta 1}(1-p_{\delta 1})\mu_{\delta 2}\int_0^t e^{-\mu_{\theta 2}u}\frac{e^{-\mu_{\delta 2}(t-u)} - e^{-\mu_{\beta 1}(t-u)}}{\mu_{\beta 1}-\mu_{\delta 2}}\,du \\ I_{2,3} &= (1-p_{\theta 1})\mu_{\theta 2}(1-p_{\beta 1})\mu_{\beta 2}p_{\delta 1}\mu_{\delta 1}\int_0^t e^{-\mu_{\theta 2}u}\frac{e^{-\mu_{\delta 1}(t-u)} - e^{-\mu_{\beta 2}(t-u)}}{\mu_{\beta 2}-\mu_{\delta 1}}\,du \\ I_{2,4} &= (1-p_{\theta 1})\mu_{\theta 2}(1-p_{\beta 1})\mu_{\beta 2}(1-p_{\delta 1})\mu_{\delta 2}\int_0^t e^{-\mu_{\theta 2}u}\frac{e^{-\mu_{\delta 2}(t-u)} - e^{-\mu_{\beta 2}(t-u)}}{\mu_{\beta 2}-\mu_{\delta 2}}\,du \end{aligned} \tag{6.34}$$

Solving $I_{2,1}$:

$$I_{2,1} = (1-p_{\theta 1})\mu_{\theta 2}p_{\beta 1}\mu_{\beta 1}p_{\delta 1}\mu_{\delta 1}\int_0^t e^{-\mu_{\theta 2}u}\frac{e^{-\mu_{\delta 1}(t-u)} - e^{-\mu_{\beta 1}(t-u)}}{\mu_{\beta 1}-\mu_{\delta 1}}\,du \tag{6.35}$$

$$\begin{aligned} I_{2,1} = \frac{(1-p_{\theta 1})\mu_{\theta 2}p_{\beta 1}\mu_{\beta 1}p_{\delta 1}\mu_{\delta 1}}{\mu_{\beta 1}-\mu_{\delta 1}}\Bigg[e^{-\mu_{\delta 1}t}\cdot\frac{1-e^{-(\mu_{\theta 2}-\mu_{\delta 1})t}}{\mu_{\theta 2}-\mu_{\delta 1}} \\ -e^{-\mu_{\beta 1}t}\cdot\frac{1-e^{-(\mu_{\theta 2}-\mu_{\beta 1})t}}{\mu_{\theta 2}-\mu_{\beta 1}}\Bigg] \end{aligned} \tag{6.36}$$

Solving $I_{2,2}$:

$$\begin{aligned} I_{2,2} = (1-p_{\theta 1})\mu_{\theta 2}p_{\beta 1}\mu_{\beta 1}(1-p_{\delta 1})\mu_{\delta 2}\cdot \\ \int_0^t e^{-\mu_{\theta 2}u}\frac{e^{-\mu_{\delta 2}(t-u)} - e^{-\mu_{\beta 1}(t-u)}}{\mu_{\beta 1}-\mu_{\delta 2}}\,du \end{aligned} \tag{6.37}$$

$$I_{2,2} = \frac{(1-p_{\theta 1})\mu_{\theta 2} p_{\beta 1}\mu_{\beta 1}(1-p_{\delta 1})\mu_{\delta 2}}{\mu_{\beta 1}-\mu_{\delta 2}} \cdot \left[e^{-\mu_{\delta 2} t} \cdot \frac{1-e^{-(\mu_{\theta 2}-\mu_{\delta 2})t}}{\mu_{\theta 2}-\mu_{\delta 2}} - e^{-\mu_{\beta 1} t} \cdot \frac{1-e^{-(\mu_{\theta 2}-\mu_{\beta 1})t}}{\mu_{\theta 2}-\mu_{\beta 1}} \right] \tag{6.38}$$

Solving $I_{2,3}$:

$$I_{2,3} = (1-p_{\theta 1})\mu_{\theta 2}(1-p_{\beta 1})\mu_{\beta 2} p_{\delta 1}\mu_{\delta 1} \cdot \int_0^t e^{-\mu_{\theta 2} u} \frac{e^{-\mu_{\delta 1}(t-u)} - e^{-\mu_{\beta 2}(t-u)}}{\mu_{\beta 2}-\mu_{\delta 1}}\, du \tag{6.39}$$

$$I_{2,3} = \frac{(1-p_{\theta 1})\mu_{\theta 2}(1-p_{\beta 1})\mu_{\beta 2} p_{\delta 1}\mu_{\delta 1}}{\mu_{\beta 2}-\mu_{\delta 1}} \left[e^{-\mu_{\delta 1} t} \cdot \frac{1-e^{-(\mu_{\theta 2}-\mu_{\delta 1})t}}{\mu_{\theta 2}-\mu_{\delta 1}} - e^{-\mu_{\beta 2} t} \cdot \frac{1-e^{-(\mu_{\theta 2}-\mu_{\beta 2})t}}{\mu_{\theta 2}-\mu_{\beta 2}} \right] \tag{6.40}$$

Solving $I_{2,4}$:

$$I_{2,4} = (1-p_{\theta 1})\mu_{\theta 2}(1-p_{\beta 1})\mu_{\beta 2}(1-p_{\delta 1})\mu_{\delta 2} \int_0^t e^{-\mu_{\theta 2} u} \cdot \frac{e^{-\mu_{\delta 2}(t-u)} - e^{-\mu_{\beta 2}(t-u)}}{\mu_{\beta 2}-\mu_{\delta 2}}\, du \tag{6.41}$$

$$I_{2,4} = \frac{(1-p_{\theta 1})\mu_{\theta 2}(1-p_{\beta 1})\mu_{\beta 2}(1-p_{\delta 1})\mu_{\delta 2}}{\mu_{\beta 2}-\mu_{\delta 2}} \left[e^{-\mu_{\delta 2} t} \cdot \frac{1-e^{-(\mu_{\theta 2}-\mu_{\delta 2})t}}{\mu_{\theta 2}-\mu_{\delta 2}} - e^{-\mu_{\beta 2} t} \cdot \frac{1-e^{-(\mu_{\theta 2}-\mu_{\beta 2})t}}{\mu_{\theta 2}-\mu_{\beta 2}} \right] \tag{6.42}$$

Accordingly:

$$\begin{aligned} f_D(t) = p_\theta p_\zeta p_\alpha (1-p_\alpha) \Bigg[& p_{\theta 1}\mu_{\theta 1} \Bigg(\frac{p_{\beta 1}\mu_{\beta 1} p_{\delta 1}\mu_{\delta 1}}{\mu_{\beta 1}-\mu_{\delta 1}} \left(\frac{e^{-\mu_{\delta 1} t}\left(e^{(\mu_{\delta 1}-\mu_{\theta 1})t}-1\right)}{\mu_{\delta 1}-\mu_{\theta 1}} - \frac{e^{-\mu_{\beta 1} t}\left(e^{(\mu_{\beta 1}-\mu_{\theta 1})t}-1\right)}{\mu_{\beta 1}-\mu_{\theta 1}} \right) \\ & + \frac{p_{\beta 1}\mu_{\beta 1}(1-p_{\delta 1})\mu_{\delta 2}}{\mu_{\beta 1}-\mu_{\delta 2}} \left(\frac{e^{-\mu_{\delta 2} t}\left(e^{(\mu_{\delta 2}-\mu_{\theta 1})t}-1\right)}{\mu_{\delta 2}-\mu_{\theta 1}} - \frac{e^{-\mu_{\beta 1} t}\left(e^{(\mu_{\beta 1}-\mu_{\theta 1})t}-1\right)}{\mu_{\beta 1}-\mu_{\theta 1}} \right) \\ & + \frac{(1-p_{\beta 1})\mu_{\beta 2} p_{\delta 1}\mu_{\delta 1}}{\mu_{\beta 2}-\mu_{\delta 1}} \left(\frac{e^{-\mu_{\delta 1} t}\left(e^{(\mu_{\delta 1}-\mu_{\theta 1})t}-1\right)}{\mu_{\delta 1}-\mu_{\theta 1}} - \frac{e^{-\mu_{\beta 2} t}\left(e^{(\mu_{\beta 2}-\mu_{\theta 1})t}-1\right)}{\mu_{\beta 2}-\mu_{\theta 1}} \right) \\ & + \frac{(1-p_{\beta 1})\mu_{\beta 2}(1-p_{\delta 1})\mu_{\delta 2}}{\mu_{\beta 2}-\mu_{\delta 2}} \left(\frac{e^{-\mu_{\delta 2} t}\left(e^{(\mu_{\delta 2}-\mu_{\theta 1})t}-1\right)}{\mu_{\delta 2}-\mu_{\theta 1}} - \frac{e^{-\mu_{\beta 2} t}\left(e^{(\mu_{\beta 2}-\mu_{\theta 1})t}-1\right)}{\mu_{\beta 2}-\mu_{\theta 1}} \right) \Bigg) \\ & + (1-p_{\theta 1})\mu_{\theta 2} \Bigg(\frac{p_{\beta 1}\mu_{\beta 1} p_{\delta 1}\mu_{\delta 1}}{\mu_{\beta 1}-\mu_{\delta 1}} \left(\frac{e^{-\mu_{\delta 1} t}\left(e^{(\mu_{\delta 1}-\mu_{\theta 2})t}-1\right)}{\mu_{\delta 1}-\mu_{\theta 2}} - \frac{e^{-\mu_{\beta 1} t}\left(e^{(\mu_{\beta 1}-\mu_{\theta 2})t}-1\right)}{\mu_{\beta 1}-\mu_{\theta 2}} \right) \\ & + \frac{p_{\beta 1}\mu_{\beta 1}(1-p_{\delta 1})\mu_{\delta 2}}{\mu_{\beta 1}-\mu_{\delta 2}} \left(\frac{e^{-\mu_{\delta 2} t}\left(e^{(\mu_{\delta 2}-\mu_{\theta 2})t}-1\right)}{\mu_{\delta 2}-\mu_{\theta 2}} - \frac{e^{-\mu_{\beta 1} t}\left(e^{(\mu_{\beta 1}-\mu_{\theta 2})t}-1\right)}{\mu_{\beta 1}-\mu_{\theta 2}} \right) \\ & + \frac{(1-p_{\beta 1})\mu_{\beta 2} p_{\delta 1}\mu_{\delta 1}}{\mu_{\beta 2}-\mu_{\delta 1}} \left(\frac{e^{-\mu_{\delta 1} t}\left(e^{(\mu_{\delta 1}-\mu_{\theta 2})t}-1\right)}{\mu_{\delta 1}-\mu_{\theta 2}} - \frac{e^{-\mu_{\beta 2} t}\left(e^{(\mu_{\beta 2}-\mu_{\theta 2})t}-1\right)}{\mu_{\beta 2}-\mu_{\theta 2}} \right) \\ & + \frac{(1-p_{\beta 1})\mu_{\beta 2}(1-p_{\delta 1})\mu_{\delta 2}}{\mu_{\beta 2}-\mu_{\delta 2}} \left(\frac{e^{-\mu_{\delta 2} t}\left(e^{(\mu_{\delta 2}-\mu_{\theta 2})t}-1\right)}{\mu_{\delta 2}-\mu_{\theta 2}} - \frac{e^{-\mu_{\beta 2} t}\left(e^{(\mu_{\beta 2}-\mu_{\theta 2})t}-1\right)}{\mu_{\beta 2}-\mu_{\theta 2}} \right) \Bigg) \Bigg]. \end{aligned} \tag{6.43}$$

6.4.3 Modelling of a P-EVCS

This section is dedicated to analytically model a single-outlet P-EVCS as a single-server queueing system with general per-EV-service as per the above-described DICT scheme and limited EV waiting spaces. The purpose of such a model is to capture the different per-P-EVCS dynamics and characterize its performance in terms of the earlier-mentioned QoS metrics. While the per-EV charging service has been characterized above to follow an Erlang-k distribution (*i.e.*, characterized by its general statistical properties relative to the typical exponential distribution), the EV arrival process to a target P-EVCS is characterized as follows. As shown in Figure 6.1(a), an arbitrary targetted P-EVCS (indicated with a red dot) is deployed within a certain area. Following the rationale in [87], EV arrivals to the entire area follow a Poisson process with a parameter of Λ EV/s. Further, it is assumed herein, also as per the guidelines of [87], that arriving EVs to the considered area shall select the closest P-EVCS to their point of arrival to receive charging service from. Without loss of generality (w.l.o.g.), it is with a probability of p that, from the perspective of any arriving EV, the target P-EVCS happens to be the closest to that EV and hence the selected service P-EVCS. The derivation of p is outside the scope of this present work. The reader is, however, referred to [87] for further details about it. Yet, what is important to this present work is that, the EV arrivals to the target P-EVCS follows a thinned Poisson process with a parameter $\lambda = \Lambda p$ EV/s. Noting the limited EV waiting space by $Q = K - 1$, the target P-EVCS can, therefore, be modelled as an $M/G/1/K$ queueing system whose fundamental QoS metrics have been characterized by Smith and MacGregor in [118] and are presented hereafter only for completeness purposes. Precisely:

• The blocking probability, denoted by P_B, quantifies the likelihood of an EV being denied service at the target P-EVCS due to the occupancy of the station's outlet and the concurrent non-availability of waiting spaces. It is given by:

$$P_B = \frac{U^{\frac{\sqrt{U}S^2-\sqrt{U}+2K}{2+\sqrt{U}S^2-\sqrt{U}}}(U-1)}{(U^2)^{\frac{1+\sqrt{U}S^2-\sqrt{U}+K}{2+\sqrt{U}S^2-\sqrt{U}}}-1} \tag{6.44}$$

where U is the P-EVCS utilization, and S^2 is the EVs' service times squared coefficient of variation.

• The effective EV arrival rate to the target P-EVCS, λ_{eff} is:

$$\lambda_{eff} = \lambda(1 - P_B) \tag{6.45}$$

• The average waiting time in the queue is:

$$\overline{W} = \frac{\lambda_{eff}k(k+1)}{2\mu^2\left(1-\frac{\lambda_{eff}k}{\mu}\right)} \tag{6.46}$$

where μ represents the EV service rate.

• The average waiting queue length as computed using Little's Law is:

$$\overline{L} = \lambda_{eff}\, \overline{W} \tag{6.47}$$

The validity and accuracy of the above-listed QoS metrics' closed-form expressions are evaluated below in Section 6.5.

6.5 Numerical Analyses and Simulations

In this section, thorough numerical analyses and simulations are performed for the purpose of verifying the correctness and accuracy of the EV service time characterizations presented in Section 6.4 and to gauge the merit of the proposed DICT scheme through a direct comparison of the target P-EVCS performance achieved under DICT as well as the two additional schemes SRS and IRS mentioned in Section 6.2. A custom-built python-based discrete-event simulator was built for this purpose.

Unless indicated otherwise, the values of the used simulation parameters are extracted from the available real-world dataset. The EV arrival rates at the target site vary over time and are determined by analyzing the penetration rate of EVs at the site using timestamps from recorded charging sessions. To capture unique charging behaviors across daily shifts and account for seasonal variations, EV arrival rates are aggregated into four-hour time windows (e.g., $2:00$ PM to $6:00$ PM) on a quarterly basis for each site throughout the analyzed year. Specifically, Site D's EV arrival rates for the year 2023 are calculated on a per-quarter basis, yielding average arrival rates of 0.0144 EV/min, 0.0126 EV/min, 0.0140 EV/min, and 0.0169 EV/min for quarters 1, 2, 3, and 4, respectively. This data-driven approach ensures that simulation inputs credibly reflect real-world EV charging demand dynamics. In addition, the Coxian-2 distributions $\widetilde{F_\lambda}(\tau)$, $\widetilde{F_\alpha}(\tau)$, and $\widetilde{F_\gamma}(\tau)$ have respective means of 29.33, 25.57, and 48.55 minutes, as well as respective standard deviations of 17.26, 16.09, and 26.1 minutes. Finally, to ensure the realization of at least a 95% confidence interval, the reported results herein are averaged over multiple simulation runs, each of which simulates the arrival of 10^6 EVs. The symbols representing the performance metrics used in the subsequent analysis, along with their corresponding definitions, are summarized in Tables 6.1 and 6.2.

6.5.1 Theoretical P-EVCS Model Verification and Validation

This section presents a systematic approach to validate the Quality of Service (QoS) metrics derived from simulation against their closed-form mathematical counterparts. Note that the

Symbol	Meaning
$\overline{U}'$	Mean utilization at 10% NDS
$\overline{W}'$	Mean waiting time at 10% NDS
$\overline{N}_B{}'$	Mean blocked EVs at 10% NDS
$\overline{N}_W{}'$	Mean waiting EVs at 10% NDS
$\overline{N}_S{}'$	Mean served EVs at 10% NDS
$\overline{U}''$	Mean utilization at 20% NDS
$\overline{W}''$	Mean waiting time at 20% NDS
$\overline{N}_B{}''$	Mean blocked EVs at 20% NDS
$\overline{N}_W{}''$	Mean waiting EVs at 20% NDS
$\overline{N}_S{}''$	Mean served EVs at 20% NDS
$\overline{U}_{\text{SRS}}$	Mean utilization at SRS
$\overline{W}_{\text{SRS}}$	Mean waiting time at SRS
$\overline{N}_B^{\text{SRS}}$	Mean blocked EVs at SRS
$\overline{N}_W^{\text{SRS}}$	Mean waiting EVs at SRS
$\overline{N}_S^{\text{SRS}}$	Mean served EVs at SRS
$\overline{U}_{DICT}$	Mean utilization at DICT
$\overline{W}_{DICT}$	Mean waiting time at DICT
$\overline{N}_B^{\text{DICT}}$	Mean blocked EVs at DICT

Table 6.1: List of Performance Metrics Symbols (Part 1).

Symbol	Meaning
$\overline{N}_W^{\text{DICT}}$	Mean waiting EVs at DICT
$\overline{N}_S^{\text{DICT}}$	Mean served EVs at DICT
$\overline{U}'_{DICT}$	Mean utilization at (10% NDS + DICT)
$\overline{W}'_{DICT}$	Mean waiting time at (10% NDS + DICT)
$\overline{N}_{B\,DICT}{}'$	Mean blocked EVs at (10% NDS + DICT)
$\overline{N}_{W\,DICT}{}'$	Mean waiting EVs at (10% NDS + DICT)
$\overline{N}_{S\,DICT}{}'$	Mean served EVs at (10% NDS + DICT)
$\overline{U}''_{DICT}$	Mean utilization at (20% NDS + DICT)
$\overline{W}''_{DICT}$	Mean waiting time at (20% NDS + DICT)
$\overline{N}_{B\,DICT}{}''$	Mean blocked EVs at (20% NDS + DICT)
$\overline{N}_{W\,DICT}{}''$	Mean waiting EVs at (20% NDS + DICT)
$\overline{N}_{S\,DICT}{}''$	Mean served EVs at (20% NDS + DICT)
$\overline{U}_{\text{IRS}}$	Mean utilization at IRS
$\overline{W}_{\text{IRS}}$	Mean waiting time at IRS
$\overline{N}_B^{\text{IRS}}$	Mean blocked EVs at IRS
$\overline{N}_W^{\text{IRS}}$	Mean waiting EVs at IRS
$\overline{N}_S^{\text{IRS}}$	Mean served EVs at IRS

Table 6.2: List of Performance Metrics Symbols (Part 2).

above-presented mathematical expressions, once verified to be highly accurate, allow for a much simpler alternative (as compared to executing complex time-exhaustive simulations) for computing performance metric values. In what follows, Site D shall be used as a target P-EVCS. This site's behavior shall be extensively simulated with simulation input parameters (*i.e.*, EV arrival rate, EV service times statistical values, etc) extracted from the realistic data records for this site on a quarterly basis. The number of EV waiting spaces is set to $Q = 1$.

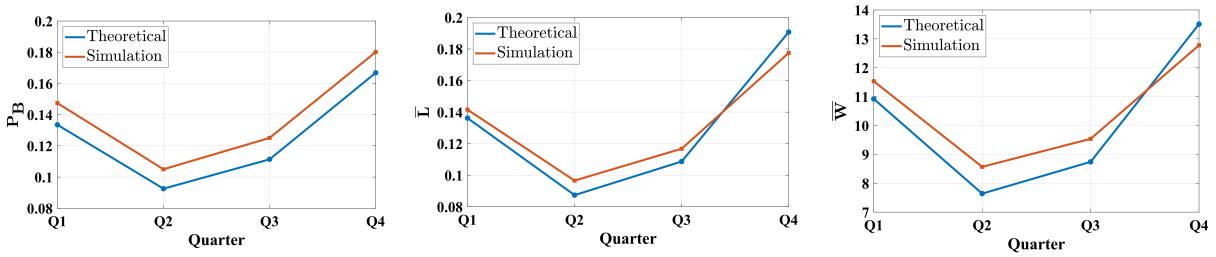

(a) Avg. Blocking Probability P_B (b) Avg. Waiting Queue Length (c) Avg. Waiting Time

Figure 6.5: Site D; Simulation v.s. (Numerical-Theory) validation, Year: 2023.

Figure 6.5(a) illustrates the comparison between simulated and numerically computed theoretical P_B values. Notably, the analysis demonstrated close alignment between the two, with an average Relative Percentage Error (RPE) of no more than 11.04%. Further analysis extended to additional sites reveals that, across these sites, the computed RPE values ranged

from 2.85% to 12.57%, indicating consistent accuracy of the numerical model in various operational contexts. These results underscore the validity of the proposed expression 6.44 and its potency to accurately substitute extensive simulation complexities through simple numerical evaluations of the given formula.

Next, the theoretical values of $\overline{L}$ and $\overline{W}$ are plotted against their simulated counterparts in Figures 6.5(b) and 6.5(c), respectively. From these figures, it is concluded that an average RPE of 3.74% is achieved for $\overline{L}$ and 5.37% is achieved for $\overline{W}$. Expanding the analysis to include additional sites, the computed RPE values for $\overline{L}$ varied between 2.08% and 5.85%, while for $\overline{W}$, they ranged from 2.48% to 6.45%. These results underscore the high accuracy of the adopted theoretical expressions in (6.46) and (6.47) and, hence, their capability to reliably replace time-exhaustive simulations.

In light of the above, the $M/G/1/K$ numerical-mathematical model offers a significant computational advantage in evaluating the long-term average QoS metrics pertaining to $3,280$ EVs in just 6.21 seconds on an Intel i7-$4510U$ CPU (4 cores, 2.6 GHz) with 16 GB RAM using Jupyter Notebook $6.5.4$. In contrast, simulations for similar datasets consume time intervals that are in the order of hours or days to generate these results. This efficiency, coupled with high accuracy indicated by low RPE values, underscores the practicality of numerically evaluating QoS metrics' expressions in working around remarkable computational overhead.

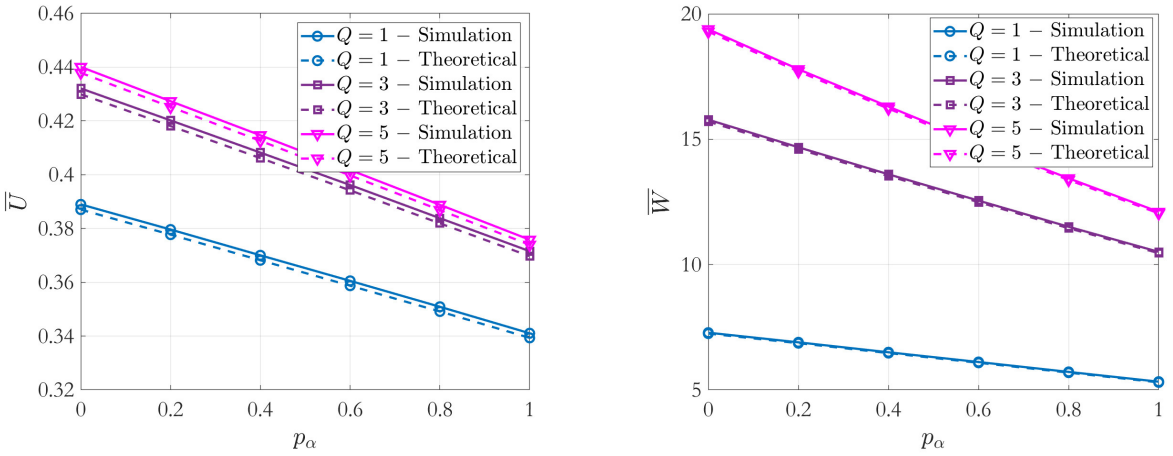

(a) $\overline{U}$ v.s. p_α (b) $\overline{W}$ v.s. p_α

Figure 6.6: Mean utilization/waiting time v.s. incentive adherence.

Now, figure 6.6(a), concurrently plots the simulated and theoretically computed average P-EVCS charger utilization, $\overline{U}$ as a function of the probability of incentive adherence, p_α for different numbers of EV waiting spaces, $Q = \{1, 3, 5\}$. With a relative error of 0.005%, these figures constitute tangible proofs of the validity of [87]'s adopted stochastic queueing model variant with the only modification consisting of replacing the EV service time distri-

bution with the highly accurate one corresponding to such service under DICT as derived herein in Eq. (6.4). A similar joint plot in Figure 6.6(b) of the simulated and theoretically computed variations of the experienced average waiting time, $\overline{W}$, at the target P-EVCS as a function of p_α further asserts the chosen model's correctness where the achieved relative error is 0.003%. These two figures clearly illustrate the decreasing trends of $\overline{U}$ and $\overline{W}$ as a function of p_α regardless of Q. Indeed, the more EV users abide by the operator's provisioned incentives, the more rapidly the P-EVCS will clear out such EVs resulting in a shorter queue size and, hence, by Little's Theorem, a reduced waiting time. Moreover, the faster EV clearance emulates a higher service rate and, thus, a smaller load (*i.e.*, utilization). Needless to mention here that a higher Q allows for more EVs to wait in line and hence increases $\overline{U}$ and $\overline{W}$. Yet, for a fixed EV arrival rate to the P-EVCS, adding more waiting spaces results in only marginal variations of these two metrics.

6.5.2 Further Discussions

The study evaluates the impact of three key Quality of Service (QoS) performance improvement techniques for P-EVCS: New Site Deployment (NDS), Site Resizing (SRS), and the Incentive-Augmented Resizing Scheme (IRS). Under NDS, the effects of increasing the number of city-wide deployed sites by 10% and 20% are analyzed, with the resulting utilization and mean waiting times represented as $\overline{U}'$, $\overline{U}''$, $\overline{W}'$, and $\overline{W}''$. The SRS approach examines the impact of adding an additional charging outlet at the target site, with the corresponding utilization and mean waiting time denoted as $\overline{U}_{\text{SRS}}$ and $\overline{W}_{\text{SRS}}$. Finally, IRS evaluates the combined effect of deploying new outlets and incentivizing EVs through the DICT scheme, with the achieved utilization and mean waiting time expressed as $\overline{U}_{\text{IRS}}$ and $\overline{W}_{\text{IRS}}$.

6.5.2.1 QoS Under Base line Waiting Queue Length (BWQL)

Assuming (BWQL) equal to the actual number of installed charging outlets at the P-EVCS as shown in Table 6.3, Figure (6.7) illustrates the numerical values of P-EVCS utilization and compares the average utilization levels under various operational strategies from 2023 through mid-2026. The baseline analysis reveals that, without interventions such as NDS, DICT, or SRS, the average utilization ($\overline{U}$) at the examined EVCS B steadily increases, reflecting a growing EV load. Specifically, utilization is projected to rise from 0.66 in 2023 to 0.88 by mid-2026, indicating significant infrastructure strain driven by the increasing EV penetration rate (λ) near the EVCS, as detailed in Table 6.3.

This analysis employs a SARIMAX-based forecasting model to predict EV arrivals in

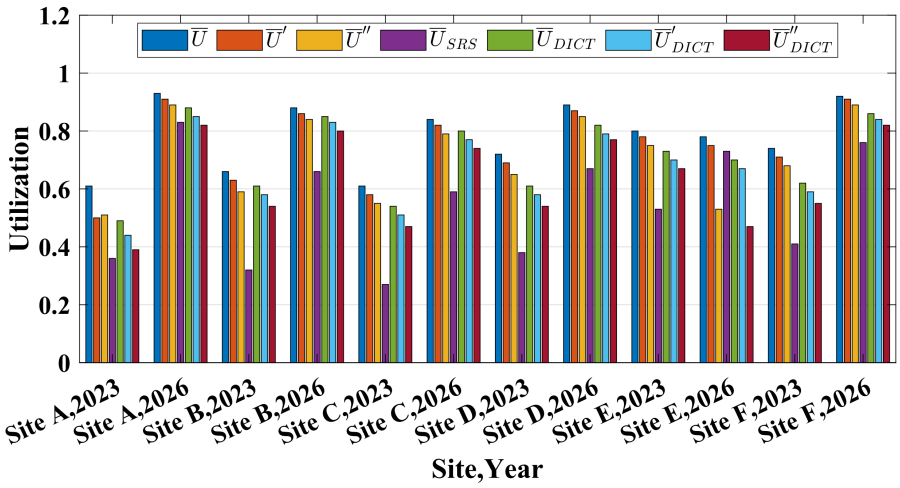

Figure 6.7: Average utilization under NDS, SRS, and DICT.

the vicinity of the examined EVCSs. This forecasting approach provides a comprehensive understanding of future increasing EV charging demands; hence, it contributes to reducing the P-EVCS load and, as a consequence, improving its performance in terms of critical QoS metrics. The projected growth trajectory highlights a potential risk of overloaded service, with significant implications for user QoS, including longer waiting times and potential service denials during peak hours. Without proactive infrastructure enhancements, the findings reflect a decline in QoS across similar EVCS locations, emphasizing the need for operational interventions to address the challenges posed by rising EV demands.

Applying NDS demonstrates notable improvements in outlet utilization across all examined sites (A through F). For instance, following Figure (6.7), at EVCS B in 2023, implementing 10% and 20% NDS results in utilization reductions ($\overline{U}'$, $\overline{U}''$) of approximately 4.66% and 9.98%, respectively. These decreases correspond to reductions in average waiting times ($\overline{W}'$, $\overline{W}''$) by 4.83% and 10.22%, as shown in Figure (6.8). Additionally, the volume of EVs experiencing blocked or delayed service significantly declines, as illustrated in Figure (6.9).

Figure 6.8: Avg. Waiting Time under NDS, SRS, and DICT.

Table 6.3: BWQL, EVs Penetration Rate (λ)

$EVCS$	$BWQL$	λ	λ'	λ''	Year
A	2	5.09	4.58	4.07	2023
A	2	13.62	12.26	10.89	2026
B	1	2.96	2.66	2.36	2023
B	1	7.59	6.82	6.06	2026
C	1	2.33	2.1	1.86	2023
C	1	5.64	5.07	4.51	2026
D	1	3.48	3.12	2.78	2023
D	1	7.37	6.63	5.89	2026
E	1	2.3	2.07	1.84	2023
E	1	4.91	4.41	3.92	2026
F	1	2.62	2.36	2.09	2023
F	1	6.82	6.13	5.45	2026

The number of blocked EVs ($\overline{N}_B{}'$, $\overline{N}_B{}''$) at EVCS (B) under NDS demonstrates notable reductions, reaching 16.89% and 32.95% for 10% and 20% NDS, respectively. These improvements extend to decreases in the average number of EVs that had to wait to receive service ($\overline{N}_W{}'$, $\overline{N}_W{}''$) and served EVs ($\overline{N}_S{}'$, $\overline{N}_S{}''$), as shown in Figures (6.10) and (6.11), respectively. Specifically, the number of EVs that waited declined by 8.66% to 17.93%, and served EVs decreased by 4.65% to 9.92% for 10% and 20% NDS, respectively. These results underscore the effectiveness of NDS in mitigating demand pressure and enhancing service quality at high-demand EVCS locations by reducing utilization, waiting times, and blocked EVs.

Across a broader range of EVCSs, the NDS strategy proves equally effective. Under a 10% NDS, utilization ($\overline{U}'$) decreases range from 3.92% to 7.54%, with the most significant impact observed at EVCS (A). At 20% NDS, the utilization ($\overline{U}''$) decreases, expanding to a range of 8.44% to 16.29%. Similarly, waiting time reductions ($\overline{W}'$, $\overline{W}''$) range from 4.27% to 8.97% at 10% NDS and 8.82% to 19.09% at 20% NDS. The most pronounced impact is seen in blocked EVs ($\overline{N}_B{}'$, $\overline{N}_B{}''$), with reductions of 16.20% to 22.23% for 10% NDS and 31.46% to 42.43% for 20% NDS, depending on site-specific factors such as service times and EV arrival rates. These findings demonstrate that NDS effectively redistributes load, preventing service overload in high-demand urban areas and improving QoS for EV users across the network.

Further enhancements in QoS can be achieved by implementing additional infrastructure

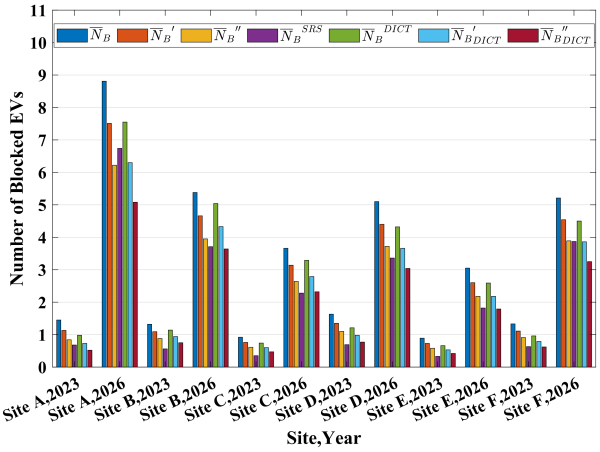

Figure 6.9: Avg. Number of Blocked EVs under NDS, SRS, and DICT.

strategies, such as the SRS approach, which involves adding an additional charging outlet with a 50 kW rate at P-EVCS, significantly enhances QoS by reducing utilization ($\overline{U}_{\text{SRS}}$) and average waiting time ($\overline{W}_{\text{SRS}}$), as demonstrated in Figures (6.7) and (6.8), respectively. This approach effectively distributes charging demand across a greater number of outlets, resulting in approximately a 50% reduction in load per charger. The alleviated infrastructure pressure minimizes waiting time, improves service availability, and fosters higher user satisfaction, contributing to a more efficient public EV charging network. By balancing charging demand, SRS enhances the resilience of EVCS (B) against peak-time demands, ensuring a smoother and more consistent service experience.

For example, in 2023, applying SRS scenario to the existing infrastructure with baseline waiting queues leads to remarkable improvements: utilization decreases by 51.12%, waiting time by 77.18%, and blocked EVs ($\overline{N}_B{}^{\text{SRS}}$) and waited EVs ($\overline{N}_W{}^{\text{SRS}}$) are reduced by 57.66% and 24.57%, respectively, as shown in Figures (6.7)–(6.10).

Additionally, the number of served EVs ($\overline{N}_S{}^{\text{SRS}}$) increases by 46.17% as shown in Figure (6.11). These results highlight SRS as an effective strategy to optimize service delivery and improve throughput at high-demand EVCS locations.These improvements underscore the effectiveness of SRS approach in enhancing operational efficiency and overall user satisfaction at the EVCSs.

Moreover, the DICT scheme emerges as a cost-effective solution for EV charging stations, requiring no additional infrastructure while offering substantial operational benefits. As a ”quick win” strategy, the DICT scheme effectively reduces session times and accelerates queue clearance. This efficiency is evident when examining the performance of EVCSs (A through F).

As shown in Figures (6.7)-(6.9), during the analyzed period from 2023 to mid-2026, the DICT scheme led to average reductions in utilization ($\overline{U}_{DICT}$), waiting times ($\overline{W}_{DICT}$), and the number of blocked EVs ($\overline{N}_B{}^{DICT}$) across these sites. For instance, ($\overline{U}_{DICT}$) dropped by

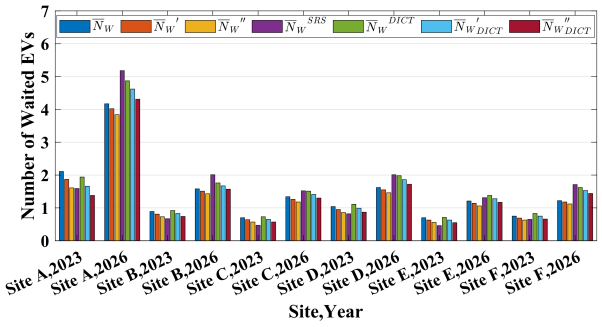

Figure 6.10: Avg. Number of Waited EVs under NDS, SRS, and DICT.

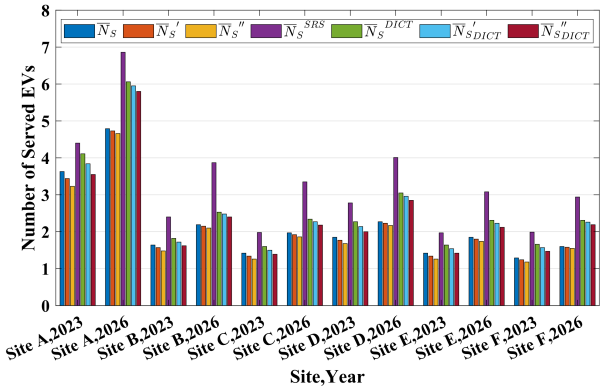

Figure 6.11: Avg. Number of Served EVs under NDS, SRS, and DICT.

ranges from 3.25% to 20.75%, ($\overline{W}_{DICT}$) reduced by 20.68% to 46.90%, and ($\overline{N}_B{}^{DICT}$) declined by 6.34% to 32.90%. These results underline DICT's efficiency in easing congestion without adding costs.

Simultaneously, the number of served EVs ($\overline{N}_S{}^{DICT}$) per site increased significantly, as shown in Figure (6.11), with a rise between 10.69% and 44.25% across the stations. This increase in served EVs highlights DICT's effectiveness in boosting throughput and reducing delays.

By mid-2026, a moderate uptick is expected in the number of EVs that have to wait before receiving service ($\overline{N}_W{}^{DICT}$), as shown in Figure (6.10), with percentages such as 11.29%, 13.08%, and up to 32.10% across EVCSs, reflecting both an increase in demand and the system's enhanced capacity to manage it more effectively. Overall, the DICT scheme proves to be a highly effective, low-cost method to enhance service efficiency and queue management.

Generally, lowering the utilization metric at public EVCSs, without compromising QoS, can mitigate electrical stress by reducing sustained high voltage and current demands, which otherwise strain connectors, wiring, and power electronics. This reduction in stress helps extend the lifespan of critical components and subsystems at the charging station, such as the Electric Vehicle Supply Equipment (EVSE). Ultimately, this approach decreases opera-

tional and maintenance costs, particularly in soft costs like labor and administrative expenses associated with repairs and replacements.

In addition, by examining the results presented in Figures (6.7)-(6.9), integrating the DICT scheme with NDS results in a notable boost in the QoS at each EVCS throughout the period from 2023 to mid-2026.

This improvement is evidenced by the variations observed in key performance metrics for each EVCS. For NDS at 10% combined with DICT, the enhancement in utilization ($\overline{U}'_{DICT}$), waiting times ($\overline{W}'_{DICT}$), and blocked EVs ($\overline{N}_{B}{}'_{DICT}$) showed respective decreases across EVCS sites: for example, the utilization dropped between 8.43% and 3.73%, waiting times reduced by ranges such as 24.70% to 21.36%, and blocked EVs declined from 14.29% to 7.09%. This combined approach also led to an average increase in the number of EVs that waited to receive service ($\overline{N}_{W}{}'_{DICT}$), ranging from 2.50% to 30.16%, and an increase in the number of served EVs ($\overline{N}_{S}{}'_{DICT}$), with increments between 9.97% and 43.02%, as shown in Figures (6.10) and (6.11), respectively.

Similarly, the NDS+DICT approach at 20% amplified these positive trends. For instance, utilization ($\overline{U}''_{DICT}$), waiting times ($\overline{W}''_{DICT}$), and blocked EVs ($\overline{N}_{B}{}''_{DICT}$) decreased further, with ranges such as 9.07% to 4.16% in utilization, 25.12% to 21.55% in waiting times, and 15.44% to 7.77% in blocked EVs. The average number of served EVs ($\overline{N}_{S}{}''_{DICT}$) rose across sites by as much as 24.45%, while waited EVs ($\overline{N}_{W}{}''_{DICT}$) also increased slightly, showing a range between 1.40% and 28.00%. These results indicate that NDS+DICT is an effective strategy for improving operational metrics and user experience across EV charging stations. The strategy demonstrates the system's adaptability to higher demand and suggests a balanced approach to managing both served and queued EVs as penetration rates grow.

Building on the gains achieved with SRS alone, combining the SRS approach with the DICT scheme results in IRS, where both the waiting queue capacity and outlet count are set to $n = N_{\text{Orig\_outlets}} + 1$, yielding substantially greater improvements than using SRS alone. This is reflected in several key performance metrics at each EVCS from 2023 to mid-2026.

As shown in Figures (6.12)-(6.14), applying SRS alone resulted in average reductions in utilization ($\overline{U}_{\text{SRS}}$), waiting times ($\overline{W}_{\text{SRS}}$), and blocked EVs ($\overline{N}_{B}{}^{\text{SRS}}$) as follows: utilization decreased by ranges between 44.25% and 14.93% across different EVCSs, waiting times saw reductions between 54.82% and 25.35%, and blocked EVs decreased by 69.55% to 35.92%. Additionally, Figure (6.14) shows the average increases in the number of served EVs ($\overline{N}_{S}{}^{\text{SRS}}$), which ranged between 55.69% and 88.14%, while the number of waited EVs ($\overline{N}_{W}{}^{\text{SRS}}$) grew by a slight increase to a moderate rise of up to 82.86%.

However, with the IRS approach, these metrics improved even further. For example, utilization ($\overline{U}_{\text{IRS}}$) decreased by a more significant range, from 54.80% to 27.43%, waiting times ($\overline{W}_{\text{IRS}}$) dropped further, from 70.40% to 44.66%, and the number of blocked EVs

($\overline{N}_B^{IRS}$) decreased by as much as 88.59% to 65.27%. The average increases in served EVs ($\overline{N}_S^{IRS}$) were particularly notable, ranging from 63.53% to 111.93%, while the number of EVs that had to wait to recieve service ($\overline{N}_W^{IRS}$) also witnessed increases, with some sites experiencing decreases, but most sites showing an increase.

Overall, these results demonstrate that the IRS approach is an effective strategy for enhancing system efficiency, accommodating higher EV traffic, reducing congestion, and improving service availability at charging stations.

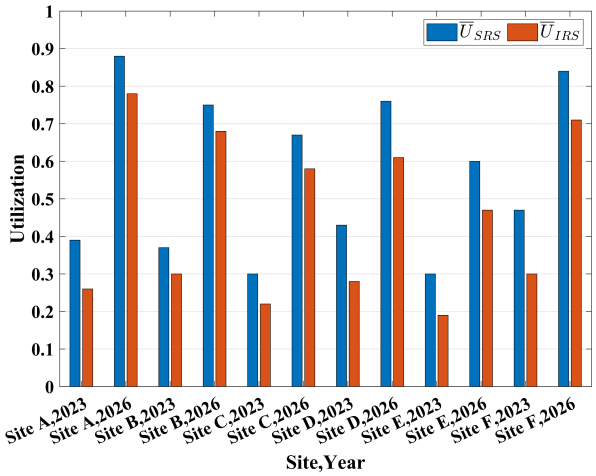

Figure 6.12: Avg. Utilization under SRS, and IRS.

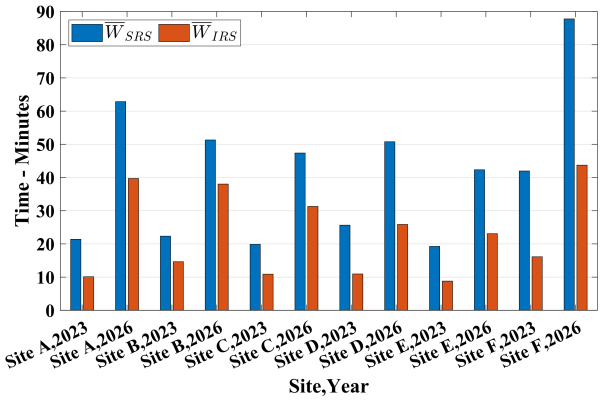

Figure 6.13: Avg. Waiting Time under SRS, and IRS.

6.5.2.2 QoS Under Extended Waiting Queue Length (EWQL)

The analysis also extends to evaluate the efficiency of the applied approaches by considering the impact of increasing the waiting queue capacity at the EVCSs. This evaluation incorporates both actual and predicted charging requests for the period from 2023 to mid-2026.

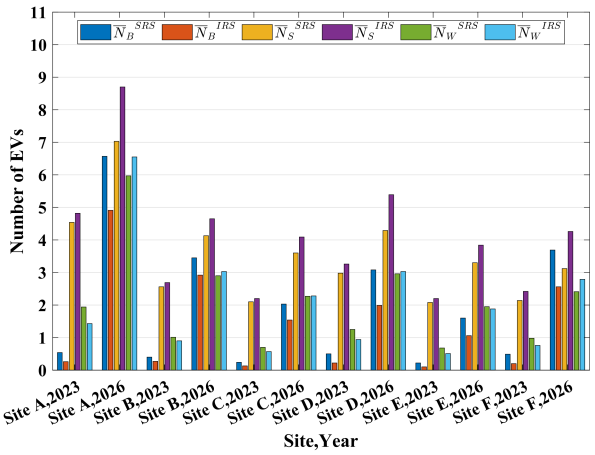

Figure 6.14: Avg. Number of Blocked/Served/Waited EVs under SRS, and IRS.

As EV arrivals continue to rise, driven by operators' expansion and deployment plans in the EVCS vicinities, the projected reductions in utilization, waiting times, and blockage rates are expected to gradually decrease over time. This forward-looking analysis provides a more comprehensive understanding of future demand, aiding in strategic capacity planning to maintain service quality amidst the increasing pressures of EV adoption.

Considering the expanded waiting queue capacity from 2023 to mid-2026, applying the NDS approach with 10% and 20% across the EVCSs (A through F) resulted in significant improvements in system performance, even as charging requests increased. By scaling the waiting queue capacity to five, which accommodates a broader range of performance changes as EV reliance on public charging grows, with room for further expansion as demand increases, each EVCS witnessed varying improvements in QoS.

For instance, under the 10% NDS scenario, the average utilization ($\overline{U}'$) decreased by 0.82% to 7.21%, helping to reduce system strain. Waiting times ($\overline{W}'$) dropped by 2.90% to 11.76%, providing a smoother experience for users, while the number of blocked EVs ($\overline{N}_B{}'$) decreased by 13.42% to 22.05%, improving service availability during peak times. Additionally, the number of served EVs ($\overline{N}_S{}'$) decreased slightly by 0.81% to 5.23%, while the number of EVs that have to wait to receive service ($\overline{N}_W{}'$) reduced by 0.69% to 10.54%.

The impacts were even more pronounced under the 20% NDS setting, where the average utilization ($\overline{U}''$) decreased by 1.44% to as much as 15.97%, and waiting times ($\overline{W}''$) dropped between 6.89% and 24.87%. The number of blocked EVs ($\overline{N}_B{}''$) showed significant reductions, ranging from 28.84% to an impressive 51.01%, highlighting the strategy's effectiveness in managing higher demand with the applied scalability in the waiting queue. Moreover, the average number of served EVs ($\overline{N}_S{}''$) decreased by 1.76% to 11.12%, and the number of waiting EVs ($\overline{N}_W{}''$) reduced by 3.04% to 22.81%. These findings illustrate the reliability of the NDS approach in improving QoS by stabilizing utilization and reducing waiting times, even across EVCSs with varying charging behavior and increased waiting

queue capacities.

Further, to assess the reliability of the SRS approach over the period from 2023 to mid-2026. In 2023, substantial decreases were observed in average utilization, waiting times, and the number of blocked EVs across all EVCSs, reflecting the initial benefits of increased capacity. These improvements indicate a positive impact on QoS, particularly during the early stages of implementation. However, by mid-2026, these metrics are expected to rise again, largely driven by the anticipated increase in EV penetration. The initial reductions, especially in 2023, demonstrate significant improvements in system performance. Still, from mid-2026 onwards, a slight upward trend in utilization, waiting times, and blocked EVs is anticipated, primarily due to the projected increase in EV penetration rates, signaling the ongoing pressure on the infrastructure despite the expanded capacity.

Therefore, tracing the changes in performance metrics for specific EVCSs from 2023 to mid-2026 reveals distinct yet consistent patterns, considering the expanded waiting queue capacity to five EVs under the SRS approach. For instance, EVCS (B) experienced reductions in utilization ($\overline{U}_{\text{SRS}}$), waiting time ($\overline{W}_{\text{SRS}}$), and blocked EVs ($\overline{N}_B{}^{\text{SRS}}$) ranging from 47.27% to 14.54%, 80.34% to 63.89%, and 77.90% to 38.23%, respectively.

Similarly, EVCS (C) exhibited declines in these metrics within the ranges of 54.37%-19.85%, 82.80%-67.66%, and 81.25%-48.80%. Other stations (A through F) demonstrated comparable trends, with utilization, waiting times, and blockage percentages significantly decreasing over this period. In contrast, the number of served EVs ($\overline{N}_S{}^{\text{SRS}}$) steadily increased across all stations. For example, EVCS (B)'s served EV count rose by 37.77%-80.92%, while EVCS (C) saw an increase from 28.43%-74.11%.

By mid-2026, this trend culminated in higher service capacity across the board, driven by elevated EV penetration rates. Consequently, the number of EVs in waiting ($\overline{N}_W{}^{\text{SRS}}$) also increased by mid-2026, climbing by 37.89%, 59.45%, 45.09%, 61.35%, 35.21%, and 77.4% for EVCSs (A through F), respectively. These results underscore the ability of the SRS scheme to effectively accommodate growing EV demand, with notable enhancements in service levels despite the rising EV arrivals.

6.6 Conclusion

This chapter addressed the ad hoc public charging infrastructure expansion strategies currently adopted by operators with particular focus turned towards EV-user-perceived QoS. Inspired by a real-world case study of an urban P-EVCS experiencing continuous performance deterioration over time regardless of new city-wide charging site deployments, a novel scheme, namely, DICT, is proposed herein to encourage EV users to limit charging their EVs' batteries beyond an $\chi = 80\%$ SoC threshold; this being motivated by the steeply

declining battery charging rate beyond χ resulting in incremental energy charges during very large time periods. The study numerically demonstrated that the Erlang-k distribution is a reliable and highly accurate mathematical model for characterizing simulator-derived service time values and the closed-form expression of the DICT scheme. Moreover, the validation of Quality of Service (QoS) metrics derived from simulation against those obtained numerically using the mathematical $M/G/1/K$ queuing model reinforces the robustness of the proposed approach. The validation utilizes the DICT scheme, with Erlang-k selected as the service time distribution. Accordingly, the average Relative Percentage Error (RPE) between simulation and numerical trends of the Blocking Probability metric from 2.85% to 12.57%, confirming the accuracy of the numerical-theoretical approach. Similarly, RPE values ranging from 2.08% to 5.85% for the waiting queue length and 2.48% to 6.45% for the waiting time further validate the reliability of the convolutional closed-form expression. Finally, the EV charging service time under DICT is characterized and fed as input to a custom-built simulator developed for the purpose of assessing the target P-EVCS's performance under DICT and benchmarking it with other schemes.

Chapter 7
A Data-Driven Framework for Improving Public EV Charging Infrastructure Deployment: Quantifying EV Demand Shifting Via Machine Learning

7.1 Problem Statement and Motivation

This work leverages operational data from Québec's foremost EV charging operators to examine the temporal dynamics of the Public-EV Charging Station (P-EVCS) deployments in major and vital cities of the povince. The primary objective is twofold: *i*) characterize how deployment strategies of new Level-3 (L3) charging sites have evolved over time and, *ii*) quantify the resulting effects of these deployments on the EV demands, congestion levels and users' Quality of Experience (QoE) pertaining to a selection of observed target sites as these new L3 fast charging sites come online. Such objectives are set in view of the fact that Québec's main cities exhibit pronounced heterogeneity in both deployment scale and EV adoption. Some cities have undergone rapid network expansion, while others have grown more incrementally. These divergent patterns reflect local factors such as urban form, EV communities, penetration rates and mobility behaviors, which collectively shape station-level outcomes such as the average EV queueing delays and overall user experience (*i.e.*, EV blocking probability, site utilization and occupancy).

To quantify the long-term QoE performance in terms of the above mentioned metrics, a set of P-EVCSs are strategically selected based on capacity characteristics, proximity to high-traffic districts, temporal usage patterns and geographic diversity to establish a controlled baseline for quantifying site level congestion relief in each examined city. These reference sites serve as benchmarks for infrastructure planning, exerting primary influence on empirical observations and network wide load conditions (underloaded, moderately loaded or overloaded). Analysis of resulting network impacts quantifies service performance improvements and the redistribution of EV demands to alleviate congestion during peak/rush

hours.

After estimating the congestion relief attributed to the newly deployed site, the analysis turns to uncovering and exploring the principal drivers of that relief at the examined sites. At the heart of this phase lies the connection between the congestion decrease in EV demand and factors (*e.g.*, the spatial distance to the newly deployed site), alongside the proximity and concentration of nearby high-traffic amenities (*e.g.*, restaurants, cafés, parking facilities, and other social hubs). Examining these resulting correlations helps service providers better understand how public EV charging behavior dynamically shifts in response to the analyzed public charging infrastructure and its surrounding EV communities. Respectively, these contextual variables are fed into a modeling framework designed to simulate and evaluate these deployment scenarios. In particular, the model explores the location of new/recent L3 site deployments to gauge how the related shifts in EV demand affect congestion at the existing network of L3 sites.

Accordingly, the calibrated model estimates congestion relief outcomes across varied spatial configurations. Service providers can then compare projected shifts in EV demand, quantify the impact of new deployments on QoE by combining historical demand data with counterfactual session forecasts, and derive evidence-based recommendations for infrastructure deployment.

Given the pronounced heterogeneity in deployment pace and scale among Québec's cities, a key challenge is to disentangle true effects of new station installations from coincident trends (for instance, rising EV adoption rates or seasonal load variations). Traditional time series forecasting approaches, particularly Deep Neural Networks (DNNs) (*e.g.*, Recurrent Neural Networks (RNNs) and Long Short Term Memory (LSTM) models) excel at capturing complex non-linear dependencies in high dimensional datasets and often outperform simpler benchmarks when properly tuned. Yet, their largely correlational nature, coupled with intensive data pre-processing and computational resource demands, can limit useful insight into the causal effects of the deployment strategies being examined.

Conversely, classical causal inference techniques, such as Instrumental Variables (IVs), Regression Discontinuity (RD), and Difference-in-Differences (DiD) rely on strong parametric assumptions and may falter amid intricate co-variate interactions and high dimensionality. In the context of EV charging, operators need robust estimates of how a newly commissioned fast charging site will contribute to attracting demands and, hence, alleviate congestion at adjacent hubs, and thereby, elevate EV drivers' QoE.

To meet these needs, this work proposes a data-driven framework that integrates the predictive capabilities of modern machine learning algorithms with explicit causal estimation. At the core of this framework is a novel technique designed to isolate the incremental effects of real world new/recent fast-chargers' deployments on EV charging request volumes at

P-EVCSs, while systematically controlling for confounders such as seasonal demand fluctuations, outlet availability, charging rates, and estimated EV growth on the roads of the province.

By simulating unobserved and validated "what if" scenarios, the developed approaches herein quantify how variations in P-EVCS locations, charging rates, charging outlet count, and proximity to different amenities would alter utilization trends and the number of charging requests; thus, providing operators and service providers with prescriptive insights into optimal P-EVCS deployments/resizing rather than mere descriptive associative counterparts (*e.g.*, more chargers $\Rightarrow$ shorter queues).

Building upon this inference engine, the study herein presents an end-to-end approach that maps estimated impacts into prescriptive plans. Moreover, this work adopts existing queueing models (*i.e.*, in [119]) to evaluate the resulting QoE improvements at select P-EVCSs and, accordingly, compare/rank potential deployment strategies. Together, these components empower service providers to move from retrospective analysis to evidence-based, forward-looking capacity planning to optimize infrastructure investments and policy decisions for Québec's rapidly evolving public EV ecosystem.

Beyond spatial impact analysis, a further research direction in this work is to monitor how EV demand at each new deployment evolves over time and to evaluate its effect on the site-level QoE. Such an assessment would reveal whether a new station truly eases pressure on existing L3 sites or, over time, becomes, by itself, a congestion hotspot. Incorporating this temporal dimension would yield a more comprehensive, forward-looking perspective on public EV charging network performance and planning effectiveness.

7.2 Novel Contributions

This chapter's main contributions are summarized as follows:

1) Proposing a novel causal inference approach that isolates the true effect of a new fast charging station's deployment on EV charging demand at neighboring stations, which goes beyond simple existing correlational analyses.

2) Ensuring that the estimated deployment effects account for critical confounders (*e.g.*, spatial proximity, dynamic outlet capacities (ports and power ratings) and local amenity access); hence, leading to reliable/credible impact quantification and measurements, which are obtained through exhaustive simulations of various deployment configurations/scenarios.

3) Tracking the temporal evolution of EV demand at new deployments to assess sustained site-level QoE impacts and detect emerging congestion hotspots; hence, providing guidelines for optimal infrastructure placement.

4) Feeding the herein-generated EV demand forecasts into accurate queueing models to

evaluate end-user QoE metrics with the objective of facilitating the selection of deployment parameters within operational and budgetary constraints; thus, empowering operators to transition from descriptive diagnostics to prescriptive investment grade decision-making and, so, cope with the rapidly evolving EV ecosystem.

7.3 Dataset Overview and Preprocessing

The dataset comprises approximately 9 million public EV charging sessions captured at $5,051$ individual charging sites across $10,285$ EV charging stations over a six year period (January 2018–June 2024). Both slow and fast charging events at varying power levels are included. Each session record provides energy delivered, start and end timestamps, site identifiers, and station address details (including postal codes). However, the dataset does not record EV arrival times or waiting durations, both of which are essential for computing QoE. This omission poses a significant challenge for QoE assessment, which is addressed in later sections. To ensure data integrity, sessions shorter than three minutes or longer than two hours, records with zero energy transfer, and entries lacking payment information are excluded. The remaining valid sessions are then sorted in ascending chronological order for each EV charging site. Sites sharing a postal code are grouped under a single site identifier to maintain consistent temporal sequencing of charging activity.

7.4 Methodology

This study develops a structured Machine Learning (ML) framework to quantify the influence of newly deployed L3 charging sites on EV demands arriving at existing public EV charging infrastructure. The adopted approach comprises three interlinked phases, namely: *i*) Data Assembly and Cleaning, *ii*) Feature Engineering, and, *iii*) Modeling and Evaluation.

7.4.1 Data Assembly and Cleaning

In this study, a comprehensive panel dataset is assembled comprising the weekly observations from all L3 charging sites in the target city, spanning 2018 through 2024. For each charging site, operational metrics, such as session counts, geographic coordinates, and outlet capacity by power rating (kW) are recorded and merged with external covariates such as Québec's EV penetration rate (sourced from the latest Statistics Canada releases [120]). Malformed entries are corrected, duplicates removed, and missing values addressed through imputation or exclusion to generate a clean, consistent dataset ready for analysis and modeling.

7.4.2 Feature Engineering

A compact yet rich set of temporal features is engineered to empower the developed framework in this study. For instance, features such as the auto-regressive lags 1–3 capture the inherent autocorrelation within the weekly session series, and a three-week rolling mean smooths out short-term spikes while emphasizing longer-term trends. The seasonality is represented continuously by applying sine and cosine transforms to the monthly index, thereby encoding the annual cycles without artificial discontinuities. Also, a COVID-19 dummy variable is activated from March 2020 through June 2021 to isolate pandemic-related demand shifts, and a station-specific time index models each site's long-term trend. Together, these temporal features furnish the models with direct access to the dependencies, autocorrelation, trend, seasonality, and exogenous shocks, that drive public EV charging demand.

In addition, spatial predictors are applied uniformly across all phases of the framework. The Pairwise Haversine distances between stations are calculated. Accordingly, local network effects are modeled by computing, for each station, an inverse-distance weighted average of neighboring stations' weekly session counts. To capture richer dynamics, the utilization metric is computed from the site's empirical charging records, this metric primarily measures the proportion of the site's charging capacity that is actually used over time, thereby, reflecting usage intensity relative to maximum throughput. As a result, this metric enables the framework to distinguish a small station operating near capacity from a larger station with idle ports, thereby enhancing both fairness and interpretability of predictions across heterogeneous public EV charging sites.

7.4.3 Estimating Counterfactual Sessions via Gradient Boosting

Estimating the counterfactual charging session volumes at incumbent stations in the absence of the new L3 deployments requires pooling all pre-deployment weekly observations and fitting a gradient boosted tree regressor within a unified scikit-learn pipeline. The predictor variables, including weekly session counts, station capacity metrics, spatial proximity indices, and contextual covariates are standardized using Standard Scaler to ensure comparability across the selected features. The temporal cross-validation is conducted via a 5-fold Time Series Split, with each fold's training set comprising the earliest 4 segments and its validation set comprising the subsequent segment. The prediction performance is assessed using the Mean Absolute Error (MAE) and the Root Mean Square Error (RMSE), thus establishing robust baseline forecasts for comparison against the post deployment period. For clarity, each cross-validation fold is evaluated on a pooled test set comprising all examined sites. Accordingly, the per-fold metric is the error averaged over all test rows in that fold. Pooling increases the effective test-set size per fold, yielding more stable, interpretable er-

ror estimates and better reflecting population-level public EV charging behavior associated with the new deployment. The pooled fold-level evaluation explicitly accounts for cross-site interactions and reduces the influence of a small number of anomalous sites on the overall results.

The HistGradient Boosting Regressor algorithm is then applied to each training subset, generating out-of-sample forecasts for the held-out periods. The trained gradient boosted regressor is then executed for generating baseline counterfactual forecasts of the weekly session counts at incumbent charging sites, these counterfactuals represent the hypothetical usage had the new deployed sites not commenced operations. The comparison of these counterfactual estimates with the actual post deployment session data yields the number of "averted" or "spillover" sessions caused by each new L3 site. The spillover rates for each site-deployment pair are then derived and learned by the regression model. This enables precise quantification and ongoing monitoring of EV demand redistribution and resulting congestion relief outcomes across the public EV charging network after each fast charging site installation, while explicitly incorporating the empirical measures of EV users adaptation to the enhanced infrastructure.

Importantly, the hyperparameter optimization is carried out with GridSearchCV using a GroupKFold cross-validation scheme. The tuning grid primarily covers the learning rate, the number of boosting iterations (n_estimators), and maximum tree depth (max_depth). The negative MSE serves as the scoring metric, thereby converting the minimization of true MSE into a maximization objective. Consequently, the parameter combination yielding the lowest MSE across the validation folds is selected to train the applied regressor.

7.4.4 Quantifying Site-Level Congestion Relief

To quantify congestion relief at a specified L3 site after a new site deployment during a time window t, it involves comparing the actual session count with the predicted sessions of the model in a hypothetical scenario that omits any new site deployment; this scenario referred to, in the sequel, as "Without Deployment". The following variables are defined:

$$\begin{aligned} S_{o,i} &\equiv \text{Total sessions offloaded from site } i, \\ S_{t,i}^{(a)} &\equiv \text{Actual total sessions at site } i, \\ \bar{S}_{t,i}^{(f)} &\equiv \text{Forecasted total sessions at site } i, \end{aligned} \tag{7.1}$$

Thus,

$$S_{o,i} = \bar{S}_{t,i}^{(f)} - S_{t,i}^{(a)}.$$

Therefore, at the newly deployed site, say site x, the total actual sessions $S_{t,x}^{(a)}$ during the post-

deployment time window t, accounting for k pre–existing L3 sites, are given by:

$$S_{t,x}^{(a)} = \sum_{k} \big(\bar{S}_{t,k}^{(f)} - S_{t,k}^{(a)}\big).$$

If

$$S_{t,x}^{(a)} > \sum_{k} \big(\bar{S}_{t,k}^{(f)} - S_{t,k}^{(a)}\big),$$

The "mis-traced" public EV demand, D_x, is computed by:

$$D_x = S_{t,x}^{(a)} - \sum_{k} \big(\bar{S}_{t,k}^{(f)} - S_{t,k}^{(a)}\big),$$

And the computed error percentage $E_{t,x}$ is given by:

$$E_{t,x} = \frac{S_{t,x}^{(a)} - \sum_k (\bar{S}_{t,k}^{(f)} - S_{t,k}^{(a)})}{S_{t,x}^{(a)}} \times 100\%.$$

During each period t, the model calibrates its parameters to minimize the error $E_{t,x}$ as $\sum_k S_{o,k}$ evolves. Although $E_{t,x}$ may initially rise, it converges to low values over time as the model adapts to the redistributed EV demand.

7.4.5 EV Public Charging Discrete-Event Simulator

A custom-built, python-based discrete event simulator is developed to characterize the public EV charging service at a given charging site and to evaluate the resulting QoE. The simulator implements an M/G/C/K queuing model and incorporates key performance metrics observed during the charging service. The simulator's input parameters are derived directly from real-world charging records for the targeted site. These parameters include the EV arrival process, the fitted general service time distribution G, the number of active charging outlets C, and the total charging site capacity (*i.e.*, finite waiting spaces) K. EV arrivals are modeled as a Poisson process with rate:

$$\lambda = \frac{N_{\text{arr}}}{T_{\text{win}}} \quad [\text{EV/s}],$$

where N_{arr} denotes the number of EV arrivals within the specified time window T_{win} (*e.g.*, $14:00$–$18:00$). The service time distribution is modeled using an Erlang-k distribution, fitted and validated against empirical charging session data from the examined charging site, ensuring that simulated charging durations accurately reflect real-world conditions. To achieve statistically accurate results, each simulation round generates 10^4 EV arrivals based on the determined arrival rates. The simulator outputs key performance metrics, including the waiting time, the number of queueing or delayed EVs according to [121], the utilization (*i.e.*, the fraction of time the site is busy), and the numbers of blocked EVs (*i.e.*, those EVs that were denied service) and served EVs during the simulated charging process.

Table 7.1: Level-3 Sites Capacities (City A & B)

SiteID	Capacity	Total (kW)
City A		
A1	(1×50 kW, 2×100 kW, 1×120 kW)	370
A2	(1×50 kW, 1×100 kW, 2×180 kW)	510
A3	(2×50 kW, 2×100 kW)	300
A4	(1×50 kW)	50
A5	(2×50 kW)	100
A6	(1×50 kW, 1×100 kW)	150
A7	(2×50 kW)	100
A8	(2×50 kW)	100
City B		
B1	(2×100 kW, 2×180 kW)	560
B2	(1×180 kW)	180

7.5 Analysis and Forecast Results Case Studies

Driven by empirical records from Québec's leading EV charging station providers, this section provides a detailed, time sequenced evaluation of recent fast charging P-EVCS deployments in two major Québec cities. Table 7.1 characterizes the recently installed L3 P-EVCSs in City A and City B alongside the existing L3 sites analyzed herein.

7.5.1 Averted vs. New Deployment Total Sessions

This section examines several recently deployed L3 charging sites selected for their high capacities and anticipated impact on the public EV charging network relative to earlier installations in the province's two principal cities. Figure 7.1 displays both the actual versus averted session counts and the corresponding $E_{t,x}$ for the recent deployments examined of both cities. In City A, two new L3 sites were deployed sequentially: Site A1 on October 10, 2022, and Site A2 on June 19, 2023. Figure 7.1(a) shows Site A1's observed sessions $S^{(a)}_{t,A1}$ against the offloaded session sum $S_{o,k}$ over 36 weekly intervals (October 16, 2022–June 18, 2023). The resulted forecasted error $E_{t,A1}$ falls from 17% to 6% by week 2, demonstrating rapid model recalibration. During December 2022–February 2023, the error oscillations between 3% and 9% reflects the seasonal and unexpected travel patterns and ice-related public EV charging behavior, yet remained within a ±8% bound. By spring 2023, $E_{t,A1}$ stabilized at 4%–6%, indicating that the cumulative offloaded-session sum $\sum_k S_{o,k}$ to closely align

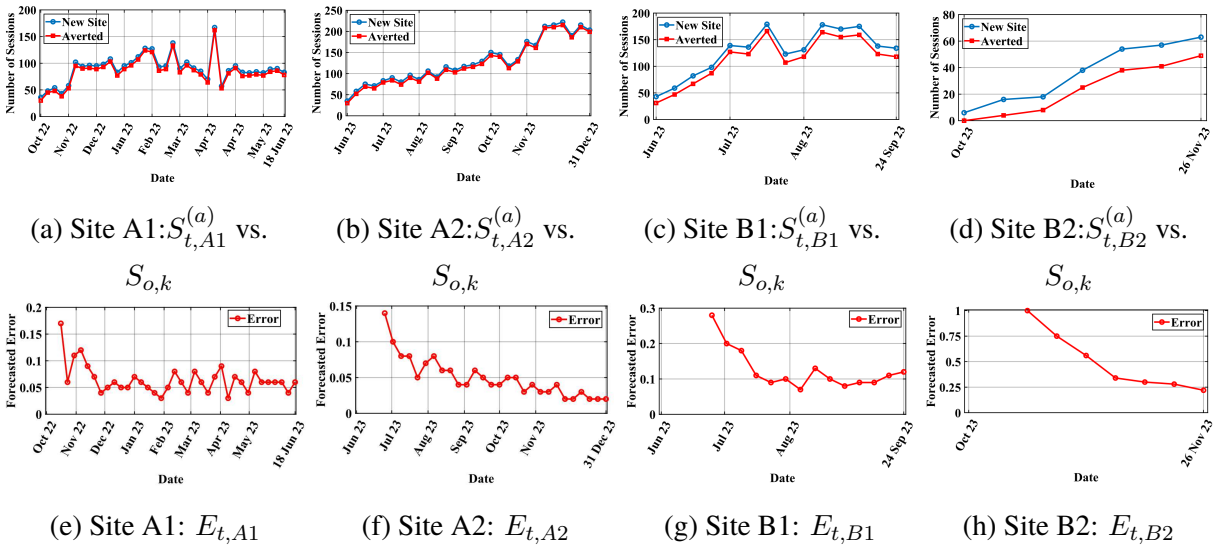

(a) Site A1:$S^{(a)}_{t,A1}$ vs. $S_{o,k}$ (b) Site A2:$S^{(a)}_{t,A2}$ vs. $S_{o,k}$ (c) Site B1:$S^{(a)}_{t,B1}$ vs. $S_{o,k}$ (d) Site B2:$S^{(a)}_{t,B2}$ vs. $S_{o,k}$

(e) Site A1: $E_{t,A1}$ (f) Site A2: $E_{t,A2}$ (g) Site B1: $E_{t,B1}$ (h) Site B2: $E_{t,B2}$

Figure 7.1: Actual vs. Averted EV Demand and Error Percentage for Deployed Sites in City A:(A1, A2), and City B:(B1, B2). Top row (a)–(d): $S^{(a)}_{t,x}$ vs. $S_{o,k}$; Bottom row (e)–(h): Corresponding $E_{t,x}$.

with the observed sessions $S^{(a)}_{t,A1}$.

In Figure 7.1(b), Site A2's actual versus averted sessions illustrate how the model immediately improves upon Site A1's baseline: the first week forecasted error in Figure 7.1(f), is 14%, already below Site A1's initial 17%. Throughout the summer, $E_{t,A2}$ remains between 6% and 8%, effectively capturing tourism-driven peaks and high-activity fluctuations. By early winter it falls under 4% and reaches a low of 2% just before the frozen season. This rapid convergence underscores the benefit of sequential deployments in refining parameter estimates and enhancing predictive accuracy by the model over time.

In the dense urban core of City B, Figure 7.1 (c) and (g) present Site B1: an initial error of 28% reduced to 11% by week 4 after incorporating offloaded demand, with a minor summer rebound to 13% and eventual stabilization at 9%–11%. Figure 7.1 (d) and (h) portray Site B2, introduced in October 2023: a first week error of 100%, halving to 56% by week 3 and falling to 22% by week 7, demonstrating the model's rapid adjustment to exceptional events.

In both cities, large initial errors led to steady state bands of 2%–8% within four to six weeks. The suburban context of City A yielded smaller calibration gaps and faster stabilization, while complex demand dynamics of City B generated larger initial discrepancies and event linked oscillations.

These results validate the ability of the applied framework to track public EV demand shifts and converge on reliable forecasts as the interval between deployments expands in different cities serving variant EV communities.

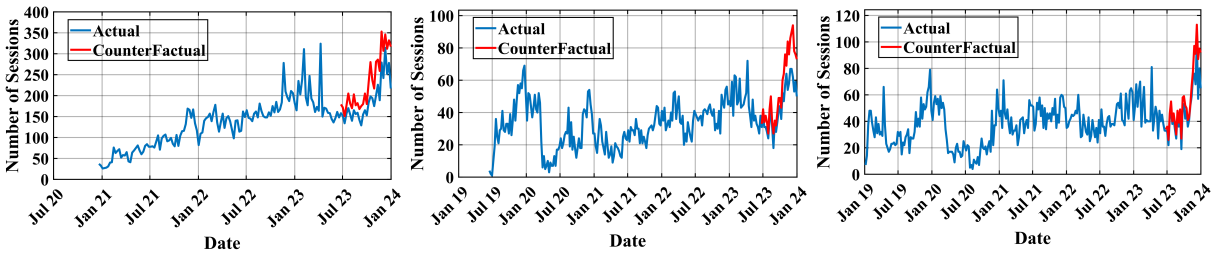

(a) Site A3 (b) Site A4 (c) Site A5

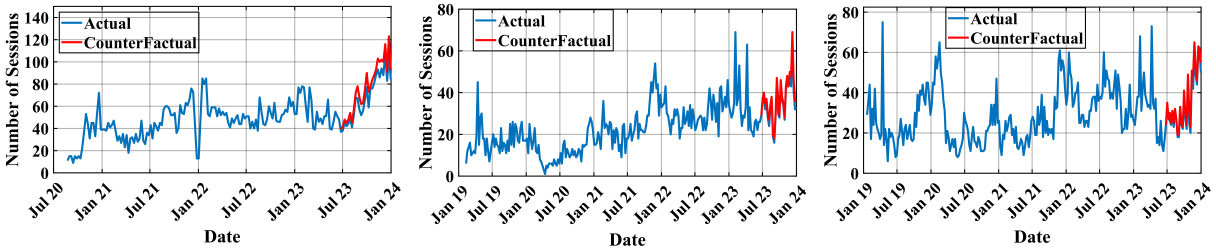

(d) Site A6 (e) Site A7 (f) Site A8

Figure 7.2: City A; Actual vs. counterfactual comparison for Sites A3–A8. Top row (a)–(c): Sites A3–A5 (within 3 km of the new Site A2, showing the strongest impact); Bottom row (d)–(f): Sites A6–A8 (beyond 3 km, where effects attenuate rapidly).

7.5.2 Estimating Counterfactual Sessions

Over the analyzed period June 2023 - December 2023 (*i.e.*, prior to the new deployment detected in Jan. 2024), in City A, the deployment of a new L3 Site A2 triggered a clear, distance and capacity dependent redistribution of public EV charging demand among neighboring L3 Sites. From the week of June 25, 2023, through December 31, 2023, the actual weekly session counts at each incumbent L3 site are compared to the counterfactual forecasts generated by the gradient boosted model discussed in section 7.4.3. Figure 7.2 presents these comparisons for sites A3–A8.

At Site A3 (Fig. 7.2(a)), situated just 1.4 kilometers (km) from Site A2 and providing 300 kilowatts (kW) charging rate total capacity, the forecasted sessions count exceeded the actual sessions by an average of 43.8 per week (approximately 14.6% of capacity). This pronounced reduction confirms that a nearby and high capacity new deployed site (i.e., Site A2) diverted a substantial portion of historic EV demand, thereby alleviating congestion at Site A3. An even larger proportional effect appeared at Site A4 (Fig. 7.2(b)), a 50 kW Site located 1.6 km from Site A2, where mean weekly averted sessions reached 11.5 (nearly 23% of capacity).

Beyond a radius of roughly 3 km from the new Site A2, the EV demand shifts attenuated rapidly. As shown in (Fig. 7.2(c)), Site A5 (100 kW at 3.2 km) experienced a moderate average decline of 7.9 sessions per week (7.9% of capacity), while more distant stations,

such Site A6 (Fig. 7.2(d)) (350 kW at 6.0 km), Site A7 (Fig. 7.2(e)) (100 kW at 8.4 km), and Site A8 (Fig. 7.2(f)) (100 kW at 9.1 km) exhibited minimal redistribution, with averted sessions of 7.8, 2.3, and 2.1 respectively (each under 3% of capacity). The spatial layout and capacities of the sites discussed above are shown in Fig. 7.3.

Figure 7.3: City A Map: Capacity and Spatial Proximity of Sites A3–A8 to A2.

These results demonstrate that high power sites' installations indeed relieve local congestion within a 3 km radius in the examined City A, with sharply diminishing benefits beyond that threshold. Moreover, the incumbent capacity modulates this spatial effect: smaller stations relinquish a larger share of their demand at comparable distances, whereas larger depots diffuse redistributed volume more broadly. Combined, the capacity normalized and absolute session count metrics indeed provide empirically grounded, spatially explicit guidance for optimizing the siting of future public EV fast charging infrastructure.

7.5.3 Simulation and QoE Evaluation: Discussion

The site-level analysis discussed in this section is mainly generated using the discrete-event simulator described in Section 7.4.5. For each studied charging site, two scenarios (Actual vs. Counterfactual (CF)) are executed and key QoE metrics are computed.

CF vs. Actual differences examined below isolate the marginal congestion effect of the high-power deployment at Site A2 discussed in Sections 7.5.1 and 7.5.2 respectively. Statistical summaries are reported in the following analysis where relevant to make the magnitude and variability of effects explicit.

Across the June to December 2023 period, the CF forecasts indicate systematically higher EV arrivals, utilization, and waiting time compared with observed (actual) values at the studied incumbents. The (CF vs. Actual) divergence is most pronounced during the late autumn peak (October to December), indicating that the presence of the high-power

deployment (*i.e.*, Site A2) delivered its largest marginal congestion relief gains when EV demand is highest. Conveniently, used QoE metrics' symbols are listed in Table 7.2.

Table 7.2: QoE metric symbols

Symbol	Definition
N_{AC}^{A}	Number of EV arrivals for actual sessions.
W_{AC}	Waiting time for actual sessions.
U_{AC}	Utilization for actual sessions.
N_{AC}^{W}	Number of waiting EVs for actual sessions.
N_{AC}^{S}	Number of served EVs for actual sessions.
N_{AC}^{B}	Number of blocked EVs for actual sessions.
N_{CF}^{A}	Number of EV arrivals for counterfactual sessions.
W_{CF}	Waiting time for counterfactual sessions.
U_{CF}	Utilization for counterfactual sessions.
N_{CF}^{W}	Number of waiting EVs for counterfactual sessions.
N_{CF}^{S}	Number of served EVs for counterfactual sessions.
N_{CF}^{B}	Number of blocked EVs for counterfactual sessions.

Site A3 (300 kW) shows the largest and most persistent CF vs. Actual gap among incumbents. Arrival volumes increase substantially under CF: weekly average arrivals rise from $\overline{N_{\text{AC}}^{\text{A}}} = 8.74$ EV/week to $\overline{N_{\text{CF}}^{\text{A}}} = 10.84$ EV/week, an absolute increase of $\Delta\overline{N^A} = +2.09$ EV/week (+23.9%). Served EVs increase in lockstep ($\Delta\overline{N^S} = \overline{N_{\text{CF}}^{\text{S}}} - \overline{N_{\text{AC}}^{\text{S}}} \approx +2.04$ EV/week, $\approx +23\%$), but these higher service counts accompany materially degraded QoE: mean queued vehicles rise from $\overline{N_{\text{AC}}^{\text{W}}} = 0.63$ to $\overline{N_{\text{CF}}^{\text{W}}} = 1.35$, blocked events become more frequent during peak weeks. These aggregate counts align with the distributional shifts in waiting time and utilization: W_{AC} at A3: minimum of 0.1138 minutes; median of 0.1745 minutes; mean of 0.4489 minutes; maximum of 1.4862 minutes. W_{CF} shifts markedly (minimum of 0.1311; median of 0.3628; mean of 0.8648; maximum of 3.0969), generating an approximate mean increase of 92.6% under CF (as shown in Fig. 7.4(a)). U_{AC} at A3: minimum of 0.00983; median of 0.02033; mean of 0.02565; maximum of 0.12945 (mean $\approx 2.57\%$). Under CF scenario, U_{CF} becomes minimum of 0.01976; median of 0.04134; mean of 0.09082; maximum of 0.26038 (mean $\approx 9.08\%$), a large relative rise (as shown in Fig. 7.5(a)). These shifts indicate a pronounced escalation in queuing and substantially higher utilization at A3 in the absence of Site A2, with the largest absolute differences con-

centrated between mid-November and December 2023.

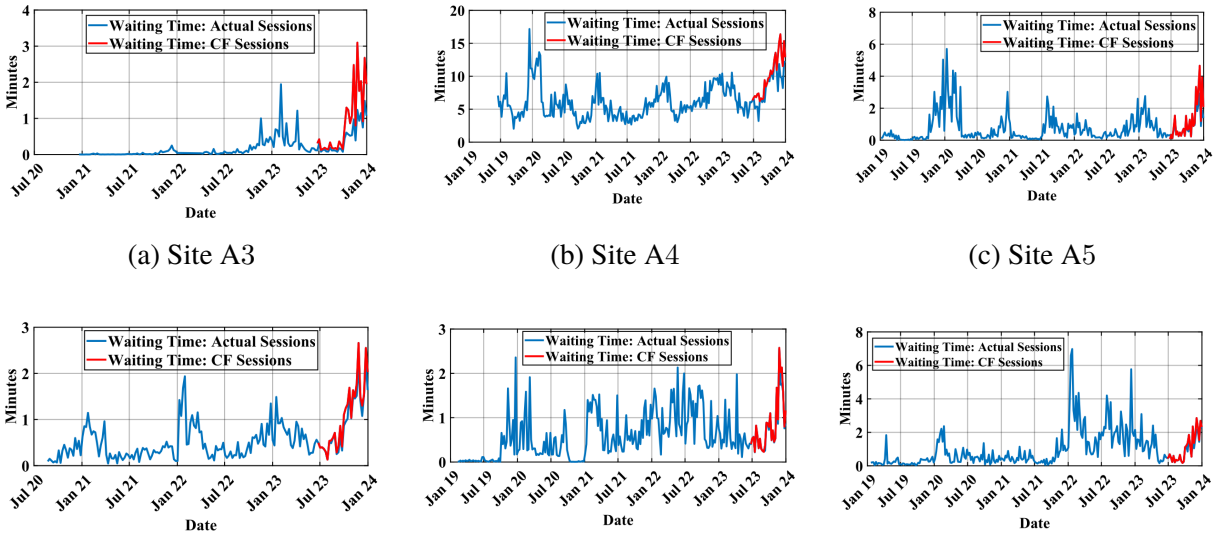

(a) Site A3 (b) Site A4 (c) Site A5

(d) Site A6 (e) Site A7 (f) Site A8

Figure 7.4: City A; Actual vs. counterfactual comparison of **waiting time** (W) for Sites A3–A8 (time window 14 : 00–18 : 00). Top row (a)–(c): Sites A3–A5 (within 3 km of the new Site A2, showing the strongest impact); Bottom row (d)–(f): Sites A6–A8 (beyond 3 km, where effects attenuate).

Site A4 (the smallest incumbent) is the most sensitive in proportional terms to redistributed EV demand. Weekly mean arrivals increase from $\overline{N^{\mathrm{A}}_{\mathrm{AC}}} = 2.24$ EV/week to $\overline{N^{\mathrm{A}}_{\mathrm{CF}}} = 2.81$ EV/week, an absolute change of $\Delta\overline{N^{A}} = +0.57$ EV/week (+25.3%). Because capacity is constrained, these modest arrival increases translate into severe blocking and queuing: blocked EVs nearly double ($\overline{N^{\mathrm{B}}_{\mathrm{CF}}} \gg \overline{N^{\mathrm{B}}_{\mathrm{AC}}}$, +93.7%), and queued EVs rise from $\overline{N^{\mathrm{W}}_{\mathrm{AC}}} = 0.66$ to $\overline{N^{\mathrm{W}}_{\mathrm{CF}}} = 0.92$ (+40.1%). These count level effects are mirrored in the waiting time and utilization distributions. W_{AC} at A4: minimum of 3.209 minutes; median of 9.235 minutes; mean of 8.521 minutes; maximum of 13.554 minutes. W_{CF} increases throughout the distribution of EV demand (minimum of 6.220; median of 9.695; mean of 10.025; maximum of 16.379), yielding a mean increase $\approx 17.7\%$ (as shown in Fig. 7.4(b)). U_{AC} at A4: minimum of 0.1449; median of 0.3077; mean of 0.3570; maximum of 0.5350 (mean $\approx 35.70\%$) rises under CF to minimum of 0.3013; median of 0.3866; mean of 0.4153; maximum of 0.6352 (mean $\approx 41.53\%$), an approximate mean uplift of 16.3% (as shown in Fig. 7.5(b)). Because A4's capacity is limited, modest arrival increases generate pronounced queuing and blocked events during the late season period; this confirms that small, capacity constrained incumbents obtain the largest proportional QoE gains when a nearby high-power node intercepts diverted demand.

Site A5 experiences moderate EV redistribution concentrated in late autumn. Weekly average arrivals increase from $\overline{N^{\mathrm{A}}_{\mathrm{AC}}} = 2.84$ EV/week to $\overline{N^{\mathrm{A}}_{\mathrm{CF}}} = 3.18$ EV/week, a rise of $\Delta\overline{N^{A}} = \overline{N^{\mathrm{A}}_{\mathrm{CF}}} - \overline{N^{\mathrm{A}}_{\mathrm{AC}}} = +0.34$ EV/week (+12.1%). Queueing and blocking grow ac-

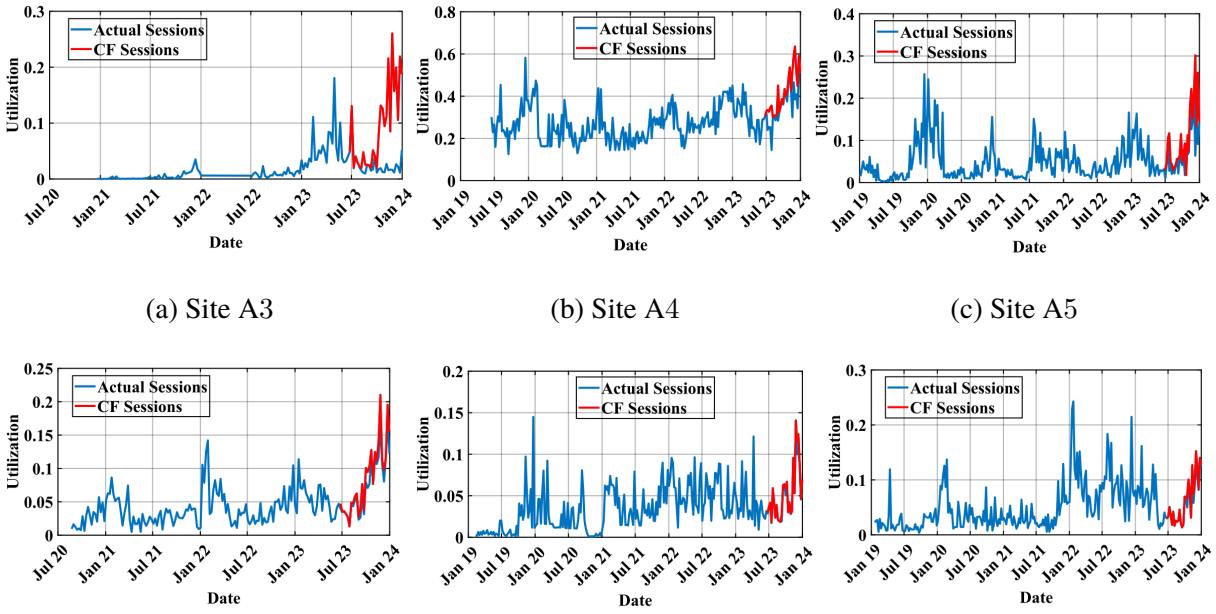

(a) Site A3 (b) Site A4 (c) Site A5

(d) Site A6 (e) Site A7 (f) Site A8

Figure 7.5: City A; Actual vs. counterfactual comparison of **utilization** for Sites A3–A8 (time window $14:00$–$18:00$). Top row (a)–(c): Sites A3–A5 (within 3 km of the new Site A2, showing the strongest impact); Bottom row (d)–(f): Sites A6–A8 (beyond 3 km, where effects attenuate rapidly).

cordingly: queued EVs increase from $\overline{N^{\mathrm{W}}_{\mathrm{AC}}} = 0.30$ to $\overline{N^{\mathrm{W}}_{\mathrm{CF}}} = 0.48$ and blocked EVs from $\overline{N^{\mathrm{B}}_{\mathrm{AC}}} = 0.018$ to $\overline{N^{\mathrm{B}}_{\mathrm{CF}}} = 0.050$, while served EVs increase from $\overline{N^{\mathrm{S}}_{\mathrm{AC}}} = 2.82$ to $\overline{N^{\mathrm{S}}_{\mathrm{CF}}} = 3.13$ on average. These count-level changes are consistent with the modest shifts in waiting and utilization: W_{AC} at A5: minimum of 0.1127 minutes; median of 0.5279 minutes; mean of 0.7962 minutes; maximum of 2.7386 minutes. W_{CF}: minimum of 0.0687; median of 0.5276; mean of 0.8542; maximum of 4.6567, resulting the waiting time increases of about 7.3% under CF (as shown in Fig. 7.4(c)). U_{AC} at A5: minimum of 0.01037; median of 0.04160; mean of 0.04847; maximum of 0.20236 (mean $\approx 4.85\%$) increases in CF to minimum of 0.01796; median of 0.04885; mean of 0.05348; maximum of 0.30144 (mean $\approx 5.35\%$), an approximate mean uplift of 10.4% (as shown in Fig. 7.5(c)). Situated near the attenuation threshold (3 km from A2) and possessing intermediate capacity, A5 receives partial diverted EV demand: measurable QoE degradation appears in peak period but severe congestion is not observed on average.

Site A6 (a larger incumbent) shows modest absolute and proportional changes.

Weekly arrivals shift from $\overline{N^{\mathrm{A}}_{\mathrm{AC}}} = 3.18$ EV/week to $\overline{N^{\mathrm{A}}_{\mathrm{CF}}} = 3.41$ EV/week, an increase of $\Delta\overline{N^{A}} = \overline{N^{\mathrm{A}}_{\mathrm{CF}}} - \overline{N^{\mathrm{A}}_{\mathrm{AC}}} = +0.23$ EV/week ($+7.3\%$). Queued EVs increase from $\overline{N^{\mathrm{W}}_{\mathrm{AC}}} = 0.33$ to $\overline{N^{\mathrm{W}}_{\mathrm{CF}}} = 0.42$ ($+26.3\%$) and blocked EVs from $\overline{N^{\mathrm{B}}_{\mathrm{AC}}} = 0.017$ to $\overline{N^{\mathrm{B}}_{\mathrm{CF}}} = 0.027$ ($+55.1\%$). Overall, these changes indicate only modest demand redistribution impacts at A6 in both absolute and proportional terms. Although absolute blocking counts remain small. These count changes are reflected in narrow shifts in waiting time and utilization: W_{AC} at A6: min-

imum of 0.1356 minutes; median of 0.5953 minutes; mean of 0.9906 minutes; maximum of 2.2377 minutes. Under CF, W_{CF} increases slightly (CF mean ≈ 1.0177 minutes; $\approx +2.7\%$ relative to Actual mean), as shown in Fig. 7.4(d). U_{AC} at A6: minimum of 0.01312; median of 0.04331; mean of 0.06184; maximum of 0.17102 (mean $\approx 6.18\%$) increases in CF to minimum of 0.01323; median of 0.04768; mean of 0.07091; maximum of 0.21030 (mean $\approx 7.09\%$), an approximate mean uplift of 14.7% (as shown in Fig. 7.5(d)). The larger capacity at A6 cushions the site: incremental arrivals are absorbed with smaller QoE impacts relative to smaller incumbents.

Sites A7 and A8 (the more distant incumbents) exhibit marginal CF vs. Actual differences and rapid attenuation of redistributed EV demand beyond 3 km. Site A7 experiences only marginal redistribution effects. Weekly mean arrivals change from $\overline{N^{\text{A}}_{\text{AC}}} = 2.06$ EV/week to $\overline{N^{\text{A}}_{\text{CF}}} = 2.10$ EV/week ($\Delta\overline{N^{A}} = +0.04$, $+1.7\%$). Queued EVs increase from $\overline{N^{\text{W}}_{\text{AC}}} = 0.17$ to $\overline{N^{\text{W}}_{\text{CF}}} = 0.19$ ($+9.3\%$), and blocked EVs from $\overline{N^{\text{B}}_{\text{AC}}} = 0.009$ to $\overline{N^{\text{B}}_{\text{CF}}} = 0.011$ ($+15.4\%$).

Broadly, these small absolute changes correspond to minimal QoE degradation at A7. Waiting time and utilization are nearly unchanged in practical terms: W_{AC}: min = 0.2204 minutes; median = 0.4406 minutes; mean = 0.7962 minutes; max = 2.5454 minutes. W_{CF} ≈ 0.8462 minutes ($\approx +6.3\%$ mean increase), as shown in Fig. 7.4(e). A7's U_{AC} mean $\approx$ 0.0411 (min = 0.01706; median = 0.03146; max = 0.14041) increases under CF to mean $\approx$ 0.0439 ($\approx +6.8\%$ relative change) (as shown in Fig. 7.5(e)). Consequently, the differences at A7 are confined to isolated weeks and are of limited operational significance. Site A8 experiences only minor redistribution effects. Weekly mean arrivals increase from $\overline{N^{\text{A}}_{\text{AC}}} =$ 2.10 EV/week to $\overline{N^{\text{A}}_{\text{CF}}} = 2.16$ EV/week ($\Delta\overline{N^{A}} = +0.06$, $+3.0\%$). Queued EVs increase from $\overline{N^{\text{W}}_{\text{AC}}} = 0.176$ to $\overline{N^{\text{W}}_{\text{CF}}} = 0.210$ ($+0.034$, $+19.3\%$), and blocked EVs from $\overline{N^{\text{B}}_{\text{AC}}} =$ 0.008 to $\overline{N^{\text{B}}_{\text{CF}}} = 0.013$ ($+0.005$, i.e., still rare). Overall, these changes represent absolute increases in arrivals and queueing at A8. Correspondingly, W_{AC}: minimum of 0.17596 minutes; median of 1.0552 minutes; mean of 0.9541 minutes; maximum of 2.5163 minutes, W_{CF} mean ≈ 1.0754 minutes ($\approx +12.7\%$ mean increase), as shown in Fig. 7.4(f). A8's U_{AC} mean ≈ 0.0562 (minimum of 0.01361; median of 0.02568; maximum of 0.12927) increases under CF to mean ≈ 0.0627 ($\approx +11.5\%$ relative change), as shown in Fig. 7.5(f). Blocked events at these sites remain rare and served EV counts are largely unchanged on average.

Taken together, CF forecasts systematically estimate higher congestion state than the observed state; however, operational significance depends strongly on incumbent capacity and proximity to the newly deployed site (*e.g.*, Site A2). Small incumbents (A4) obtain the largest proportional QoE improvements from proximate high-power diversion; mid-sized, nearby sites (A3, A5) obtain the largest absolute congestion relief concentrated in peak weeks; and larger or more distant stations (A6–A8) either absorb redistributed volume or

receive negligible diverted flows with modest QoE impact. Also, seasonality amplifies CF vs. Actual divergence, for instance, the October to December 2023 period witnessed the largest absolute differences in waiting time and utilization across the examined sites.

Finally, Site A2 operated primarily as an absorptive high-power site throughout the examined period, with weekly $N_{\mathrm{AC}}^{\mathrm{A}}$ rising from low single digits in summer to a late autumn/early winter peak (mean of 6.07 EV/week; median of 5.15; maximum of 12.0), and $N_{\mathrm{AC}}^{\mathrm{S}}$ EVs closely tracking demand (maximum of 11.94). The simulation results show minimal QoE degradation for most weeks: W_{AC} remained very low (minimum of 0.0017 minutes; median of 0.063 minutes; mean of 0.174 minutes; maximum of 0.80 minutes; as shown in Fig. 7.6(a)), U_{AC} is modest (mean $\approx 2.2\%$ with peaks $\approx 9.4\%$; as shown in Fig. 7.6(b)), and $N_{\mathrm{AC}}^{\mathrm{B}}$ EVs is negligible (≈ 0.04 total). Late season weeks exhibited localized stress, with $N_{\mathrm{AC}}^{\mathrm{W}}$ EVs peaking at 1.38 and short episodes of queuing under seasonal demand spikes. These findings confirm that A2 effectively intercepted and absorbed diverted demand during peak weeks, relieving smaller nearby sites, while maintaining ample headroom for most of the period. Operationally, A2's profile supports its role as an effective congestion mitigation deployment but suggests value in monitoring the peak periods (*e.g.*, late autumn), considering EV demand-aware operational measures to prevent transient queuing as seasonal load intensifies.

Accordingly, the policy and operational implications follow directly from these outcomes: (1) siting high-power L3 capacity where it can intercept dense, high variance demand within roughly a 3 km radius threshold (adjusted regionally to reflect local EV community characteristics) results the greatest marginal QoE improvements; (2) small, capacity constrained incumbents obtain the largest proportional benefits, while mid-sized nearby incumbents obtain the largest absolute congestion relief during peak demand; and, (3) absorptive Sites such as A2 should be closely monitored during peak EV demand periods (*e.g.*, late autumn), as the observed maxima in waiting time and utilization indicate short episodes of queuing that could be mitigated through demand-aware operational measures (*e.g.*, dynamic pricing windows, temporary or backup capacity, or rerouting of EV requests).

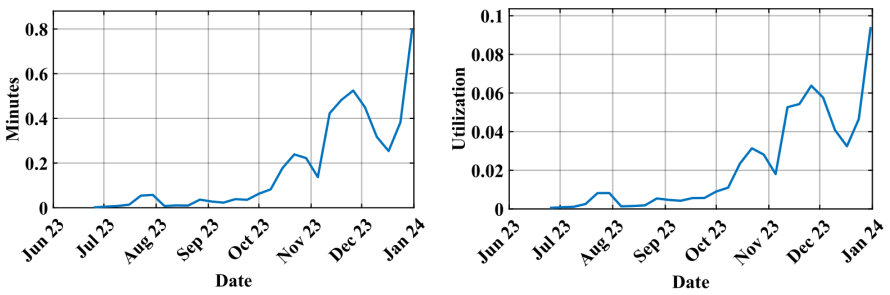

(a) Waiting time (b) Utilization

Figure 7.6: Site A2. (a) Waiting time, (b) utilization; Analysis window: $14:00$–$18:00$.

7.6 Conclusion

This study develops a data-driven framework for quantifying the site level impacts of L3 public fast charger deployments and for translating those impacts into practical and applicable useful QoE metrics. The core contributions are a causal inference pipeline that isolates the deployment effect of a new high-power sites from confounding influences (*e.g.*, spatial proximity, dynamic outlet capacity, and local amenity access), a scenario based spatial model that simulates alternative relocation/deployment configurations, and a temporal monitoring component that detects evolving congestion hotspots following each deployment. Forecasts of counterfactual session counts are generated by a gradient boosted model and are then fed into an accurate M/G/C/K queueing model with with realistic empirically fitted service times. Exhaustive simulations were conducted to evaluate the EV user-perceived QoE performance in terms of blocking probability, average waiting time, utilization and queue length. Using a case study of two major cities, this work shows that high power L3 installations principally relieve local congestion within roughly a 3 km radius, with capacity normalized effects larger for small incumbent public EV charging sites and more diffuse reductions for large depots. Sequential deployments also improved model calibration and forecasting accuracy: the forecasted error converged rapidly after each deployment, and the framework successfully captured seasonal and event driven demand fluctuations. Overall, the methodology transforms descriptive diagnostics into prescriptive, investment-grade decision support: operators can use the proposed pipeline to compare deployment options, estimate congestion relief benefits, and select site and capacity parameters that balance performance and budgetary constraints.

Chapter 8
Conclusion and Next Steps for Research

The accelerating global shift from fossil-fuel transport to electric mobility, driven by mounting urgency to address climate change, places EVs and public charging infrastructure at the center of modern urban mobility and power-system planning. This thesis presents a coherent, data-driven program of work that improves how operators and infrastructure planners model, monitor, and manage public EV charging to optimize and maintain EV users Quality of Experience (QoE) during the service. Our contributions are fivefold, each corresponding to a major work in this thesis.

First, we perform an accurate empirical and analytical study of real-world charging-session records and use the resulting insights to construct more accurate queueing models for public EV charging sites. Contrary to common assumptions, per-site EV arrivals do not always follow Poisson processes. Second, we develop a site-level, data-driven framework for novel QoE performance metrics and EV demand forecasting for the Public Charging Infrastructure (PCI). We design a forecast model that accurately predicts the evolution of EV charging requests at each site and apply it to 14 representative locations to examine trends in occupancy, utilization, blocking probability, and queue length.

Third, we present an interactive, operator-focused mapping and analysis tool that converts empirical charging session records into spatio-temporal intelligence to support QoE assessment and guide infrastructure planning. The tool supports configurable temporal granularity (monthly, quarterly, daily), per-site QoE metrics (utilization, blocking probability, waiting time, EV battery state-of-charge statistics, peak load factor, etc.), amenity and competitor overlays, and a hexagonal choropleth view that highlights congestion hot spots. Fourth, we introduce DICT, a novel demand-informed charging threshold scheme that discourages EV users from charging beyond an $(\chi = 80\%)$ State of Charge (SoC) threshold to reduce long, low-power tail charging sessions that inflate service times and degrade QoE. Fifth, we develop a causal, data-driven pipeline machine learning model to quantify site-level impacts of L3 fast-charger deployments and translate those impacts into practical QoE metrics. The core contributions are: (a) a causal-inference model that isolates the deployment effect from confounders (spatial proximity, dynamic outlet capacity, local amenity access), and (b) a temporal monitoring component that detects evolving congestion hot spots after each deployment.

Taken together, these contributions represent a tightly coupled set of theory, simulation, forecasting, modeling, and operator tools that advance both the science and practice of public EV charging planning. They demonstrate how empirical session data, when combined with appropriate statistical characterization, validated queueing models, and causal-spatial analyses can meaningfully improve forecasting, investment prioritization, and demand-management strategies.

Future research should systematically extend and address the empirical and modeling limitations and capabilities identified in this thesis to improve the reliability and accuracy of waiting-time estimates, planning tools, and EV demand and QoE analysis. Priority should be given to collecting high-fidelity field data (precise arrival timestamps) and running validation studies that compare modeled versus observed queueing outcomes; complementary work must develop scenario-driven arrival and service-time models that capture realistic perturbations such as planned/unplanned station outages, temporary decommissioning, municipal rerouting, special events, and seasonal or weather-driven variability. To implement these scenarios, embed them in stress tests and sensitivity analyses to quantify how surrounding EV charging capacity absorbs redirected EV demands, how quickly stations queues grow, and which investments or short-term measures (e.g., time limits, reservation enforcement, targeted dynamic pricing) best maintain user QoE during disruptions.

Methods and models should progress from retrospective analysis to near-real-time performance support and assessment, and incorporate behavioral factors such as balking probability, the probability that an arriving driver, after seeing a station's current queue length or estimated waiting time, decides not to enter that station's queue (in this thesis, balking was represented as the number of blocked EVs, i.e., arrivals denied service when no waiting slots were available; future work should extend this treatment to other balking mechanisms such as drivers deterred by long expected waits or partial-capacity conditions), and reneging probability, the hazard that a driver who has joined the queue abandons before service. Because balking hides latent demand across the network and reneging reduces realized throughput and skews waiting time and reliability metrics, jointly modelling both yields corrected wait and blocking estimates, quantifies lost versus recoverable demand, and enables planners to evaluate policy levers (reservations, pricing, real-time information) that reduce abandonment and improve QoE. Future work should also extend the interactive mapping and analytics tool to ingest periodic, processed session feeds from studied cities and additional Quebec municipalities so operators and planners have province-wide, up-to-date statistics.

Additionally, incorporate two contextual data layers into the QoE analysis discussed in this thesis. The first, an electrical constraint layer, encodes smart grid and site topology and explicit equipment limits, transformer nameplate ratings and measured loading, feeder ampacity, spare capacity, distributed generation ties, voltage/phase constraints, and protec-

tion settings to evaluate the physical feasibility of proposed chargers and incremental public EV loads. The second, a utility-telemetry layer, supplies time-series Supervisory Control and Data Acquisition (SCADA), Advanced Metering Infrastructure (AMI), and Phasor Measurement Unit (PMU) style measures (feeder and transformer loading, substation demand curves, voltage profiles, and event flags for faults, outages, and EV demand response). Together these streams enable planners to correlate EV charging demand with grid stress, run realistic what-if scenarios, and support near-real-time alerting, while ensuring appropriate privacy, security, and access controls.

Moreover, integrate Distributed Energy Resources (DERs) and grid flexibility models into the expansion and deployment workflows by extending the queueing models and forecasting frameworks discussed in this thesis to represent on-site generation (solar, wind), behind the meter and centralized storage, and Vehicle-to-Grid (V2G) interactions, including their intermittency and state-of-charge dynamics. Specifically, co-optimize the public charging outlets siting and sizing with storage/DER capacity under stochastic demand and renewable supply to evaluate hybrid solutions that trade capital for operational flexibility and to quantify local hosting capacity, energy peak-demand relief, and resilience under outages or surges. In addition, future work should study fleet management, including monitoring, scheduling, routing, and State-of-Charge (SoC) management of commercial, shared, or municipal vehicle fleets, and embed these fleet controls into the deployment and QoE analysis to optimize and extend the capabilities of the public EV charging and better accommodate the growing EV communities into the public network more efficiently.

On the policy and market front, broaden the public EV demand management beyond the DICT scheme studied here to include dynamic pricing, time-window incentives, reservation-aware scheduling, EV SoC/distance-aware prioritization, and targeted incentives to draw EVs to underutilized sites. Accurately design and field-test these instruments, evaluating not only QoE (blocking, waiting, utilization) but also economic outcomes (revenue, cost-effectiveness) and behavioral acceptance through controlled and implemented models. Finally, implement and compare new, competitive, coherent, and robust machine-learning (ML)/Artificial Intelligence (AI) models to perform causal inference of EV fast-charging deployments; evaluate each model's accuracy and select the most reliable for downstream charging-session causal estimates. Building on these selected causal estimates, tightly couple the causal-inference and forecasting outputs with modern ML optimization: apply the causal estimates of deployment impacts as inputs to constrained optimization algorithms that recommend site locations, capacities, and sequencing to meet configured QoE thresholds (e.g., utilization, average waiting time, peak-load factor) while respecting smart-grid constraints and budget limits.

Appendix:

List of Publications

Journal Articles

1. N. Al-Dahabreh, M. Khabbaz, M. A. Sayed, R. Atallah and C. Assi, "A data-driven framework for improving public EV charging infrastructure: Modeling and forecasting," in *IEEE Transactions on Intelligent Transportation Systems*, vol. 25, no. 6, pp. 5935–5948, 2023.

2. M. Elhattab, M. Khabbaz, N. Al-Dahabreh, R. Atallah and C. Assi, "Leveraging real-world data sets for QoE enhancement in public electric vehicles charging networks," in *IEEE Transactions on Network and Service Management*, vol. 21, no. 1, pp. 217–231, 2023.

Conference Proceedings

1. N. Al-Dahabreh, M. Khabbaz, M. A. Sayed, R. Atallah and C. Assi, "A Novel Data-driven Incentive-based Charging Service Truncation Scheme To Improve the QoS Performance of Public EV Charging Stations," in *2024 IEEE International Conference on Smart Mobility (SM)*, 2024, pp. 147–152.

2. R. Atallah, N. Al-Dahabreh, M. A. Sayed, K. Sarieddine, M. Elhattab, M. Khabbaz and C. Assi, "Quality of Service Evaluation and Forecast for EV Charging Based on Real-World Data," in *2023 19th International Conference on Wireless and Mobile Computing, Networking and Communications (WiMob)*, 2023, pp. 280–285.

Submitted / Under Review

1. N. Al-Dahabreh, M. Khabbaz, M. A. Sayed, R. Atallah and C. Assi, "A Novel Data-driven Incentive-based Charging Service Truncation Scheme to Improve the QoS Performance of Public EV Charging Stations," (Regular Papers), received by the Administrative Center for *IEEE Transactions on Intelligent Transportation Systems*, Oct. 21, 2025 (under review).

2. N. Al-Dahabreh, M. Khabbaz, M. A. Sayed, R. Atallah and C. Assi, “A Data-Driven Framework for Improving Public EV Charging Infrastructure Deployment: Quantifying EV Demand Shifting Via Machine Learning,” (Regular Papers), received by the Administrative Center for *IEEE Transactions on Intelligent Transportation Systems*, Sept. 30, 2025 (under review).

Software / Tools

1. N. Al-Dahabreh, “Interactive Decision-Support Tool for QoE Analysis at Public EV Charging Stations” (full code implementation, documentation of use, demos, and installation instructions), delivered to Hydro-Québec, Sept. 2024.

Bibliography

[1] R. Irle and T. Geggus. (2024, September) Is the global EV market slowing down? Autovista24 (Autovista Group). [Online]. Available: https://autovista24.autovistagroup.com/news/is-the-global-ev-market-slowing-down/

[2] IEA. (2025) Global EV outlook 2025. International Energy Agency. [Online]. Available: https://www.iea.org/reports/global-ev-outlook-2025

[3] ——. (2024) Number of electric light-duty vehicles per public charging point and kilowatt per electric light-duty vehicle, 2023. IEA - Data & Statistics, Chart. Licence: CC BY 4.0. [Online]. Available: https://www.iea.org/data-and-statistics/charts/number-of-electric-light-duty-vehicles-per-public-charging-point-and-kw-per-electric-light-duty-vehi

[4] ——. (2025) Number of electric light-duty vehicles per public charging point and kilowatt per electric light-duty vehicle, 2024. IEA - Data & Statistics, Chart. Licence: CC BY 4.0. [Online]. Available: https://www.iea.org/data-and-statistics/charts/number-of-electric-light-duty-vehicles-per-public-charging-point-and-kilowatt-per-electric-light-duty

[5] Wikipedia contributors. (2025) Trouvé tricycle. Wikipedia – Die freie Enzyklopädie. Last edited: 9 May 2025; License: Creative Commons Attribution-ShareAlike. [Online]. Available: https://de.wikipedia.org/w/index.php?title=Trouv%C3%A9_Tricycle&oldid=255858350

[6] ——. (2025) General motors EV1. Wikipedia – The Free Encyclopedia. Last edited: 23 September 2025; License: Creative Commons Attribution-ShareAlike 4.0. [Online]. Available: https://en.wikipedia.org/w/index.php?title=General_Motors_EV1&oldid=1312857491

[7] ElectricCarCharger.au. (n.d.) The short history of electric car chargers. ElectricCarCharger.au (Proelecx Pty Ltd). No publication date listed on page; site footer: Proelecx Pty Ltd. [Online]. Available: https://electriccarcharger.au/short-history-of-electric-car-chargers/

[8] AALED. (2024, September) The history of EV charging. AALED – Blog. Posted: September 3, 2024. [Online]. Available: https://aaled.ca/the-history-of-ev-charging/

[9] S. Varshney, K. P. Panda, M. Gupta, M. Shah, B. A. Srinivas, M. Bajaj, V. Blazek, and L. Prokop, "Stochastic modeling of electric vehicle infrastructure using queueing-theoretical approach," *Results in Engineering*, vol. 25, p. 104149, 2025.

[10] E. Circuit, "Vehicle characteristics and impact on charging," 2024, available at: Electric Circuit - Vehicle Characteristics and Impact on Charging.

[11] IEA. (2025) Trends in electric car markets — global EV outlook 2025. IEA Analysis. [Online]. Available: https://www.iea.org/reports/global-ev-outlook-2025/trends-in-electric-car-markets-2

[12] T. Geggus. (2025, February) What are the global EV market's most successful brands? Autovista24 (Autovista Group). [Online]. Available: https://autovista24.autovistagroup.com/news/what-are-the-global-ev-markets-most-successful-brands/

[13] S. Bukold. (2025, July) The global electric car market in 2025 (july update). EnergyComment. [Online]. Available: https://www.energycomment.de/the-global-electric-car-market-in-2025-july-update/

[14] 1Charging. (n.d.) The 80/20 ev charging rule: Ev battery charging best practices. [Online]. Available: https://1charging.com/the-80-20-ev-charging-rule-ev-battery-charging-best-practices/

[15] S. S. Ali *et al.*, "An overview of electric vehicle charging data acquisition and grid connection standards for power system studies and EV-grid integration," in *Proceedings of the IEEE AUPEC*, 2021.

[16] Open Data Team (Perth & Kinross). (2021) Electric vehicle charging station usage in perth and kinross. [Online]. Available: https://data.pkc.gov.uk/dataset/ev-charging-data

[17] A.-O. Yvenn *et al.*, "A review of electric vehicle load open data and models," *Energies*, vol. 14, no. 8, 2021.

[18] M. Lahariya *et al.*, "Defining a synthetic data generator for realistic electric vehicle charging sessions," in *Proceedings of the ACM e-Energy*, 2020.

[19] M. Akil *et al.*, "Impact of electric vehicle charging profiles in data-driven framework on distribution network," in *Proceedings of the IEEE International Conference on Smart Grid (icSmartGrid)*, 2021.

[20] ——, "Uncoordinated charging profile of EVs based on an actual charging session data," in *Proceedings of the IEEE International Conference on Renewable Energy Research and Applications (ICRERA)*, 2021.

[21] M. Lahariya *et al.*, "Synthetic data generator for electric vehicle charging sessions: Modeling and evaluation using real-world data," *Energies*, vol. 13, no. 6, 2020.

[22] M. Akil *et al.*, "Energy management for EV charging based on solar energy in an industrial microgrid," in *Proceedings of the IEEE International Conference on Renewable Energy Research and Applications (ICRERA)*, 2020.

[23] T. Harighi *et al.*, "Overviewing quality of electric vehicle charging stations' service evaluation," *International Journal of Smart Grid*, vol. 2, no. 1, 2018.

[24] A. Moradipari *et al.*, "Mobility-aware electric vehicle fast charging load models with geographical price variations," *IEEE Transactions on Transportation Electrification*, vol. 7, no. 2, 2021.

[25] P. Xu *et al.*, "Dynamic pricing at electric vehicle charging stations for queueing delay reduction," in *Proceedings of the IEEE International Conference on Distributed Computing Systems (ICDCS)*, 2017.

[26] S. Gonzalez *et al.*, "Routing and charging facility location for EVs under nodal pricing of electricity: A bilevel model solved using special ordered set," *IEEE Transactions on Smart Grid*, 2022, pp. 99 (preprint).

[27] C. B. Saner *et al.*, "A cooperative hierarchical multi-agent system for EV charging scheduling in presence of multiple charging stations," *IEEE Transactions on Smart Grid*, vol. 13, no. 3, 2022.

[28] S. Guner *et al.*, "Stochastic energy storage capacity model of EV parking lots," *IET Generation, Transmission & Distribution*, vol. 11, no. 7, 2017.

[29] S. S. Fazeli *et al.*, "Two-stage stochastic choice modeling approach for electric vehicle charging station network design in urban communities," *IEEE Transactions on Intelligent Transportation Systems*, vol. 22, no. 5, 2021.

[30] X. Huang *et al.*, "Research on parking sharing strategies considering user overtime parking," *PLoS One*, vol. 15, no. 6, 2020.

[31] F. M. Aboshady *et al.*, "Stochastic modeling of vehicle arrival for the uk's first electric vehicle charging forecourt," in *Proceedings of the IEEE Innovative Smart Grid Technologies (ISGT)*, 2021.

[32] J. Liu *et al.*, "Optimal EV charging scheduling by considering the limited number of chargers," *IEEE Transactions on Transportation Electrification*, vol. 7, no. 3, 2021.

[33] C. Lian *et al.*, "Optimal EV charging scheduling considering the charging characteristics of EV batteries," in *Proceedings of the IEEE iSPEC*, 2021.

[34] Y. Yuan *et al.*, "Scheduling online EV charging demand response via v2v auctions and local generation," *IEEE Transactions on Intelligent Transportation Systems*, 2021, pp. 99 (preprint).

[35] H. Akbari *et al.*, "Modeling and optimization of phev charging queues," in *Proceedings of the IEEE Canadian Conference on Electrical and Computer Engineering (CCECE)*, 2015.

[36] I. Zenginis *et al.*, "Analysis and quality of service evaluation of a fast charging station for electric vehicles," *Energy*, vol. 112, 2016.

[37] M. Rashid, T. Elfouly, and N. Chen, "A comprehensive survey of electric vehicle charging demand forecasting techniques," *IEEE Open Journal of the Vehicular Technology Society*, vol. 5, 2024.

[38] J. Soares, B. Canizes, C. Lobo, Z. Vale, and H. Morais, "Electric vehicle scenario simulator tool for smart grid operators," *Energies*, vol. 5, no. 6, pp. 1881–1899, 2012.

[39] J. F. Brady and M. O'Mahony, "Modelling charging profiles of electric vehicles based on real-world electric vehicle charging data," *Sustainable Cities and Society*, vol. 26, pp. 203–216, 2016.

[40] M. K. Gerritsma, T. A. AlSkaif, H. A. Fidder, and W. G. J. H. M. van Sark, "Flexibility of electric vehicle demand: Analysis of measured charging data and simulation for the future," *World Electric Vehicle Journal*, vol. 10, no. 1, p. 14, 2019.

[41] M. G. Flammini, G. Prettico, A. Julea, G. Fulli, A. Mazza, and G. Chicco, "Statistical characterisation of the real transaction data gathered from electric vehicle charging stations," *Electric Power Systems Research*, vol. 166, pp. 136–150, 2019.

[42] N. Sadeghianpourhamami, N. Refa, M. Strobbe, and C. Develder, "Quantitive analysis of electric vehicle flexibility: a data-driven approach," *International Journal of Electrical Power & Energy Systems*, vol. 95, pp. 451–462, 2018.

[43] J. Zhu, Z. Yang, Y. Guo, J. Zhang, and H. Yang, "Short-term load forecasting for electric vehicle charging stations based on deep learning approaches," *Applied Sciences*, vol. 9, no. 9, p. 1723, 2019.

[44] T. Unterluggauer *et al.*, "Electric vehicle charging infrastructure planning for integrated transportation and power distribution networks: A review," *eTransportation*, vol. 12, 2022.

[45] S. Vashisth *et al.*, "Multi-stage planning of fast charging stations for pevs using traffic-based approach," *Sustainable Energy, Grids and Networks*, vol. 30, 2022.

[46] O. Hafez *et al.*, "Queueing analysis based pev load modeling considering battery charging behavior and their impact on distribution system operation," *IEEE Transactions on Smart Grid*, vol. 9, no. 1, 2016.

[47] (2016) Waterloo region transportation tomorrow survey. [Online]. Available: http://dmg.utoronto.ca/transportation-tomorrow-survey/tts-reports

[48] Z. Yi *et al.*, "Electric vehicle demand estimation and charging station allocation using urban informatics," *Transportation Research Part D: Transport and Environment*, vol. 106, 2022.

[49] L. Page *et al.*, "The pagerank citation ranking: Bringing order to the web," Stanford InfoLab, Technical Report, 1999. [Online]. Available: http://ilpubs.stanford.edu:8090/422/

[50] A. Orzechowski *et al.*, "A data-driven framework for medium-term electric vehicle charging demand forecasting," *Energy and AI*, vol. 14, 2023.

[51] M. E. Kabir *et al.*, "Demand-aware provisioning of electric vehicles fast charging infrastructure," *IEEE Transactions on Vehicular Technology*, vol. 69, no. 7, 2020.

[52] M. E. Khodayar *et al.*, "Hourly coordination of electric vehicle operation and volatile wind power generation in scuc," *IEEE Transactions on Smart Grid*, vol. 3, no. 3, 2012.

[53] Y. Cao *et al.*, "An optimized ev charging model considering tou price and soc curve," *IEEE Transactions on Smart Grid*, vol. 3, no. 1, 2012.

[54] J. Antoun *et al.*, "A data driven performance analysis approach for enhancing the qos of public charging stations," *IEEE Transactions on Intelligent Transportation Systems*, vol. 23, no. 8, 2022.

[55] M. B. Arias *et al.*, "Electric vehicle charging demand forecasting model based on big data technologies," *Applied Energy*, vol. 183, 2016.

[56] Y. Mu *et al.*, "A spatial-temporal model for grid impact analysis of plug-in electric vehicles," *Applied Energy*, vol. 114, 2014.

[57] H. Wang *et al.*, "Load characteristics of electric vehicles in charging and discharging states and impacts on distribution systems," in *Proceedings of SUPERGEN*, China, 2012.

[58] K. Qian *et al.*, "Modeling of load demand due to ev battery charging in distribution systems," *IEEE Transactions on Power Systems*, vol. 26, no. 2, 2011.

[59] A. Lojowska *et al.*, "From transportation patterns to power demand: Stochastic modeling of uncontrolled domestic charging of electric vehicles," in *Proceedings of the IEEE Power and Energy Society General Meeting*, United States, 2011.

[60] T.-Y. Ma *et al.*, "Multistep electric vehicle charging station occupancy prediction using hybrid LSTM neural networks," *Energy*, vol. 244, 2022.

[61] J. Bergstra *et al.*, "Algorithms for hyper-parameter optimization," in *Advances in Neural Information Processing Systems*, 2011.

[62] G. S. Linoff *et al.*, *Data Mining Techniques: For Marketing, Sales and Customer Relationship Management*. John Wiley & Sons, 2011.

[63] A. J. Smola *et al.*, "A tutorial on support vector regression," *Statistics and Computing*, vol. 14, 2004.

[64] T.-K. Ho, "Random decision forest," in *Proceedings of the IEEE International Conference on Document Analysis and Recognition*, Canada, 1995.

[65] Y. Freund *et al.*, "A decision-theoretic generalization of on-line learning and an application to boosting," *Journal of Computer and System Sciences*, vol. 55, no. 1, 1997.

[66] M. H. Amini *et al.*, "Arima-based decoupled time series forecasting of electric vehicle charging demand for stochastic power system operation," *Electric Power Systems Research*, vol. 140, 2016.

[67] S. K. Manujith *et al.*, "Comparative analysis of deep learning models for electric vehicle charging load forecasting," *Journal of the Institution of Engineers (India): Series B*, vol. 104, 2023.

[68] H. Woo, Y. Son, J. Cho, S. Kim, and S. Choi, "Optimal expansion planning of electric vehicle fast charging stations," *Applied Energy*, vol. 342, p. 121116, 2023.

[69] H. Gan, W. Ruan, M. Wang, Y. Pan, H. Miu, and X. Yuan, "Bi-level planning of electric vehicle charging stations considering spatial–temporal distribution characteristics of charging loads in uncertain environments," *Energies*, vol. 17, no. 12, p. 3004, 2024.

[70] R. Brahmachary and I. Ahmed, "Optimal distribution network expansion and ev charging station allocation based on load forecasted using machine learning," *IEEE Transactions on Industry Applications*, 2025.

[71] Y. Li, S. Chai, X. Zhang, G. Wang, R. Zhu, and E. Chung, "Stpnet: Quantifying the uncertainty of electric vehicle charging demand via long-term spatiotemporal traffic flow prediction intervals," *IEEE Transactions on Intelligent Transportation Systems*, 2023.

[72] H. Zhao, H. Yang, Y. Wang, D. Wang, and R. Su, "Attention based graph bi-lstm networks for traffic forecasting," in *2020 IEEE 23rd International Conference on Intelligent Transportation Systems (ITSC)*. IEEE, 2020, pp. 1–6.

[73] A. Orzechowski, L. Lugosch, H. Shu, R. Yang, W. Li, and B. H. Meyer, "A data-driven framework for medium-term electric vehicle charging demand forecasting," *Energy and AI*, vol. 14, p. 100267, 2023.

[74] Y. Bao, F. Chang, J. Shi, P. Yin, W. Zhang, and D. W. Gao, "An approach for pricing of charging service fees in an electric vehicle public charging station based on prospect theory," *Energies*, vol. 15, no. 14, p. 5308, 2022.

[75] F. Meng, W. Pei, Q. Zhang, Y. Zhang, B. Ma, and L. Li, "Research on the capacity of charging stations based on queuing theory and energy storage scheduling optimization sharing strategy," *Journal of Energy Storage*, vol. 96, p. 112673, 2024.

[76] L. Cui, Q. Wang, H. Qu, M. Wang, Y. Wu, and L. Ge, "Dynamic pricing for fast charging stations with deep reinforcement learning," *Applied Energy*, vol. 346, p. 121334, 2023.

[77] Y. Li, J. Wang, W. Wang, C. Liu, and Y. Li, "Dynamic pricing-based electric vehicle charging station location strategy using reinforcement learning," *Energy*, vol. 281, p. 128284, 2023.

[78] L. Bitencourt, W. N. Silva, B. H. Dias, T. P. Abud, B. Borba, and P. Peters, "Comprehensive methodology for assessing the impact of vehicle-to-grid integration in power system expansion planning," *Renewable Energy Focus*, p. 100718, 2025.

[79] L. Su, K. M. Gurumurthy, and K. M. Kockelman, "Siting and sizing of public–private charging stations: Impacts on household and electric vehicle fleets," *Transportation Research Part A: Policy and Practice*, vol. 195, p. 104436, 2025.

[80] R. Riemann *et al.*, "Optimal location of wireless charging facilities for electric vehicles: Flow-capturing location model with stochastic user equilibrium," *ELSEVIER TRP C: ET*, vol. 58, 2015.

[81] C. Cisiszár *et al.*, "Urban public charging station locating method for electric vehicles based on land use approach," *ELSEVIER JTG*, vol. 74, 2019.

[82] Z. Sun *et al.*, "Locating charging stations for electric vehicles," *ELSEVIER TP*, vol. 98, 2020.

[83] C. Hecht *et al.*, "Electric vehicle rout planning using real-world charging infrastructure in germany," *ELSEVIER eTransp.*, vol. 10, 2021.

[84] C. A. Vandet *et al.*, "Optimal placement and sizing of charging infrastructure for EVs under information-sharing," *ELSEVIER TSFC*, vol. 187, 2023.

[85] A. Kapoor *et al.*, "Optimal planning of fast EV charging stations in a coupled transportation and electrical power distribution network," *IEEE TASE*, 2023, pP:99.

[86] Q. Yang *et al.*, "Optimal sizing of pev fast charging stations with markovian demand characterization," *IEEE TSG*, vol. 10, no. 4, 2019.

[87] M. Elhattab *et al.*, "Leveraging real-world data sets for qoe enhancement in public Electric Vehicles charging networks," *IEEE TNSM*, vol. 21, no. 1, 2024.

[88] F. B. Hüttel *et al.*, "Mind the gap: Modelling difference between censored and uncensored Electric Vehicle charging demand," *ELSEVIER TRP C: ET*, vol. 153, 2023.

[89] ——, "Modelling censored mobility demand through censored quantile regression neural networks," *IEEE TITS*, vol. 23, no. 11, 2022.

[90] Z. Rafi, R. Sheinberg, S. N. Gowda, K. S. Sigarchi, and R. Gadh, "A framework for optimal sizing of heavy-duty electric vehicle charging stations considering uncertainty," *World Electric Vehicle Journal*, vol. 16, no. 6, p. 318, 2025.

[91] J. A. Guerrero-Silva, J. I. Romero-Gelvez, A. J. Aristizábal, and S. Zapata, "Optimization and trends in ev charging infrastructure: A pca-based systematic review," *World Electric Vehicle Journal*, vol. 16, no. 7, p. 345, 2025.

[92] E. Ucer *et al.*, "Modeling and analysis of a fast charging station and evaluation of service quality for electric vehicles," *IEEE Transactions on Transportation Electrification*, 2019.

[93] Quebec Ministry of Energy and Natural Resources. (2022) Public charging stations. [Online]. Available: https://vehiculeselectriques.gouv.qc.ca/english/decouvrir/recharge/recharge-publique.asp

[94] The Electric Circuit. The electric circuit. [Online]. Available: https://lecircuitelectrique.com/

[95] Electric Vehicle Council. (2021) Electric vehicle consumer behavior. Fuels Institute. [Online]. Available: https://www.fuelsinstitute.org/Research/Reports/EV-Consumer-Behavior/EV-Consumer-Behavior-Report.pdf

[96] D. Said *et al.*, "Queuing model for evs charging at public supply stations," in *Proceedings of IEEE International Wireless Communications and Mobile Computing Conference (IWCMC)*, 2013.

[97] H. Chen *et al.*, "Plug-in electric vehicle charging congestion analysis using taxi travel data in the central area of beijing," arXiv preprint arXiv:1712.07300, 2017. [Online]. Available: http://arxiv.org/abs/1712.07300

[98] I. Zenginis *et al.*, "Analysis and quality of service evaluation of a fast charging station for Electric Vehicles," *Energy*, vol. 112, 2016.

[99] M. Khabbaz *et al.*, "A simple free-flow traffic model for vehicular intermittently connected networks," *IEEE Transactions on Intelligent Transportation Systems*, vol. 13, no. 3, 2012.

[100] M. Khabbaz, "Ieee 802.11 wireless mesh networks: Accurate mac modeling and novel routing metrics and protocol design proposals," M.Sc.E. Thesis, Lebanese American University, 2008.

[101] D. Anderson *et al.*, "Measurement of abb's prototype fast charging station for electric vehicles," M.Sc. Thesis, Chalmers University of Technology, 2012.

[102] D. V. Lindley, "The theory of queues with a single server," *Proceedings of the Cambridge Philosophical Society*, vol. 48, 1952.

[103] F. Spitzer, "The wiener–hopf equation whose kernel is a probability density," *Duke Mathematical Journal*, vol. 24, 1957.

[104] N. U. Prabhu, *Wiener–Hopf Techniques in Queueing Theory*, ser. Mathematical Methods in Queueing Theory. Springer, 1974.

[105] L. Kleinrock, *Queueing Systems, Volume I: Theory*. Wiley-Interscience, 1975.

[106] W. L. Smith, "On the distribution of queueing times," *Proceedings of the Cambridge Philosophical Society*, vol. 49, 1953.

[107] S. Foss, "The $G/G/1$ queue," in *Wiley Encyclopedia of Operations Research and Management Science*. Wiley, 2011.

[108] D. G. Zill *et al.*, *Advanced Engineering Mathematics, 3rd Edition*. Jones & Bartlett, 2006.

[109] D. R. Cox, “A use of complex probabilities in the theory of stochastic processes,” *Proceedings of the Cambridge Philosophical Society*, vol. 51, 1955.

[110] E. C. Titchmarsh, *Theory of Functions*. Oxford University Press, 1952.

[111] IEA. (2022) Global ev outlook 2022. IEA. Paris. [Online]. Available: https://www.iea.org/reports/global-ev-outlook-2022

[112] K. Chatfield *et al.*, “The devil is in the details: an evaluation of recent feature encoding methods,” in *BMVC*, vol. 2, no. 4, 2011.

[113] B. Roy. All about categorical variable encoding. [Online]. Available: https://towardsdatascience.com/all-about-categorical-variable-encoding-305f3361fd02

[114] A. I. McLeod and K. W. Hipel, “Seasonal time series models in engineering and environmental studies,” *Journal of the American Statistical Association*, vol. 76, no. 374, pp. 31–36, 1981.

[115] J. Fattah, “Forecasting of demand using arima model,” *International Journal of Engineering Business Management*, vol. 10, 2018.

[116] WiTricity, “The 80% rule,” The 80% Rule - WiTricity, 2024, accessed: 2024-12-20.

[117] M. Khabbaz, “Ieee 802.11 wireless mesh networks: Accurate mac modeling and novel routing metrics and protocol design proposals,” 2008, doctoral dissertation.

[118] J. Smith, “Optimal design and performance modelling of m/g/1/k queueing systems,” *Mathematical and Computer Modelling*, vol. 39, no. 9-10, pp. 1049–1081, 2004.

[119] N. Al-Dahabreh, M. Khabbaz, M. A. Sayed, R. Atallah, and C. Assi, “A novel data-driven incentive-based charging service truncation scheme to improve the qos performance of public ev charging stations,” in *Proceedings of the IEEE International Conference on Smart Mobility (SM)*, 2024, pp. 147–152.

[120] Statistics Canada, “Statistics canada official website,” 2024, government of Canada; Accessed: 2024-12-20. [Online]. Available: https://www.statcan.gc.ca/en/start

[121] N. Al-Dahabreh, M. A. Sayed, K. Sarieddine, M. Elhattab, M. J. Khabbaz, R. F. Atallah, and C. Assi, “A data-driven framework for improving public ev charging infrastructure: Modeling and forecasting,” *IEEE Transactions on Intelligent Transportation Systems*, vol. 25, no. 6, pp. 5935–5948, 2023.